Measurements of b-hadron lifetimes and the calibration and performance of the LHCb tracking system

THÈSE N° 6198 (2014)

PRÉSENTÉE LE 23 MAI 2014
À LA FACULTÉ DES SCIENCES DE BASE
LABORATOIRE DE PHYSIQUE DES HAUTES ÉNERGIES 3
PROGRAMME DOCTORAL EN PHYSIQUE

ÉCOLE POLYTECHNIQUE FÉDÉRALE DE LAUSANNE

POUR L'OBTENTION DU GRADE DE DOCTEUR ÈS SCIENCES

PAR

Frédéric Guillaume DUPERTUIS

EPFL

ÉCOLE POLYTECHNIQUE
FÉDÉRALE DE LAUSANNE

Suisse
2014

A ma grand-mère Jacqueline Dupertuis Tossings
et mon grand-père Antonio Domato Camba
qui nous ont quittés lors de ce travail de thèse
et qui laissent un grand vide derrière eux.

La plus grande récompense qu'un homme obtienne pour son labeur
n'est pas ce qu'il en a retiré, mais en quoi cela l'a transformé.
— John Ruskin

Remerciements

Je souhaite tout d'abord remercier mon directeur de thèse, Tatsuya Nakada, pour m'avoir donné l'opportunité de faire ce travail de thèse et pour avoir corrigé celui-ci. Ma reconnaissance va à Olivier Schneider qui m'a donné la passion pour le domaine de la physique des particules et qui a toujours trouvé du temps pour discuter avec moi de certains aspects de ma thèse. Je remercie également nos secrétaires, Erika Luthi et Esther Hofmann, qui ont réussi à réduire mes tâches administratives au strict minimum pour que je puisse disposer de plus de temps libre pour réaliser ma recherche. Je remercie le directeur de notre laboratoire, Aurélio Bay, ainsi que, Tâm Minh Tran, MER, les professeurs honoraires Maurice Gailloud et Raymond Weill pour leur soutien et les discussions que nous avons eues.

Je remercie les membres de mon jury de thèse, Prof. Henrik Rønnow, Prof. Christophorus Grab, Dr. Niels Tuning et Dr. Olivier Callot pour pour avoir lu, examiné et corrigé ce document et pour leur présence lors de l'examen de thèse.

Cette thèse n'aurait très certainement pas été aussi fructueuse sans l'encadrement exemplaire de nos fonctionnaies et collaborateurs scientifiques du laboratoire. De simples remerciements ne suffiront pas à exprimer ma gratitude envers Frédéric Blanc, mon homonyme, qui m'a toujours soutenu, écouté, conseillé et corrigé mes documents lors de ces quatre années de thèse. Je remercie aussi mes collègues "British" du laboratoire, Greig Cowan, Matthew Needham, Mark Tobin et Paul Szczypka qui ne m'ont pas seulement accompagné et encadré dans mon travail, mais qui m'ont aussi aidé à perfectionner mon anglais de façon significative. Merci à Guido Haefli, pour le temps passé à m'en apprendre davantage sur les cartes d'acquisition TELL1 de l'expérience LHCb.

Merci à Raphael Märki, qui depuis plus de 5 ans a été mon collègue de bureau, mon ami, avec qui j'ai énormément partagé. A mon ancien collègue et à présent ami, Johan Luisier, pour son encadrement lors de la reprise des tâches de service et du perfectionnement dans le domaine de la programmation. A mon ancien collègue et ami, Vincent Fave, pour l'aide et les discussions partagées au coin café, de même qu'à tous mes collègues pour les discussions, les rires, les repas de midi pris ensemble. A mes collègues "exotiques", Julien Rouvinet, Pierre Jaton et Bastien Muster pour les moments partagés dans leur bureau.

Remerciements

Merci à mes collègues de la collaboration LHCb, Francesca Dordei, Thomas Nikodem, Yasmine Amhis pour le merveilleux travail coopératif entrepris pour mener à bien l'analyse des temps de vie des hadrons b. Merci à Wouter Hulsbergen, Silvia Borghi, Abraham Gallas, Helge Voss, Sandra Saornil, Richard Jocobsson et Jeroen Van Tilburg pour leur soutien lors de mes tâches de service durant mes deux premières années de thèse, ainsi que tous ceux qui m'ont, de près ou de loin, aidé pendant ces quatre années de thèse.

A ma compagne, Virginie Dutrannois, qui m'a soutenu, encouragé, aimé et supporté depuis plus de 10 ans à présent.

Je remercie finalement mes parents, Loulou Dupertuis, Jean-François Aebi, Bernard Dupertuis, mes grand-parents, Jacqueline Dupertuis[†], Roger Dupertuis, Sara Domato, Antonio Domato[†], mon frère, Mickaël Dupertuis, qui m'ont toujours soutenu lors de mes longues études entreprises jusqu'à ce jour.

Lausanne, 28th March 2014   F.D.

Résumé

L'expérience LHCb a été conçue pour faire des mesures de haute précision. Le détecteur LHCb a d'excellentes capacités pour trouver les points de désintégration, la mesure de quantités de mouvement et l'identification des particules, grâce à une géométrie du détecteur et une stratégie de déclenchement adaptés pour l'étude de désintégrations rares et de violation de CP des quarks b et c.

Pour faire des mesures de précision, le détecteur doit être parfaitement calibré et son efficacité doit être suivi au cours du temps pour atteindre les performances requises.
Les cartes TELL1 sont responsables de l'acquisition et le pré-traitement des données brutes provenant du détecteur. De nouveaux effets sur les signaux émis par de la puce de lecture, le Beetle, du trajectographe interne (IT) and trajectographe Turicensis (TT) ont été découverts. Ces effets dépendent de la configuration de l'en-tête émis sur le Beetle. Des stratégies sont proposées afin de corriger les effets induis par l'entête des signaux et sont implémentées dans le firmware des cartes TELL1 de l'IT et du TT. De plus, des algorithmes plus rapides et des programmes sont développés pour effectuer la calibration des cartes TELL1 et le suivi des constantes issues de la calibration et tout ça est réalisé par une tâche quotidienne et unique. L'efficacité, la résolution spatiale de détection et le rapport signal sur bruit de l'IT et du TT sont mesurés et suivis pour les périodes d'acquisition de données en 2011 et 2012 en utilisant des échantillons propres de mésons J/ψ se désintégrant en une paire de deux muons.
Une nouvelle procédure pour l'alignement vertical (y) du trajectographe de LHCb est proposée en exploitant la présence de régions inactives dans le trajectographe. En utilisant cette procédure, cela permet d'aligner verticalement l'IT, le TT et le trajectographe externe (OT) avec une précision inférieure à 200 μm.

Une étude préliminaire des données collectées en 2010 par LHCb a montré un grand potentiel du détecteur pour les mesures de temps de vie des hadrons b dont les désintégrations contiennent des mésons J/ψ dans leurs états finaux. Le système de déclenchement utilisé de 2010 jusqu'au milieu de l'année 2011 sélectionnait les J/ψ sans prérequis sur la distance séparant le vertex de désintégration de ceux-ci et le point de collision des protons dont ils sont issus, donnant lieu à une dépendance linéaire de l'efficacité de reconstruction du temps de vie des hadrons b. A partir de l'été 2011, une nouvelle ligne de déclenchement fut utilisée pour sélectionner des hadrons b se désintégrant en un méson J/ψ avec un vertex de désintégration significativement déplacé par rapport au point de collisions des protons. Cette ligne de dé-

clenchement exploite la distance de vol finie des hadrons b pour réduire le taux de rétention du système de déclenchement. Cette condition requise sur le déplacement des J/ψ introduit des inefficacités supplémentaires dépendantes du temps de désintégration des hadrons b qui ne sont plus linéaires. Une investigation approfondie de ces efficacités pour cette nouvelle ligne de déclenchement est nécessaire pour les mesures de temps de vie des hadrons b.

L'analyse de la totalité des 1.0 fb^{-1} de données collectées par LHCb en 2011, des mesures de temps de vie dans cinq canaux de désintégration sont réalisées : $B^+ \to J/\psi\, K^+$, $B^0 \to J/\psi\, K^{*0}$, $B_s^0 \to J/\psi\, \phi$, $B^0 \to J/\psi\, K_S^0$ et $\Lambda_b^0 \to J/\psi\, \Lambda$. Les temps de vie mesurés dans ces cinq canaux sont :

$$\tau_{B^+ \to J/\psi\, K^+} = 1.637 \pm 0.004\,(\text{stat}) \pm 0.003\,(\text{syst})\,\text{ps},$$

$$\tau_{B^0 \to J/\psi\, K^{*0}} = 1.524 \pm 0.006\,(\text{stat}) \pm 0.004\,(\text{syst})\,\text{ps},$$

$$\tau_{B^0 \to J/\psi\, K_S^0} = 1.415 \pm 0.027\,(\text{stat}) \pm 0.006\,(\text{syst})\,\text{ps},$$

$$\tau_{B_s^0 \to J/\psi\, \phi} = 1.499 \pm 0.013\,(\text{stat}) \pm 0.005\,(\text{syst})\,\text{ps},$$

$$\tau_{\Lambda_b^0 \to J/\psi\, \Lambda} = 1.480 \pm 0.011\,(\text{stat}) \pm 0.005\,(\text{syst})\,\text{ps},$$

qui sont les mesures les plus précises actuellement et sont compatibles avec les prédictions théoriques et les valeurs moyennes mondiales. A partir des temps de vie mesurés dans les canaux $B^0 \to J/\psi\, K^{*0}$ et $B^0 \to J/\psi\, K_S^0$, le rapport de la différence des largeurs de désintégration, $\Delta\Gamma_d$, à la largeur moyenne de désintégration, Γ_d, pour le système $B^0 - \overline{B}^0$ est donné par

$$\frac{\Delta\Gamma_d}{\Gamma_d} = -0.044 \pm 0.025\,(\text{stat}) \pm 0.011\,(\text{syst}),$$

qui est aussi compatible avec les moyennes mondiales et les prédictions théoriques.

Abstract

The LHCb experiment was designed to perform high precision measurements. The LHCb detector has excellent vertexing, momentum measurement and particle identification capabilities, with a detector geometry and trigger strategy specially adapted for the study of rare decays and CP violation of b- and c-quarks.

For accurate measurements, the detector needs to be perfectly calibrated and its performance monitored to achieve the required performance.

The LHCb TELL1 boards are responsible for the acquisition and the pre-processing of the raw data. New effects on signals emitted by the front-end chip, the Beetle, of the Inner Tracker (IT) and Tracker Turicensis (TT) due to the different header configurations are discovered. Strategies to correct for these header effects are proposed and are implemented in the firmware of the IT and TT TELL1 boards. In addition, faster algorithms are developed to perform the calibration of the TELL1 boards and software is developed to perform the full calibration and a monitoring process as a single daily job.

The IT and TT hit efficiencies, hit spatial resolutions and signal-over-noise ratios were monitored and measured for the 2011 and 2012 data taking periods using clean samples of J/ψ particles decaying into a muon pair.

A novel procedure is proposed to align the LHCb tracking system in the vertical direction (y) exploiting the presence of insensitive regions in the tracking system. Using this procedure, it allows to align the IT, the TT and the Outer Tracker (OT), to be aligned vertically with a precision better than 200 μm.

A preliminary analysis of the small dataset recorded in 2010 by LHCb showed great potential to measure b-hadron lifetimes in decays with a J/ψ meson in the final state. The trigger system used from 2010 to the middle of 2011 selected J/ψ mesons without any requirement on the distance between the J/ψ decay vertex and the proton proton (pp) interaction point, leading to a linear dependence of the reconstruction efficiency as a function of the b-hadron decay time. Starting from Summer 2011, a new trigger line was used to select b hadrons with a significantly displaced decay vertex from the pp interaction point into a J/ψ. This trigger line exploits the finite flight distance of b hadrons in order to reduce the trigger rate. This displacement requirement introduces additional inefficiencies as a function of the b-hadron decay time which is no longer linear. Therefore, a deep understanding of the b-hadron decay time efficiency of this new trigger line is required for the measurements of b-hadron lifetimes.

Remerciements

Analysing the full 1.0 fb^{-1} data sample recorded in 2011, b-hadron lifetime measurements are performed for five decay modes: $B^+ \to J/\psi\, K^+$, $B^0 \to J/\psi\, K^{*0}$, $B^0_s \to J/\psi\, \phi$, $B^0 \to J/\psi\, K^0_S$ and $\Lambda^0_b \to J/\psi\, \Lambda$. The measured lifetimes in these decay modes are:

$$\tau_{B^+ \to J/\psi\, K^+} = 1.637 \pm 0.004\,(\text{stat}) \pm 0.003\,(\text{syst})\,\text{ps},$$

$$\tau_{B^0 \to J/\psi\, K^{*0}} = 1.524 \pm 0.006\,(\text{stat}) \pm 0.004\,(\text{syst})\,\text{ps},$$

$$\tau_{B^0 \to J/\psi\, K^0_S} = 1.415 \pm 0.027\,(\text{stat}) \pm 0.006\,(\text{syst})\,\text{ps},$$

$$\tau_{B^0_s \to J/\psi\, \phi} = 1.499 \pm 0.013\,(\text{stat}) \pm 0.005\,(\text{syst})\,\text{ps},$$

$$\tau_{\Lambda^0_b \to J/\psi\, \Lambda} = 1.480 \pm 0.011\,(\text{stat}) \pm 0.005\,(\text{syst})\,\text{ps},$$

which are the world's best measurements and are compatible with theoretical predictions and world averages. From the lifetime measurements in $B^0 \to J/\psi\, K^{*0}$ and $B^0 \to J/\psi\, K^0_S$ decay modes, the ratio of the decay-width difference, $\Delta\Gamma_d$, to the average decay width, Γ_d, for the $B^0 - \overline{B}^0$ system is measured to be

$$\frac{\Delta\Gamma_d}{\Gamma_d} = -0.044 \pm 0.025\,(\text{stat}) \pm 0.011\,(\text{syst}),$$

which is also compatible with world averages and theoretical predictions.

Table of Contents

1 The Standard Model of particle physics and *B* physics

1.1 The Standard Model of particle physics

The *Standard Model of particle physics* (SM) [1–3] is a quantum field theory that describes the propagation and interaction of the known elementary particles that are summarised in Table 1.1. In the SM, there are two kinds of particles: *Fermions* with spin 1/2 that follow Fermi-Dirac statistics and gauge *bosons* of spin 0, 1 or 2 that follow the Bose-Einstein statistics. Among the fermions, there are six *leptons*: electron (e^-), muon (μ^-), tau (τ^-), electron neutrino (ν_e), muon neutrino (ν_μ) and tau neutrino (ν_τ). And, there are six *quarks*: down (d), up (u), strange (s), charm (c), beauty/bottom (b) and truth/top (t). In addition to these twelve elementary particles (q), each has its own *anti-particles* ($\overline{q}$), thus there are twenty-four fermions in the SM. Whereas the leptons can be freely moving elementary particles, the quarks are always bound inside *hadrons*. Among hadrons, there are *mesons* that have quark content ($q\overline{q}'$) and *bayrons* having the quark combination ($qq'q''$). The *proton* (uud) and *neutron* (udd) are well-known baryons.

In nature, there are four identified interactions. The *nuclear strong interaction* or just *strong interaction* is responsible for quark confinement inside hadrons. The strong interaction is mediated by bosons called *gluons* (g). The *electromagnetic* interaction, driven by the photon (γ), is responsible for the attraction and repulsion of charged particles (six quarks that have either charge $+2/3$ or $-1/3$) and the three charged leptons (e^-, μ^-, τ^-) according to their electric charge. Then, the *nuclear weak interaction* or just *weak interaction*, mediated by the

Table 1.1: List of the particles of the Standard Model. The three families of fermions on the left and bosons responsible of the interactions on the right.

ν_e	ν_μ	ν_τ	$W^\pm/Z^0$
e^-	μ^-	τ^-	γ
u	c	t	g
d	s	b	
1	2	3	h

charged $W^\pm$ and neutral Z^0 bosons, are responsible for neutron decay, for example, through emission of a $W^\pm$ boson.

Finally, there is the gravitational force. This interaction however, driven by an hypothetical boson called the graviton, is not part of the SM. *Spontaneous symmetry breaking* (SBB) generates the masses of the $W^\pm$ and Z^0 bosons, and manifests itself as the *Higgs boson* [4–6]. One of the greatest news of this century in the field of particle physics, is the discovery of a Higgs-like boson by two LHC experiments in June 2012 [7, 8]. Following this discovery, Peter Higgs and François Englert received the prestigious Nobel Prize in Physics in 2013. Through *Yukawa couplings*, the Higgs field gives rise to fermion masses. Within the SM, the strong interaction is described by *Quantum Chromo Dynamic* (QCD) theory, the electromagnetic interaction by *Quantum Electro Dynamics* (QED) and the weak interaction in the framework of the *ElectroWeak Theory* (EWT).

Among several arguments, the fact that the SM do not include the gravitation, presently well-described by *General Relativity* (GR), and also because theorists would prefer to have a theory that unifies the three first interactions, and even the four interactions, makes the SM an incomplete theory. The discovery of physics beyond the SM, called *New Physics* (NP), is and will be one of the main goal of searches in the field of particle physics over the twenty-first century. Up to now, no significant sign of NP is observed.

1.2   Weak interaction and CKM matrix

In the SM, several quantum numbers are introduced in the model with their conservations to account for all the experimental results. For example, the *strangeness* (*s* quark), the *charm* (*c* quark), the *bottomness* (*b* quark) and the *topness* (*t* quark) quantum numbers conservation is introduced to avoid the decay of the $s/c/b/t$ quarks through strong and electromagnetic interactions. This is the *flavour conservation of strong and electromagnetic interactions*. However, the quarks can change their flavour by the $W^\pm$ bosons exchange of the weak interaction. The W^+ interaction coupling to quarks is proportional to

$$(u,c,t)\gamma^\mu W^+_\mu \begin{pmatrix} d' \\ s' \\ b' \end{pmatrix} = (u,c,t)\gamma^\mu W^+_\mu V_{\text{CKM}} \begin{pmatrix} d \\ s \\ b \end{pmatrix}, \qquad V_{\text{CKM}} = \begin{pmatrix} V_{ud} & V_{us} & V_{ub} \\ V_{cd} & V_{cs} & V_{cb} \\ V_{td} & V_{ts} & V_{tb} \end{pmatrix}, \qquad (1.1)$$

where W^+_μ is the W^+ field, γ^μ the Dirac matrices and V_{CKM} a 3×3 unitary matrix ($V_{\text{CKM}} V^\dagger_{\text{CKM}} = \mathbb{1}$) called the *Cabibbo-Kobayashi-Maskawa* (CKM) *matrix* [9, 10] that links the *flavour eigenstates* (d,s,b) to the *mass eigenstates* (d',s',b'). The CKM matrix can be parametrised using three angles and one irreducible phase that is called the *weak phase* [10]. This phase is the source of all *CP violation* effects, *i.e.* asymmetry between particles and anti-particles, in flavour-changing processes in the SM. A commonly-used parametrisation for the CMK matrix elements [11] is

given by

$$V_{\text{CKM}} = \begin{pmatrix} c_{12}c_{13} & s_{12}c_{13} & s_{13}e^{-i\delta} \\ -s_{12}c_{23} - c_{12}s_{23}s_{13}e^{i\delta} & c_{12}c_{23} - s_{12}s_{23}s_{13}e^{i\delta} & s_{23}c_{13} \\ s_{12}s_{23} - c_{12}c_{23}s_{13}e^{i\delta} & -c_{12}s_{23} - s_{12}c_{23}s_{13}e^{i\delta} & c_{23}c_{13} \end{pmatrix}, \tag{1.2}$$

where $s_{ij} = \sin(\theta_{ij})$, $c_{ij} = \cos(\theta_{ij})$ and δ the weak CP-violating phase. A more widely used parametrisation of the CKM matrix is the one proposed by Wolfenstein [12, 13] given by

$$s_{12} = \lambda = \frac{|V_{us}|}{\sqrt{|V_{ud}|^2 + |V_{us}|^2}}, \qquad s_{13} = A\lambda^2 = \lambda \left| \frac{V_{cb}}{V_{us}} \right|,$$

$$s_{13}e^{i\delta} = V_{ub}^* = A\lambda^3(\rho + i\eta) = \frac{A\lambda^3(\overline{\rho} + i\overline{\eta})\sqrt{1 - A^2\lambda^4}}{\sqrt{1 - \lambda^4}[1 - \lambda^2(\overline{\rho} + i\overline{\eta})]}, \tag{1.3}$$

where $\lambda = \sin(\theta_{12}) = \sin(\theta_C) \approx 0.225$ [14] with the Cabibbo angle $\theta_C \approx 13.02°$ and $\overline{\rho} + i\overline{\eta} = -\frac{V_{ud}V_{ub}^*}{V_{cd}V_{cb}^*}$. The presence of CP violation is given by $\eta \neq 0$. Since λ is small, the CKM matrix is usually expanded in powers of λ [15]:

$$V_{\text{CKM}} = \begin{pmatrix} 1 - \frac{1}{2}\lambda^2 & \lambda & A\lambda^3(\rho - i\eta) \\ -\lambda & 1 - \frac{1}{2}\lambda^2 & A\lambda^2 \\ A\lambda^3(1 - \rho - i\eta) & -A\lambda^2 & 1 \end{pmatrix} + \mathcal{O}(\lambda^4), \tag{1.4}$$

up to λ^4 and:

$$V_{\text{CKM}} = \begin{pmatrix} 1 - \frac{1}{2}\lambda^2 - \frac{1}{8}\lambda^4 & \lambda & A\lambda^3(\rho - i\eta) \\ -\lambda + A^2\lambda^5(1 - \rho - i\eta) & 1 - \frac{1}{2}\lambda^2 - \frac{1}{8}\lambda^4(1 + 4A^2) & A\lambda^2 \\ A\lambda^3(1 - \rho - i\eta) + \frac{1}{2}A\lambda^5(\rho + i\eta) & -A\lambda^2 + A\lambda^4(1 - \rho - i\eta) & 1 - \frac{1}{2}A^2\lambda^2 \end{pmatrix} + \mathcal{O}(\lambda^6) \tag{1.5}$$

up to λ^6. The expansion in powers of λ is useful to get an estimate of the strength of weak interaction transitions. For example, a $b \rightarrow c$ transition is given by V_{cb} which is of order λ^2 and transitions within the same quark family are of order unity. Also it is important to know in which process CP violation can appear and with which amplitude.

The unitarity of the CKM matrix gives six off-diagonal relations. Two of them are important for this thesis:

$$V_{ud}V_{ub}^* + V_{cd}V_{cb}^* + V_{td}V_{tb}^* = 0, \tag{1.6}$$

$$V_{us}V_{ub}^* + V_{cs}V_{cb}^* + V_{ts}V_{tb}^* = 0. \tag{1.7}$$

These two relations describe two triangles in the $(\overline{\rho}, \overline{\eta})$ complex plane where the first one is generally called *"the" unitary triangle* where the relation 1.6 is divided by $V_{cd}V_{cb}^*$. A sketch of this unitary triangle is shown in Fig. 1.1. The angles of the unitary triangle (α, β, γ) can be studied using decays of B mesons $(d\overline{b})$ and are expected to have similar size from the determination of the magnitude of the sides of the triangle from various weak decay branching

fractions. The second triangle is more narrow triangle that is particularly relevant for the neutral B_s^0 mesons ($s\bar{b}$). The corresponding angle β of the second triangle is called β_s and expected to be very small ($\mathcal{O}(\lambda^2)$) [14]. The angles in terms of the CKM matrix are summarised in Eq. 1.8.

$$\alpha \equiv \phi_2 \equiv \arg\left[-\frac{V_{td}V_{tb}^*}{V_{ud}V_{ub}^*}\right], \qquad \beta \equiv \phi_1 \equiv \arg\left[-\frac{V_{cd}V_{cb}^*}{V_{td}V_{tb}^*}\right],$$

$$\gamma \equiv \phi_3 \equiv \arg\left[-\frac{V_{ud}V_{ub}^*}{V_{cd}V_{cb}^*}\right], \qquad \beta_s \equiv \chi \equiv \arg\left[-\frac{V_{cb}V_{cs}^*}{V_{tb}V_{ts}^*}\right]. \tag{1.8}$$

In order to test the SM, the goal is to measure enough quantities to over-constrain the system and look for discrepancies which would be sign of NP. This can be seen by global fits to the measurements of the angles and sides of the unitary triangle and examining whether a unique solution of $\bar{\rho}$ and $\bar{\eta}$ can be obtained. The latest results of the CKMFitter group [14] are shown in Fig. 1.2 which presents, for the moment, a consistent picture of the CKM paradigm.
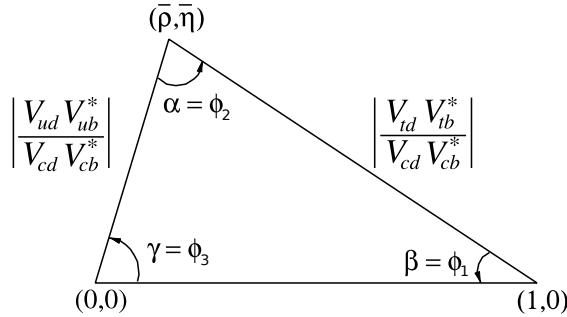

Figure 1.1: The Unitary Triangle with the CKM angles α, β, γ [15].
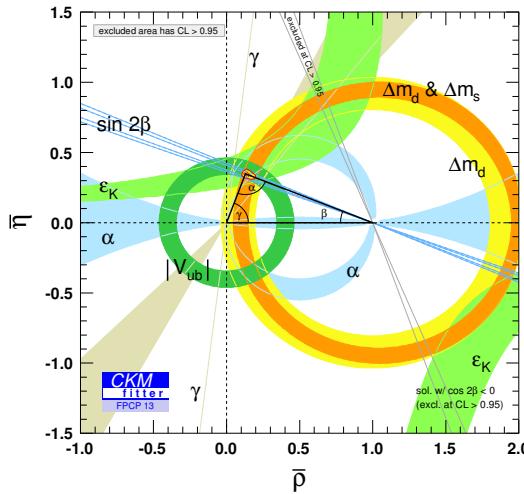

Figure 1.2: CKM global fit results obtained by the CKMFitter group [14].

1.3   *B* physics

This review of *B* physics is inspired from [15–20].

1.3.1   Oscillation of neutral *B* mesons

Neutral *B* mesons are given by the following quark contents:

$$|B^0\rangle = |d\bar{b}\rangle, \qquad |\overline{B}^0\rangle = |\bar{d}b\rangle, \tag{1.9}$$

$$|B_s^0\rangle = |s\bar{b}\rangle, \qquad |\overline{B}_s^0\rangle = |\bar{s}b\rangle. \tag{1.10}$$

The first important characteristic of *B* mesons is their long lifetimes. This allowed the discovery of one of the most interesting phenomena appearing in the K^0, D^0, B^0 and B_s^0 systems, hereafter denoted by M^0, their oscillation to their anti-particles with time, *i.e.* $M^0 \leftrightarrow \overline{M}^0$. The oscillation is possible through box diagrams, as shown in Fig. 1.3 for the case of B_s^0 mesons, because the mass and weak eigenstates are not the same. This means that a neutral *B* system produced at $t = 0$ can be taken as a quantum superposition of B^0 and $\overline{B}^0$:

$$|\psi(0)\rangle = a(0)|B^0\rangle + b(0)|\overline{B}^0\rangle, \tag{1.11}$$

and similarly for B_s^0 mesons. Hereafter, what is stated for B^0 mesons also works for B_s^0 mesons. To highlight the *B* meson oscillation, the time evolution of the system needs to be considered including the possible decay final states of the *B* meson, f_i, as

$$|\psi(t)\rangle = a(t)|B^0\rangle + b(t)|\overline{B}^0\rangle + \sum_i c_i(t)|f_i\rangle, \tag{1.12}$$

with $|a(0)|^2 + |b(0)|^2 = 1$ and $c_i(0) = 0$ as initial conditions. The fact that the time scale of the weak interaction is much larger than the strong and EM interactions, the Wigner-Weisskopf approximation can be used to neglect all the weak interactions among the final states. This leads to a simplified Schrödinger equation using the Dirac picture with an effective Hamiltonian $\boldsymbol{H}_{\text{eff}}$ that is linked to the weak interaction Hamiltonian:

$$i\partial_t \begin{pmatrix} a(t) \\ b(t) \end{pmatrix} = \boldsymbol{H}_{\text{eff}} \begin{pmatrix} a(t) \\ b(t) \end{pmatrix} = \begin{pmatrix} \boldsymbol{H}_{11} & \boldsymbol{H}_{12} \\ \boldsymbol{H}_{21} & \boldsymbol{H}_{22} \end{pmatrix} \begin{pmatrix} a(t) \\ b(t) \end{pmatrix} = \left(\boldsymbol{M} - \frac{i}{2}\boldsymbol{\Gamma} \right) \begin{pmatrix} a(t) \\ b(t) \end{pmatrix}, \tag{1.13}$$
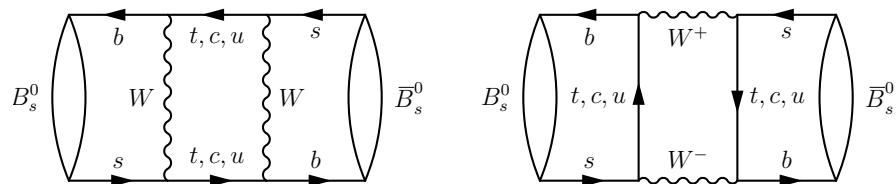

Figure 1.3: Box diagrams contributing to the $B_s^0 - \overline{B}_s^0$ mixing [21].

where $\boldsymbol{H}_{\text{eff}}$ is a 2×2 effective Hamiltonian which is non-Hermitian due to the Wigner-Weisskopf approximation. The 2×2 Hermitian matrices $\boldsymbol{M}$ and $\boldsymbol{\Gamma}$ are linked to $(M^0, \overline{M}^0) \leftrightarrow (M^0, \overline{M}^0)$ transitions through off-shell for $\boldsymbol{M}$ and on-shell intermediate states for $\boldsymbol{\Gamma}$. The diagonal elements are linked to the flavour-conserving transitions and the off-diagonal ones the flavour-changing transitions. Solving Eq. 1.13 assuming CPT invariance of the effective Hamiltonian ($\boldsymbol{H}_{11} = \boldsymbol{H}_{22} = \boldsymbol{H}_0$), the eigenvalues $\lambda_{\pm}$ are given by

$$\lambda_{\pm} \equiv m_{\pm} - \frac{i}{2}\Gamma_{\pm} = \boldsymbol{H}_0 \pm \sqrt{\boldsymbol{H}_{12}\boldsymbol{H}_{21}} = \boldsymbol{H}_0 \pm \sqrt{\left(\boldsymbol{M}_{12} - \frac{i}{2}\boldsymbol{\Gamma}_{12}\right)\left(\boldsymbol{M}_{12}^* - \frac{i}{2}\boldsymbol{\Gamma}_{12}^*\right)}. \tag{1.14}$$

The eigenvectors $B_{\pm}$ are given by

$$|B_{\pm}\rangle = \frac{1}{\sqrt{1 + \left|\frac{q}{p}\right|^2}}\left(|B^0\rangle \pm \frac{q}{p}|\overline{B}^0\rangle\right), \qquad |p|^2 + |q|^2 = 1, \tag{1.15}$$

where q and p are complex numbers and their ratio is given by

$$\frac{q}{p} = \sqrt{\frac{\boldsymbol{H}_{21}}{\boldsymbol{H}_{12}}} = \sqrt{\frac{\boldsymbol{M}_{21} - \frac{i}{2}\boldsymbol{\Gamma}_{21}}{\boldsymbol{M}_{12} - \frac{i}{2}\boldsymbol{\Gamma}_{12}}} = \sqrt{\frac{\boldsymbol{M}_{12}^* - \frac{i}{2}\boldsymbol{\Gamma}_{12}^*}{\boldsymbol{M}_{12} - \frac{i}{2}\boldsymbol{\Gamma}_{12}}}. \tag{1.16}$$

The time-evolution of an initially produced B^0 and $\overline{B}^0$ at $t = 0$, respectively, is given by

$$|B^0(t)\rangle = g_+(t)|B^0\rangle + \frac{q}{p}g_-(t)|\overline{B}^0\rangle,$$

$$|\overline{B}^0(t)\rangle = g_+(t)|\overline{B}^0\rangle + \frac{p}{q}g_-(t)|B^0\rangle, \tag{1.17}$$

with

$$g_{\pm}(t) = \frac{1}{2}\left(e^{-i\lambda_+ t} \pm e^{-i\lambda_- t}\right). \tag{1.18}$$

In order to further describe the properties of the eigenvectors, a deeper look at the matrix elements of $\boldsymbol{H}_{\text{eff}}$ is required. In the case of CP conservation, it can be shown that:

$$\boldsymbol{M}_{12} = \boldsymbol{M}_{21}e^{-2i\phi_{CP}} = \boldsymbol{M}_{12}^* e^{-2i\phi_{CP}}, \tag{1.19}$$

$$\boldsymbol{\Gamma}_{12} = \boldsymbol{\Gamma}_{21}e^{-2i\phi_{CP}} = \boldsymbol{\Gamma}_{12}^* e^{-2i\phi_{CP}}, \tag{1.20}$$

where ϕ_{CP} is the phase introduced after applying the CP transformation to a $|B^0\rangle$ as

$$CP|B^0\rangle = e^{i\phi_{CP}}|\overline{B}^0\rangle. \tag{1.21}$$

In the case of CP violation by the weak interaction, extra weak phases ϕ_M and ϕ_Γ are added to $\boldsymbol{M}_{12}$ and $\boldsymbol{\Gamma}_{12}$:

$$\boldsymbol{M}_{12} = \boldsymbol{M}_{12}^* e^{-2i\phi_{CP}}e^{2i\phi_M}, \qquad\qquad \boldsymbol{\Gamma}_{12} = \boldsymbol{\Gamma}_{12}^* e^{-2i\phi_{CP}}e^{2i\phi_\Gamma}. \tag{1.22}$$

The matrix elements $\boldsymbol{M}_{12}$ and $\boldsymbol{\Gamma}_{12}$ can therefore be expressed as

$$\boldsymbol{M}_{12} = |M_{12}|e^{i(\phi_M - \phi_{CP} + n\pi)}, \qquad\qquad \boldsymbol{\Gamma}_{12} = |\Gamma_{12}|e^{i(\phi_\Gamma - \phi_{CP} + n'\pi)}, \qquad\qquad (1.23)$$

where n and n' are integers that need to be set according to the decay width spectrum convention of the eigenvectors. These are the two first degrees of freedom (DOF) of the system. The third and last DOF (n'') is the sign solution $(-1)^{n''}$ when taking the square-root of $\sqrt{\boldsymbol{H}_{12}\boldsymbol{H}_{21}}$ or $\sqrt{\boldsymbol{H}_{21}/\boldsymbol{H}_{12}}$. It can be shown that the CP eigenvalue of $B_\pm$ is given by

$$CP|B_\pm\rangle = \pm(-1)^{n''}|B_\pm\rangle, \qquad\qquad (1.24)$$

where the choice of the parity of n'' gives the CP parity of $B_\pm$. The physical implications of the choices for n and n' are found when developing the eigenvalues $\lambda_\pm = m_\pm - \frac{i}{2}\Gamma_\pm$:

$$m_\pm = \boldsymbol{M}_0 \pm (-1)^{n+n''}|\boldsymbol{M}_{12}|, \qquad\qquad (1.25)$$
$$\Gamma_\pm = \boldsymbol{\Gamma}_0 \pm (-1)^{n'+n''}|\boldsymbol{\Gamma}_{12}|. \qquad\qquad (1.26)$$

Experimental results concluded that the heavier eigenvector is CP odd and has the smaller decay width. This means that the lighter mass eigenstate B_L can be linked to B_+ and heavier mass state B_H to B_- and the eigenvectors of Eq. 1.15 can be rewritten as

$$|B_L\rangle = p|B^0\rangle + q|\overline{B}^0\rangle,$$
$$|B_H\rangle = p|B^0\rangle - q|\overline{B}^0\rangle, \qquad\qquad (1.27)$$

which implies that:

$$n'' \to \text{even} \to n'' = 0,$$
$$n \to \text{odd} \to n = 1,$$
$$n' \to \text{even} \to n' = 0.$$

The phase ϕ_{CP} can be kept free in all the computations, and it can be shown that is a non-physical phase and therefore is arbitrary. A useful convention is to set it to π to have the phase of $\boldsymbol{M}_{12}$ being equal to the mixing weak phase ϕ_M. The matrix elements $\boldsymbol{M}_{12}$ and $\boldsymbol{\Gamma}_{12}$ are finally given by

$$\boldsymbol{M}_{12} = |M_{12}|e^{i\phi_M}, \qquad\qquad \boldsymbol{\Gamma}_{12} = |\Gamma_{12}|e^{i(\phi_\Gamma - \pi)}. \qquad\qquad (1.28)$$

The average mass, m, average decay width, Γ, mass difference, Δm, and decay width difference, $\Delta\Gamma$, of the eigenvectors $B_{L,H}$ are therefore defined and linked to the eigenvalues $\lambda_{L,H}$ as

$$\Delta m \equiv m_H - m_L = \Re(\lambda_H - \lambda_L), \qquad\qquad m \equiv \frac{m_H + m_L}{2} = \frac{\Re(\lambda_H + \lambda_L)}{2},$$

$$\Delta\Gamma \equiv \Gamma_L - \Gamma_H = -2\Im(\lambda_L - \lambda_H), \qquad\qquad \Gamma \equiv \frac{\Gamma_H + \Gamma_L}{2} = -\frac{\Im(\lambda_H + \lambda_L)}{4}. \qquad (1.29)$$

In the case where $|\Gamma_{12}/M_{12}|$ is small as expected in the SM, the ratio q/p can be expressed by

$$\frac{q}{p} = -e^{-i\phi_M}\left\{1 - \frac{1}{2}\left|\frac{\Gamma_{12}}{M_{12}}\right|\sin(\phi_M - \phi_\Gamma) + \mathcal{O}\left(\left|\frac{\Gamma_{12}}{M_{12}}\right|^2\right)\right\}, \tag{1.30}$$

where the phase difference $\phi_M - \phi_\Gamma = 0 + \mathcal{O}(m_c^2/m_b^2)$ in the SM.

The probability to have a $B^0, \overline{B}^0$ after a time t with a $B^0, \overline{B}^0$ initially produced at $t = 0$ is given by

$$\begin{aligned}
|\langle B^0|B^0(t)\rangle|^2 &= |g_+(t)|^2 = \frac{e^{-\Gamma t}}{2}\left(\cosh\frac{\Delta\Gamma}{2}t + \cos\Delta m t\right), \\
|\langle \overline{B}^0|B^0(t)\rangle|^2 &= \left|\frac{q}{p}\right|^2|g_-(t)|^2 = \left|\frac{q}{p}\right|^2\frac{e^{-\Gamma t}}{2}\left(\cosh\frac{\Delta\Gamma}{2}t - \cos\Delta m t\right), \\
|\langle B^0|\overline{B}^0(t)\rangle|^2 &= \left|\frac{p}{q}\right|^2|g_-(t)|^2 = \left|\frac{p}{q}\right|^2\frac{e^{-\Gamma t}}{2}\left(\cosh\frac{\Delta\Gamma}{2}t - \cos\Delta m t\right), \\
|\langle \overline{B}^0|\overline{B}^0(t)\rangle|^2 &= |g_+(t)|^2 = \frac{e^{-\Gamma t}}{2}\left(\cosh\frac{\Delta\Gamma}{2}t + \cos\Delta m t\right).
\end{aligned} \tag{1.31}$$

From these equations, the B meson oscillation can be noticed by the cosine terms.

1.3.2 Decay of *B* mesons

In Sec. 1.3.1, the decay of the B meson was not specified. The decay amplitude of a $B, \overline{B}$ to a final state f and its CP-conjugate $\overline{f}$ with the decay Hamiltonian $\boldsymbol{H}_\mathrm{D}$ are defined as

$$\begin{aligned}
A_f &= \langle f|\boldsymbol{H}_\mathrm{D}^\dagger|B\rangle, & \overline{A}_f &= \langle f|\boldsymbol{H}_\mathrm{D}|\overline{B}\rangle, \\
A_{\overline{f}} &= \langle \overline{f}|\boldsymbol{H}_\mathrm{D}^\dagger|B\rangle, & \overline{A}_{\overline{f}} &= \langle \overline{f}|\boldsymbol{H}_\mathrm{D}|\overline{B}\rangle.
\end{aligned} \tag{1.32}$$

For charged B mesons, the oscillation is impossible, therefore only transitions $B^+ \to f$ and $B^- \to \overline{f}$ are allowed. The *time-dependent decay rate* of a charged B to a final state f is defined as

$$\frac{\mathrm{d}\Gamma}{\mathrm{d}t}(B^+(t) \to f) = |\langle f|\boldsymbol{H}_\mathrm{D}^\dagger|B^+(t)\rangle|^2. \tag{1.33}$$

The time-dependent decay rate of $B^+(B^-)$ to a final state $f(\overline{f})$ is simply given by

$$\begin{aligned}
\frac{\mathrm{d}\Gamma}{\mathrm{d}t}(B^+(t) \to f) &= N_f|A_f|^2 e^{-\Gamma t}, \\
\frac{\mathrm{d}\Gamma}{\mathrm{d}t}(B^-(t) \to \overline{f}) &= N_f|\overline{A}_{\overline{f}}|^2 e^{-\Gamma t}.
\end{aligned} \tag{1.34}$$

where N_f is a time-independent normalisation factor.

For the neutral *B* mesons, the way to get the decay rates is the same, but with a complication coming from the oscillation. For further convenience, two parameters, λ_f, $\overline{\lambda}_{\overline{f}}$, are defined as

$$\lambda_f = \frac{q}{p}\frac{\overline{A}_f}{A_f}, \qquad \frac{1}{\overline{\lambda}_{\overline{f}}} \equiv \lambda_{\overline{f}} = \frac{q}{p}\frac{\overline{A}_{\overline{f}}}{A_{\overline{f}}}. \tag{1.35}$$

Using Eq. 1.17 and the equivalent of Eq. 1.33, The four decay rates of neutral $(B^0, \overline{B}^0)$ mesons decaying to a final states $(f, \overline{f})$ are given by

$$\frac{\mathrm{d}\Gamma}{\mathrm{d}t}(B^0(t) \to f) = N_f |A_f|^2 \left\{ |g_+(t)|^2 + |\lambda_f|^2 |g_-(t)|^2 + 2\Re[\lambda_f g_+^*(t)g_-(t)] \right\},$$

$$\frac{\mathrm{d}\Gamma}{\mathrm{d}t}(\overline{B}^0(t) \to f) = N_f |A_f|^2 \left|\frac{p}{q}\right|^2 \left\{ |g_-(t)|^2 + |\lambda_f|^2 |g_+(t)|^2 + 2\Re[\lambda_f g_+(t)g_-^*(t)] \right\},$$

$$\frac{\mathrm{d}\Gamma}{\mathrm{d}t}(B^0(t) \to \overline{f}) = N_f |\overline{A}_{\overline{f}}|^2 \left|\frac{q}{p}\right|^2 \left\{ |g_-(t)|^2 + |\overline{\lambda}_{\overline{f}}|^2 |g_+(t)|^2 + 2\Re[\overline{\lambda}_{\overline{f}} g_+(t)g_-^*(t)] \right\},$$

$$\frac{\mathrm{d}\Gamma}{\mathrm{d}t}(\overline{B}^0(t) \to \overline{f}) = N_f |\overline{A}_{\overline{f}}|^2 \left\{ |g_+(t)|^2 + |\overline{\lambda}_{\overline{f}}|^2 |g_-(t)|^2 + 2\Re[\overline{\lambda}_{\overline{f}} g_+^*(t)g_-(t)] \right\}. \tag{1.36}$$

Developing $|g_\pm(t)|^2$ using Eq. 1.18, the four final decay rates are obtained:

$$\frac{\mathrm{d}\Gamma}{\mathrm{d}t}(B^0(t) \to f) = N_f |A_f|^2 \frac{1+|\lambda_f|^2}{2} e^{-\Gamma t}.$$
$$\left(\cosh\frac{\Delta\Gamma}{2}t + A_f^{\Delta\Gamma}\sinh\frac{\Delta\Gamma}{2}t + C_f\cos\Delta mt - S_f\sin\Delta mt \right), \tag{1.37}$$

$$\frac{\mathrm{d}\Gamma}{\mathrm{d}t}(\overline{B}^0(t) \to f) = N_f |A_f|^2 \left|\frac{p}{q}\right|^2 \frac{1+|\lambda_f|^2}{2} e^{-\Gamma t}.$$
$$\left(\cosh\frac{\Delta\Gamma}{2}t + A_f^{\Delta\Gamma}\sinh\frac{\Delta\Gamma}{2}t - C_f\cos\Delta mt + S_f\sin\Delta mt \right), \tag{1.38}$$

$$\frac{\mathrm{d}\Gamma}{\mathrm{d}t}(B^0(t) \to \overline{f}) = N_f |\overline{A}_{\overline{f}}|^2 \left|\frac{q}{p}\right|^2 \frac{1+|\overline{\lambda}_{\overline{f}}|^2}{2} e^{-\Gamma t}.$$
$$\left(\cosh\frac{\Delta\Gamma}{2}t + \overline{A}_{\overline{f}}^{\Delta\Gamma}\sinh\frac{\Delta\Gamma}{2}t - \overline{C}_{\overline{f}}\cos\Delta mt + \overline{S}_{\overline{f}}\sin\Delta mt \right), \tag{1.39}$$

$$\frac{\mathrm{d}\Gamma}{\mathrm{d}t}(\overline{B}^0(t) \to \overline{f}) = N_f |\overline{A}_{\overline{f}}|^2 \frac{1+|\overline{\lambda}_{\overline{f}}|^2}{2} e^{-\Gamma t}.$$
$$\left(\cosh\frac{\Delta\Gamma}{2}t + \overline{A}_{\overline{f}}^{\Delta\Gamma}\sinh\frac{\Delta\Gamma}{2}t + \overline{C}_{\overline{f}}\cos\Delta mt - \overline{S}_{\overline{f}}\sin\Delta mt \right), \tag{1.40}$$

where

$$A_f^{\Delta\Gamma} = -\frac{2\Re\lambda_f}{1+|\lambda_f|^2}, \qquad C_f = \frac{1-|\lambda_f|^2}{1+|\lambda_f|^2}, \qquad S_f = \frac{2\Im\lambda_f}{1+|\lambda_f|^2},$$

$$\overline{A}_{\overline{f}}^{\Delta\Gamma} = -\frac{2\Re\overline{\lambda}_{\overline{f}}}{1+|\overline{\lambda}_{\overline{f}}|^2}, \qquad \overline{C}_{\overline{f}} = \frac{1-|\overline{\lambda}_{\overline{f}}|^2}{1+|\overline{\lambda}_{\overline{f}}|^2}, \qquad \overline{S}_{\overline{f}} = \frac{2\Im\overline{\lambda}_{\overline{f}}}{1+|\overline{\lambda}_{\overline{f}}|^2}. \tag{1.41}$$

1.3.3 *CP* violation in *B* systems

Three types of *CP* violation can be considered:

CP violation in mixing:

    CP violation in mixing, also called *indirect CP violation*, occurs when the oscillation probability of $B^0 \to \overline{B}^0$ is not equal to the one of $\overline{B}^0 \to B^0$. From the Eq. 1.31, the presence of *CP* violation in mixing is given by

$$\left| \frac{q}{p} \right| \neq 1. \tag{1.42}$$

From Eq. 1.30, there is indirect *CP* violation when the relative phase $\phi_M - \phi_\Gamma$ is not 0 or π. The ratio $|q/p|$ can be measured using the semileptonic decay of neutral *B* mesons: $B^0 \to l^+ X$, $\overline{B}^0 \to l^- X$. Computing the asymmetry of wrong-sign decays ($B^0 \to l^- X$, $\overline{B}^0 \to l^+ X$) assuming $|A_{l^+ X}| = |A_{l^- X}|$ (which is reasonable in the SM), the ratio $|q/p|$ can be measured:

$$A_{\text{SL}}(t) = \frac{\frac{\mathrm{d}\Gamma}{\mathrm{d}t}(\overline{B}^0(t) \to l^+ X) - \frac{\mathrm{d}\Gamma}{\mathrm{d}t}(B^0(t) \to l^- X)}{\frac{\mathrm{d}\Gamma}{\mathrm{d}t}(\overline{B}^0(t) \to l^+ X) + \frac{\mathrm{d}\Gamma}{\mathrm{d}t}(B^0(t) \to l^- X)} = \frac{1 - |q/p|^2}{1 + |q/p|^2} = A_{\text{SL}}. \tag{1.43}$$

CP violation in decay:

    CP violation in decay, also called *direct CP violation*, occurs when the decay probability of $B \to f$ is not equal to that of $\overline{B} \to \overline{f}$; This implies:

$$\left| \frac{\overline{A}_{\overline{f}}}{A_f} \right| \neq 1. \tag{1.44}$$

To understand the source of this *CP* violation, the amplitudes A_f and $\overline{A}_{\overline{f}}$ need to be further described. The amplitudes are sums of different decay processes generating the same final state with their phases coming from the strong and weak interactions, as

$$A_f = \sum_j |A_j| e^{i(\delta_j + \phi_j)}, \qquad \overline{A}_{\overline{f}} = \sum_k |\overline{A}_k| e^{i(\delta_k - \phi_k)}, \tag{1.45}$$

where δ is a strong phase that does not change its sign under *CP* and ϕ is a weak phase that changes its sign under *CP*. From these expressions, direct *CP* violation can occur with at least two decay processes with different strong and weak phases between them.

The ratio $|\overline{A}_{\overline{f}}/A_f|$ can be measured using decays of charged *B* mesons, where the oscillation is absent, performing the following asymmetry:

$$A_{f^\pm}(t) = \frac{\frac{\mathrm{d}\Gamma}{\mathrm{d}t}(B^-(t) \to f^-) - \frac{\mathrm{d}\Gamma}{\mathrm{d}t}(B^+(t) \to f^+)}{\frac{\mathrm{d}\Gamma}{\mathrm{d}t}(B^-(t) \to f^-) + \frac{\mathrm{d}\Gamma}{\mathrm{d}t}(B^+(t) \to f^+)} = \frac{|\overline{A}_{\overline{f}}/A_f|^2 - 1}{|\overline{A}_{\overline{f}}/A_f|^2 + 1} = A_{f^\pm}. \tag{1.46}$$

***CP* violation in the interplay between oscillation and decay:**

CP violation in the interplay between oscillation and decay can only occur for neutral B^0 and $\overline{B}^0$ decaying to the same final state f, even in the absence of direct and indirect CP violation. Hereafter, f is taken as a CP final state f_{CP}. This CP violation appears when:

$$\Im\lambda_{CP} \neq 0 \, . \tag{1.47}$$

This can be obtained by measuring the following asymmetry:

$$A_{f_{CP}}(t) = \frac{\frac{\mathrm{d}\Gamma}{\mathrm{d}t}(\overline{B}^0(t) \to f^{CP}) - \frac{\mathrm{d}\Gamma}{\mathrm{d}t}(B^0(t) \to f^{CP})}{\frac{\mathrm{d}\Gamma}{\mathrm{d}t}(\overline{B}^0(t) \to f^{CP}) + \frac{\mathrm{d}\Gamma}{\mathrm{d}t}(B^0(t) \to f^{CP})} \tag{1.48}$$

In the case of no direct CP violation ($|q/p| = 1$) and indirect CP violation ($|\overline{A}_{CP}/A_{CP}| = 1$) which is correct in the SM up to a good precision for B's decaying to a CP eigenstate, the CP asymmetry is given by

$$A_{f_{CP}}(t) = \frac{\Im\lambda_{CP}\sin\Delta mt}{\cosh\frac{\Delta\Gamma}{2}t - \Re\lambda_{CP}\sinh\frac{\Delta\Gamma}{2}t}. \tag{1.49}$$

This expression can be further simplified in the case of the B^0 system where $\Delta\Gamma$ vanishes to good precision:

$$A_{f_{CP}}(t) = \Im\lambda_{CP}\sin\Delta mt. \tag{1.50}$$

The amplitude of the sinusoid in the CP asymmetry is the size of CP violation in the interplay between oscillation and decay.

In order to understand the source of a non-zero $\Im\lambda_{CP}$, λ_{CP} needs to be further developed. It can be shown that $A_{f_{CP}}$ and $\overline{A}_{f_{CP}}$ are linked as

$$\overline{A}_{f_{CP}} = -\eta_{CP}(f_{CP})e^{i2\phi_D}A_{f_{CP}}. \tag{1.51}$$

where $\eta_{CP}(f_{CP})$ is the sign of the CP eigenvalue of the final state f_{CP} as $CP|f_{CP}\rangle = \eta_{CP}(f_{CP})|f_{CP}\rangle$, ϕ_D is the weak phase of the decay as $A_{f_{CP}} = |A_{f_{CP}}|e^{i(\delta_D-\phi_D)}$ with the strong phase δ_D and the minus sign that comes from the convention that $\phi_{CP} = \pi$.

Using 1.30, 1.51 and assuming no CP violation in mixing, λ_{CP} is given by

$$\Im\lambda_{CP} \cong \eta_{CP}(f_{CP})\Im\left\{e^{-i(\phi_M-2\phi_D)}\right\} = -\eta_{CP}(f_{CP})\sin(\phi_M - 2\phi_D). \tag{1.52}$$

where CP violation in the interplay between oscillation and decay occurs in the difference between the weak phase of the oscillation and the one of the decay.

2 The Large Hadron Collider and the LHCb experiment

2.1 The Large Hadron Collider

The *Large Hadron Collider* (LHC) [22] at CERN is the largest and most powerful proton-proton (pp) collider in the world. It is located a hundred meters underground and straddles the Franco-Swiss boarder near Geneva, Switzerland. The LHC is installed in the twenty seven km tunnel of the former CERN collider, the *Large Electron-Positron* (LEP). The LHC was designed to accelerate proton beams up to an energy of 7 TeV, leading to a center-of-mass energy of $\sqrt{s}$ = 14 TeV. However, following an accident involving interconnections between the superconducting dipole magnets, the LHC was operated at reduced energies of $\sqrt{s}$ = 7 TeV in 2010 and 2011 and $\sqrt{s}$ = 8 TeV during 2012. The LHC is fed by a chain of accelerators with increasing energies (see Fig. 2.1) to reach the nominal LHC injection energy of 450 GeV. Protons from the source are first accelerated by a linear accelerator (LINAC), they go through the *Booster*, the *Proton Synchrotron* (PS), the *Super Proton Synchrotron* (SPS) and finally into the LHC itself.

Four large experiments (ATLAS, ALICE, CMS and LHCb) are located around the LHC ring as shown in Fig. 2.2. ATLAS [23] and CMS [24] are the multiple-purpose detectors that together discovered the Higgs boson in 2012 for which Higgs and Engelbert received the Nobel prize of physics in 2013. ALICE [25] is a detector dedicated to the study of high density media known as *quark-gluon plasma* from proton-lead and lead-lead collisions. Finally, LHCb is an experiment dedicated to the study of the asymmetry between matter and antimatter present in systems containing *b* or *c* quarks.

Figure 2.1: Overview of the CERN accelerators.
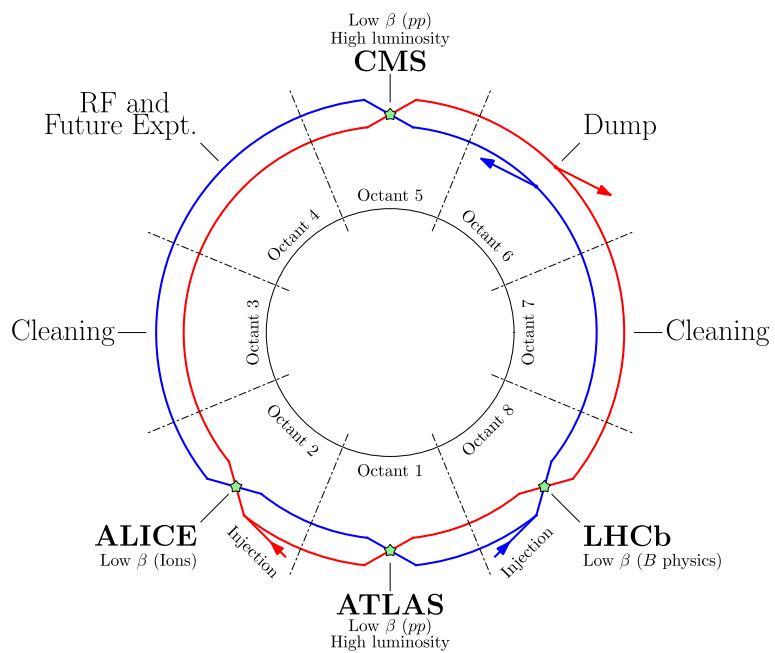
Figure 2.2: Schematic view of the LHC interaction points and detector locations [26].

2.2 The LHCb experiment

The *Large Hadron Collider beauty*, LHCb, experiment [27] is located at point 8 of the LHC and uses the cavern of the former LEP experiment *Delphi*. LHCb is a single-arm forward spectrometer (see Fig. 2.4) that exploits the forward production of the *b*- and *c*-quarks pairs from pp collisions as shown in Fig. 2.3 for *b*-quarks at $\sqrt{s} = 7$ TeV. The LHCb angular coverage starts at 15 mrad and finishes at 250 (300) mrad in the vertical (horizontal) plane. The LHCb coordinate system uses an orthogonal set of coordinates, *x*, *y*, *z*, where the *z* is set to the beam, the *y* is directed away from the Earth and the *x* goes through Fig. 2.4.
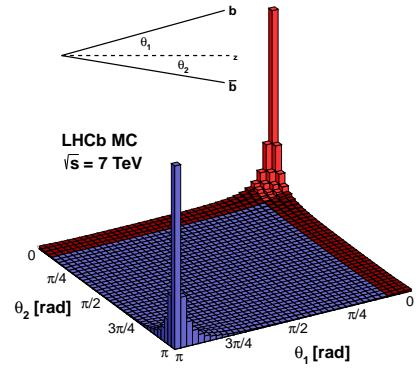
Figure 2.3: b and $\overline{b}$ pair production angles with respect to the beam direction at $\sqrt{s} = 7$ TeV.

The LHCb experiment is composed of several sub-detectors. The tracking system comprises a vertex and tracking detector called the *VErtex LOcator* (VELO), the *Tracker Turicensis* (TT) upstream of a *normal conducting dipole* with an integrated field of 4 Tm and downstream of the magnet, the *Inner Tracker* (IT) surrounding the beryllium beam-pipe and around the IT, the *Outer Tracker* (OT) both separated in three *T stations* (T1 to T3). *Particle identification* (PID) is provided by two *Ring Imaging CHerenkov* detectors (RICH1,2), *Electromagnetic CALorimeter* (ECAL) with its *Pre-Shower* (PS) and *Scintillator Pad Detector* (SPD), *Hadronic CALorimeter* (HCAL) and finally five *muon chambers* (M1 to M5).
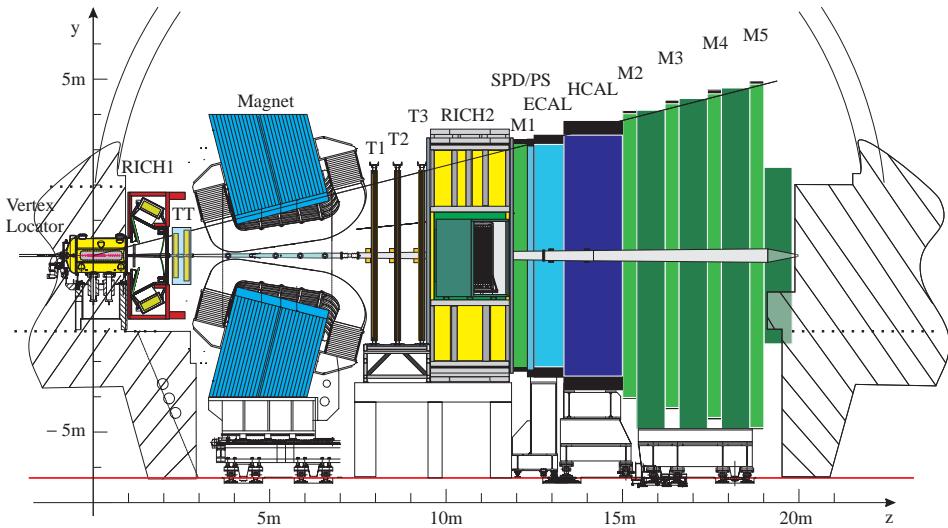
Figure 2.4: Sideshow of the LHCb detector.

2.2.1 Tracking system

VErtex LOcator (VELO)

The VELO [28] is a silicon micro-strip detector surrounding the interaction point, identi-
fies vertexes and performs the first track-finding steps. The sensitive region of the VELO is
composed of n-on-n silicon micro-strip half-disk sensors with two different read-out strip
geometries: r-type and ϕ-type sensors which measure the radial distance r and ϕ direction
in polar coordinates, respectively. The VELO is composed of twenty-one stations where each
station is separated in independent left and right halves that can be moved apart during the
beam injection period and closed once the beams are stable. Each side station has one r-type
and one ϕ-type sensor. Figure 2.5 shows the layout of the VELO. The VELO is about one meter
long.

The silicon sensors are 8.4 cm in diameter, have an inner hole with radius 0.8 cm and provide an
excellent measurement of vertex positions and impact parameters. The impact parameter res-
olution of a track is measured to be $\sigma_{IP} = 11.6 \pm 23.4/p_T$ μm in x and $\sigma_{IP} = 11.2 \pm 23.2/p_T$ μm
in y, where the *transverse momentum* (p_T) of the particle with respect to the beam axis p_T is in
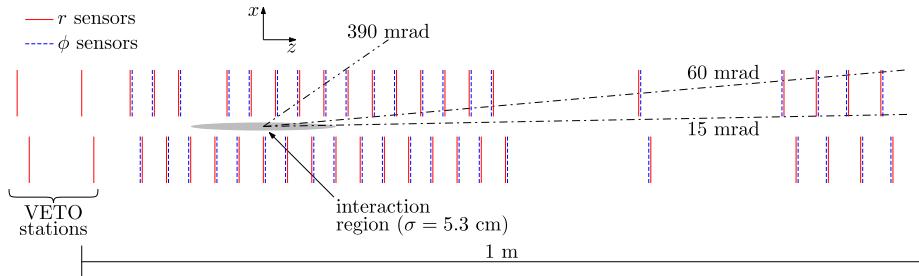

Figure 2.5: Overview of the VErtex LOcator (VELO). [26]
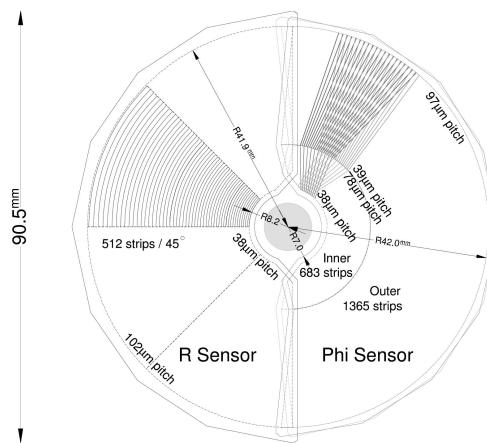
Figure 2.6: Overview of the r- and ϕ-type VELO sensors.

GeV/*c*. The strip pitch ranges from 38 to 108 μm (38 to 97 μm) for *r* (ϕ) sensors and the sensor thickness is 300 μm. The position of each sensor in the half-frames was verified, ascertained in a lab, hereafter referred as the *VELO metrology*, before installing the two VELO halves in the VELO vessel in the cavern. In total, the VELO has 172'032 read-out channels.

Tracker Turicensis (TT)

The TT [29] is a silicon micro-strip detector covering a total area of about 7.9 m^2 upstream of the dipole magnet and separated in two stations, TTa and TTb. Each station has two layers. Its role is to improve the track momentum resolution and to detect long-lived particles that decay outside the VELO. TTa is composed of (X-U) layers and TTb of (V-X) layers, where the X layers have read-out striping running vertically (0 degree relative to the vertical axis), and the U and V *stereo* layers are rotated by +5° and -5° counter-clockwise, respectively.

The TT is made of p-on-n HPK silicon micro-strip sensors from Hammamatsu Photonics. Since the sensors are exposed to high track multiplicity, they are cooled to an operating temperature of 0 °C to minimise radiation damage and avoid thermal runaway.

The TT read-out modules contain from one to four silicon sensors connected one after the other. The layout of a TT full module is shown in Fig. 2.7. This results in read-out strips that can be up to 37 cm long. The strip pitch is 183 μm and the sensor thickness is 500 μm. The hit resolution is about 50 μm. In total, the TT has 143'360 read-out channels.
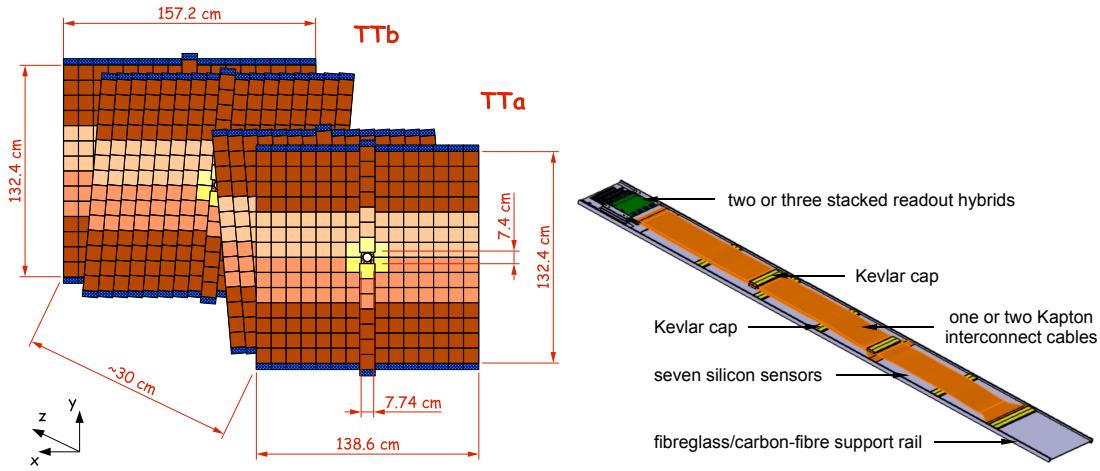

Figure 2.7: The TT layout with its four layers where each quasi-square element is a silicon sensor and the front-end electronics are presented in dark blue rectangles (*left*) and a TT half-module layout with 4-2-1 silicon-sensors read-out modules (*right*).

Inner Tracker (IT)

The IT [30] is also a silicon micro-strip detector. Together with the TT, the IT is a part of the *Silicon Tracker* (*ST*). Its role is to detect charged particles in the high track density region around the beam-pipe. It is located downstream of the dipole magnet in front of each OT station. It is separated in three stations where each station is composed of four boxes. Each box has four layers made of seven read-out modules as shown in Fig. 2.8, and arranged in a strip layout X1-U-V-X2 similar to that of the TT. The IT covers an area of about 4.2 m^2. The boxes directly above and below the beam-pipe are made of single-sensor modules, called *short modules*, the remaining boxes are made of two bonded silicon sensor modules, called *long modules*.

The IT strip pitch is 198 μm and the p-on-n sensor thickness is 320 (410) μm for single (double) silicon sensor(s) modules called short (long) modules where an example of a long module is shown in Fig. 2.8. The hit resolution is about 50 μm. In total, the IT has 129'024 read-out channels.

Outer Tracker (OT)

The OT [31] is a gaseous straw-tube detector filled with an Ar/CO$_2$/O$_2$ (70%/28.5%/1.5%) gas mixture. Its role is to detect charged particles in the low track density region around the IT and covers a large area of about 340 m^2. The OT is separated in three stations where each station has four layers in a (X1-U)-(V-X2) configuration. Each station is separated physically for the left and right sides with respect to the beam-pipe into two *C-frames* (X1-U) and (V-X2). Each layer is separated in two *mono-layers*. It is located behind each IT station and its acceptance starts just before the end of the IT coverage. The OT has different types of modules, the long F modules and the S1, S2, S3 modules that are cut in two pieces to leave space for the IT as shown in Fig. 2.9. The straw tube and anode wire diameters are 5 mm and 25 μm respectively and arranged as shown in Fig. 2.9. The hit resolution is about 200 μm. In total, the OT has 53'760 straw tubes.
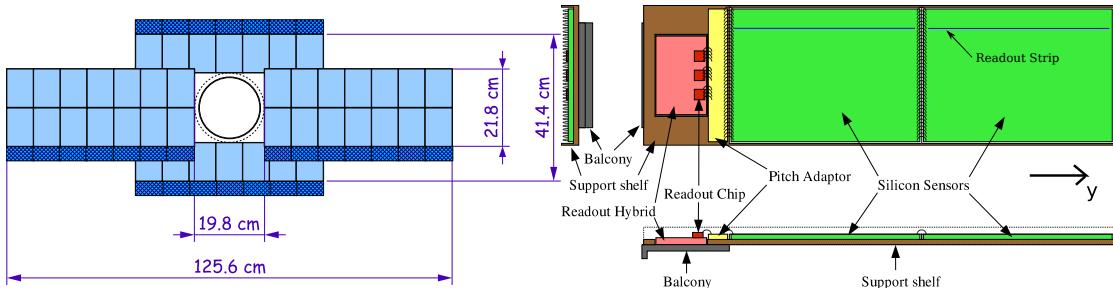
Figure 2.8: The first IT station layout where only one layer is shown. In light blue are the sensors, the front-end electronics are shown in dark blue (*left*). Layout of a long IT module (*right*).
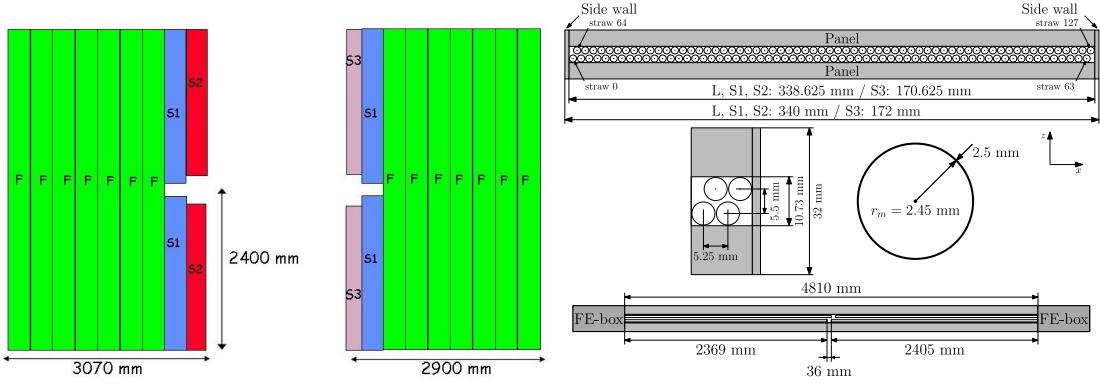
Figure 2.9: An OT layer layout (*left*). An OT module layout with a top view at the top and side view at the bottom (*right*) [26].

2.2.2 Particle identification

Ring Imaging CHerenkov (RICH)

Once a charged particle is travelling faster than the speed of light in a medium, Cherenkov light is produced at an angle that depends on the velocity of the particle (see Fig. 2.10) and the refractive index of the radiator. Taking the momentum from the tracker and the velocity from the RICH detectors, the mass can be determined and therefore provide particle identification. In order to perform high precision measurements in *b*- and *c*-physics, it is important to be able to efficiently separate kaons from pions over a wide momentum range. To do so, two RICH detectors are used.

RICH1 [32] is responsible for providing PID in the low- to mid-momentum range from 1 to 60 GeV/*c* using aerogel and fluorobutane (C_4F_{10}) in the acceptance range from 25 mrad to
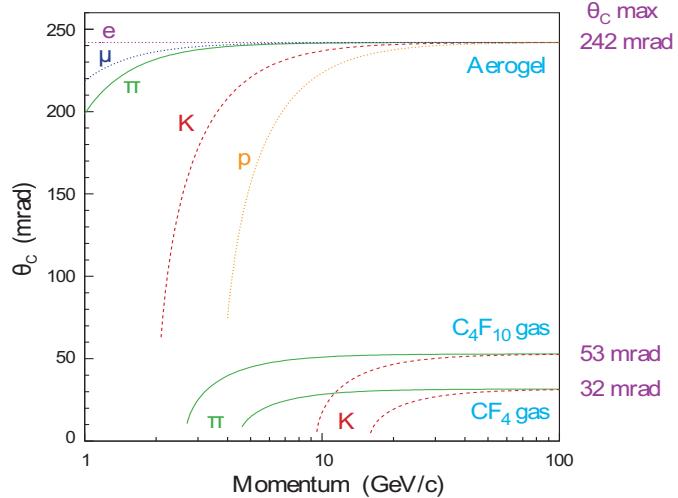
Figure 2.10: Cherenkov angle as a function of track momentum for different particles.

250 (300) mrad in the vertical (horizontal) plane. RICH1 is located inbetween the VELO and the TT. Figure 2.11 shows the design of the RICH1 mirror configuration to guide the Cherenkov photons to *Hybrid Photon Detectors* (*HPD*).

RICH2 [32] is responsible for the high-momentum range from 15 to 100 GeV/c in the acceptance range from 15 mrad to 100 (120) mrad in the vertical (horizontal) plane where most of the high-momentum tracks are produced. RICH2 uses tetrafluoromethane (CF_4) as its radiator. Figure 2.11 shows the RICH2 layout.

**Electromagnetic CALorimeter (ECAL), Pre-Shower (PS) and Scintillator Pad Detector (SPD)**

The ECAL [33] is used for the detection and measurement of the energy of electrons and photons. The ECAL uses shashlik technology, *i.e.* a sandwich of alternating scintillator and lead in the plane normal to the beam direction. Scintillation light produced by the shower of particles generated by the lead plates is read out by Wave-Length Shifter (WLS) fibres coupled to *PhotoMultiplier Tubes* (PMTs). A SPD is installed in front of the ECAL to separate electrons from photons. The ECAL needs longitudinal segmentation to reject background coming from charged pions and keep electrons. The PS is installed downstream from the SPC and upstream from the ECAL with a lead shield between the SPD and PS. The SPD and PS use scintillator pads read out by WLS fibres coupled to *MultiAnode PhotoMultiplier Tubes* (MAPMT). The acceptance range of the ECAL is from 25 mrad up to 300 (250) mrad in the horizontal (vertical) plane. The relative energy resolution of the ECAL is given by $\sigma_E/E = 10\%/\sqrt{E} \oplus 1\%$ where E is in GeV. In total, the ECAL has 6016 channels.
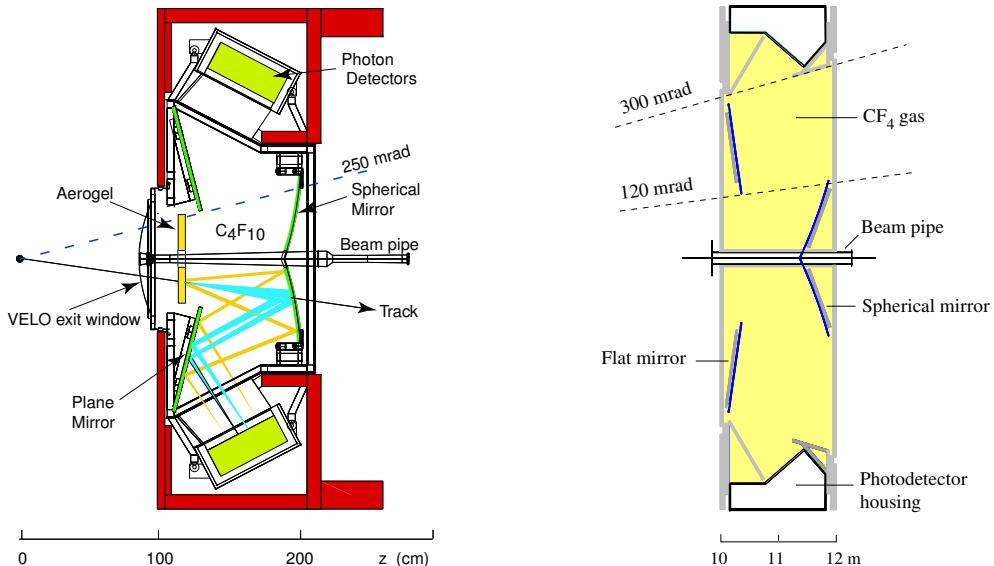
Figure 2.11: RICH1 layout from the side (*left*). RICH2 layout from the top (*right*).

Hadronic CALorimeter (HCAL)

The HCAL [33] is used for the detection and measurement of the energy of hadrons such as pions and kaons for the first level trigger. An HCAL cell is a sampling device made of alternating iron and scintillator tiles where the tiles are along the beam direction. The HCAL has the same acceptance coverage as the ECAL. The relative energy resolution of the HCAL is given by $\sigma_E/E = (69 \pm 5)\%/\sqrt{E} \oplus (9 \pm 2)\%$ where E is in GeV. In total, the HCAL has 1468 channels.

Muon system (M1 to M5)

The muon system [34] is a gaseous detector separated in five stations (M1 to M5) as shown in Fig. 2.12 interleaved by 80 cm thick iron filters of. The gaseous detectors are *Multi-Wire Proportional Chambers* (MWPC) except for the innermost part of M1 where *triple GEM detectors* are used due to the high track density. The first station is located before the calorimeters to gain in lever arm to estimate the p_T of muons at the trigger level. The acceptance ranges from 20 (16) to 308 (256) mrad in the horizontal (vertical) plane. The muon system has 1380 chambers and covers a total area of 435 m². Each muon chamber is made of four layers of MPWC except for M1 where two layers are used, as shown in Fig. 2.12. The chambers have a hit efficiency better than 99% and achieve a trigger efficiency greater than 95% for muons. A fast gas mixture ($Ar/CO_2/CF_4$ 40/55/5%) is used to allow trigging on muons at 40 MHz.
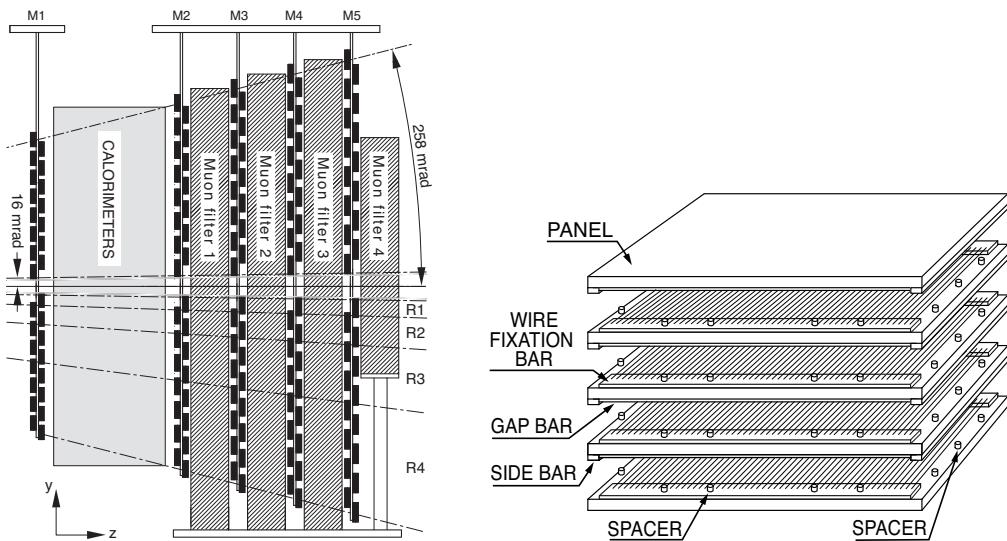
Figure 2.12: Muon chambers locations with the muons filters (*left*). Muon chamber's MWPC layout (*right*).

2.2.3 Trigger system

At the LHC, the collision rate was designed to be very high, up to 40 MHz, based on the fact that more than 99% of the pp collisions are not of interest. It would not be possible to record events at a rate of 40 MHz, only at about a few kHz. A trigger system [35] is therefore required to perform the reduction from 40 MHz down to few kHz. Since LHCb is mainly interested in heavy flavour physics and the signatures of these decays are the presence of high transverse momentum tracks (p_T), high *transverse energy* (E_T) in the calorimeters and displaced vertices, because b- and c-quarks fly over few centimetres. The presence of displaced vertices implies that some of decay products from the vertex have large *impact parameter* (IP) with respect to the *production vertex* (PV). In order to perform the reduction, a two-stage trigger was chosen by LHCb, a hardware stage called the *Level-0* (L0) and a software stage called the *High Level Trigger* (HLT) that runs on commercial off-the-shelf computers. Figure 2.13 shows the reduction flow in 2012 with the different exploited signatures and various rates.

Level-0 (L0)

The L0 trigger uses mainly the calorimeters and muon chambers. The basic idea behind the L0 trigger is to select events that contain high p_T muons and high E_T hadrons, electrons and photons. The L0 trigger reduces the data rate from 40 MHz down to 1 MHz.
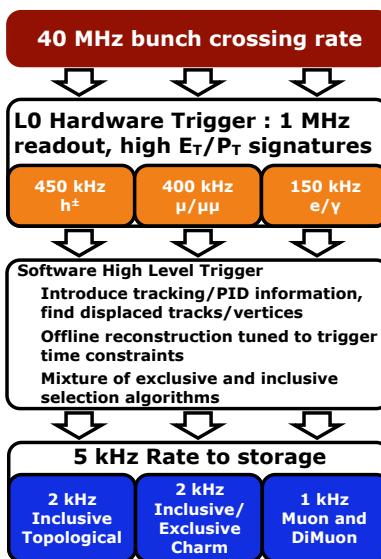
Figure 2.13: Trigger work flow with relevant exploited signatures and rates in 2012.

High Level Trigger (HLT)

The HLT is separated into two stages: HLT1 and HLT2, and runs on about 29'000 CPU cores. At the HLT1 level, the full detector information is read out, and vertexing, tracking and basic PID can be performed by reconstructed the tracks. The used signatures are again mainly the presence of high p_T tracks, high E_T calorimeter clusters (photons and π^0), high di-muon mass and tracks with large IP. It must be noted that at the HLT1 level, all the trigger lines are kept *inclusive*, meaning that only common decays products to various decay processes are selected. After the HLT1, the rate goes down to about 70 kHz.

The HLT2 is a combination of mainly inclusive algorithms and some algorithms that reconstruct entirely decay processes, called *exclusive* algorithms. The main lines are topological lines using *Multi-Variate Analysis* (MVA) with different sets of kinematic and position variables as input, exclusive charm lines and high mass displaced di-hadron/lepton lines. After the HLT2, the event rate goes down to about 5 kHz in 2012 and the events are finally stored on tape for further offline analysis.

2.2.4 LHCb software

A brief summary of the relevant software projects used in LHCb is given in the next lines.

Trigger

The software project that runs the full HLT algorithms is called `Moore` [36]. It runs on the trigger farm with the different algorithms mentioned in the previous sub-section. Most of the cuts values that are used for each trigger lines are stored and tagged as *Trigger Configuration Keys* (TCKs).

Event reconstruction

The software package for the offline full event reconstruction is called `Brunel` [37]. As for `Moore`, it performs the vertexing, tracking and PID, and provide a set of particles identified as pions, kaons, photons, π^0, J/ψ, K_S^0, ϕ, ... An important aspect of the tracking for this thesis is the different types of tracks as shown in Fig. 2.14. The three relevant track types are the *VELO segments*, *long tracks* made out of a VELO segment and a T track with possible TT hits on track and *downstream tracks* made out of a TT segment and a T track for tracks originating from long-lived particles such as K_S^0 and Λ that decayed outside of the VELO.

Stripping and Analysis

The output of `Brunel` is separated in different streams and further reduction is performed by creating mainly exclusive lines to select specific decays, for example $B^+ \to J/\psi K^+$, $B_s^0 \to J/\psi \phi$,

$B_s^0 \rightarrow D_s^- \pi$. Important inclusive lines are kept for data-mining but with tighter requirements or prescales such as the inclusive $J/\psi \rightarrow \mu^+ \mu^-$ line. This step performs the so-called *Stripping* using the software project called `DaVinci` [38]. `DaVinci` is also used to analysis the data and create *tuples* that are stored in files that will be further analysed with `ROOT` [39] or/and `RooFit` [40] programs to perform fits and plots.

Simulation

The parton-parton collision and hadronisation simulation is performed by `PYTHIA` [41] with some specific tunings [42], interfaced to `EvtGen` [43] for the decay of the hadrons and leptons for standard productions. The QED corrections to the decay is generated by the `PHOTOS` package [44], *i.e.* the emission of radiation photons. The interactions of particles with detector material and their tracking in the magnetic field are simulated by `GEANT4` [45, 46]. Everything is packed in the `Gauss` software package [47]. And finally, the detector response is provided by the software package called `Boole` [48]. The output of `Boole` is stored in the same format than the one used for real data.

Databases

The event reconstruction is performed using geometry information stored in the *Detector Description DB* (*DDDB*) and calibration and alignment parameters stored in the *LHCB CONDition* (*LHCBCOND*) database.
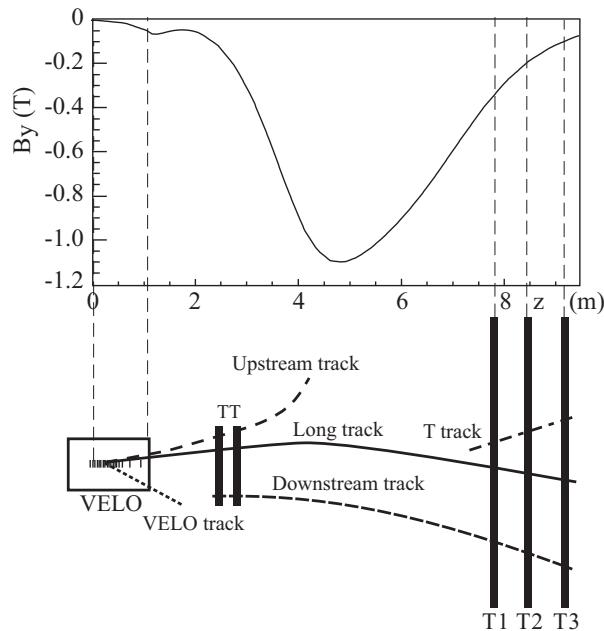
Figure 2.14: The different LHCb track types and the vertical magnetic field intensity as a function of z position.

2.2.5 Run-I summary

The amount of recorded data is given by the *integrated luminosity*. The luminosity $\mathcal{L}$ is the parameter that connects the collision rate R to the cross section σ as

$$R = \mathcal{L} \cdot \sigma, \qquad\qquad (2.1)$$

where R is in s^{-1}, σ in cm^2 and therefore $\mathcal{L}$ in $cm^{-2}s^{-1}$. Integrating the rate for the period of data taking to obtain the total number of collisions, the *integrated luminosity L*, is used. Instead of using cm^{-2} for L, the *inverse barn* (b^{-1}) is used where the barn equals to 10^{-24} cm^2. The amount of integrated luminosity recorded by LHCb per year is of the order of the *inverse femtobarn* (fb^{-1}) that corresponds to about 10^{11} $b-\bar{b}$ pairs.

On November 23rd, 2009, all four LHC experiments observed their first collisions at $\sqrt{s} = 0.9$ TeV. LHCb recorded a very small sample of about 7 μb^{-1} and published its first physics result on the prompt K_S^0 production [49]. In 2010, about 36 pb^{-1} were recorded at $\sqrt{s} = 7$ TeV that lead to a significant amount of results on various aspects of the *b*- and *c*-physics. In 2011, about 1 fb^{-1} were recorded at $\sqrt{s} = 7$ TeV and this corresponds the dataset used in this thesis. In 2012, about 2 fb^{-1} at an increased centre-of-mass energy of $\sqrt{s} = 8$ TeV were recorded. Figure 2.15 summarises the excellent performance of the LHC accelerator and the LHCb experiment.
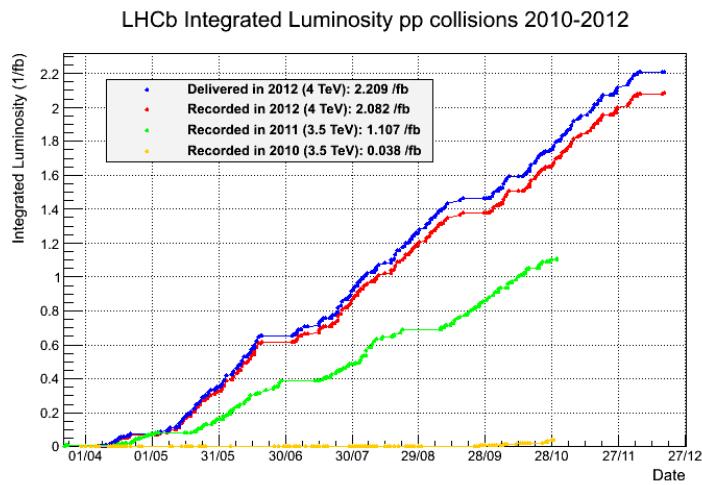
Figure 2.15: LHCb recorded integrated luminosity as a function of time from 2010 to 2012.

3 The calibration and performance of the LHCb tracking system

3.1 ST TELL1 calibration

3.1.1 Beetle chip, digitizer board and TELL1 board

The front-end chip that is used for both the IT and TT is version 1.3 of the *Beetle* [50] originally developed for the VELO. The Beetle is responsible for acquiring, shaping and storing signals into analogue pipelines with a given *Pipeline Column Number* (PCN) and transmitting signal information for L0-accepted events. Each Beetle reads 128 micro-strips and sends the data through four analogue ports to the *digitizer boards* [51] via 5m copper cables. Figure 3.1 shows the information chain sent by the Beetle at 40 MHz on the four ports and Fig. 3.2 the legend of the chain content. Each analogue port sends first a header and then the information of the 32 strips follows. The header information is given by the two voltage states corresponding to a *pseudo-bit*.

The digitizer board contains an *analogue-to-digital converter* (ADC). These boards are located in *service boxes* [52]. These service boxes are placed at the bottom of the IT stations and at the side of TT, both outside the LHCb geometrical acceptance. The signal amplitude is coded in 8 bits. The output signal of the Beetle has a non-zero baseline and the gain is set such that the baseline corresponds to 128 ADC counts. The pseudo header-bit 0 (1) is 40 ADC counts below (above) the baseline. The average ADC count for the strip without signal is called the
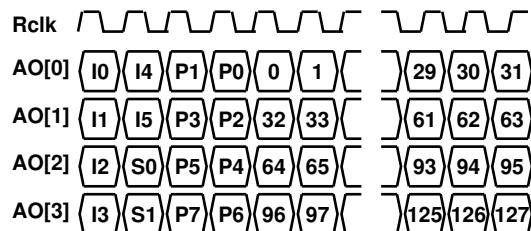
Figure 3.1: Layout of the signal chain sent by the Beetle through four analogue ports. [50]

pedestal and its spread the *noise*. The properties of the Beetle chip were characterised and its parameters tuned during test beams periods. It has an I^2C *interface* to set the operating parameters of the chip with the slow control system. The reminder of the signal after 25 ns is about 30% of its peak voltage. The result of the digitizer board is further shipped to *TELL1 boards* using *Vertical-Cavity Surface-Emitting Lasers* (VCSELs) through optical fibres.

Bit		Description
I0	LeadingBit	always active ($= 1$)
I2	ActiveEDC	1 indicates active error detection and correction (EDC) logic
I3	ParCompChTh	(even) parity of register *CompChTh* (reg. no. 20, cf. table 14)
I4	ParCompMask	(even) parity of register *CompMask* (reg. no. 21, cf. table 14)
S0		LSB of register *SEUcounter* (reg. no. 23, cf. table 14)
S1		bit 1 of register *SEUcounter* (reg. no. 23, cf. table 14)
P0		LSB of pipeline column number
P1		bit 1 of pipeline column number
P2		bit 2 of pipeline column number
P3		bit 3 of pipeline column number
P4		bit 4 of pipeline column number
P5		bit 5 of pipeline column number
P6		bit 6 of pipeline column number
P7		MSB of pipeline column number
special for **Beetle1.3**:		
I1	ParPCN	(even) parity of pipeline column number (PCN)
I5	ParTpSelect	(even) parity of register *TpSelect* (reg. no. 22, cf. table 14)
special for **Beetle1.4** and **Beetle1.5**:		
I1	ParTpSelect	(even) parity of register *TpSelect* (reg. no. 22, cf. table 14)
I5	ParPCN	(even) parity of pipeline column number (PCN)

Figure 3.2: Legend of the signal chain sent by the Beetle through four analogue ports. [50]
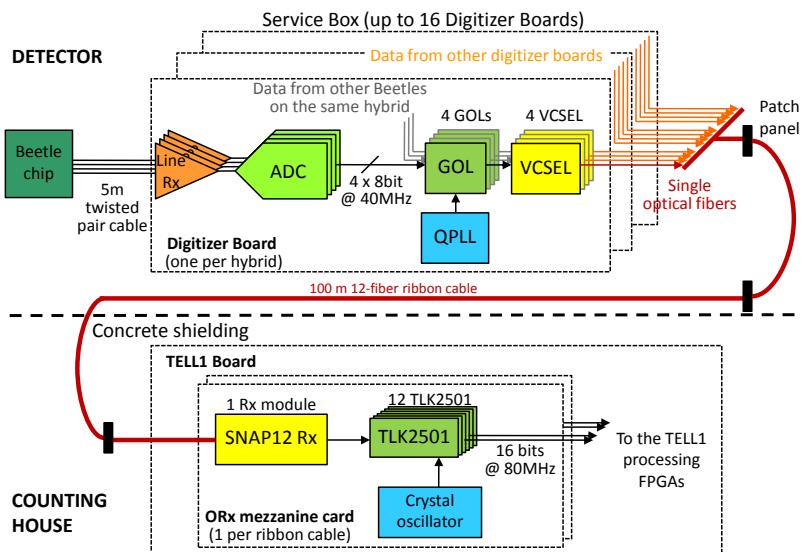

Figure 3.3: Read-out chain used by the IT and TT for the Beetle to the TELL1 board passing through the digitizer boards.

Table 3.1: The conversion table between the different granularities and their corresponding number of channels.

1 Strip	↔	1 channel
1 Beetle port	↔	32 channels
1 TELL1 PP-FPGA processing channel	↔	64 channels
1 Beetle/VCSEL	↔	128 channels
1 Read-out sector	↔	384/512 channels for IT/TT
1 TELL1 PP-FPGA	↔	768 channels
1 TELL1	↔	3072 channels

In the LHCb experiment, the acquisition, the *zero-suppression* and the *clusterisation* are performed by *TELL1 boards* developed at EPFL [53]. The zero-suppression is mainly the process that subtracts the pedestal in order to identify strips with signal. The clusterisation is the process that groups together strips with signals coming from the same particle, called *clusters*. The TELL1 boards are located in an area with low radioactivity. The ST group uses 90 TELL1 boards to process the data coming from the IT and TT sub-detectors via optical fibres. Twelve optical fibres are packed in one ribbon cable. One TELL1 board has two optical receivers using two ORX mezzanine cards. The data is split in four and processed by a *Parallel-Processing-Field-Programmable Gate Array* (PP-FPGA) each. Every PP-FPGA has twelve processing channels to perform the zero-suppression and clusterisation. The result of this process is sent to the trigger farms for event reconstruction. Figure 3.3 shows the full read-out chain used by the IT and TT. Table 3.1 summarises the granularities present for IT and TT and the corresponding number of channels.

The TELL1 can be configured in two ways using either *configuration* (CFG) *files* or *PVSS recipes*, where *PVSS* is the software framework that is used to control the LHCb detector. The TELL1 recipes can be created from CFG files or XML files. The creation of TELL1 recipes from XML files is performed using a PVSS library and control interface developed at EPFL [54]. The XML files are called *config XML* files and they are stored in a conditions database called *COND*.

3.1.2   TELL1 board processing

For the zero-suppression and clusterisation processes of the TELL1, three consecutive steps are made. First, the *header correction*, followed by the pedestal subtraction, the *linear common mode subtraction* (LCMS) and finally, the clusterisation.

Before reviewing the different processing steps, the different sources that can form clusters should be identified. The first source is the signal, i.e. charge deposition from a charged particle crossing the silicon. The second one is noise due to thermal excitation of the silicon. The last source is *spillover*, also called *out-of-time* pileup in other experiments, where clusters contain signal from the previous bunch crossing.

In order to monitor the TELL1 processing and calibrate the clustering parameters, a bit-perfect emulator of the TELL1 processing was developed at EPFL [55], hereafter called the *TELL1 emulator*. It is written in C++. Four relevant types of data are available with the TELL1 emulator: *Non-zero suppressed ADC counts* (NZS ADCs), *pedestal-subtracted header-corrected ADC counts* (PedSub ADCs), *ADC counts after LCMS* (LCMS ADCs) and the *list of clusters*. Among those types, only the NZS ADCs and the list of clusters is available with the TELL1.

The three processes that the TELL1 is performing are described in the following lines.

Header correction and pedestal subtraction

One of the known features of the information sent by the Beetle chip is that the pedestal values of the first six strips, for each port, shift when any of the header bit changes its status. This is known that 9 out of 16 header bits (P0 to P7 and I1 in Fig. 3.1) change their status continuously since they compose the PCN counter.

Two other header bits (S0 and S1 in Fig. 3.1) are expected to change their status as well, since they compose the counter for the *Single Event Upset* (SEU). The SEU is due to large ionisation by a particle hitting an electronics element of the Beetle chip and changing its status. This is a very rare phenomenon and changes of those header bits were not seen until a procedure was established for long-term monitoring of the ST data. Figure 3.4 demonstrates that the pedestal value shifts are correlated with at least the status of those two header bits. The remaining header bits are not supposed to change their status.

However, a careful look at results presented in Fig. 3.4 show that the header bit (I4) is changing as well and further studies showed that the header bit (I3) is also changing. Those two header bits are the parity bits of the two registers CompChTh and CompMask, which are not usually initialised when a data taking is resumed after the injection of new beams in the LHCb where the Beetle chips are switched off. Unfortunately, the registers do not come back to the same
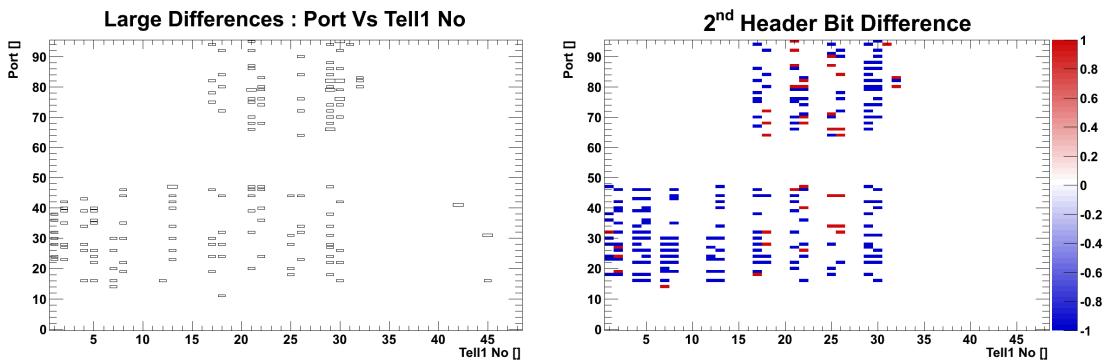

Figure 3.4: Shift in pedestal values between two set of calibration results by TELL1 and Beetle port numbers (*left*) and second header bit flips by TELL1 and Beetle port numbers (*right*) for the TT.

states after switching on the chips. Based on this discovery, it was decided to initialise all the Beetle registers after every switch-on. Despite this new measure, the shift of the pedestal values are inevitable as explained above for the header bits-S0 and S1. For the clustering, this header dependent shift of the pedestal values must be corrected in the TELL1, based on the transmitted header. Since the 9 header bits are continuously changing, corrections to the pedestal values are easily obtained from calibration runs where non-zero suppressed data are available. Statistics of the calibration data available for the other header bit cases are too small to obtain corrections. Therefore, corrections are made based on the available corrections for the case of the 9 headers. For this, we assume that the shift in the pedestal values are due to the charge of the pseudo-bit in the proceeding time bucket in the same analogue port. For example, the expected pedestal value for the Strip-0 data with the status of bit-I4 changed, in Fig. 3.1, is identical to that of Strip-1 data with the status of the bit-P1 changed. This assumption was successfully tested with the calibration data as shown in Figs. 3.5 and 3.6. Based on this assumption, pedestal value corrections for all the header configurations of the three last header bits are calculated and applied for the pedestal subtraction process.

For the pedestal subtraction process, the calibrated pedestal is subtracted for each channel from the ADC count obtained after correcting for header effects. This gives the PedSub ADCs dataset. In the case that the channel is masked, i.e. the *channel mask* is equal to 1, the PedSub ADC is set to 0.
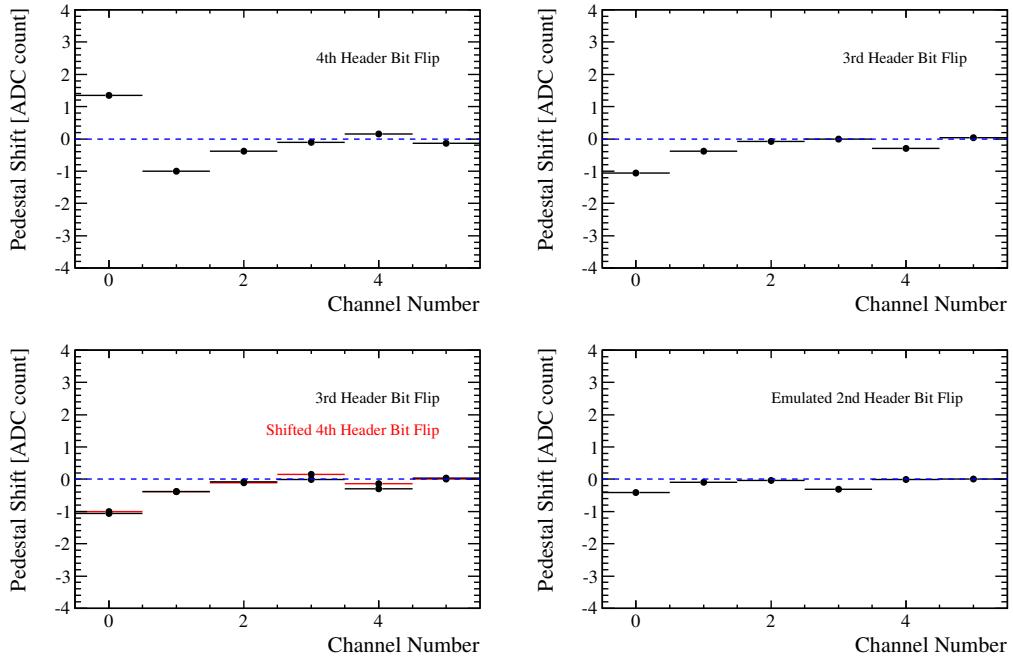
Figure 3.5: Pedestal shift between pseudo-bit 1 and 0 for the six first signal channels of IT for the last header bit (*top, left*) for the third header bit (*top, right*). Overlay of the two top plots where the first plot results are shifted by one channel (*bottom, left*). Emulated Pedestal shift between pseudo-bit 1 and 0 for the second header bit (*bottom, right*).

Table 3.2: Clustering threshold coefficients.

Threshold type	Coefficient
Hit	2.5
CMS	4
Confirmation	5
Spillover	10

Linear common mode subtraction (LCMS)

In order to perform the LCMS process and form clusters, thresholds are used. Each threshold is set as a coefficient times the noise level in ADC counts. These *threshold coefficients* correspond to given values of the *signal-over-noise ratio* (S/N) and they are summarised in Table 3.2. This gives a constant level of noise clusters whilst maintaining the signal hit efficiency. The thresholds coefficients were optimised using test beam data to find the best compromise between signal clustering efficiency and noise clusters rate.

During test beam studies, it was discovered that the Beetle chip has some large common mode noise. The common mode has two components, a global shift and a slope as a function of the ADC counts for every 32 channels corresponding to one analogue port of a Beetle chip.
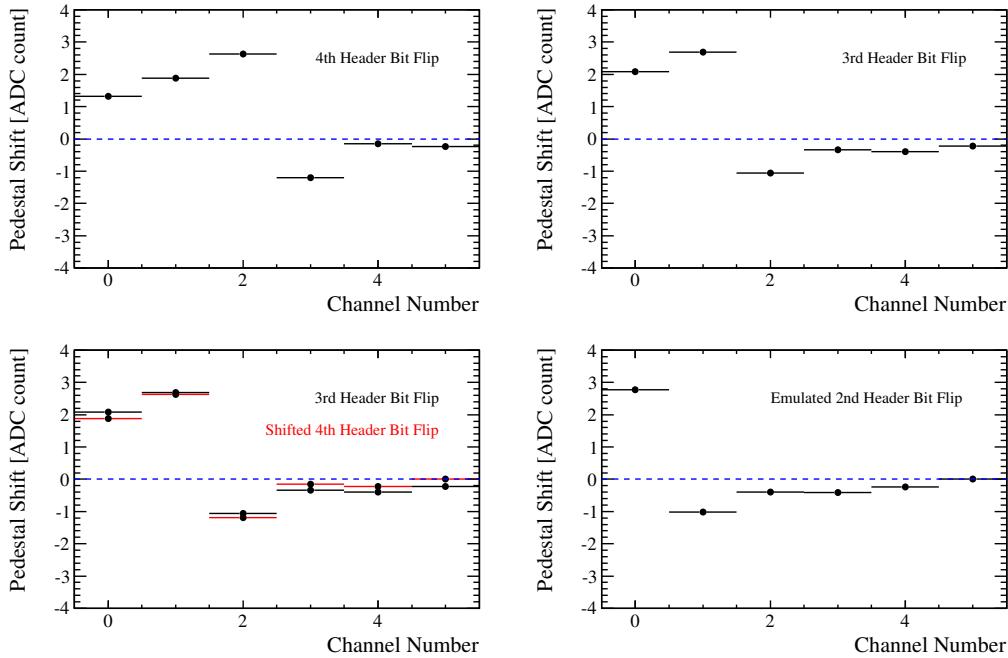

Figure 3.6: Pedestal shift between pseudo-bit 1 and 0 for the six first signal channels of TT for the last header bit (*top, left*) for the third header bit (*top, right*). Overlay of the two top plots where the first plot results are shifted by one channel (*bottom, left*). Emulated Pedestal shift between pseudo-bit 1 and 0 for the second header bit (*bottom, right*).

Table 3.3: Calibration parameters with their granularities.

1 Pedestal	/	channel
1 Hit threshold	/	channel
1 CMS threshold	/	channel
1 Channel masking	/	channel
1 Confirmation threshold	/	TELL1 PP processing channel
1 Spillover threshold	/	TELL1 PP processing channel
48 Header corrections	/	Beetle port

Therefore, the TELL1 first subtracts the average ADC counts of the 32 channels from each channel. To avoid that signal biases the average and slope estimates, the signal channels are identified by their ADC counts being larger than a threshold value ($> 4 \times$ LCMS noise), called *CMS threshold*. A temporary ADC count vector is formed with the ADC of the signal strips set to 0. Finally, the slope is computed using the temporary vector and subtracted from the ADC counts that includes signal. The result of the LCMS gives the LCMS ADCs dataset. The noise ADC value that one obtained after the LCMS process is called *LCMS noise*.

Clusterisation

The clusterisation starts from a set of LCMS ADCs. The first step is to search for signal by looking for *seeds*. Seeds are channels having their LCMS ADC counts larger than a threshold value ($> 2.5 \times$ LCMS noise), called the *hit threshold*. Clusters are then formed by combining adjacent seeds. The cluster size cannot exceed 4 strips, if this happens the cluster is split. Finally, the cluster is accepted if its charge is larger than a certain threshold ($> 5 \times$ LCMS noise), called *confirmation threshold*. If the cluster charge is lower than the *spillover threshold* ($< 10 \times$ LCMS noise), and higher than the confirmation threshold, the spillover flag is set to 1. The spillover flag is meant to indicate that the cluster could be generated by a charged particle from the previous bunch crossing. It can be used to discard these clusters from the previous spill by cutting on the number of hits on the track with spillover flag set to 1. The position of the cluster is determined from a weighted average of its ADC channel counts.

All the parameters needed for these processes are summarised in Table 3.3 with the required granularity for the parameters. In total, 3072 pedestals, masks, hit and CMS thresholds, 4608 header corrections and 48 confirmation and spillover thresholds need to be calibrated. Table 3.4 summarises in which database the relevant parameters are stored.

Table 3.4: Location of parameters used and resulting from the calibration in the COND and LHCBCOND databases.

COND	LHCBCOND
Channels masks	Strips masks
TELL1 analogue links masks	Beetles masks
TELL1 links masks	Sectors masks
Pedestals	Common mode noise
Header corrections	LCMS noise
Thresholds	Thresholds coefficients

3.1.3 TELL1 board calibration

These are the particular contributions made to the calibration, operation and monitoring of the IT and TT during this research work over the period from 2011 to 2013:

- improvement and correction of the existing calibration codes.

- creation of scripts to mask strips, Beetle ports and Beetles.

- creation of a script that analyses the noise to look for problematic channels.

- creation of a script that launches the calibration chain in a single job.

- commissioning of the PVSS user interface to create TELL1 recipes.

- commissioning of inter-fill calibration data taking process.

- automatic offline monitoring using inter-fill calibration datasets.

- maintenance of the ST LHCBCOND and COND databases.

The calibration process is composed of five unique steps:

1. Channel masking

2. Pedestal calibration

3. Header correction calibration

4. Clustering parameters calibration

5. Monitoring

All these steps are described in the following sections.

3.1.4 Channel masking

An important ingredient to perform any calibration is to start from an up-to-date list of masked channels. The very first list was made after the module production, burn-in tests and quality checks. Every time a channel needs to be masked, the config XML is updated and new TELL1 recipes are created. Several sources of channel masking were identified during the three years of operation of the IT and TT: *Broken bonds, dead VCSELs, noisy strips* and *broken connector pins.*

Apart from the TELL1 processing, the masked list is important for cluster decoding, monitoring, simulation and measuring performance of the detectors such as the hit efficiency described in Sec. 3.2.

The bond between the micro-strip and the pitch adapter can break. In order to keep a robust and reliable TELL1 processing, it is important to mask these bonds before the next LHC refill. The diagnostic is to find and identify channels with very low raw noise of about 1 ADC count. To help identifying broken bonds, the calibration job was extended to include a software that looks for channels that have a significant drop in noise with respect to its neighbours within a Beetle port. All identified channels that are not already masked in the LHCBCOND are added to the calibration report for further manual check.

The IT and TT suffered from dying VCSELs from the beginning of LHCb operation at a rate of about five dead VCSELs per year for IT and TT. The diagnostic of a dead VCSEL is when error banks with the tag *TlkLinkLoss* are sent from the corresponding TELL1 for each event. Once this happens, the TELL1 link needs to be masked as soon as possible.

Few groups of channels can show increase of the noise up to the level of 90 ADC counts. This increases the number of noise clusters and those strips must be masked as soon as possible. The source of this issue is assumed to be due to a pinhole formation in the isolation between the micro-strip and the silicon bulk.

In IT, it happened at least twice that two sets of 32-channels had to be masked. This can be due to a dead Beetle port, but the more favoured explanation is that pins of the connectors at the IT detector box used to connect the long cables transmitting the data coming from the Beetle chips to the digitizer boards, are broken. These pins are fragile because they are tiny and densely packed in the IT to limit the material budget in the acceptance.

3.1.5 Pedestal calibration

The calibration of the pedestal values was previously performed using the automatic update of pedestal algorithm that can be used by the TELL1. This algorithm was found to be slow and only sensitive to the last few hundred events and not the entire dataset used by the calibration process. Therefore, a new algorithm, called STPedestalEstimator, was written that performs

the iterative computation of an arithmetic mean for the event number n:

$$< \text{ADC} >_n = \frac{\text{ADC}_n + < \text{ADC} >_{n-1} (n-1)}{n}.$$

(3.1)

STPedestalEstimator is significantly faster, has faster convergence and is sensitive to the whole calibration dataset but is not tolerant to outliers, e.g. charged particle passing through the silicon at the given place. This new algorithm is therefore not suitable for pedestal estimation during collision periods. However, regular calibration datasets are taken without any beam in the LHC, thus the STPedestalEstimator algorithm was used for 2011-2012 calibration. The estimated pedestals are stored in the COND database.

It was observed by the VELO group that the pedestals change depending on the L0 rate at which the dataset is recorded. For 2010 and 2011 data taking periods, the calibration was obtained from calibration datasets recorded at a very low L0 rate of few hundred hertz. In 2012, inter-fill calibration datasets were recorded centrally with a L0 rate larger than 900 kHz. The dependence of the pedestals on the L0 rate was re-discovered. Therefore, from early 2012 onwards, the calibration is performed based on high-L0-rate data.

3.1.6   Header correction calibration

The optimised procedure to obtain the corrections for the effect of header dependent pedestal shifts for the data coming from one analogue port of a Beetle chip are presented. Average pedestal values obtained from the previous procedure are subtracted from the ADC count for each strip. In this way, possible gain variation effects in the strip ADC counts are corrected. Two effects remain after pedestal subtractions: the header dependent pedestal shifts in the first six strips and a common mode affecting all the 32 strips. In order to isolate the header dependent shifts, the common mode must be subtracted first. This can be estimated from the 26 strips not affected by the header effect assuming that the shape is linear w.r.t. the strip numbers. This is done by calculating a mean of the ADC counts for strips-7 to 19 and 20 to 32. From the two averages, a linear extrapolation gives the common mode contributions to the first six strips which are thus subtracted from each ADC count. From those ADC counts, corrections for the header dependent pedestal shifts for the eight possible header patterns are obtained and stored in the COND database. The corrections can be as large as 7 ADC counts and therefore are coded in four bits. It must be noted that the pedestal values are appropriately shifted in order to exploit the four bit dynamic range available for the header correction process.

3.1.7   Clustering parameter calibration

As previously mentioned, the thresholds values used in the clustering are obtained from some coefficients and the estimated LCMS noise level. In the LHCBCOND database, it is not the raw and LCMS noise values that are stored but the *Common Mode* (CM) and LCMS noises, where

the CM noise is given by

$$(\text{CM noise})^2 = (\text{RAW noise})^2 - (\text{LCMS noise})^2 \tag{3.2}$$

The common mode noise is needed for the digitisation performed in the simulation.

A new algorithm to estimate the raw and LCMS noises is written. It is significantly faster than the previous one where the pedSub ADCs and LCMS ADCs were stored in profile histograms to estimate their spread. The new algorithm uses the same philosophy as the estimate of the pedestal. The noise is the square-root of the variance of the ADC counts:

$$\text{Noise} = \sqrt{<(\text{ADC} - \overline{\text{ADC}})^2>} = \sqrt{<\text{ADC}^2> - \overline{\text{ADC}}^2} \tag{3.3}$$

The noise can be estimated by computing adaptive estimates of $<\text{ADC}^2>$ and $\overline{\text{ADC}}^2$.

3.1.8 Monitoring

All the parameters obtained after the calibration process are constantly monitored by comparing the values in use and newly calculated ones from data collected during calibration runs. A new program produces various monitoring plots such as the differences in pedestal, noise values and also the status of the second header bit for example.

3.1.9 Summary

Figure 3.7 summarises the calibration chain. A single BASH script was written to perform all these steps. In 2012, the code used by the VELO group to launch their own calibration process was modified to launch the ST calibration automatically from inter-fill calibration data. At the end of the job, all the summary plots are sent to the ST calibration expert, including the list of potentially problematic channels. These results are used to judge the quality of the current calibration and based on those results, the decision to change the calibration is made.
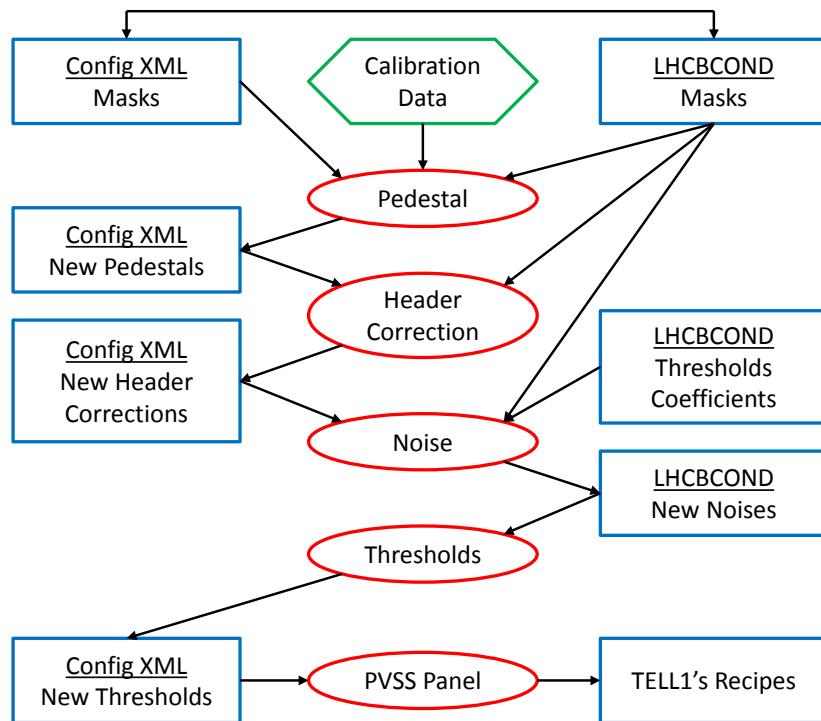
Figure 3.7: Schematic of the calibration chain.

3.2 ST performance

3.2.1 Introduction

Relevant variables to demonstrate the performance of the IT and TT and their results are presented in this section.

Hit efficiency

The *hit efficiency* is the probability that a cluster will be reconstructed when a charged particle crosses an active silicon sensor. This efficiency depends on the silicon sensor thickness and the clustering parameters. The sensor should be thick enough to obtain a good signal-to-noise ratio and thin enough to reduce multiple scattering. Once the signal size is large enough, the clustering algorithms and parameters need to be set to get a signal hit efficiency larger than 99% and a noise cluster rate of about 10^{-5} required for efficient tracking. Since the hit efficiency directly impacts the reconstruction efficiency of a track, it needs to be monitored. Two hit efficiencies will be measured, the average hit efficiency of the reconstructed tracks and the *sector hit efficiency* which is the average hit efficiency of each sector.

The hit efficiency is measured in the following way: from a sample of tracks, a search window is opened for each IT and TT module where a hit is expected, *i.e.* the track crosses geometrically the active region of the module using the knowledge of the positions and geometrical description of the modules. If a hit is found within the search window then the found hits counter, i.e. the numerator of the efficiency, is incremented. The number of expected hits is the denominator of the efficiency.

Measuring hit efficiency comes with several caveats that need to be considered. The first one is that experimentally it is difficult to disentangle hit and tracking efficiencies. In order to construct a long track, some sub-detectors are used for which hit efficiency wants to measured. This is the case for the IT but not for the TT for which hits are added to the track to improve the long track resolution if hits are found within reasonable search window. Ideally, the tracking algorithm would be launched excluding one by one each module to measure its hit efficiency. This procedure is extremely computationally intensive, therefore not attempted. What makes the measurement still feasible and unbiased is that the number of hits required in the tracking is significantly lower than the number of tracking layers and that the hit efficiency is greater than 99%. The tracking actually requires nine hits in the T-stations whereas twelve layers are actually available.

A second point is the presence of *ghost tracks* in the tracks sample. Ghost tracks are the result of a wrong combination of hits. Their direct effect is to artificially lower the measured hit efficiency. To address this point, in the upcoming results, as for the alignment, daughter tracks from clean samples of $J/\psi \to \mu^+ \mu^-$ mesons are used which contain low numbers of ghost tracks.

A third point is the presence of real and close-by tracks that can enhance the measured hit efficiency, ie extra hits can leak in the search window. A track isolation requirement is added to the code that measures the hit efficiency by asking no more than one found hit per sector.

A fourth point is the knowledge of the modules positions, *i.e.* the alignment, and the finite precision on the prediction of the hit position, *i.e.* the track resolution. These two elements drive the size of the search window. They also affect the hit efficiency measurement for tracks close from sensor edges. In addition, the edges of the sensors are inefficient due to guard rings. These effects are suppressed by removing expected hits from the computation for tracks crossing the module within an edge tolerance.

A fifth point is the effect of multiple scattering. The search window should be larger than the one expected from pure hit resolution and misalignments, in order to account for small variation of the track direction due to multiple scattering after each material crossing. The effect of the multiple scattering decreases with increasing momentum, therefore a cut on the track momentum is applied.

And the last point is the effect of the decay and absorption of charged particles. A long track can be reconstructed without the third T-station if nine hits are found in the two first stations although the track decayed just before the third T-station or stopped in the previous station. This effect is suppressed by the use of muons from J/ψ decays where segments are found in the muons stations, *i.e.* tracks that traverse the whole tracker.

Hit resolution

The *hit resolution* is the spread of the *unbiased hit residuals* distribution. The hit residual is the cluster central position with respect to the position where the extrapolated particle crossed the silicon sensor. The unbiased hit residual is the case where the hits found in the module are excluded from the track fit. The resolution mainly depends on the micro-strip pitch, ie the inter-strip distance, and the amount of charge sharing which depends on the amount of energy deposited by the particle. The expected hit resolution for the IT and TT is between 50 and 60 μm.

The sub-detector hit resolution is taken as the sum of the unbiased hit residuals of the modules, which means that remaining misalignments are included in the hit resolution. The spread of all the module mean unbiased residuals is called the *sector biased resolution*. The sector biased resolution is driven by remaining misalignments and statistical fluctuations.

Signal-to-noise ratio

The *signal-to-noise ratio* is the cluster charge divided by the noise of the cluster's central strip. During the R&D and testing periods with particle beams, it was found that a signal-to-noise ratio better than 10 is required to keep a hit efficiency over 99%.

Table 3.5: Selections for hit resolution, signal-to-noise ratio and efficiency measurements.

Decay mode	Cut	Hit resolution, S/N	Hit efficiency
$\mu^{\pm}$	$p_T(\mu^{\pm})$	> 0.55 GeV/c	> 0.55 GeV/c
	$p(\mu^{\pm})$	> 10 GeV/c	> 10 GeV/c
	$\chi^2_{\text{track}}/\text{nDoF}(\mu^{\pm})$	< 3	< 2
	$\chi^2_{\text{Velo segment}}/\text{nDoF}(\mu^{\pm})$	$-$	< 2
	$\chi^2_{\text{T track}}/\text{nDoF}(\mu^{\pm})$	$-$	< 2
	$\chi^2_{\text{Match}}/\text{nDoF}(\mu^{\pm})$	$-$	< 2
	clone distance $(\mu^{\pm})$	> 5000	> 5000
$J/\psi \to \mu^+\mu^-$	$\Delta\ln\mathscr{L}_{\mu\pi}(\mu^{\pm})$	> 0	> 0
	$\chi^2_{\text{vtx}}/\text{nDoF}(J/\psi)$	< 16	< 16
	Decay Length Sig. (J/ψ)	> 3	> 3
	$M(\mu^+\mu^-)$	$\in [3060, 3140]$ MeV/c^2	$\in [3060, 3140]$ MeV/c^2

Table 3.6: Specific requirements used for hit efficiency measurements for IT and TT separately.

Requirement	IT	TT
Search window	0.4 mm	0.4 mm
Min expected sectors	6	2
Min stations passed	3	1
Sensor edges tolerance in X	2 mm	2 mm
Sensor edges tolerance in Y	2 mm	2 mm
Single hit per sector	Yes	Yes

3.2.2 Track selection

The J/ψ candidates are taken from the inclusive detached J/ψ stripping line from Stripping20 the selection of which is given in Chap. 4. The muons of these selected J/ψ decays are refitted and extra track quality and momentum cuts are applied. The final selections are summarised in Table 3.5. A momentum cut is applied to reduce multiple scattering and absorption effects. Tighter and extra track χ^2 cuts are used for hit efficiency measurements to further reduce the number of ghost tracks. The list of the cuts and requirements used for hit efficiency measurements are summarised in Table 3.6.

3.2.3 Results

Table 3.7 summarises all the results of hit efficiency, sector hit efficiency, hit resolution, sector biased resolution and signal-to-noise ratio obtained from data and MC for both IT and TT. All the distributions from which these results were extracted can be found in Appendix A.

The first result is that the measured hit efficiency in MC is not 100% for both IT and TT. For the IT, it is partially due to sectors presenting high common mode noise levels for which a lower hit efficiency is set at the digitalisation step, based on results obtained in 2010 [56].

Table 3.7: Hit efficiency, sector hit efficiency, hit resolution, sector biased resolution and signal-to-noise ratio measurements for IT and TT from data and MC.

	Measurement	2011 Data	2012 Data	MC2011	MC2012
	Hit efficiency	99.82%	99.88%	99.92%	99.92%
	Sector hit efficiency	99.82%	99.86%	99.91%	99.90%
IT	Hit resolution	50.3 μm	54.9 μm	53.8 μm	53.9 μm
	Sector biased resolution	9.6 μm	10.7 μm	1.2 μm	1.6 μm
	Signal-over-Noise ratio	17.3	17.4	17.6	17.6
	Hit efficiency	99.73%	99.76%	99.90%	99.89%
	Sector hit efficiency	99.77%	99.79%	99.89%	99.89%
TT	Hit resolution	52.6 μm	53.4 μm	47.8 μm	48.0 μm
	Sector biased resolution	30.0 μm	28.4 μm	1.8 μm	1.7 μm
	Signal-over-Noise ratio	14.1	14.1	14.2	14.3

However, it was found that the hit inefficiency is not applied to the correct read-out sectors as illustrated in Fig. A.2. This will be fixed for the next simulation round. However, for the TT, all the read-out sectors are set to be 100% efficient. A deeper investigation shows some evidence that the sectors with a large number of masked strips are less efficient by a factor of up to one per mille. This can be easily understood from the clustering algorithms. The last part of the hit inefficiency possibly come from some remaining ghost tracks and badly reconstructed tracks. In data, the hit efficiency is worse by 1-2 per mille. This is due to the significantly worse purity of the J/ψ samples in data compared to MC. The hit efficiency for 2012 is a bit better than 2011, possibly due to improvements made in the calibration before the 2012 data taking.

Hit resolutions measured in data are worse than MC, because of the additional remaining misalignments that are present in data. However, the measured hit resolution in 2011 for IT is significantly smaller than in 2012 data and the MC. This is not understood and requires further investigation. Sector biased resolutions are measured to be below 2 μm in MC where there is no misalignment and therefore are due to statistical fluctuations. In data, the number of reconstructed J/ψ events is two up to three times larger than MC, and so the statistical fluctuations are expected to be smaller than MC. Thus, the measured sector bias resolutions in data are dominated by misalignment effects. Whereas the misalignments for IT are within an acceptable range, they are unexpectedly large for TT and require further investigation by alignment experts.

Signal-to-noise ratio measurements are in relatively good agreement with MC and are above the limit of 10. Below this value, the hit efficiency will decrease. Looking at Fig A.10, it can be noticed that twelve sectors of the top and bottom boxes have significantly larger signal-to-noise ratios compared to the other modules. This is known to come from the thicker sensors installed in these boxes. However, the signal-to-noise ratio obtained in MC for the four sectors in the IT2 Bottom box is significantly different to the data results. This can be due to a poor charge calibration of these sectors.

3.3 Tracker vertical alignment

The vertical alignment procedure and the results obtained in 2011 for the IT and TT were presented at the 2011 IEEE NSS international conference in Valencia, Spain. This section is highly inspired by the proceedings contributed by the author for this conference [57].

3.3.1 Introduction

Survey measurements were performed during assembly and after installation of the IT, TT and OT in the LHCb cavern. The nominal positions of the modules are stored in the DDDB database. If the survey measurements are significantly different from the nominal positions, the differences are stored into the LHCb conditions database called *LHCBCOND*.

For the IT, the survey precision of the position of the boxes in x and y is about 1 mm and 2 mm in z. Inside the box, positions of the modules are known to within 100 μm.

For the TT, the survey precision on the position of the whole box is about 0.5 mm. Positions of the modules inside the box are known to below 100 μm.

For the OT, the survey accuracy of the C-Frames positions is about 1 mm assuming that the C-Frames are flat objects where another millimetre can be added due to deformations. The accuracy of the relative alignment between the X1 and U (V and X2) layers is about 200 μm by construction, but the survey accuracy is about 0.4-0.5 mm.

To profit from the excellent resolution of the detector, the tracker must be aligned well below its single hit resolution which is better than 60 μm for the ST and 200 μm for the OT. Therefore, the accuracy of the survey is clearly not sufficient.

The required accuracy can be achieved using track-based alignment. The procedure is based on the minimisation of a global chi-square function (χ^2) with both track and alignment parameters [58–60]. The idea is to minimise a global χ^2 value based on tracks residuals.

The vertical position (y) of tracks in LHCb is obtained using a combination of X and U/V measurements. This introduces what is identified as a *weak mode* in the alignment: relative x shift of an X-type module with respect to a U/V-type module is almost indistinguishable from a y shift of both modules. In order to partially solve this ambiguity, the survey constraints are used. The large uncertainty difference between the relative x positions between the modules (0.1/0.1/0.5 μm for IT/TT/OT) and the absolute y position of the module (1/0.5/2 mm for IT/TT/OT) survey position accuracies can lead to non-physical vertical movements. This is what was observed when aligning the tracker in the y-direction with the track-based alignment: the TT box position moved by 4 mm in the y direction for example which is physically impossible. Therefore, another strategy is required to vertically align the tracker.

3.3.2 Relevant insensitive regions perpendicular to vertical axis

In order to motivate the new vertical alignment procedure a deeper look into the tracker geometry is needed. For the IT and TT, each silicon sensor is surrounded by guard rings that lead to an inactive peripheral width of 1.37 mm for TT and 1 mm for IT. In addition, readout modules with more than one silicon sensor have a bond gap of 0.15 mm between sensors. For the OT, the F modules have two insensitive gaps of 36 mm in each monolayer and the monolayers are shifted in the y direction by 36 mm as shown in Fig. 2.9. For the S modules, the insensitive gaps are much larger to leave the innermost part of the tracker to the IT and the expected values are summarised in Table 3.10. The gap separation for S modules is expected to vanish.

From the measured y-hit distributions, the y position of those insensitive regions can be measured. They give the y position of the modules with respect to the survey measurements. In the local frame of:

- IT and TT 1-sensor modules: The average y position of the edges is at y equals zero.

- TT 2-sensors modules: The y position of the gap is at y equals zero.

- TT 3-sensors modules: The average y position of the two gaps is at y equals zero.

- TT 4-sensors modules: The y position of the central gap is at y equals zero.

- OT modules: The average y position of the two gaps of the monolayers is at y equals zero.

Any shift with respect to zero is a vertical misalignment according to the VELO alignment, since tracks found by the VELO are used as discussed in the next section.
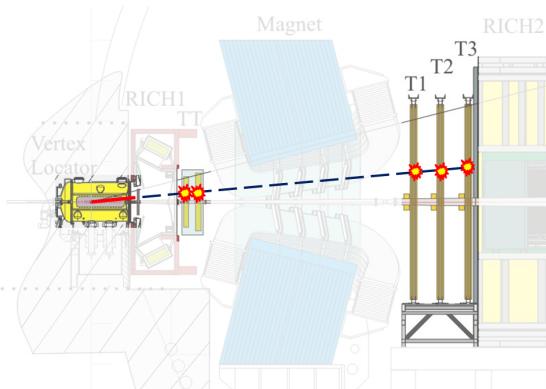

Figure 3.8: VELO segment extrapolation using data with the spectrometer dipole switched off.

3.3.3 Vertical alignment using track extrapolation with magnet off data

The new vertical alignment procedure requires a y-hit spectrum where the y position must be provided by another sub-detector than the one to be aligned. This can be performed at LHCb with VELO track segments extrapolated to the tracker modules using data recorded with the spectrometer dipole switched off (Fig. 3.8). In practise, once the track is extrapolated to the module, a search window is opened. A window size of 4 mm is used for the IT and TT, and 10 mm for the OT. If a hit is found within the search window, the extrapolated y position of the VELO segment is stored in the y-hit distribution of the module.

Since the TT is close to the VELO, the track extrapolation resolution is good enough to see and fit the inter-sensor gaps. However, the IT is 8 to 10 m downstream of the VELO and in this case not all IT modules present sharp gaps in y-hit distributions. The strategy to fit gaps for more than one silicon sensor TT module and edges for single sensor ST and OT modules is chosen.

In both cases, error functions are chosen to fit the hit distributions from which we can obtain the y alignment measurement. In order to remove non-uniformity in y-hit distributions due to the distribution of the VELO track segments, the y-hit distribution is divided by the extrapolated y spectrum to obtain an efficiency distribution. Results of fits to edges and gaps are shown in Figs. 3.9, 3.10, 3.11 and 3.12. The reason for a non-vanishing spectrum outside the sensitive region is due to hits from nearby tracks leaking into the search window, presence of noise clusters and the scattering of low momentum particles. The reason of a measured efficiency not equal to 100% and not always uniform as function of the y direction, is assumed to be due to ghost VELO segments and scattering/absorption of low momentum particles.

3.3.4 Active lengths, gap widths and two-gap distances

One important output and cross-check of the method are the measurements of active lengths, gap widths and distances. The distance between the two error functions is the *active length* for the IT/TT, *gap width* for the OT and the distance between the two-gap centres is the *two-gap distance* for TT/OT. Tables 3.8, 3.9 and 3.10 summarise the expected values taken from
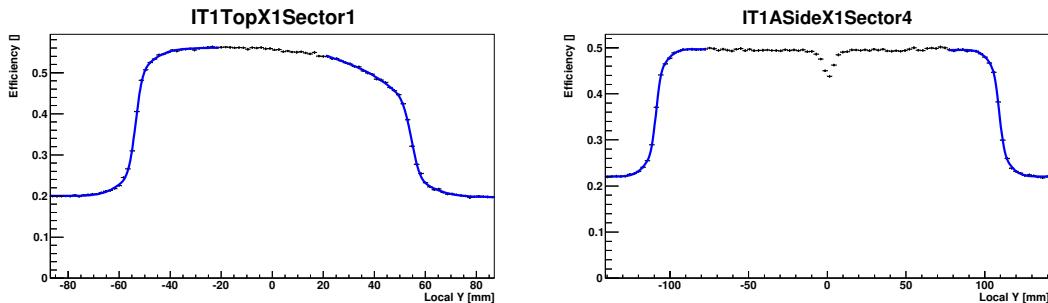

Figure 3.9: y-hit distribution obtained from the 2011 dataset of a short (*left*) and long (*right*) IT modules where error functions are used to fit the edges.
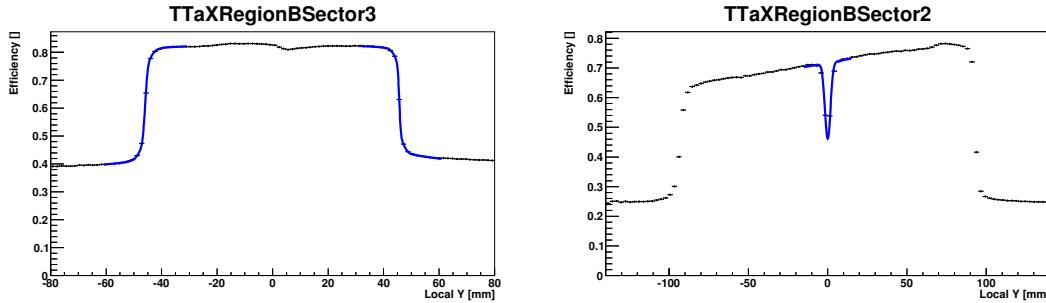
Figure 3.10: *y*-hit distribution obtained from the 2011 dataset of a 1-sensor (*left*) and 2-sensors (*right*) TT module where error functions are used to fit the edges.
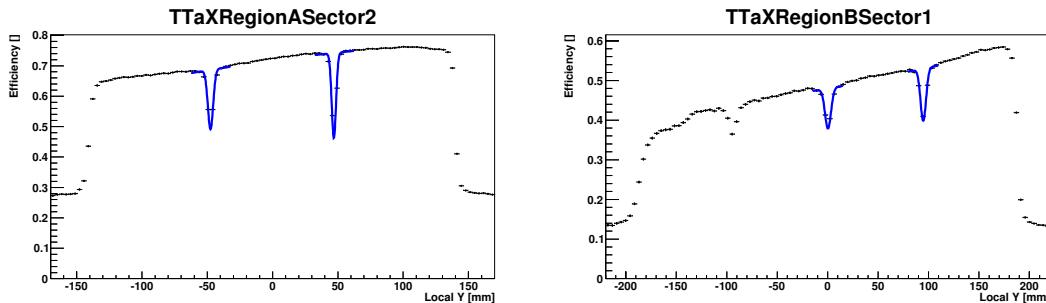

Figure 3.11: *y*-hit distribution obtained from the 2011 dataset of a 3-sensors (*left*) and 4-sensors (*right*) TT module where error functions are used to fit the gaps.
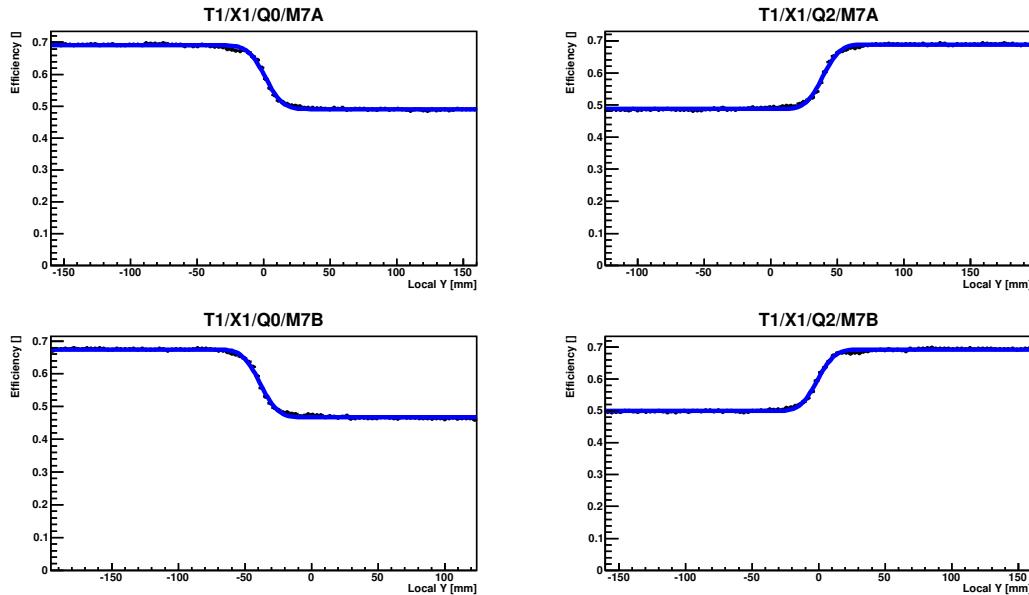

Figure 3.12: *y*-hit distribution obtained from the 2011 dataset of a OT module centre where error functions are used to fit the edges.

Table 3.8: Expected and measured active lengths in mm for TT 1-sensor, IT short and long modules from real data and MC.

Active length	IT short module	IT long module	TT 1-sensor module
Expected	108.00	218.15	91.68
2010 MC	108.10 ± 0.03	218.23 ± 0.02	91.70 ± 0.01
2011 Data	108.09 ± 0.02	218.24 ± 0.02	91.60 ± 0.01
2012 Data	108.04 ± 0.02	218.25 ± 0.02	91.64 ± 0.01

Table 3.9: Expected and measured two-gap distances in mm for TT 3/4-sensor, OT F and S modules from real data and MC.

Two-gap distance	TT 3/4-sensors modules	OT F modules	OT S modules
Expected	94.60	36.00	0.00
2010 MC	94.56 ± 0.04	35.43 ± 0.05	0.033 ± 0.004
2011 Data	94.50 ± 0.02	37.12 ± 0.17	0.10 ± 0.01
2012 Data	94.54 ± 0.01	37.16 ± 0.16	0.10 ± 0.01

Table 3.10: Expected and measured OT gap widths in mm from real data and MC.

Gap width	OT F mod.	OT S1 mod.	OT1 S23 mod.	OT2 S23 mod.	OT3 S23 mod.
Expected	36.00	200.00	386.00	400.00	414.00
2010 MC	35.53 ± 0.08	224.58 ± 0.04	409.3 ± 0.2	424.2 ± 0.5	438.0 ± 0.3
2011 Data	38.48 ± 0.12	200.61 ± 0.04	387.5 ± 0.3	401.1 ± 0.3	413.6 ± 0.4
2012 Data	38.43 ± 0.12	200.65 ± 0.12	387.4 ± 0.3	401.2 ± 0.3	414.0 ± 0.3

technical drawings, results from 2010 MC simulation, 2011 data and 2012 data without any magnetic field. The 2012 results are based on an alignment database that includes corrected y positions obtained from the 2011 dataset. Two-dimensional plots of the measured and expected lengths and distances obtained from MC, 2011 and 2012 datasets can be found in the appendix B.

For the IT, active length measurements from real data and MC are longer by about 100 μm with respect to expectation from the detector geometry, thus showing a bias in fitting edges. However, the results between real data and MC are in good agreement.

For the TT, active length and two-gap distances measurements in MC simulation are in good agreement with the expectations. The first interesting outcome is that measured distances with data are smaller than expected. This can be caused by z misalignments of the TT with respect to the VELO. It is known in LHCb that the track-based alignment favours a displaced TT by 1-2 mm away from the VELO with respect to survey. The alignment database used for the 2011 results is the one where the TT system z position is fixed to the survey value. For 2012, the z position of the TT is aligned in the z direction and the length and distances are closer to expectation compared to 2011. Therefore, theses results go in the direction of a relative displacement of the TT with respect to the VELO as favoured by the software alignment.

Table 3.11: Measured IT boxes relative y positions with respect to the survey positions from real data and MC.

Dataset	Box	IT1	IT2	IT3
2010 MC	ASide	-0.03 ± 0.02	$+0.04 \pm 0.02$	-0.01 ± 0.03
	Bottom	$+0.05 \pm 0.04$	$+0.12 \pm 0.05$	$+0.13 \pm 0.05$
	CSide	$+0.03 \pm 0.02$	-0.05 ± 0.02	$+0.00 \pm 0.02$
	Top	-0.05 ± 0.04	-0.10 ± 0.04	-0.09 ± 0.05
2011 data	ASide	$+0.21 \pm 0.02$	$+0.26 \pm 0.08$	$+0.00 \pm 0.05$
	Bottom	-0.11 ± 0.07	$+0.35 \pm 0.07$	-0.01 ± 0.09
	CSide	$+0.17 \pm 0.05$	-0.11 ± 0.03	$+0.12 \pm 0.03$
	Top	$+0.46 \pm 0.05$	$+0.28 \pm 0.09$	$+0.21 \pm 0.09$
2012 data	ASide	-0.20 ± 0.02	-0.05 ± 0.05	-0.13 ± 0.04
	Bottom	-0.09 ± 0.06	-0.04 ± 0.07	-0.14 ± 0.08
	CSide	-0.18 ± 0.03	-0.17 ± 0.03	-0.24 ± 0.03
	Top	-0.18 ± 0.04	-0.10 ± 0.09	-0.17 ± 0.08

For the OT, the gap widths measurements for S modules in MC are larger by about 24 mm with respect to expectations. Checking the implementation of the geometry of the OT, it was discovered that the vertical positions of the S modules were wrong leading to a 24 mm larger gap. This was corrected for in the next round of MC simulations. Subtracting 24 mm from the gap widths of S modules, the MC results are in agreement with expectations, except for a 0.5 mm shift of the gap widths for the F modules. Concerning the two-gap distances of the OT, some biases in the measurements are also observed in MC simulation with respect to expectations. Significant differences are measured for both gap widths and two-gap distances for the OT in data. The source of these issues is not understood yet and further investigation is required.

3.3.5 Vertical alignment results

Tables 3.11, 3.12 and 3.13 summarise the relative y positions with respect to the survey positions measured for IT boxes, TT box and OT stations obtained from MC, 2011 and 2012 datasets. All the MC results are compatible with 0 where some biases close to about 100 μm are measured in the case of the IT boxes. All the data results are found to be no larger than 1 mm with a statistical error smaller than 100 μm, which confirms the quoted survey accuracies. Furthermore, it was found that within two IT boxes, i.e. IT1CSide and IT2ASide, the y misalignment between the two bi-layers are significantly different. For IT1CSide, the y position difference is about 380 ± 60 μm and for IT2ASide is about 750 ± 60 μm. It was agreed with the alignment group to correct the IT boxes, the TT box and OT stations y positions with the 2011 results summarised in Tables 3.11, 3.12 and 3.13. It was also decided to correct the y position of the bi-layers with significant shifts in y. The implementation of the corrections in the database was successfully checked. Two-dimensional plots of the measured y position of each IT/TT/OT module can be found in Appendix B.

Table 3.12: Measured TT box relative y positions with respect to the survey positions from real data and MC.

Dataset	TT	TTa	TTb
2010 MC	-0.03 ± 0.03	-0.03 ± 0.03	-0.03 ± 0.04
2011 Data	-0.23 ± 0.03	-0.33 ± 0.04	-0.14 ± 0.03
2012 Data	-0.03 ± 0.02	-0.14 ± 0.03	$+0.06 \pm 0.02$

Table 3.13: Measured OT station relative y positions with respect to the survey positions from real data and MC.

Dataset	OT	OT1	OT2	OT3
2010 MC	$+0.01 \pm 0.03$	$+0.00 \pm 0.06$	-0.03 ± 0.07	$+0.05 \pm 0.05$
2011 Data	$+0.33 \pm 0.04$	$+0.37 \pm 0.08$	$+0.16 \pm 0.06$	$+0.45 \pm 0.08$
2012 Data	-0.52 ± 0.07	-0.34 ± 0.13	-0.58 ± 0.11	-0.64 ± 0.08

3.3.6 LHCb alignment strategy

First, the VELO is internally aligned with VELO segments and tracks crossing the sensor half overlaps and the vertex constraint is used [61]. Secondly, the vertical alignment of the tracker (IT, TT, OT) using data without magnetic field is performed. This vertical alignment method completely depends on the VELO alignment as already mentioned. Thirdly, the global alignment is performed for the tracker with tracks from vertex- and mass-constrained resonances [62]. Finally, the RICH mirrors are aligned.

4 Measurement of decay time acceptances for b hadrons decaying to a J/ψ meson

4.1 Introduction

In particle physics, some particles parameters of interest, such as its lifetime, are accessible through measurements of their *decay time t* defined, for moving particles, as

$$t = m\frac{\vec{d} \cdot \vec{p}}{|\vec{p}|^2},$$

(4.1)

where $\vec{d}$ is the flight direction between the candidate *decay vertex* and the PV, m the candidate invariant mass and $\vec{p}$ its momentum. With the 2010 dataset, first studies of lifetimes of b hadrons decaying to a J/ψ meson were performed [63] and showed a great potential for LHCb to reach the world best measurements of b-hadron lifetimes already with 1 fb^{-1} of data. However, complications in measuring lifetimes due to the detection efficiency appearing as a function of decay time, hereafter referred as *decay time acceptance*, are discovered. Several sources of decay time acceptances were identified. First, acceptances that depend linearly on decay time with inefficiencies appearing at high decay times, hereafter called *upper decay time acceptances*, were found to come from the forward geometry of LHCb, reconstruction algorithms and some selection cuts [64]. There are also non-linear acceptances that dominate at low decay times, called *lower decay time acceptances*, which arise due to the trigger and in some cases from the stripping cuts applied. In general, the trigger has a non-negligible impact on the decay time acceptance and its behaviour highly depends on the decay products which the trigger algorithms are designed to select. In this thesis, only b hadrons decaying to a J/ψ meson are considered, where the J/ψ decays into a muon pair.

Section 4.2 presents a study on the relevant HLT and stripping lines for $b \rightarrow J/\psi X$ channels. Section 4.3 presents a way to determine lower decay time acceptance effects induced by the trigger and stripping using real data (data-driven method). Section 4.4 summarises the various sources of upper decay time acceptances. Finally, Sec. 4.5 presents various options on how to determine and combine lower and upper decay time acceptances and some analysis examples.

4.2 Selection

4.2.1 Trigger lines

For an analysis, it is mandatory to know which cuts and requirements were applied to the candidate when passing through the trigger system. Therefore, it is important to know if the candidate of interest for a given analysis is the cause or not of a given trigger line firing. In order to do that, a search among the particles that caused the line to fire is performed to know whether some constitu of them are part of the decay products of the candidate or not. Three cases are defined: *Triggered On Signal* (TOS), *Triggered Independently of Signal* (TIS) and *Triggered On Both* (TOB). A candidate is said to be TOS for a given line if all the tracks reconstructed online that fired the trigger line are part of the decay chain of the candidate. The candidate is said to be TIS if the trigger line would still fired after erasing all the tracks that belong to the decay chain of the candidate. A candidate is TOB in the case where the trigger line was fired, but it is neither TOS or TIS. In the case of a $B_s^0 \to J/\psi \phi$ candidate and di-muons triggers, it is TOS if both muons of the J/ψ fire the di-muon line, it is TIS if another di-muon in the event fires the line and TOB if one muon from the given J/ψ is combined with an other muon of the event to fire the line.

In order to identify the most efficient trigger lines to select events with *b* hadrons decaying into final states containing a J/ψ ($b \to J/\psi X$), a sample of offline-selected $B_s^0 \to J/\psi \phi$ candidates are used (see Table 4.5), where ϕ decays into $K^+ K^-$. A fit of the $J/\psi K^+ K^-$ invariant mass is performed to extract the B_s^0 signal yield. The fit uses two Gaussian functions for the signal and an exponential function for the background for each TOS, TIS and TOB category and this for a set of relevant trigger lines. The measured yields in each category and trigger line are further divided by the total yield of $B_s^0 \to J/\psi \phi$ candidates to obtain what is called the *accept fraction* for each trigger line. For the HLT1 trigger, the relevant lines are `Hlt1DiMuonHighMass`, `Hlt1TrackMuon` and `Hlt1TrackAllL0` [65, 66] as shown in Fig. 4.1. For the `Hlt1DiMuonHighMass` line, two oppositely charged tracks with hits in the muon chambers, momentum larger than 5 GeV/c, p_T larger than 0.5 MeV/c and track χ^2 smaller than 4 are combined. The smallest distance between the two tracks (DOCA) must be smaller than 0.2 mm, the two tracks must form a vertex with a χ^2 value from the vertex fit (χ^2_{vtx}) smaller than 25 and the di-muon mass must be larger than 2.7 GeV/c. The `Hlt1TrackMuon` (`Hlt1TrackAllL0`) line mainly selects tracks with p_T larger than 1 (1.7) GeV/c, momentum greater than 8 (10) GeV/c, IP to all the PVs larger than 0.1 mm and impact parameter χ^2 (χ^2_{IP}) greater than 16. The relevant HLT1 lines to select $b \to J/\psi X$ candidates are summarised in Table 4.1.

Figure 4.2 shows the accept fractions of a set of HLT2 lines for the 340 pb^{-1} dataset recorded before Summer 2011. The most-efficient HLT2 line is `Hlt2DiMuonJPsi` [67] that selects muon pairs with an invariant mass within a ±120 MeV/c^2 mass window around the J/ψ world-average mass [68]. The `Hlt2DiMuonJPsi` selection can be found in Table 4.2. Figure 4.3 shows the fractions of events accepted by HLT2 lines for the 670 pb^{-1} dataset recorded during Summer 2011 and beyond. The `Hlt2DiMuonJPsi` line accept fraction dropped significantly due to
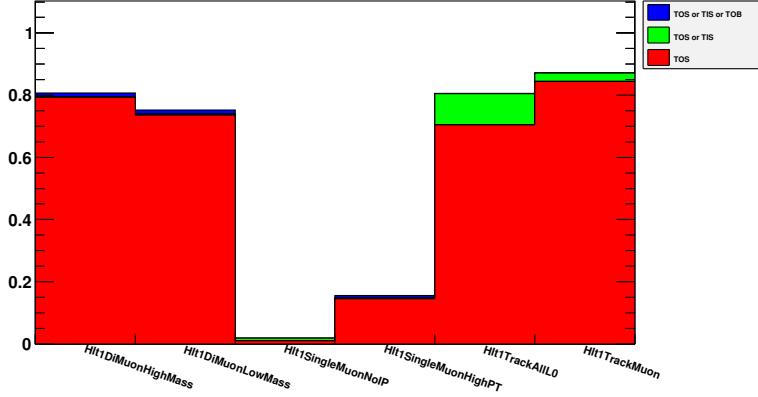
Figure 4.1: Relevant HLT1 trigger line accept fractions in 2011 from real data for $B_s^0 \to J/\psi\phi$ candidates.
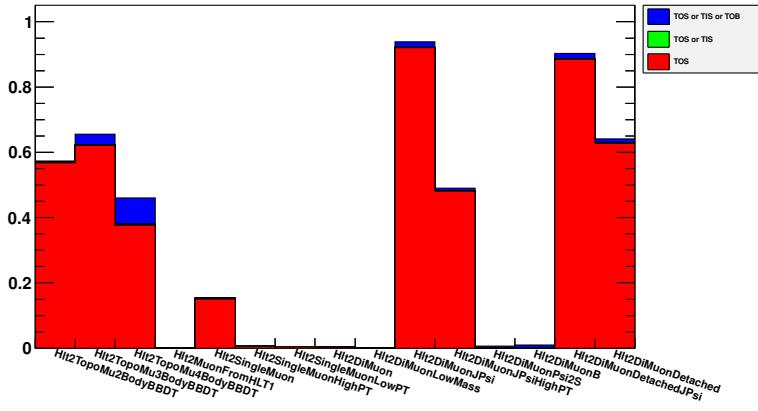
Figure 4.2: Relevant HLT2 trigger line accept fractions before Summer 2011 from real data for $B_s^0 \to J/\psi\phi$ candidates.
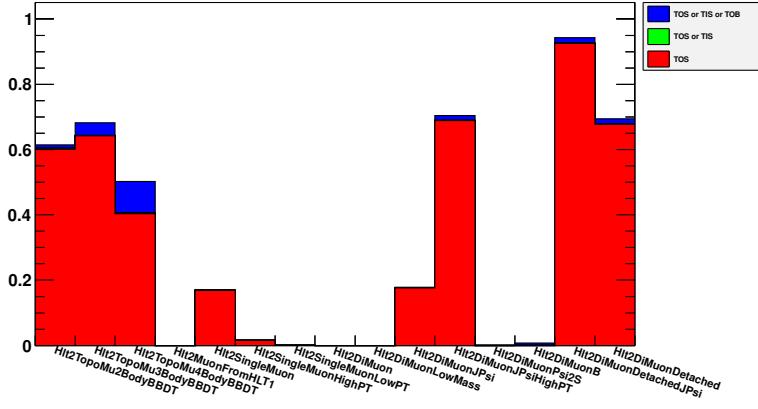
Figure 4.3: Relevant HLT2 trigger line accept fractions from Summer 2011 and beyond from real data for $B_s^0 \to J/\psi\phi$ candidates.

Table 4.1: Relevant HLT1 line selections for $b \to J/\psi X$ modes.

	Hlt1DiMuonHighMass	Hlt1TrackMuon	Hlt1TrackAllL0
L0	L0-Muon/L0-DiMuon	L0-Muon/L0-DiMuon	L0-Physics
Track p_T	$> 0.5\,\text{GeV}/c$	$> 1.0\,\text{GeV}/c$	$> 1.7\,\text{GeV}/c$
Track p	$> 6.0\,\text{GeV}/c$	$> 8.0\,\text{GeV}/c$	$> 10.0\,\text{GeV}/c$
Track χ^2/nDoF	< 4	< 2	< 2
Track IP	-	> 0.1 mm	> 0.1 mm
Track χ^2_{IP}	-	> 16	> 16
Di-muon DOCA	< 0.2 mm	-	-
Di-muon χ^2_{vtx}	< 25	-	-
Di-muon mass	$> 2.7\,\text{GeV}/c^2$	-	-
Prescale	1	1	1

Table 4.2: Relevant HLT2 line selections for $b \to J/\psi X$ modes with the prescale of `Hlt2DiMuonJPsi` before Summer 2011 (*) and during Summer 2011 and beyond (**).

	Hlt2DiMuonJPsi	Hlt2DiMuonDetachedJPsi
Track χ^2/nDoF	< 5	< 5
Di-muon mass window	$m_{J/\psi} \pm 0.12$ GeV/c^2	$m_{J/\psi} \pm 0.12$ GeV/c^2
Di-muon χ^2_{vtx}	< 25	< 25
Decay Length Sig.	-	> 3
Prescale	$1^*/0.2^{**}$	1

a prescale factor set to 0.2 for this line to cope with the increase in luminosity of the LHC and the LHCb bandwidth limitation. The most-efficient HLT2 line is `Hlt2DiMuonDetachedJPsi`.

The `Hlt2DiMuonDetachedJPsi` selection is the same than the `Hlt2DiMuonJPsi` line except for an additional requirement on the *decay length significance* (DLS) of the *J*/*ψ* with respect to the PV that has the smallest impact parameter with the *J*/*ψ* flight direction. The DLS cut forces the candidate to have flown and these candidates are said to be *detached*. The complicated selection of the HLT2 topological lines with at least one muon (`Hlt2TopoMu2,3,4BodyBBDT`) based on a *Bonsai Boosted Decision Tree* (BBDT) are described in [69].

Whereas the acceptance of the `Hlt2DiMuonJPsi` and `Hlt1DiMuonHighMass` lines are linear as a function of the decay time, meaning no lower decay time acceptance, the `Hlt2DiMuonDetachedJPsi`, `Hlt1TrackMuon` and `Hlt1TrackAllL0` are not. This is presented in Sec. 4.3.1. For `Hlt2DiMuonDetachedJPsi`, it is due to the DLS cut on the *J*/*ψ*, the IP and χ^2_{IP} cuts on the *J*/*ψ* daughter tracks for the `Hlt1Track` lines and χ^2_{IP} cuts on the daughter tracks and a flight-distance χ^2 (χ^2_{FD}) cut for the `Hlt2TopoMu2,3,4BodyBBDT` lines. From the measured accept fractions, the following trigger strategies can be proposed based on the trade-off between most efficient set of trigger lines and flatter lower decay time acceptances:

1) `Hlt2DiMuonJPsi` TOS and `Hlt1DiMuonHighMass` TOS

2) `Hlt2DiMuonDetachedJPsi` TOS and `Hlt1DiMuonHighMass` TOS

3) `Hlt2DiMuonDetachedJPsi` TOS and (`Hlt1DiMuonHighMass` TOS or `Hlt1TrackMuon` TOS)

Table 4.3: Accept fractions results obtained from a sample of $B_s^0 \to J/\psi\,\phi$ decays reconstructed in 2011 for different trigger strategies.

Trigger strategy	Accept fraction [%]
No. 1	38.8 ± 0.5
No. 2	75.4 ± 0.6
No. 3	87.8 ± 0.8
No. 4	89.8 ± 0.8
No. 5	91.4 ± 0.8
No. 6	95.1 ± 0.8

4) `Hlt2DiMuonDetachedJPsi` TOS and (`Hlt1DiMuonHighMass` TOS or `Hlt1TrackMuon` TOS or `Hlt1TrackAllL0` TOS)

5) (`Hlt2DiMuonDetachedJPsi` TOS or `Hlt2DiMuonJPsi` TOS) and (`Hlt1DiMuonHighMass` TOS or `Hlt1TrackMuon` TOS or `Hlt1TrackAllL0` TOS)

6) (`Hlt2DiMuonDetachedJPsi` TOS or `Hlt2DiMuonJPsi` TOS or `Hlt2TopoMu2,3,4BodyBBDT` TOS) and (`Hlt1DiMuonHighMass` TOS or `Hlt1TrackMuon` TOS or `Hlt1TrackAllL0` TOS)

The measured accept fractions, for offline-selected $B_s^0 \to J/\psi\,\phi$ candidates, in each trigger strategy, are summarised in Table 4.3. A trigger strategy can be defined where about 39% of the candidates have no acceptance effect for small decay times. Trigger strategies having accept fractions up to about 95% can also be defined. The choice of the best trigger strategy for a given analysis is driven by the size of the systematic uncertainty on the lifetime that can be tolerated. This will be discussed in Sec. 4.5. These accept fractions are measured using $B_s^0 \to J/\psi\,\phi$ candidates, but for other decay modes, the accept fractions can be slightly different because of different kinematics, decay topologies and decay products.

4.2.2 Stripping lines

There are four types of stripping lines for $b \to J/\psi X$ modes: an inclusive detached J/ψ line called `FullDSTDiMuonJpsi2MuMuDetachedLine`, an inclusive high p_T J/ψ line called `FullDSTDiMuonJpsi2MuMuLine`, a detached exclusive line for exclusive decays such as $B_s^0 \to J/\psi\,\phi$ that is called `BetaSBs2JpsiPhiDetachedLine` and a non-detached prescaled exclusive line like `BetaSBs2JpsiPhiPrescaledLine` for $B_s^0 \to J/\psi\,\phi$ decays.

The inclusive detached J/ψ stripping line has a cut on the DLS of the J/ψ larger than 3 that creates a lower decay time acceptance. However, the acceptance shape is different from that of the `Hlt2DiMuonDetachedJPsi` trigger line, because the requirement to select the best PV is the one with smallest IP for the trigger and with smallest χ^2_{IP} for the stripping/offline. This generates small differences to the lower decay time acceptance shapes as shown in Sec. 4.3.2. The non-detached inclusive line has a large p_T cut on the J/ψ and its daughters which makes this line unusable for some studies involving $b \to J/\psi X$ decays. Table 4.4 summarises the cuts for the two inclusive J/ψ stripping lines.

Table 4.4: Inclusive detached J/ψ stripping line (`FullDSTDiMuonJpsi2MuMuDetachedLine`) and inclusive high p_{T} (`FullDSTDiMuonJpsi2MuMuLine`) of Stripping17b.

Decay mode	Cut	Detached	High p_{T}
$\mu^{\pm}$	$\Delta\ln\mathscr{L}_{\mu\pi}(\mu^{\pm})$	> 0	> 0
	$p_{\mathrm{T}}(\mu^{\pm})$	> 0.55 GeV/c	> 0.65 GeV/c
	$p(\mu^{\pm})$	$-$	> 10 GeV/c
	$\chi^2_{\mathrm{track}}/\mathrm{nDoF}(\mu^{\pm})$	< 5	< 5
	clone distance $(\mu^{\pm})$	> 5000	> 5000
$J/\psi \to \mu^+\mu^-$	$p_{\mathrm{T}}(J/\psi)$	$-$	> 3 GeV/c
	$\chi^2_{\mathrm{vtx}}/\mathrm{nDoF}(J/\psi)$	< 16	< 16
	Decay Length Sig. (J/ψ)	> 3	$-$
	$M(\mu^+\mu^-)$	$\in [2997, 3197]$ MeV/c^2	$\in [3010, 3170]$ MeV/c^2

In general, the exclusive di-muon lines have no inefficiency for small decay times, however there is a complication coming from the decay time estimate used in the stripping for the detached lines. In the stripping, the decay time, $t_{\mathrm{Propertime}}$, is computed using the Propertime-Fitter algorithm, whereas in the final analysis the decay time t_{DTF} is obtained from a kinematic *decay-tree fit* (DTF) [70]. From simulation studies, it was found that the DTF decay time t_{DTF} is more accurate, but requires more CPU time that cannot be afforded in the stripping. Since the estimators are not the same ones and a cut at 0.2 ps is applied in the stripping, a lower decay time acceptance effect around 0.2 ps is created. In Sec. 4.3.2, the decay time acceptance of the stripping will be further investigated. The non-detached stripping lines are often heavily prescaled and they are used to study the decay time resolution. As an example, Table 4.5 summarises the cuts for the detached exclusive lines to select $B_s^0 \to J/\psi\,\phi$ decays, where the non-detached prescaled line has no cut on $t_{\mathrm{PropertimeFitter}}$ and a prescale of 0.15. Table 4.5 summarises the offline selection that is used for $B_s^0 \to J/\psi\,\phi$ candidates in this chapter where the χ^2_{IP}, the *impact parameter χ^2 to the next best PV* ($\chi^2_{\mathrm{IP,next}}$) is used to remove candidates with an incorrectly associated PV, the lower bound on the *DTF decay time* (t_{DTF}) and finally the *DTF χ^2 per degree of freedom* ($\chi^2_{\mathrm{DTF(B+PV)}}/\mathrm{nDoF}$) as a powerful discriminant to separate signal from background. If more than one candidate per event is found, the one with the smallest $\chi^2_{\mathrm{DTF(B+PV)}}/\mathrm{nDoF}$ is kept.

Table 4.5: Exclusive detached $B_s^0 \to J/\psi\,\phi$ stripping line (`BetaSBs2JpsiPhiDetachedLine`) of Stripping17b and the offline selection that is used in this chapter.

Decay mode	Cut parameter	Stripping 17b	Offline
all tracks	$\chi^2_{\text{track}}/\text{nDoF}$	< 5	< 4
	clone distance	> 5000	> 5000
$J/\psi \to \mu^+\mu^-$	$\Delta\ln\mathscr{L}_{\mu\pi}(\mu^\pm)$	> 0	> 0
	$p_{\text{T}}(\mu^\pm)$	$-$	$> 0.5\,\text{GeV}/c$
	$\chi^2_{\text{vtx}}/\text{nDoF}(J/\psi)$	< 16	< 16
	$|M(\mu^+\mu^-) - M(J/\psi)|$	$< 80\,\text{MeV}/c^2$	$< 60\,\text{MeV}/c^2$
$\phi \to K^+K^-$	$\Delta\ln\mathscr{L}_{K\pi}(K^\pm)$	> -2	> 0
	$p_{\text{T}}(\phi)$	$> 1\,\text{GeV}/c$	$> 1\,\text{GeV}/c$
	$M(\phi)$	$\in [980, 1050]\,\text{MeV}/c^2$	$\in [1008, 1032]\,\text{MeV}/c^2$
	$\chi^2_{\text{vtx}}/\text{nDoF}(\phi)$	< 16	< 16
$B_s^0 \to J/\psi\,\phi$	$M(B_s^0)$	$\in [5200, 5550]\,\text{MeV}/c^2$	$\in [5200, 5550]\,\text{MeV}/c^2$
	$\chi^2_{\text{vtx}}/\text{nDoF}(B_s^0)$	< 10	< 10
	$\chi^2_{\text{DTF(B+PV)}}/\text{nDoF}(B_s^0)$	$-$	< 5
	$\chi^2_{\text{IP}}(B_s^0)$	$-$	> 25
	$\chi_{\text{IP,next}}(B_s^0)$	$-$	< 50
	$t_{\text{PropertimeFitter}}(B_s^0)$	$> 0.2\,\text{ps}$	$> 0.2\,\text{ps}$
	$t_{\text{DTF}}(B_s^0)$	$-$	$> 0.3\,\text{ps}$

4.3 Lower decay time acceptance

4.3.1 Swimming technique

Chronologically, the first attempt to obtain the lower decay time acceptance from real data was performed using a technique called the *Swimming* technique [71]. The idea is to move the online-reconstructed PVs toward the reconstructed B candidate along the reconstructed B flight direction in steps and simulate the decisions of the relevant trigger/stripping lines at each step as shown in Fig. 4.4. The proper way would be to move the decay products rather than the PVs, but it is technically much more complicated.

The distributions of points where the simulated trigger/stripping decision changes for each candidate gives the acceptances of the trigger/stripping lines considered.

An important point with the Swimming technique is that the b-hadron candidate and the PVs are already reconstructed in the event sample used. This means that any reconstruction effect for b-hadron candidates and PVs that create decay time dependant reconstruction efficiencies will not be described by the Swimming. In addition, the PVs are moved and not the B candidate which makes some differences. When the B candidate is moved, the secondary particles may not have enough hits in the VELO at large decay times to be reconstructed. However, an additional algorithm can be used to check geometrically if a track would have enough VELO hits to be reconstructed after changing the decay time.

The Swimming is performed using $B_s^0 \to J/\psi\,\phi$ offline-selected candidates (see Tab. 4.5) to obtain the decay time acceptances of the relevant trigger lines.
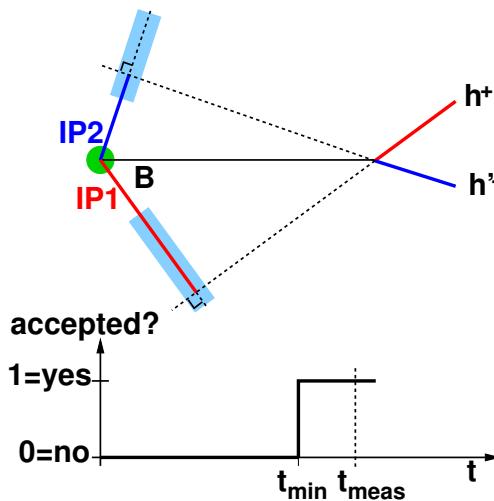

Figure 4.4: Sketch of the mechanism performed by the Swimming technique that moves the PVs toward the candidate along the flight direction and simulate the trigger line responses (here impact parameters) as a function of the recalculated decay time for that position [71].

Hlt2DiMuonJPsi and Hlt1DiMuonHighMass lines

Figures 4.5 and 4.6 show the acceptance found by the Swimming for `Hlt2DiMuonJPsi` and `Hlt1DiMuonHighMass` lines. No decay time acceptance effect for small decay times is found, as expected from the selections used in these lines.

Hlt2DiMuonDetachedJPsi line

Figure 4.7 shows the measured acceptance by the Swimming for the `Hlt2DiMuonDetachedJPsi` line. The effect of the DLS cut on the acceptance should be a turn-on curve that starts at zero and reaches a plateau at large decay times. The results show the expected turn-on shape, however the acceptance reaches a maximum around 1 fs and then drops down near 5-10 fs
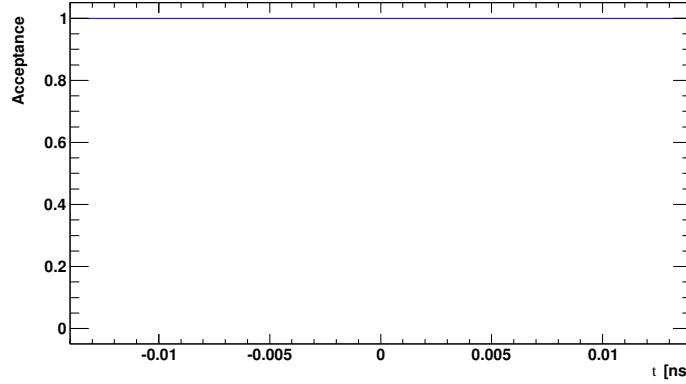
Figure 4.5: Decay time acceptance obtained with the Swimming technique for the `Hlt2DiMuonJPsi` line obtained from a sample of $B_s^0 \to J/\psi\,\phi$ decays reconstructed from the 2011 dataset.
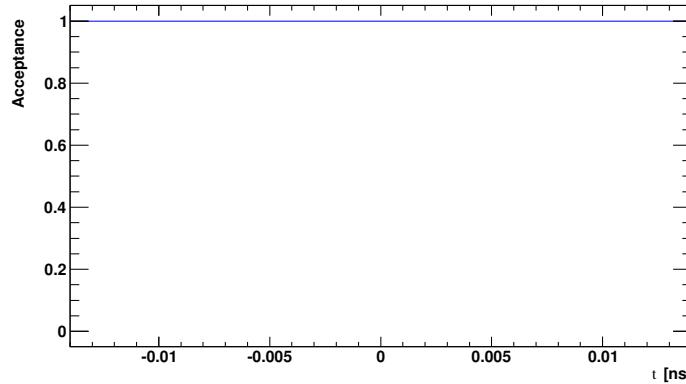
Figure 4.6: Decay time acceptance obtained with the Swimming technique for the `Hlt1DiMuonHighMass` line obtained from a sample of $B_s^0 \to J/\psi\,\phi$ decays reconstructed from the 2011 dataset.

before going up again at large decay times. This effect is due to the selection of the PV used to compute the decay length significance. The decay time is computed with respect to the best PV of the *b*-hadron candidate. For the DLS cut on the *J/ψ*, it is performed with the best PV of the *J/ψ*. Since the *b*-hadron and the *J/ψ* momentum directions are not identical, the selected PVs for the two cases are not necessarily the same. Therefore, this drop at large decay times and the non-zero efficiency at negative decay times are understood as coming from the different selection of the best PV in the two cases. This explanation is tested by selecting events with only one reconstructed PV. Figure 4.8 shows the acceptance for events with only one reconstructed PV. It demonstrates that the case with one PV only gives an acceptance with just a turn-on shape that confirms the previous argument.
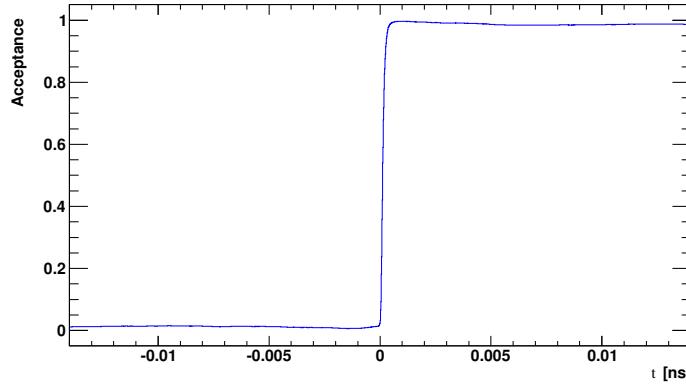

Figure 4.7: Decay time acceptance obtained with the Swimming technique for the `Hlt2DiMuonDetachedJPsi` line obtained from a sample of $B_s^0 \to J/\psi\,\phi$ decays reconstructed from 2011 dataset.
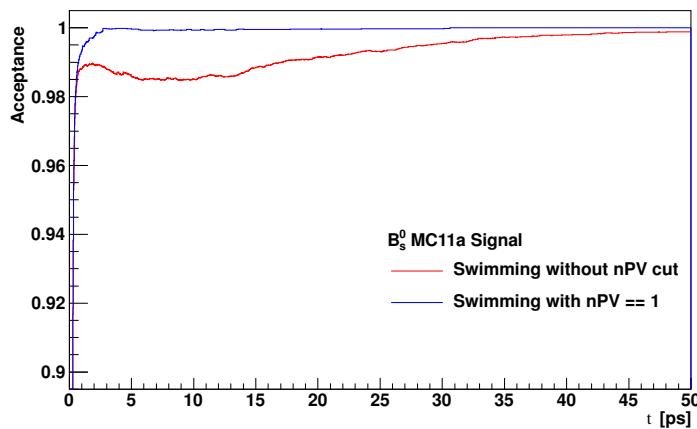

Figure 4.8: Decay time acceptance obtained with the Swimming technique for the `Hlt2DiMuonDetachedJPsi` line for events with a single PV (red) and without any restriction (blue) obtained from a sample of $B_s^0 \to J/\psi\,\phi$ decays reconstructed from 2011 dataset.

Hlt1TrackMuon and Hlt1TrackAllL0 lines

The cuts that introduce inefficiencies in the small decay time region of these lines are the IP and χ^2_{IP} cuts. Figures 4.9 and 4.10 show the acceptances of these two lines that exhibit a turn-on shape in the negative and positive times, but with significantly slower turn-on. Since a particle decay time distribution is exponential, the total loss in yield due to this turn-on at small decay times is non-negligible.

This study using the Swimming technique helped to characterise the decay time acceptances of the relevant trigger lines for $B \rightarrow J/\psi X$ channels. However, as it will be shown in Sec. 4.3.2 and as already mentioned, there are reconstruction effects that make these acceptances incomplete.
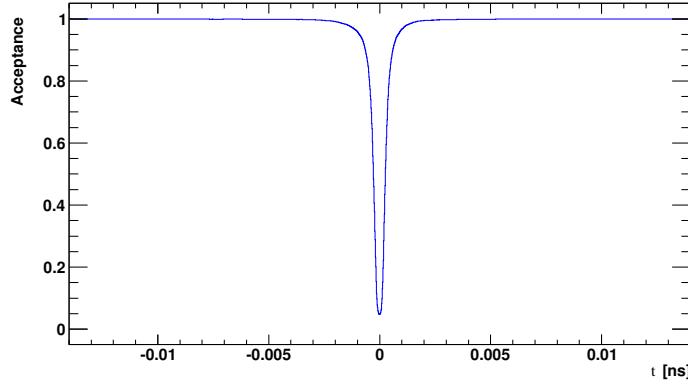

Figure 4.9: Decay time acceptance obtained with the Swimming technique for the Hlt1TrackMuon line obtained from a sample of $B^0_s \rightarrow J/\psi \phi$ decays reconstructed from 2011 dataset.
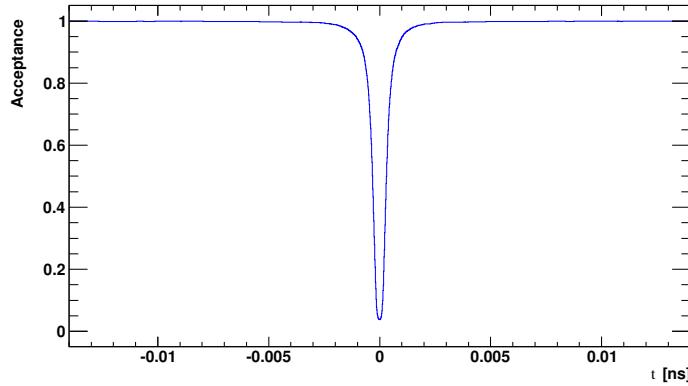

Figure 4.10: Decay time acceptance obtained with the Swimming technique for the Hlt1TrackAllL0 line obtained from a sample of $B^0_s \rightarrow J/\psi \phi$ decays reconstructed from 2011 dataset.

4.3.2 Overlap and ratio techniques

The selection codes of the `Hlt2DiMuonDetachedJPsi` and `Hlt2DiMuonJPsi` lines are identical, except for the additional DLS cut and a online-reconstructed PV. The lower decay time acceptance $\varepsilon_1(t)$ of the `Hlt2DiMuonDetachedJPsi` line can be obtained relative to that of `Hlt2DiMuonJPsi` from the ratio:

$$\varepsilon_1(t) = \frac{n_A(t)}{n_A(t) + n_B(t)} \tag{4.2}$$

where

- n_A = # candidates passing {(`Hlt2DiMuonDetachedJPsi` TOS) and (`Hlt2DiMuonJPsi` TOS) and (`Hlt1DiMuonHighMass` TOS)},

- n_B = # candidates passing {(not `Hlt2DiMuonDetachedJPsi` TOS) and (`Hlt2DiMuonJPsi` TOS) and (`Hlt1DiMuonHighMass` TOS)}.

The two categories, A and B, written in this way are *disjoint sets*, *i.e.* independent sets. The efficiency is measured with respect to the trigger lines {(`Hlt2DiMuonJPsi` TOS) and (`Hlt1DiMuonHighMass` TOS)}, because they have no acceptance at small decay times and therefore called *unbiased trigger lines*. However, it does not mean that the {(`Hlt2DiMuonJPsi` TOS) and (`Hlt1DiMuonHighMass` TOS)} trigger path is not presenting any acceptance at large decay times. The relative efficiency measured using this ratio allows the lower and upper decay time acceptances to be measured separately.

The signal yield in each category can be obtained in two ways. Firstly, by counting the number of candidates using signal MC events which implies that the relativ efficiency follows a binomial distribution. However, this method is sensitive to differences between the acceptances obtained from MC and data. Secondly, by fitting for the signal yield in real data or MC using the *b*-hadron invariant mass for example. In this case the efficiency will not follow entirely a binomial distribution anymore because the yields are obtained from a fit that gives an additional uncertainty. For this latter case, the fit parameters $\{n_A; n_B\}$ are changed to $\{n_A; \varepsilon_1\}$ to allow Minuit and its MINOS algorithm to calculate asymmetric errors on the relative efficiency ε_1.

The acceptance $\varepsilon_1(t)$ is measured in several decay time bins. Since the turn-on shape of the `Hlt2DiMuonDetachedJPsi` line appears at small decay times, more bins are needed in this region. Therefore, asymmetric bins are used. The bins boundaries are required to have similar statistical uncertainties over all the bins for the distribution following an exponential $e^{-t/\tau}$ where τ is taken as the world-average lifetime of the particle. The effect of the binning on the measured lifetime is addressed in in Sec. 4.3.3.

A technique that measures a relative efficiency exploiting the overlap between the `Hlt2DiMuonJPsi` and `Hlt2DiMuonDetachedJPsi` lines is called an *overlap technique*. Since the relative efficiency follows a quasi-binomial distribution and is close to 100%, the uncertainty on the

efficiency is small. Another possibility would have been to perform the ratio {(Hlt2DiMuonDetachedJPsi TOS) and (Hlt1DiMuonHighMass TOS)} over {(Hlt2DiMuonJPsi TOS) and (Hlt1DiMuonHighMass TOS)} without asking for (Hlt2DiMuonJPsi TOS) in the numerator. But, generating events with a relative efficiency of 90% for the Hlt2DiMuonDetachedJPsi line to the Hlt2DiMuonJPsi one and a prescale factor of 0.5 (weighted average prescale factor of the Hlt2DiMuonJPsi line in 2011), the uncertainty on the relative efficiency ε_1 is more than three times better than the one without the requirement (Hlt2DiMuonJPsi TOS) in the numerator.

The combination of lines {(Hlt2DiMuonDetachedJPsi TOS) and (Hlt1DiMuonHighMass TOS)} is called *almost unbiased* since its efficiency relative to the unbiased trigger lines only varies within few per-cents.

Figure 4.11 shows the acceptance obtained with the Swimming and overlap techniques for offline-selected $B_s^0 \to J/\psi\phi$ candidates for simulation data (see Tab. 4.5). The difference between the two curves are due to reconstruction effects, which are not included in the Swimming technique. In the overlap technique, the tracks and an offline PV are already reconstructed, but an online-reconstructed PV is required for the Hlt2DiMuonDetachedJPsi line, but not for the Hlt2DiMuonJPsi line. Thus, the discrepancy should come from differences in the PV reconstruction between the trigger and offline cases. Figure 4.12 shows the average number of online-reconstructed PVs for a given number of offline PVs which presents some differences. In addition, the PV is not *refitted* in the trigger compared to stripping/offline. The standard *PV refitting* procedure consists in removing the signal candidate tracks from the PV, if some of them were associated to it, and refit the PV with the remaining tracks.
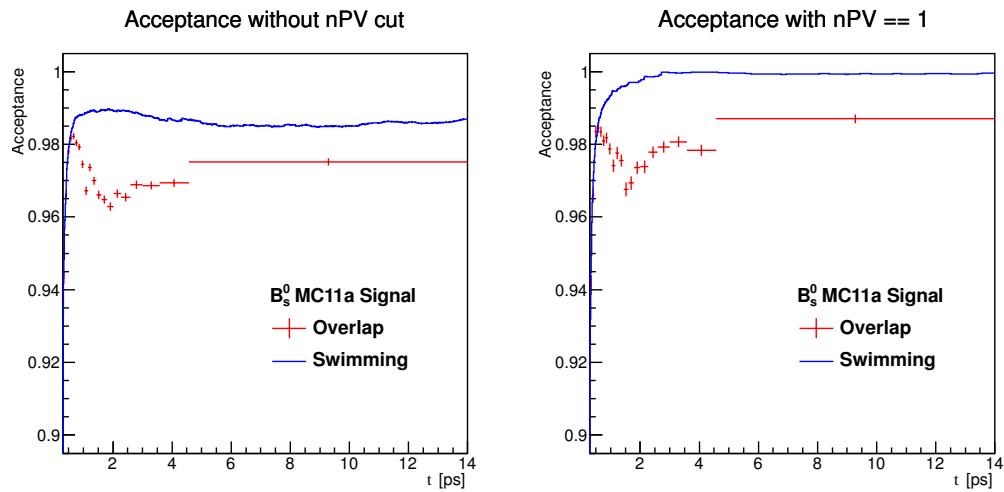

Figure 4.11: Decay time acceptance of Hlt2DiMuonDetachedJPsi measured using the Swimming technique (blue) and the overlap technique (red) without any requirement on the number of reconstructed PV (*left*) and with only one reconstructed PV in the event (*right*) from a sample of $B_s^0 \to J/\psi\phi$ decays reconstructed in 2011.

Since signal candidate tracks can be used to find and build the PV, a drop in the relative efficiency $\varepsilon_1(t)$ can be created. At small decay times, the PV position is correctly determined by the tracks originating from the PV and possibly even with one or more tracks from the signal candidate. For intermediate decay times, the *b*-hadron candidate is still close enough to the PV so that some tracks from the PV can be associated with the signal tracks to build a fake low-multiplicity PV. In this case, the best PV can be the fake PV and the DLS will be very small, which means that the *J/ψ* candidate will not pass the requirement to be larger than 3, and therefore it induces a loss in trigger efficiency. This means that decay channels with many charged tracks coming from the *b*-hadron decay vertex should present a larger drop in efficiency than the ones with only fewer tracks. Figure 4.13 shows the decay time acceptance obtained from simulation using the overlap technique for $B^0 \to J/\psi\, K_s^0$ (two tracks from the *B* vertex), $B^+ \to J/\psi\, K^+$ (three tracks from the *B* vertex) and $B_s^0 \to J/\psi\, \phi$ (four tracks from the *B* vertex) that confirms the expected trend concerning the dip present in the acceptance distribution. At large decay times, the density of tracks originating from the PV is lower in the vicinity of the signal candidate and therefore the probability to build a fake PV is smaller, which implies that the relative efficiency $\varepsilon_1(t)$ goes up. Figure 4.14 shows again the `Hlt2DiMuonDetachedJPsi` acceptance as a function of decay time, but for different number of PVs in the event, and this time obtained with the overlap technique for $B_s^0 \to J/\psi\, \phi$ from simulation and $B^+ \to J/\psi\, K^+$ from real data. Here, it can be noticed that the dip depth depends also on the number of PVs since it is correlated to the track multiplicity of the event.

A last complication with the overlap technique is the change in the prescale factor for the `Hlt2DiMuonJPsi` line over the 2011 run period. If no additional treatment is performed, a larger weight to the events before Summer 2011 will be given. This can bias the measurement of the acceptance for the `Hlt2DiMuonDetachedJPsi` line, because this line is sensitive to the
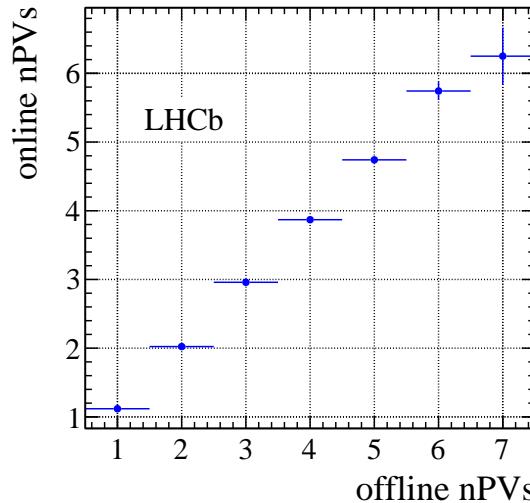

Figure 4.12: Average number of PVs reconstructed offline as a function of the given number of PVs reconstructed online from a sample of $B_s^0 \to J/\psi\, \phi$ decays reconstructed in 2011 [72].

number of PVs and can be different before and after Summer 2011. To account for this change, the candidates are reweighted according to their time period with a weight of $\frac{1}{5-4f}$ before Summer 2011 and $\frac{5}{5-4f}$ after, where f is the fraction of candidates that were reconstructed before Summer 2011. Another solution would be to split the year in two sets and the first set use only `Hlt2DiMuonJPsi` and the next set `Hlt2DiMuonDetachedJPsi`.

The next point is the usage of the more efficient trigger strategies 3) and 4) presented in Table 4.3. Since the almost unbiased trigger set yields about 75% of the candidates and that the overlap technique is statistically powerful, enhanced trigger strategies must be separated in at least two disjoint sets where one of them would be the almost unbiased set. The trigger strategy 4) for example can be separated in two disjoint sets as

$$\text{F and (G or H)} = \underbrace{\text{(F and G)}}_{\text{Set I}} \text{ or } \underbrace{\text{(F and not G and H)}}_{\text{Set II}}, \tag{4.3}$$
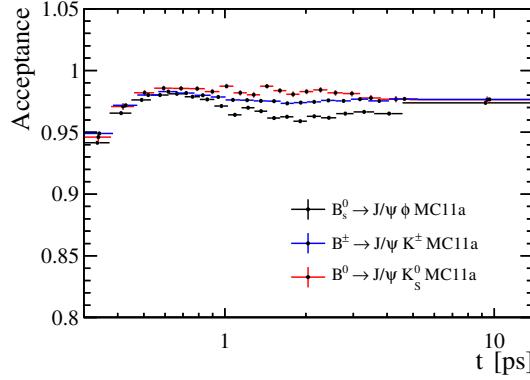

Figure 4.13: Decay time acceptance of `Hlt2DiMuonDetachedJPsi` measured using the overlap technique for channels with two ($B^0 \to J/\psi K_s^0$), three ($B^+ \to J/\psi K^+$) and four ($B_s^0 \to J/\psi \phi$) prompt tracks from 2011 MC samples.
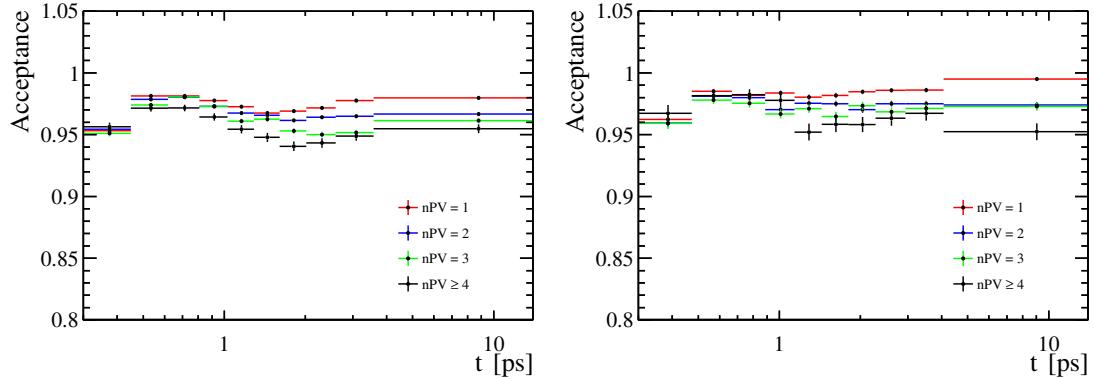

Figure 4.14: Decay time acceptance of `Hlt2DiMuonDetachedJPsi` measured using the overlap technique from a MC sample of $B_s^0 \to J/\psi \phi$ decays and a sample of $B^+ \to J/\psi K^+$ decays reconstructed in 2011 from real data for different number of reconstructed PVs.

where F = `Hlt2DiMuonDetachedJPsi TOS`, G = `Hlt1DiMuonHighMass TOS` and H = (`Hlt1TrackMuon TOS` or `Hlt1TrackAllL0 TOS`).

Unfortunately, for Set II, the overlap technique cannot be used because there are no `Hlt1Track` lines without IP and χ^2_{IP}. However, a simple ratio:

$$\varepsilon_2(t) = \frac{n_C(t)}{n_{A+B}(t)} \tag{4.4}$$

can be used to obtain the relative efficiency of Set II to the unbiased trigger lines, where

- n_C = # candidates passing (`Hlt2DiMuonDetachedJPsi TOS`) and (not `Hlt1DiMuonHighMass TOS`) and (`Hlt1TrackMuon TOS` or `Hlt1TrackAllL0 TOS`),

- n_{A+B} = # candidates passing (`Hlt2DiMuonJPsi TOS`) and (`Hlt1DiMuonHighMass TOS`)

Since Set I contains a set of requirements that fully bias the lifetime, it is called *fully biased* trigger set.

The categories C and A+B are disjoint sets. This method is called the *ratio technique*. In this case, the relative efficiency does not follow a quasi-binomial distribution and it will be shown that its propagated error to the lifetime is significantly larger than the one from the overlap technique as presented in Sec. 4.3.3. An important caveat in this case is that the numerator and denominator can have different decay time acceptances at large decay times unlike the overlap case. This can create additional complications depending on the technique that is used to correct for the upper decay time acceptance as will become clear in Sec. 4.4. Finally, Fig. 4.15 shows the lower decay time acceptances obtained with the overlap and ratio techniques for $B^0_s \to J/\psi\,\phi$ and $B^0 \to J/\psi\,K^{*0}$. There is an overall good agreement among the acceptances.
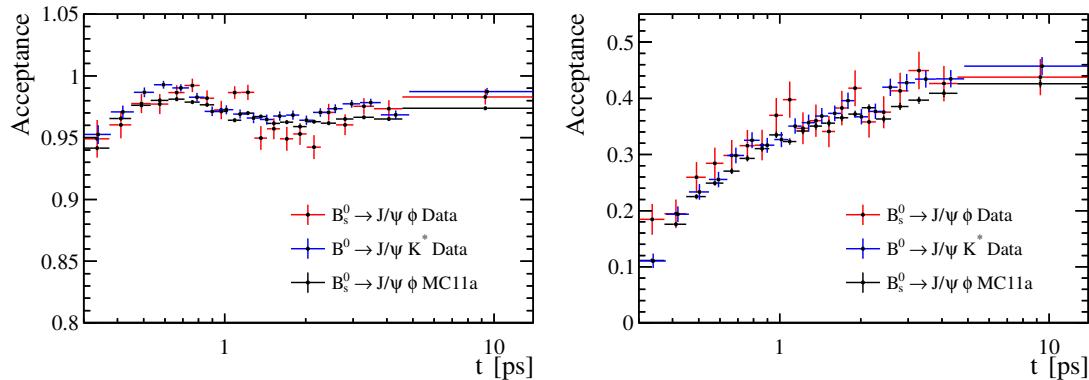

Figure 4.15: Decay time acceptances for almost unbiased events using the overlap technique (*left*) and for fully biased events using the ratio technique (*right*) from samples of $B^0_s \to J/\psi\,\phi$ decays (data and MC) and $B^0 \to J/\psi\,K^{*0}$ decays (data).

The usage of the trigger strategies 5) and 6) given in Table 4.3 complicates the techniques to obtain the trigger acceptances, because of the additional HLT2 lines. The trigger strategies 5) and 6) can be separated as

$$
\text{(E or F) and (G or H)} = \underbrace{\text{(F and G)}}_{\text{Set I}} \text{ or } \underbrace{\text{(F and not G and H) or (E and not F and G and H)}}_{\text{Set III}}, \quad (4.5)
$$

where E is the additional HLT2 lines and the trigger lines {(`Hlt2DiMuonDetachedJPsi` TOS) and (`Hlt1DiMuonHighMass` TOS)} are kept as Set I.

The acceptance of Set III can be measured using the ratio:

$$
\varepsilon_3(t) = \frac{n_J + n_K\,(t)}{n_J + n_L\,(t)}, \quad (4.6)
$$

where J is the common set between the numerator and denominator, K the set when added to J gives Set III and L the set when added to J gives the unbiased set.

The usage of trigger strategies 5) and 6) has not been considered in this thesis, because of some tight p_T cut in the HLT2 topological lines that are problematic for the angular acceptance in the ϕ_s analysis. Also, because of the small gain in statistical uncertainty compared to the trigger strategy 4).

The usage of the overlap and ratio techniques are possible because of the existence of an unbiased spectrum for their denominators. This means that the stripping must not present any bias at small decay times since every candidate must pass both the trigger and a stripping line. For the exclusive stripping lines, their selections are often do not create any inefficiencies at small decay times except for the lower decay time boundary usually set to 0.2 ps. In general, for every detached exclusive line there is a prescaled non-detached exclusive line, *i.e.* without the decay time cut at 0.2 ps that can be used to use the overlap technique to obtain the acceptance induced by this cut. Figure 4.16 shows the stripping acceptance for $B_s^0 \rightarrow J/\psi\,\phi$ decays from simulation. The decay time distribution is flat above 0.3 ps. This motivates restricting the study to decays with $t > 0.3$ ps for $b \rightarrow J/\psi X$ analyses.

For the inclusive detached J/ψ stripping line (`FullDSTDiMuonJpsi2MuMuDetachedLine`), there is no prescaled line with the same cuts except the DLS cut as for the `Hlt2DiMuonDetachedJPsi` trigger line. The available inclusive unbiased J/ψ stripping lines have much tighter p_T cuts on the J/ψ and its daughters than the detached line. These cuts are found to significantly change the measured acceptance for the `FullDSTDiMuonJpsi2MuMuDetachedLine` line if this high p_T stripping line is used with the overlap technique. Therefore, this high p_T line cannot be used. An efficient solution to measure the acceptance of the inclusive detached J/ψ stripping line is to use the exclusive lines of a given channel when it is available in the overlap technique. The lower decay time acceptances of the almost unbiased trigger set and the inclusive

detached *J/ψ* stripping line would be given separately, using the overlap technique, by

$$\varepsilon_{1,\text{Trigger}}(t) = \frac{n_A(t)}{n_A(t) + n_B(t)}, \tag{4.7}$$

$$\varepsilon_{1,\text{Stripping|Trigger}}(t) = \frac{n_C(t)}{n_C(t) + n_D(t)}, \tag{4.8}$$

 where

- n_A = # candidates passing (Hlt2DiMuonDetachedJPsi TOS) and (Hlt2DiMuonJPsi TOS) and (Hlt1DiMuonHighMass TOS) and (Exclusive Detached Stripping),

- n_B = # candidates passing (not Hlt2DiMuonDetachedJPsi TOS) and (Hlt2DiMuonJPsi TOS) and (Hlt1DiMuonHighMass TOS) and (Exclusive Detached Stripping),

- n_C = # candidates passing (Hlt2DiMuonDetachedJPsi TOS) and (Hlt1DiMuonHighMass TOS) and (Inclusive Stripping) and (Exclusive Detached Stripping),

- n_D = # candidates passing (Hlt2DiMuonDetachedJPsi TOS) and (Hlt1DiMuonHighMass TOS) and (not Inclusive Stripping) and (Exclusive Detached Stripping),

The requirement that events pass the exclusive line can modify the real decay time acceptance for small decay times of the trigger and inclusive detached *J/ψ* stripping. In Chap. 5, this last point is addressed when measuring *b*-hadron lifetimes from the inclusive *J/ψ* stripping line. Here, only the case with the almost unbiased trigger strategy is presented with the inclusive detached *J/ψ* stripping line, but it can be enhanced with two additional ratios for the fully biased trigger set.
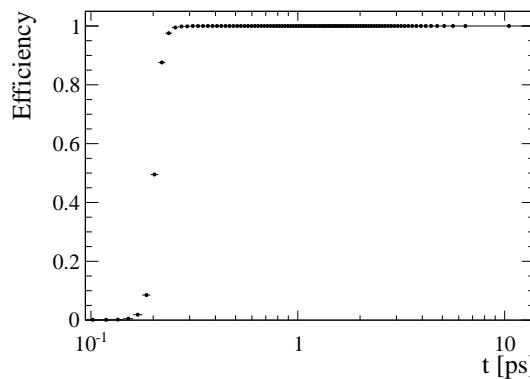

Figure 4.16: Decay time acceptance of the detached exclusive stripping line for $B_s^0 \to J/\psi \phi$ decays using the overlap with the non-detached stripping line from simulation.

4.3.3 Uncertainties

In the previous section, techniques to measure decay time acceptances for small decay times were presented. Efficiency histograms can be used to describe the lower decay time acceptance, and can be included as a PDF in the time-dependant maximum likelihood fits. In this way the statistical uncertainty due to the finite control samples which have no decay time acceptance for small decay times is not propagated to the likelihood, nor to the fitted parameters. This uncertainty can be estimated through the use of histograms obtained from pseudo-experiment data, called *toy histograms*, obtained from the nominal histograms. Several toy histograms are created by fluctuating the relative efficiencies in each decay time bin within their uncertainties. The spread of a variable resulting from the set of toy histograms is considered as the statistical uncertainty of the overlap and ratio techniques. However, there is an overlap between the sample used for the fit and the control sample used to obtain the decay time acceptances for small decay times. The total statistical uncertainty on a variable x, σ_x^{tot}, is calculated as:

$$(\sigma_x^{\text{tot}})^2 = (\sigma_x^{\text{fit}})^2 + (\sigma_x^{\text{hist}})^2 + 2 \cdot \sigma_x^{\text{fit}} \cdot \sigma_x^{\text{hist}} \cdot \rho \tag{4.9}$$

where σ_x^{fit} is the statistical uncertainty given by the unbinned maximum likelihood fit on the variable x, σ_x^{histos} is obtained by performing fits with the toy histograms, and ρ is the correlation between the two uncertainties. The correlation ρ is obtained from the pseudo-experiment data. In the case of the trigger strategy with the two trigger sets, almost unbiased and fully biased sets, there are four disjoints sets required for the fit and to obtain the acceptances:

- A = (Hlt2DiMuonDetachedJPsi TOS) and (Hlt2DiMuonJPsi TOS) and (Hlt1DiMuonHighMass TOS),

- B = (not Hlt2DiMuonDetachedJPsi TOS) and (Hlt2DiMuonJPsi TOS) and (Hlt1DiMuonHighMass TOS)

- C = (Hlt2DiMuonDetachedJPsi TOS) and (not Hlt1DiMuonHighMass TOS) and (Hlt1TrackMuon TOS or Hlt1TrackAllL0 TOS)

- D = (Hlt2DiMuonDetachedJPsi TOS) and (not Hlt2DiMuonJPsi TOS) and (Hlt1DiMuonHighMass TOS)

The toy histograms are generated from the simulated decay time efficiency histograms obtained from a MC sample of $B_s^0 \rightarrow J/\psi\,\phi$ decays and this for different number of decay time bins. The simulated histograms are transformed into a smoothed PDF to test the binning effects. The total yield of events passing the almost unbiased and fully biased trigger sets is constrained to 25'500 events to match the 2011 $B_s^0 \rightarrow J/\psi\,\phi$ dataset. Finally, for each sample, a fit to the decay time is performed with the toy histograms and another one using the "true" histograms used for the generation. From the fit using the toy and simulated histograms, two lifetimes, τ and τ', are obtained. The following parameters are obtained from the fit: δ_τ the

Table 4.6: $B_s^0 \to J/\psi\,\phi$ MC toys results for almost unbiased events only. The parameter definitions are given in the text.

# bins	δ_τ [fs]	$\delta_{\tau'}$ [fs]	$\sigma_{\mathrm{stat}}^{\mathrm{tot}}$ [fs]	$\sigma_{\mathrm{stat}}^{\mathrm{fit}}$ [fs]	$\sigma_{\mathrm{stat}}^{\mathrm{hist}}$ [fs]	ρ [%]
5	1.6	0.0	10.2	10.1	2.5	-10.4
10	0.5	0.0	10.1	10.1	2.6	-12.3
20	0.2	0.0	10.2	10.1	2.7	-12.5
30	0.2	0.0	10.1	10.1	2.7	-13.0
40	0.1	0.0	10.2	10.1	2.7	-12.0
50	0.1	0.0	10.1	10.1	2.7	-12.3

Table 4.7: $B_s^0 \to J/\psi\,\phi$ MC toys results for almost unbiased and fully biased events. The parameter definitions are given in the text.

# bins	δ_τ [fs]	$\delta_{\tau'}$ [fs]	$\sigma_{\mathrm{stat}}^{\mathrm{tot}}$ [fs]	$\sigma_{\mathrm{stat}}^{\mathrm{fit}}$ [fs]	$\sigma_{\mathrm{stat}}^{\mathrm{hist}}$ [fs]	ρ [%]
5	5.2	0.0	10.1	9.2	4.5	-4.0
10	2.0	0.0	10.1	9.2	4.8	-5.7
20	0.8	0.0	10.2	9.2	5.0	-5.8
30	0.4	0.0	10.2	9.2	5.0	-5.9
40	0.4	0.0	10.3	9.3	5.0	-5.9
50	0.2	0.0	10.2	9.2	5.1	-5.9

mean of the $\tau - \tau_{\mathrm{gen}}$ distribution and $\sigma_{\mathrm{stat}}^{\mathrm{tot}}$ its spread, $\delta_{\tau'}$ the mean of $\tau' - \tau_{\mathrm{gen}}$ distribution and $\sigma_{\mathrm{stat}}^{\mathrm{fit}}$ its spread, and $\sigma_{\mathrm{stat}}^{\mathrm{hist}}$ the spread of $\tau - \tau'$. Once these parameters are measured, the correlation can be computed. Table 4.6 shows the results on the parameters entering Eq. 4.9 using only events from the almost unbiased trigger set for $B_s^0 \to J/\psi\,\phi$ dataset. Table 4.7 shows the same results including the events passing the fully biased trigger set in addition.

The value of δ_τ gives the bias for the measured lifetime introduced by the finite binning of the histograms. The results on $\delta_{\tau'}$ indicate the consistency in the generation and the fit to the decay time distributions, where the value must be compatible with zero within statistical uncertainties. It can be seen that, the statistical uncertainty on the lifetime coming from the histograms, $\sigma_{\mathrm{stat}}^{\mathrm{hist}}$, is about a third of the statistical uncertainty of the fit to the data, $\sigma_{\mathrm{stat}}^{\mathrm{fit}}$, in the case of the almost unbiased trigger sets and a half in the case with the two trigger sets. The important outcome of this study is that the combined statistical uncertainties from the fit and the histograms are equal in both two cases. However, the bias on the measured lifetime induced by the binning is larger when both trigger sets are used. Therefore, the case with only the almost unbiased trigger set is favoured to obtain the best lifetime measurement. The correlation ρ is small and thus can be neglected, and $\sigma_{\mathrm{stat}}^{\mathrm{hist}}$ is treated as a systematic uncertainty.

4.4   Upper decay time acceptance

Section 4.3 describes how decay time acceptance effects can be separated into two pieces. The decay time acceptance effect at small decay times coming from the trigger and stripping can be parametrised using the overlap and ratio techniques. The part where the decay time efficiency is linearly dependent on the decay time itself must now be characterised.

4.4.1   The β factor

The acceptance effect at large decay times was first observed when measuring the lifetime with a MC sample using events which pass the unbiased trigger lines {(Hlt2DiMuonJPsi TOS) and (Hlt1DiMuonHighMass TOS)} and stripping lines (BetaSBs2JpsiPhiDetachedLine for $B_s^0 \rightarrow J/\psi\,\phi$ for example) at small decay times. Large shifts in lifetimes of a few tens of fs depending on the decay channel were measured. Simulation studies show that the decay time efficiency at large decay times can be described by a linear function:

$$\epsilon(t) \propto (1 + \beta t), \tag{4.10}$$

where β is the parameter, hereafter referred as the β *factor* [63], that quantifies the size of the inefficiencies at large decay times.

The easiest way to obtain the β factor is to fit the following PDF to a simulated decay time distribution that has no efficiency loss at small decay times:

$$\left(e^{-t'/\tau_{\mathrm{gen}}} \otimes G(t - t'; 0, \sigma_{\mathrm{res}})\right)(1 + \beta t), \tag{4.11}$$

where τ_{gen} is the lifetime used for the MC generation and σ_{res} the width of the Gaussian function that describes the decay time resolution. By fixing all the parameters except β in the fit, the β factor can be obtained.

Another solution is to identify and correct for all the source of decay time biases at large decay times, as presented in the next sub-sections, and perform a fit to measure the lifetime with and without corrections to measure the β factor directly from real data. However, correcting for lifetime biases implies cutting some non-negligible amount of signal events and enlarge the background level. Therefore loosing statistical power on the fit parameters, a process which may not be appropriate for every analysis as summarised in Sec. 4.5.

4.4.2   Investigation strategy

A detailed study of the reconstruction and selection steps affecting the decay time distribution in the region of large decay times was performed by another LHCb group. A summary of this study is presented in the following sub-sections based on [64].

To illustrate the various reconstruction and selection effects on the lifetime measurement, Fig. 4.17 shows simulation studies of lifetime measurements where measured lifetimes are obtained from a fit to the generated decay time distribution after each reconstruction and selection steps for the $B_s^0 \to J/\psi\,\phi$ channel.

The two major causes of acceptance effects at large decay times are:

1. VELO geometrical acceptance and reconstruction efficiency.

2. PV refitting and *B* candidates selection.

4.4.3 VELO geometrical acceptance and reconstruction efficiency

From the nominal interaction position, the angular reconstruction coverage of the VELO ranges from 15 to 390 mrad. However, the angular acceptance changes as a function of the *z* position. Therefore, the angular acceptance of the *b*-hadron decay products depends on the *z* position of the decay vertex. The *z* distribution of the interaction points has a spread of a few centimetres and *b*-hadrons can also fly a distance of few centimetres. The combination of these two facts creates a detection efficiency for *b*-hadron decay products that varies depending on the decay position. These effects can be reduced by introducing a restriction in the track angles and requiring *z* positions of the reconstructed PV to be in a narrow range. These restrictions defines a *fiducial volume*. Requiring the tracks to have a pseudo-rapidity in the range from 2 to 4.5 and the PV *z* position in the range of ±100 mm remove the acceptance
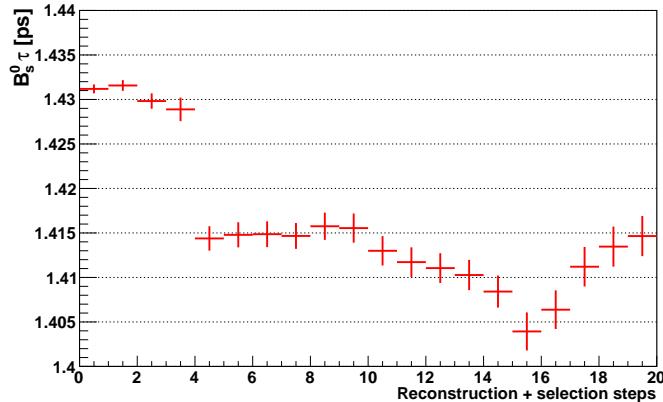

Figure 4.17: Measured lifetime after each reconstruction and selection step for the $B_s^0 \to J/\psi\,\phi$ channel without correction where the generated lifetime is 1.431 ps. 0: All generated candidates, 1: Fiducial cuts, 2: hasVelo, 3: hasVeloAndT, 4: isVeloRec and hasVeloAndT, 5: isLongReconstructed, 6: isReconstructed, 7: isTrackChi2, 8: isJpsiSelected, 9: isPhiPIDmass, 10: isPhiVtx, 11: isBIPChi2, 12: isBDTF, 13: is2ndBestIP, 14: isL0Triggered, 15: isHLT1Triggered, 16: isHLT2Triggered, 17: isStrip, 18: isBiasedTriggered, 19: Reconstructed lifetime. The selection of each step is given in Appendix C [64].

effect induced by the VELO geometrical acceptance for tracks coming from the B decay vertex. However, it reduces the signal yield by about 10-20 %.

A second effect related to the VELO comes from the pattern recognition algorithm to find tracks with hits in the VELO (*FastVelo*) [73]. FastVelo can run in two modes, the faster but more restrictive one is used in HLT1 and the slower but more efficient one is used in HLT2 and offline. It was found that the FastVelo algorithm has a non-uniform track finding efficiency as a function of IP_z of the track. The IP_z of a track is the distance of closest approach to the z-axis, defined as:

$$IP_z = \frac{\left|(\vec{d} - \vec{v}) \cdot (\vec{p} \times \vec{z})\right|}{\left|\vec{p} \times \vec{z}\right|}, \tag{4.12}$$

where $\vec{p}$ is the momentum vector of the track at its creation point $(\vec{d})$, $\vec{v}$ the average position of the PVs in each data taking period and $\vec{z} = (0, 0, 1)$ is the LHCb z direction.

The FastVelo efficiency for decay tracks of a b-hadron as a function of IP_z of the track is presented in Fig. 4.18 for different decay channels. Some differences are observed and they were found to be due to different kinematics of the particles. In addition, significant differences between HLT1 and HLT2/offline FastVelo are observed in the real data as evident in Fig. 4.19.

The distributions were obtained from real data using a tag-and-probe technique where the K^+ of $B^+ \to J/\psi K^+$ is reconstructed as a downstream track and the two FastVelo algorithm versions are run separately. Figure 4.18 shows the $J/\psi K^+$ invariant mass where the K^+ is reconstructed as a downstream track. The tracking efficiency as a function of the IP_z of the track is measured as the probability to match a long track to the downstream track. Figure 4.19 shows the measured VELO tracking efficiency as a function of the IP_z of the track for both HLT1 and HLT2/offline cases from data using the *sPlot* technique [74], explained later, on the
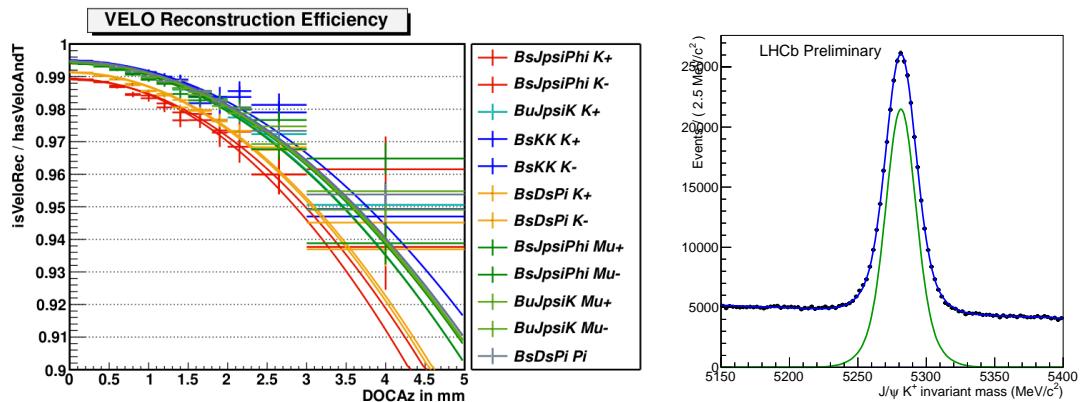

Figure 4.18: VELO tracking efficiency as a function of IP_z for tracks coming from various decays (left). The $J/\psi K^+$ invariant mass when the kaon is reconstructed as a downstream track (right) [64].

Table 4.8: VELO tracking efficiency, *a* and *c* parameters, obtained from real data for kaon tracks reconstructed using the HLT1 (left) and the HLT2/offline (right) FastVelo algorithms.

	a	c [mm^{-2}]
HLT1	0.9759 ± 0.0005	-0.0093 ± 0.0007
HLT2/offline	0.9831 ± 0.0004	-0.0041 ± 0.0005

$J/\psi K^+$ invariant mass. The efficiency distributions are parametrised using parabolas of the form:

$$\epsilon(\text{IP}_z) = a \times (1 + c \times \text{IP}_z^2), \tag{4.13}$$

where the *a* and *c* parameters obtained from data are summarised in Table 4.8.

The significant difference between the two FastVelo modes is mainly due to the requirement of four pairs of r and ϕ hits for HLT1 compared to three for HLT2/offline.

The VELO tracking efficiencies for a given decay such as $B_s^0 \to J/\psi \phi$ are combined as follows:

$$\epsilon^{B_s^0 \to J/\psi \phi} = \epsilon^{\mu^-} \cdot \epsilon^{\mu^+|\mu^-} \cdot \epsilon^{K^-|\mu^+\mu^-} \cdot \epsilon^{K^+|K^-\mu^+\mu^-}, \tag{4.14}$$

where the series of efficiencies ϵ are multiplied in a conditional sequence to reduce correlation between the tracks. From MC simulation, it is observed that the *c* parameter found using $B^+ \to J/\psi K^+$ as control channel is not exactly the same for every track of every decay. It is assumed that this is due to different kinematic and phase space distributions. To account for these changes in *c* parameters, a scale factor S^i, called *MC scale factor*, is obtained from a fit to the distribution of the number of matched downstream tracks to long tracks to the total number of downstream tracks as a function of the IP$_z$ of every track of the decay *i*:

$$\epsilon^i \propto (1 + S^i \times c \times (\text{IPz})^2) \tag{4.15}$$
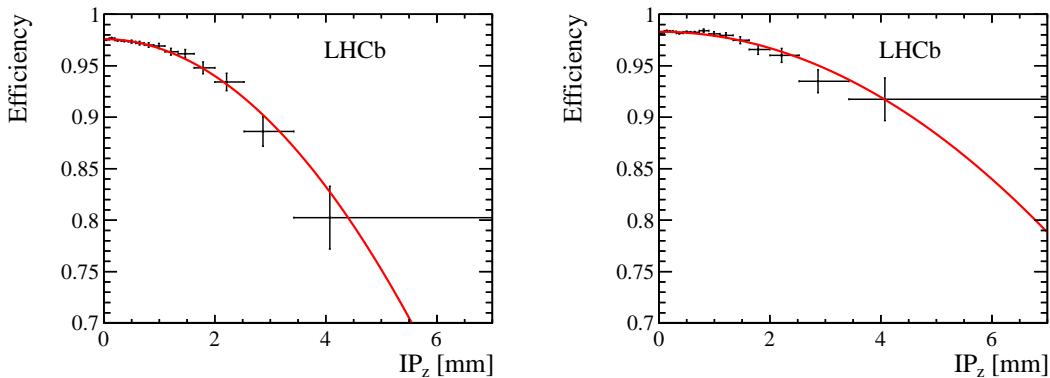

Figure 4.19: VELO tracking efficiency as a function of IP$_z$ for downstream kaons from $B^+ \to J/\psi K^+$ channel using a tag-and-probe technique for HLT1 (left) and HLT2/offline (right) [64].

where c is obtained from MC using the tag-and-probe technique on $B^+ \to J/\psi K^+$. Scale factor results are given in Table 5.8. If more statistics were available for the control sample, binning the FastVelo efficiency for multiple variables such as the pseudo-rapidity and the azimuthal angle ϕ of the track is expected to reduce the shift of the MC scale factors from unity.

4.4.4 PV refitting and B candidate selection

It was found that cuts on the B DTF, vertex, IP to the PV and K^*/ϕ vertex χ^2 bias the measured lifetime due to the default LHCb PV refitting algorithm and the small opening angle between the K^*/ϕ decay products. The default LHCb PV refitting algorithm removes the tracks used to reconstruct the b hadron when the PV is refitted. A new PV refitting algorithm was proposed that deletes all signal tracks from the track pool and re-launch completely the PV finding algorithm instead of simply refitting the PV. As shown in Fig. 4.20, the new PV refitting code removes the bias on the lifetime induced by the χ^2 cuts previously mentioned.

At the end of Sec. 4.3.2, it was pointed out that due to the difference between the stripping estimate of the decay time and the one used in the offline analysis, a decay time acceptance is induced by the lower bound cut of 0.2 ps on the decay time. It was shown in [64] that the difference in the decay time estimate between the stripping with the old PV refitting and the DTF decay time with the new PV refitting makes that the stripping acceptance goes beyond 0.3 ps and therefore bias the lifetime when starting the fit from 0.3 ps. Therefore, the inclusive J/ψ stripping line is needed for all the b-hadron lifetime measurements presented in Chap. 5.

The issue with the cut on the K^*/ϕ vertex χ^2 was found to come from the small opening angle between the two kaons from the ϕ and between the kaon and the pion from the K^{*0} decays. The average K^*/ϕ vertex χ^2 depends on the b-hadron decay time and cutting on this variables creates an efficiency drop at large decay times. For the K^*/ϕ vertex χ^2, the solution is to remove this cut. However, for the DTF kinematic fit which uses several quantities including the K^*/ϕ vertex χ^2, the solution to prevent an efficiency drop at large decay times is to enlarge significantly the K^*/ϕ daughter's track uncertainties. However, this enlarges the background level which cannot be afforded in every analysis.

Figure 4.20 summarises again the measured lifetime from the fit to the decay time distribution obtained from simulation after each reconstruction and selection step, but this time including the corrections described in the previous two sub-sections (fiducial cuts on the tracks, VELO tracking efficiency calibration, new PV refitting algorithm and ignoring the the K^*/ϕ daughters tracks uncertainties).

After all these corrections, the measured lifetime is unbiased, as the visible variations are compatible with statistical fluctuations. These corrections work for b-hadron decays where all the charged tracks come from the b-hadron decay vertex but not for channels like $B^0 \to J/\psi K^0_S$ and $\Lambda^0_b \to J/\psi \Lambda$ where the K^0_S and Λ are neutral particles decaying into two charged particles away from the b-hadron decay vertex. This point is addressed in Sec 4.4.5.

4.4.5   Reconstruction of particles decaying outside the VELO

K_S^0 and Λ can decay inside or outside the VELO. If their decay products leave enough hits in VELO stations, their tracks can be reconstructed with the VELO and create a long track. Otherwise, they can create a downstream track. This means K_S^0 and Λ can be reconstructed as either two long tracks (LL) or two downstream tracks (DD). Combinations of a long and a downstream track are not used in LHCb because their signal yields are small with a large amount of background. Figure 4.21 shows the measured lifetime from the fit to the decay time distribution obtained from simulation after each reconstruction and selection step for the $B^0 \to J/\psi \, K_S^0$ channel with K_S^0 reconstructed as LL/DD. It can be observed that all the corrections presented earlier work except for step 3 which corresponds to the requirement to have the K_S^0 daughters tracks within the VELO acceptance for LL and within the TT acceptance and not in the VELO acceptance for DD. In order to solve this issue, all the K_S^0 are reconstructed as downstream tracks completely ignoring the VELO information (FullDD).

Figure 4.22 shows the measured lifetime from the fit to the decay time distribution obtained from simulation after each reconstruction and selection step for the $B^0 \to J/\psi \, K_S^0$ channel with K_S^0 reconstructed as FullDD. A fit to the fully corrected decay time distribution shows that the measured lifetime is now also unbiased within MC statistical uncertainties for the $B^0 \to J/\psi \, K_S^0$ channel. Similar conclusion is obtained for $\Lambda_b^0 \to J/\psi \, \Lambda$.
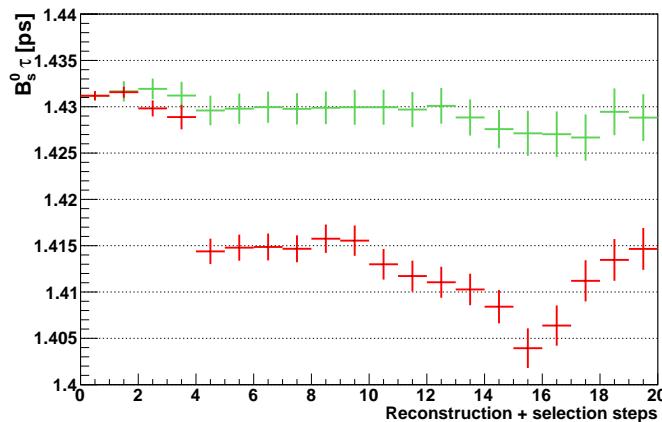

Figure 4.20: Measured lifetime after each reconstruction and selection step for the $B_s^0 \to J/\psi \, \phi$ channel with (green points) and without (red points) corrections applied where the generated lifetime is 1.431 ps. 0: All generated candidates, 1: Fiducial cuts, 2: hasVelo, 3: hasVeloAndT, 4: isVeloRec and hasVeloAndT, 5: isLongReconstructed, 6: isReconstructed, 7: isTrackChi2, 8: isJpsiSelected, 9: isPhiPIDmass, 10: isPhiVtx, 11: isBIPChi2, 12: isBDTF, 13: is2ndBestIP, 14: isL0Triggered, 15: isHLT1Triggered, 16: isHLT2Triggered, 17: isStrip, 18: isBiasedTriggered, 19: Reconstructed lifetime. The selection of each step is given in Appendix C [64].
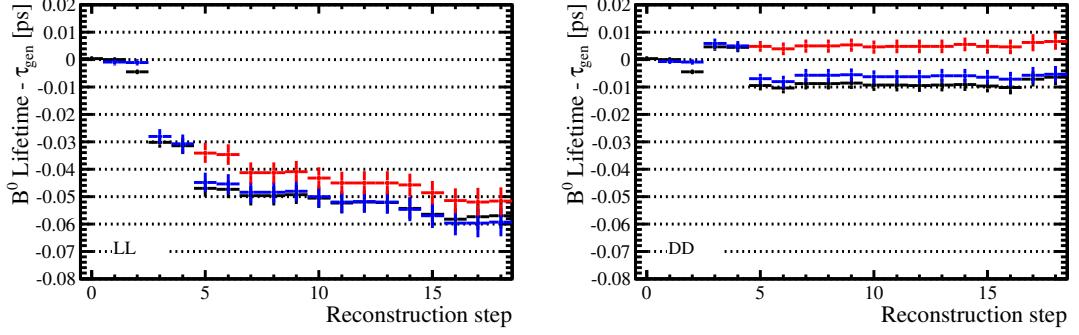
Figure 4.21: Difference between measured lifetime and lifetime used in the event generation after each reconstruction and selection step for the $B^0 \to J/\psi \, K^0_s$ channel with K^0_s reconstructed as LL and DD. No correction (black points), fiducial cuts (blue points), full corrections (red points) and full corrections with tighter cuts involving an uncertainty (orange points). 0: All generated candidates, 1: Momenta, 2: hasMuVelo, 3: hasVelo|hasMuVeloAndPiPiTTNoVelo, 4: hasVeloAndT|hasMuVeloAndPiPiTTNoVeloAndT, 5: isMuVeloOfflinePiPiVeloOfflineRec and hasVeloAndT|isMuVeloOfflineRec and hasMuVeloAndPiPiTTNoVeloAndT, 6: isLongReconstructed|isLLDDReconstructed, 7: isKSVtxSelected, 8: isJpsiVtxSelected, 9: isTrackSelected, 10: isKSDLSSelected, 11: isKSSelected, 12: isJpsiSelected, 13: isBVtxSelected, 14: isBSelected, 15: isSelected, 16: isL0Triggered, 17: isHlt1Triggered, 18: isHlt2Triggered. The selection of each step is given in Appendix C.
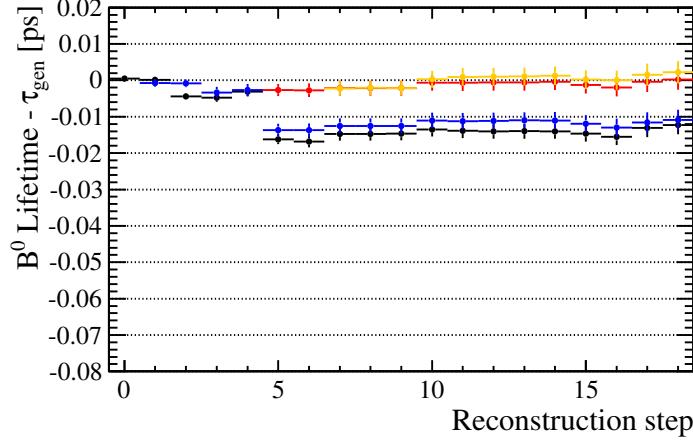

Figure 4.22: Difference between measured lifetime and lifetime used in the event generation after each reconstruction and selection step for the $B^0 \to J/\psi \, K^0_s$ channel with K^0_s reconstructed as FullDD. No correction (black points), fiducial cuts (blue points), full corrections (red points) and full corrections with tighter cuts involving an uncertainty (orange points). 0: All generated candidates, 1: Momenta, 2: hasMuVelo, 3: hasMuVeloAndPiPiTT, 4: hasMuVeloAndPiPiTTAndT, 5: isMuVeloOfflineRec and hasMuVeloAndPiPiTTAndT, 6: isLLFullDDReconstructed, 7: isKSVtxSelected, 8: isJpsiVtxSelected, 9: isTrackSelected, 10: isKSDLSSelected, 11: isKSSelected, 12: isJpsiSelected, 13: isBVtxSelected, 14: isBSelected, 15: isSelected, 16: isL0Triggered, 17: isHlt1Triggered, 18: isHlt2Triggered. The selection of each step is given in Appendix C.

Table 4.9: Summary of the various options to choose the trigger strategy and the techniques to get the efficiencies for small and large decay times.

Goal	The best lifetime		Other than the lifetime	
Uncertainties	$\sigma_{stat} \sim \sigma_{syst}$	$\sigma_{stat} >> \sigma_{syst}$	$\sigma_{stat} \sim \sigma_{syst}$	$\sigma_{stat} >> \sigma_{syst}$
Trigger Strategy	Almost unbiased	Almost unbiased Exclusively biased	Almost unbiased Exclusively biased	Almost unbiased Exclusively biased
Lower decay time acceptance	Overlap from Data	Overlap/Ratio from MC	Overlap/Ratio from Data	Overlap/Ratio from MC
Upper decay time acceptance	Full corrections from Data	β factor from MC	β factor from Data	β factor from MC
Examples	b-hadron lifetimes $\rightarrow$ Sec. 5 [75]	Ξ_b^- & Ω_b^- lifetimes	Weak phase ϕ_s $\rightarrow$ [21]	-

4.4.6 Uncertainties

As shown in Figs. 4.20 and 4.22, the lifetime obtained after applying all the corrections is, within one standard deviation of the MC statistical uncertainty and therefore can be considered unbiased. Hence, the MC statistical uncertainty should be taken as a systematic uncertainty. However, a shift with respect to the lifetime used in the event generation might become present with more MC statistics. Therefore, this shift is subtracted from the measured lifetime. The only part that is calibrated is the VELO reconstruction inefficiency as function of the IP_z of the track with a statistical uncertainty from a limited control sample size and the uncertainties on the MC scale factors. The full statistical uncertainty on the c parameter is propagated to the uncertainty of the measured lifetime as a systematic uncertainty. For the MC scale factors, the observed deviation from unity in simulation appears to be too large to be wrong, thus it was decided to only propagate to the lifetime systematic uncertainty half of the shift from unity.

4.5 Summary

Table 4.9 summarises various options for the trigger strategy and the techniques that can be used to obtain efficiencies for small and large decay times.

5 Measurements of b-hadron lifetimes, lifetime ratios and $\Delta\Gamma_d$

5.1 Introduction

The total decay width, which is the inverse of the lifetime, can be calculated by the heavy quark expansion (HQE) theory in inverse powers of the b-quark mass, m_b. At zeroth order, the lifetime of b hadrons that decay through the weak interaction are equal. First corrections appear at the order of $1/m_b^2$. The HQE calculation of lifetime ratios are robust as several terms related to kinetic and chromomagnetic operators cancel, and can be predicted with an accuracy of few percent. Therefore, lifetime ratios are powerful tests of HQE. It is also important to point out that the CPT theorem implies that the lifetimes of the b hadron and its CP conjugate are equal, thus their ratio should be 1. Interesting lifetime ratios to test HQE involving b hadrons are $\frac{\tau_{B^+}}{\tau_{B^0}}, \frac{\tau_{B_s^0}}{\tau_{B^0}}$ and $\frac{\tau_{\Lambda_b^0}}{\tau_{B^0}}$, and to test CPT symmetry, $\frac{\tau_{B^+}}{\tau_{B^-}}, \frac{\tau_{B^0}}{\tau_{\overline{B}^0}}$ and $\frac{\tau_{\Lambda_b^0}}{\tau_{\overline{\Lambda}_b^0}}$. Since the world's best measurements of several b-hadron lifetimes are already expected using the 1.0 fb^{-1} collected in 2011, the decision was taken to measure absolute b-hadron lifetimes and then compute lifetime ratios from the results.

The decay modes considered for this analysis are $B^+ \to J/\psi\, K^+$, $B^0 \to J/\psi\, K^{*0}$, $B^0 \to J/\psi\, K_s^0$, $B_s^0 \to J/\psi\, \phi$ and $\Lambda_b^0 \to J/\psi\, \Lambda$. The world-average central value of the Λ_b^0 lifetime has changed significantly since the first measurements made at the end of the past century. Around 2003, the LEP measurements and CDF Run-I data showed the lifetime ratio of Λ_b^0 and B^0 to be about 0.8 with an uncertainty of 0.05. Theoretical expectations of this lifetime ratio are close to unity. Significant amounts of theoretical work were devoted to the computation of this lifetime ratio using HQE. Lowering the lifetime ratio to 0.9 was possible, but not as low as 0.8. Therefore, the Λ_b^0 lifetime became one of the important measurements for the Run-II of Tevatron experiments, CDF and DØ. With the results of CDF and DØ, the world average of the lifetime ratio $\tau_{\Lambda_b^0}/\tau_{B^0}$ was 0.930 ± 0.020 in early 2012 [76]. Reducing the uncertainty down is an important goal for LHC experiments looking to test HQE. The analysis of b-hadron lifetimes took almost two years to control all the acceptance effects and evaluate the systematic uncertainties. ATLAS and CMS measured the Λ_b^0 lifetime using the $\Lambda_b^0 \to J/\psi\, \Lambda$ decay mode whereas LHCb with $\Lambda_b^0 \to J/\psi\, pK^-$. Even though the same precision would not be reached

Table 5.1: Early 2012 theoretical predictions and world average values of *b*-hadron lifetimes and lifetime ratios.

Observable	Prediction	World average
τ_{B^+} [ps]	–	1.641 ± 0.008
τ_{B^0} [ps]	–	1.519 ± 0.007
$\tau_{B_s^0}$ [ps]	–	1.516 ± 0.011
$\tau_{\Lambda_b^0}$ [ps]	–	1.429 ± 0.024
τ_{B^+}/τ_{B^0}	1.063 ± 0.027	1.079 ± 0.007
$\tau_{B_s^0}/\tau_{B^0}$	1.00 ± 0.01	0.993 ± 0.009
$\tau_{\Lambda_b^0}/\tau_{B^0}$	0.88 ± 0.05	0.930 ± 0.020

with $\Lambda_b^0 \rightarrow J/\psi\,\Lambda$ decays compared to $\Lambda_b^0 \rightarrow J/\psi\,pK^-$ decays, it is still an important input to the world average of the Λ_b^0 lifetime.

Table 5.1 summarises the early 2012 theoretical predictions of *b*-hadron lifetime ratios and world averages of lifetimes and lifetime ratios as of early 2012. Figure 5.1 summarises the status on the measurement of Λ_b^0 lifetime including the latest results not included in [76].

Experimentally, the lifetime of a *b* hadron is measured by fitting a single exponential to its decay time distribution. In the case of charged *b* hadrons, the decay time distribution is just an exponential. However, for cases involving neutral *B* mesons where the weak eigenstates rather than the flavour eigenstates have definite mass, decay width and decay width difference $\Delta\Gamma$, the decay time distribution is a sum of two exponentials when the flavour at production
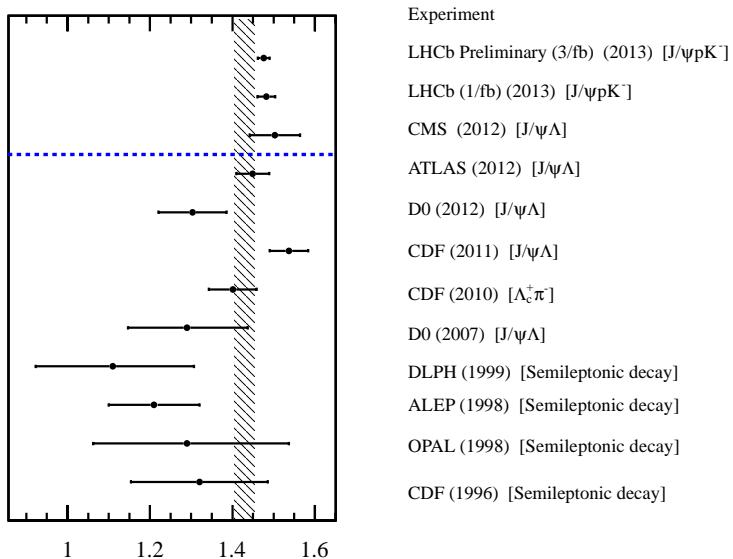

Figure 5.1: Summary of Λ_b^0 lifetime measurements where the values below the horizontal dashed line were used for the PDG2013 results [77].

is not identified. In this case, measuring two exponentials with a single exponential, the measured lifetime is called the *effective lifetime*. In order to obtain the dependencies of the effective lifetime on the mixing and CP parameters, the untagged rates of $B^0/\overline{B}^0(t) \to f$ and $B^0/\overline{B}^0(t) \to \overline{f}$ need to be defined:

$$\langle \frac{\mathrm{d}\Gamma}{\mathrm{d}t}(B^0/\overline{B}^0(t) \to f)\rangle \equiv \frac{\mathrm{d}\Gamma}{\mathrm{d}t}(B^0(t) \to f) + \frac{\mathrm{d}\Gamma}{\mathrm{d}t}(\overline{B}^0(t) \to f),\tag{5.1}$$

$$\langle \frac{\mathrm{d}\Gamma}{\mathrm{d}t}(B^0/\overline{B}^0(t) \to \overline{f})\rangle \equiv \frac{\mathrm{d}\Gamma}{\mathrm{d}t}(B^0(t) \to \overline{f}) + \frac{\mathrm{d}\Gamma}{\mathrm{d}t}(\overline{B}^0(t) \to \overline{f}),\tag{5.2}$$

and also the CP-averaged untagged rate [78]:

$$\langle \frac{\mathrm{d}\Gamma}{\mathrm{d}t}(B^0/\overline{B}^0(t) \to f/\overline{f})\rangle \equiv \frac{\langle \frac{\mathrm{d}\Gamma}{\mathrm{d}t}(B^0/\overline{B}^0(t) \to f)\rangle + \langle \frac{\mathrm{d}\Gamma}{\mathrm{d}t}(B^0/\overline{B}^0(t) \to \overline{f})\rangle}{2}$$

$$= R_L e^{-\Gamma_L t} + R_H e^{-\Gamma_H t},\tag{5.3}$$

where

$$R_L = \frac{1}{2}N_f \left\{ |A_f|^2 \frac{1+|\lambda_f|^2}{2}\left(1+\left|\frac{p}{q}\right|^2\right)\left(1-A_f^{\Delta\Gamma}\right) + |\overline{A}_{\overline{f}}|^2 \frac{1+|\overline{\lambda}_{\overline{f}}|^2}{2}\left(1+\left|\frac{q}{p}\right|^2\right)\left(1-\overline{A}_{\overline{f}}^{\Delta\Gamma}\right) \right\}\tag{5.4}$$

and

$$R_H = \frac{1}{2}N_f \left\{ |A_f|^2 \frac{1+|\lambda_f|^2}{2}\left(1+\left|\frac{p}{q}\right|^2\right)\left(1+A_f^{\Delta\Gamma}\right) + |\overline{A}_{\overline{f}}|^2 \frac{1+|\overline{\lambda}_{\overline{f}}|^2}{2}\left(1+\left|\frac{q}{p}\right|^2\right)\left(1+\overline{A}_{\overline{f}}^{\Delta\Gamma}\right) \right\}.\tag{5.5}$$

The effective lifetime is given by the decay time mean expectation value of the CP-averaged untagged rate [78]:

$$\tau_f^{\mathrm{eff}} = \frac{\int_0^\infty t \,\langle \frac{\mathrm{d}\Gamma}{\mathrm{d}t}(B^0/\overline{B}^0(t) \to f/\overline{f})\rangle \,\mathrm{d}t}{\int_0^\infty \langle \frac{\mathrm{d}\Gamma}{\mathrm{d}t}(B^0/\overline{B}^0(t) \to f/\overline{f})\rangle \,\mathrm{d}t} = \frac{\frac{R_L}{\Gamma_L^2}+\frac{R_H}{\Gamma_H^2}}{\frac{R_L}{\Gamma_L}+\frac{R_H}{\Gamma_H}} = \frac{1}{\Gamma}\frac{1}{1-y^2}\left(\frac{1+2A^{\Delta\Gamma}y+y^2}{1+A^{\Delta\Gamma}y}\right),\tag{5.6}$$

where

$$A^{\Delta\Gamma} \equiv \frac{R_H - R_L}{R_H + R_L}, \qquad y \equiv \frac{\Delta\Gamma}{2\Gamma}.\tag{5.7}$$

For $B^0 \to J/\psi K^{*0}$ decays, under the assumption that it is uniquely a *flavour-specific decay* ($\overline{A}_f = A_{\overline{f}} = 0$), $A^{\Delta\Gamma} = 0$. For $B^0 \to J/\psi K_S^0$ which decays into a CP-odd final state, $A^{\Delta\Gamma} \approx \cos 2\beta$ to a good precision in the SM with β the CKM angle of the unitary triangle defined in Chap. 1. Therefore, the effective lifetimes measured in the decays $B^0 \to J/\psi K^{*0}$ and $B^0 \to J/\psi K_S^0$ are

given by

$$\tau^{\text{eff}}_{B^0 \to J/\psi K^{*0}} = \frac{1}{\Gamma_d} \frac{1}{1 - y_d^2} \left(1 + y_d^2\right), \tag{5.8}$$

$$\tau^{\text{eff}}_{B^0 \to J/\psi K_S^0} = \frac{1}{\Gamma_d} \frac{1}{1 - y_d^2} \left(\frac{1 + 2\cos(2\beta) y_d + y_d^2}{1 + \cos(2\beta) y_d} \right). \tag{5.9}$$

This implies that measuring the effective lifetimes of $B^0 \to J/\psi K^{*0}$ and $B^0 \to J/\psi K_S^0$ and using the world-average value of β, measurements of $\Delta\Gamma_d$ and Γ_d can be obtained [79]. Within the SM, $\Delta\Gamma_d/\Gamma_d$ is expected to be very small with $\Delta\Gamma_d/\Gamma_d = (42 \pm 8) \times 10^{-4}$ [80, 81], however NP can significantly enlarge $\Delta\Gamma_d$ [79]. Hence, measuring $\Delta\Gamma_d$ is an important test of the SM and it is performed in this analysis. The current measurements of $\Delta\Gamma_d$ are all compatible with the SM prediction. The world average of the ratio $|\Delta\Gamma_d/\Gamma_d|$ is given by $|\Delta\Gamma_d/\Gamma_d| = 0.015 \pm 0.018$ using Belle and BaBar measurements [68].

For $B_s^0 \to J/\psi\phi$, the expression for $A^{\Delta\Gamma}_{B_s^0 \to J/\psi\phi}$ is more complicated because the $B_s^0 \to J/\psi\phi$ decay mode is a pseudo-scalar meson (spin 0, odd parity) decaying to two vector mesons (spin 1). This implies that the angular momentum l between the J/ψ and the ϕ can take values $l = \{0, 1, 2\}$. The n-even angular momentum states are CP even ($\eta_{CP} = +1$) and the remaining odd state is CP odd ($\eta_{CP} = -1$), therefore $J/\psi\phi$ final states are a mixture of CP-odd and CP-even states. In order to distinguish final states having different CP eigenvalues, the total decay amplitude is disentangled in three angular momentum states, A_0 ($l = 0$), $A_\perp$ ($l = 1$) and $A_\parallel$ ($l = 2$) where $|A_0|^2 + |A_\perp|^2 + |A_\parallel|^2 = 1$. The $\{0, \perp, \parallel\}$ are defined in the transversity basis and can be used to disentangle the different angular momentum states in an angular analysis of the decay products as performed in [21]. From the decay rates in [82], the $A^{\Delta\Gamma}_{B_s^0 \to J/\psi\phi}$ is given by

$$A^{\Delta\Gamma}_{B_s^0 \to J/\psi\phi} = \cos\phi_s \left(|A_\perp|^2 - |A_0|^2 - |A_\parallel|^2\right), \tag{5.10}$$

or in R_L and R_H terms:

$$R_L = \frac{1}{2} \left((1 + \cos\phi_s)|A_0|^2 + (1 + \cos\phi_s)|A_\parallel|^2 + (1 - \cos\phi_s)|A_\perp|^2\right), \tag{5.11}$$

$$R_H = \frac{1}{2} \left((1 - \cos\phi_s)|A_0|^2 + (1 - \cos\phi_s)|A_\parallel|^2 + (1 + \cos\phi_s)|A_\perp|^2\right), \tag{5.12}$$

where $\phi_s \approx -2\beta_s$ to good precision in the SM with β_s the very small angle of the second unitary triangle defined in Chap. 1.

5.2   Selection

As mentioned in Chap. 4, the selections of the exclusive stripping lines for $B^0 \rightarrow J/\psi\, K^{*0}$ and $B_s^0 \rightarrow J/\psi\, \phi$ decays create decay time acceptances at large decay times due to the small angle between the final states of the K^{0*} and ϕ. Also, the difference in K_S^0 and Λ reconstruction using downstream and long tracks biases the lifetime of $B^0 \rightarrow J/\psi\, K_S^0$ and $\Lambda_b^0 \rightarrow J/\psi\, \Lambda$. This can be avoided by reconstructing all the tracks forming the K_S^0 and Λ ignoring the VELO information (FullDD). Furthermore, events with a reconstructed decay time below 0.2 ps are discarded for all the five decay modes using the PropertimeFitter algorithm which introduces a loss in efficiency in the small decay time region that goes further than 0.3 ps. For the stripping, the inclusive J/ψ line (FullDSTDiMuonJpsi2MuMuDetachedLine) is used for all the fives decay modes.

Tables 5.2 to 5.7 summarise the selection cuts for the five decay modes. Some of these selection cuts have been optimised during the first analysis of b-hadron lifetimes using the 2010 dataset [63]. No cut is applied to the vertex χ^2 of the K^{0*} and the ϕ. The K^{0*} and ϕ daughter tracks are not used for the $\chi^2_{\text{DTF(B+PV)}}$/nDoF and χ^2_{IP} determination, so that the cuts on those variables do not introduce any drop in the acceptance for large decay times. For the reconstruction of K_S^0 and Λ in the $B^0 \rightarrow J/\psi\, K_S^0$ and $\Lambda_b^0 \rightarrow J/\psi\, \Lambda$ decay channels, daughter particles are reconstructed by the downstream tracking algorithm and the stripping was reapplied starting from the inclusive detached J/ψ stripping candidates. Finally, some minor adjustments were made to the selections with the experience acquired with the 2011 dataset. Concerning the trigger strategy, the almost unbiased set {Hlt2DiMuonDetachedJPsi TOS and Hlt1DiMuonHighMass TOS} is used. The best signal candidate is selected based on the best $\chi^2_{\text{DTF(B+PV)}}$/nDoF. A cut on the decay time significance of the K_S^0 and Λ with respect to the b-hadron vertex removes backgrounds from $B^0 \rightarrow J/\psi\, K^{*0}$ and $\Lambda_b^0 \rightarrow J/\psi\, pK^-$. The invariant mass window ranges for signal candidates are optimised to exclude backgrounds peaking around the b-hadron mass. For $B^0 \rightarrow J/\psi\, K_S^0$ and $B^0 \rightarrow J/\psi\, K^{*0}$, the upper mass bound is set to 5340 GeV/c^2 to exclude $B_s^0 \rightarrow J/\psi\, K_S^0$ and $B_s^0 \rightarrow J/\psi\, \overline{K}^{*0}$ events respectively. For $B^+ \rightarrow J/\psi\, K^+$, the lower mass bound is set to 5170 GeV/c^2 to exclude partially reconstructed background from $B^0 \rightarrow J/\psi\, K^{*0}$ where the pion from the K^{*0} is missed (*feed-down*). The lower bound on the accepted decay time is set to 0.3 ps because it almost entirely suppresses the prompt background. For $B^0 \rightarrow J/\psi\, K_S^0$ and $\Lambda_b^0 \rightarrow J/\psi\, \Lambda$ decays, this lower bound is pushed up to 0.45 ps to compensate for the 50% worse decay time resolution due to the downstream tracks used in the K_S^0 and the Λ reconstruction as presented in Sec. 5.5. The calibration sample $B^+ \rightarrow J/\psi\, K^+$ with the K^+ reconstructed with the downstream algorithm shows a hint of lifetime bias in data for events where the z coordinate of the PV (PV$_z$) is below -50 mm, but it is less significant in MC. Therfore, a cut is applied to remove events with PV$_z$ less than -50 mm for $B^0 \rightarrow J/\psi\, K_S^0$ and $\Lambda_b^0 \rightarrow J/\psi\, \Lambda$ decay modes rather than -100 mm for the three other decay modes. This effect is possibly due to the TT geometrical acceptance.

Table 5.2: Stripping and offline selections for the $B^+ \to J/\psi K^+$ decay mode.

Decay mode	Cut parameter	Stripping17b	Final Selection
all tracks	$\chi^2_{\text{track}}/\text{nDoF}$	< 5	< 4
	clone distance	> 5000	> 5000
$J/\psi \to \mu^+\mu^-$	$\Delta\ln\mathscr{L}_{\mu\pi}(\mu^{\pm})$	> 0	> 0
	$p_{\text{T}}(\mu^{\pm})$	> 0.55 GeV/c	> 0.55 GeV/c
	$\chi^2_{\text{vtx}}/\text{nDoF}(J/\psi)$	< 20	< 16
	DLS (J/ψ)	> 3	> 3
	$M(\mu^+\mu^-)$	$\in [3030, 3150]$ MeV/c^2	$\in [3030, 3150]$ MeV/c^2
K^+	$\Delta\ln\mathscr{L}_{K\pi}(K^+)$	–	> 0
	$p_{\text{T}}(K^+)$	–	> 1 GeV/c
	$p(K^+)$	–	> 10 GeV/c
$B^+ \to J/\psi K^+$	$M(B^+)$	–	$\in [5170, 5400]$ MeV/c^2
	$\chi^2_{\text{IP}}(B^+)$	–	< 25
	$\chi^2_{\text{IP,next}}(B^+)$	–	> 50
	$\chi^2_{\text{vtx}}/\text{nDoF}(B^+)$	–	< 10
	$\chi^2_{\text{DTF(B+PV)}}/\text{nDoF}(B^+)$	–	< 5
	$t_{\text{DTF}}(B^+)$	–	$\in [0.3, 14.0]$ ps

The analysis is performed using the 1.0 fb^{-1} LHCb dataset recorded in 2011. High statistic MC samples with standard conditions found in 2011 are used for each decay channel. The lifetime values used for the generation are 1.638 ps for $B^+ \to J/\psi K^+$, 1.525 ps for $B^0 \to J/\psi K^{*0}$ and $B^0 \to J/\psi K_{\text{S}}^0$ and 1.380 ps for $\Lambda_b^0 \to J/\psi \Lambda$. For $B_s^0 \to J/\psi \phi$, the two lifetimes, the transversity amplitudes and ϕ_s are given in Tab. 5.5. This gives an effective lifetime of 1.4293 ps in the range from 0 to infinity and 1.4297 ps in the range from 0.3 to 14 ps by integrating Eq. 5.6 over this range.

Table 5.3: Stripping and offline selections for the $B^0 \to J/\psi K^{*0}$ decay mode.

Decay mode	Cut parameter	Stripping17b	Final Selection
all tracks	$\chi^2_{\text{track}}/\text{nDoF}$	< 5	< 4
	clone distance	–	> 5000
$J/\psi \to \mu^+\mu^-$	$\Delta\ln\mathscr{L}_{\mu\pi}(\mu^\pm)$	> 0	> 0
	$p_{\text{T}}(\mu^\pm)$	$> 0.55\,\text{GeV}/c$	$> 0.55\,\text{GeV}/c$
	$\chi^2_{\text{vtx}}/\text{nDoF}(J/\psi)$	< 20	< 16
	DLS (J/ψ)	> 3	> 3
	$M(\mu^+\mu^-)$	$\in [3030, 3150]\,\text{MeV}/c^2$	$\in [3030, 3150]\,\text{MeV}/c^2$
$K^* \to K^+\pi^-$	$\Delta\ln\mathscr{L}_{K\pi}(K^+)$	–	> 0
	$p_{\text{T}}(K^*)$	–	$> 1.5\,\text{GeV}/c$
	$p_{\text{T}}(\pi^-)$	–	$> 0.3\,\text{GeV}/c$
	$M(K^+\pi^-)$	–	$\in [826, 966]\,\text{MeV}/c^2$
$B^0 \to J/\psi K^*$	$M(B^0)$	–	$\in [5150, 5340]\,\text{MeV}/c^2$
	$\chi^2_{\text{IP}}(B^0)$	–	< 25
	$\chi^2_{\text{IP,next}}(B^0)$	–	> 50
	$\chi^2_{\text{DTF(B+PV)}}/\text{nDoF}(B^0)$	–	< 5
	$t_{\text{DTF}}(B^0)$	–	$\in [0.3, 14.0]\,\text{ps}$

Table 5.4: Stripping and offline selections for the $B_s^0 \to J/\psi\phi$ decay mode.

Decay mode	Cut parameter	Stripping17b	Final Selection
all tracks	$\chi^2_{\text{track}}/\text{nDoF}$	< 5	< 4
	clone distance	–	> 5000
$J/\psi \to \mu^+\mu^-$	$\Delta\ln\mathscr{L}_{\mu\pi}(\mu^\pm)$	> 0	> 0
	$p_{\text{T}}(\mu^\pm)$	$> 0.55\,\text{GeV}/c$	$> 0.55\,\text{GeV}/c$
	$\chi^2_{\text{vtx}}/\text{nDoF}(J/\psi)$	< 20	< 16
	DLS (J/ψ)	> 3	> 3
	$M(\mu^+\mu^-)$	$\in [3030, 3150]\,\text{MeV}/c^2$	$\in [3030, 3150]\,\text{MeV}/c^2$
$\phi \to K^+K^-$	$\Delta\ln\mathscr{L}_{K\pi}(K^\pm)$	–	> 0
	$p_{\text{T}}(\phi)$	–	$> 1.0\,\text{GeV}/c$
	$M(K^+K^-)$	–	$\in [1008, 1032]\,\text{MeV}/c^2$
$B_s^0 \to J/\psi\phi$	$M(B_s^0)$	–	$\in [5200, 5550]\,\text{MeV}/c^2$
	$\chi^2_{\text{IP}}(B_s^0)$	–	< 25
	$\chi^2_{\text{IP,next}}(B_s^0)$	–	> 50
	$\chi^2_{\text{DTF(B+PV)}}/\text{nDoF}(B_s^0)$	–	< 5
	$t_{\text{DTF}}(B_s^0)$	–	$\in [0.3, 14.0]\,\text{ps}$

Table 5.5: Parameters used for the MC generation of $B_s^0 \to J/\psi\,\phi$ decays.

Parameter	Value
$\tau_H \equiv 1/\Gamma_H$	1.536875 ps
$\tau_L \equiv 1/\Gamma_L$	1.407125 ps
$|A_0(0)|$	0.775
$|A_\parallel(0)|$	0.49
$|A_\perp(0)|$	0.40
ϕ_s	-0.04

Table 5.6: Re-stripping and offline selections for the $B^0 \to J/\psi\,K_S^0$ decay mode.

Decay mode	Cut parameter	Restripping17b K_S^0 DD	Final selection K_S^0 DD
all tracks	$\chi^2_{\text{track}}/\text{nDoF}$	< 5 (10)	< 4
	clone distance	> 5000	> 5000
$J/\psi \to \mu\mu$	$\Delta\ln\mathcal{L}_{\mu\pi}(\mu^\pm)$	> 0	> 0
	$p_T(\mu^\pm)$	> 0.55 GeV/c	> 0.55 GeV/c
	$\chi^2_{\text{vtx}}/\text{nDoF}(J/\psi)$	< 20	< 16
	DLS (J/ψ)	> 3	> 3
	$|M(\mu^+\mu^-) - M(J/\psi)|$	< 100 MeV/c^2	< 60 MeV/c^2
$K_S^0 \to \pi^+\pi^-$	$p_T(\pi^\pm)$	> 0.25 GeV/c	> 0.25 GeV/c
	$p(\pi^\pm)$	> 2 GeV/c	> 2 GeV/c
	DTF ctSig wrt B^0 vtx(K_S^0)	–	> 3
	$p_T(K_S^0)$	–	> 1 GeV/c
	$\chi^2_{\text{vtx}}/\text{nDoF}(K_S^0)$	< 25	< 25
	$|M(\pi^+\pi^-) - M(K_S^0)|$	< 15 MeV/c^2	< 6 MeV/c^2
$B^0 \to J/\psi K_S^0$	$M(B^0)$	–	$\in [5150, 5340]$ MeV/c^2
	$\chi^2_{\text{IP}}(B^0)$	–	< 25
	$\chi_{\text{IP,next}}(B^0)$	–	> 50
	$\chi^2_{\text{vtx}}/\text{nDoF}(B^0)$	–	< 25
	$\chi^2_{\text{DTF(B+PV)}}/\text{nDoF}(B^0)$	–	< 5
	$t_{\text{DTF}}(B^0)$	–	$\in [0.45, 14.0]$ ps

Table 5.7: Re-stripping and offline selections for the $\Lambda_b^0 \to J/\psi\,\Lambda$ decay mode.

Decay mode	Cut parameter	Restripping17b Λ^0 DD	Final selection Λ^0 DD
all tracks	$\chi^2_{\text{track}}/\text{nDoF}$	$< 5\,(10)$	< 4
	clone distance	> 5000	> 5000
$J/\psi \to \mu^+\mu^-$	$\Delta\ln\mathscr{L}_{\mu\pi}(\mu^\pm)$	> 0	> 0
	$p_{\text{T}}(\mu^\pm)$	$> 0.55\,\text{GeV}/c$	$> 0.55\,\text{GeV}/c$
	$\chi^2_{\text{vtx}}/\text{nDoF}(J/\psi)$	< 20	< 16
	DLS (J/ψ)	> 3	> 3
	$|M(\mu^+\mu^-) - M(J/\psi)|$	$< 100\,\text{MeV}/c^2$	$< 60\,\text{MeV}/c^2$
$\Lambda \to p\pi^-$	$p_{\text{T}}(\pi^-)$	$> 0.1\,\text{GeV}/c$	$> 0.1\,\text{GeV}/c$
	$p_{\text{T}}(p)$	$> 0.5\,\text{GeV}/c$	$> 0.5\,\text{GeV}/c$
	$p(p,\pi^-)$	$> 2\,\text{GeV}/c$	$> 2\,\text{GeV}/c$
	DTF ctSig wrt Λ_b^0 vtx(Λ)	–	> 3
	$p_{\text{T}}(\Lambda)$	–	$> 1\,\text{GeV}/c$
	$\chi^2_{\text{vtx}}/\text{nDoF}(\Lambda)$	< 25	< 25
	$|M(p\pi) - M(\Lambda)|$	$< 15\,\text{MeV}/c^2$	$< 6\,\text{MeV}/c^2$
$\Lambda_b^0 \to J/\psi\,\Lambda$	$M(\Lambda_b^0)$	–	$\in [5500, 5740]\,\text{MeV}/c^2$
	$\chi^2_{\text{IP}}(\Lambda_b^0)$	–	< 25
	$\chi_{\text{IP,next}}(\Lambda_b^0)$	–	> 50
	$\chi^2_{\text{vtx}}/\text{nDoF}(\Lambda_b^0)$	–	< 25
	$\chi^2_{\text{DTF(B+PV)}}/\text{nDoF}(\Lambda_b^0)$	–	< 5
	$t_{\text{DTF}}(\Lambda_b^0)$	–	$\in [0.45, 14.0]\,\text{ps}$

5.3   Maximum likelihood fit

In order to measure the lifetime, a simultaneous fit to the invariant mass of the *b* hadron and its decay time distribution is performed using the expected distributions. The *probability density functions* (PDFs) for the mass and decay time and two different fitting techniques are presented below.

5.3.1   Invariant mass PDF

The signal PDF for the mass is parametrised as a sum of two Gaussian functions:

$$\mathscr{S}(m) = f_{m,\text{sig}}\, G(m; \mu, \sigma_1) + (1 - f_{m,\text{sig}})\, G(m; \mu, \sigma_1 r_m), \tag{5.13}$$

where m is the measured mass, μ the mean of the Gaussians, σ_1 the width of the first Gaussian, r_m the ratio of widths of the second to the first Gaussian and $f_{m,\text{sig}}$ the fraction of the first Gaussian. An alternative function is investigated in Sec. 5.7.6.

A single exponential function is used for the background:

$$\mathscr{B}(m) = e^{\alpha_{\text{bkg}} m}. \tag{5.14}$$

5.3.2   Decay time PDF

The signal decay time PDF is parametrised using a single exponential function convolved with a Gaussian representing resolution effects and further multiplied by the trigger ($\text{Acc}_{\text{trigger}}$) and stripping ($\text{Acc}_{\text{stripping|trigger}}$) efficiency histograms:

$$\mathscr{S}(t) = \text{Acc}_{\text{trigger}}(t) \times \text{Acc}_{\text{stripping|trigger}}(t) \times \left[e^{-t'/\tau} * G(t - t'; \Delta, \sigma_{\text{res}}) \right](t) \tag{5.15}$$

where Δ is the decay time offset, σ_{res} the decay time resolution and τ the lifetime. Decay time trigger and stripping efficiency results are presented in Sec. 5.4 and decay time resolutions ones in Sec. 5.5.

For the background, It was found that three exponential functions are required when fitting the decay time distribution of the events in the sideband regions around the signal masses. Therefore, a sum of three exponential functions are used:

$$\mathscr{B}(t) = \left[\left(f_{\text{LL},1}\, e^{-t'/\tau_{\text{LL},1}} + f_{\text{LL},2}\, e^{-t'/\tau_{\text{LL},2}} + (1 - f_{\text{LL},1} - f_{\text{LL},2})\, e^{-t'/\tau_{\text{LL},3}} \right) * G(t - t'; \Delta, \sigma_{\text{res}}) \right](t), \tag{5.16}$$

where $\tau_{\text{LL},1}, \tau_{\text{LL},2}, \tau_{\text{LL},3}$ are the long-lived background average decay time and $f_{LL,1}, f_{LL,2}$ their relative fractions.

5.3.3 Fitting techniques

The first technique used is the classical two-dimensional fit to the mass and decay time distributions called *cFit*. The product of the mass and decay time PDF s is constructed separately for signal and background assuming that the two distributions are uncorrelated. The function that is fitted to the observed invariant mass and decay time distributions is given by

$$\mathscr{P}_{cFit}(m, t) = N_{\text{sig}} \times \mathscr{S}(m) \times \mathscr{S}(t) + N_{\text{bkg}} \times \mathscr{B}(m) \times \mathscr{B}(t), \tag{5.17}$$

where N_{sig} and N_{bkg} are the signal and background yields, respectively.

The second fit is based on the *sPlot* technique [74], where a fit to the invariant mass distribution is performed using a sum of signal and background mass PDFs $\mathscr{S}(m)$ and $\mathscr{B}(m)$:

$$\mathscr{P}(m) = N_{\text{sig}} \times \mathscr{S}(m) + N_{\text{bkg}} \times \mathscr{B}(m). \tag{5.18}$$

This allows signal from background to be separated using weights called *sWeights*. A sWeighted fit using $\mathscr{S}(t)$ is performed on the decay time distribution to measure the lifetime. This technique is called the *sFit* [83] and requires that the mass and decay time distributions are uncorrelated.

The negative log likelihood that is minimised for the cFit using the IP_z weights w_i to correct for the VELO track reconstruction inefficiencies, is given by

$$-\ln(\mathscr{L}_{cFit}) = -\alpha_{cFit} \sum_{\text{events i}} w_i \ln(\mathscr{P}_{cFit}(m, t)), \tag{5.19}$$

where $\alpha_{cFit} = \sum_i w_i / \sum_i w_i^2$ is introduced to correct for the effects of IP_z weights on the measured uncertainties of the fit parameters such as the lifetime.

The negative log likelihood for the sFit is similar to the one for the cFit, except that the sWeights W_i are also included:

$$-\ln(\mathscr{L}_{sFit}) = -\alpha_{sFit} \sum_{\text{events i}} w_i W_i \ln(\mathscr{S}(t)), \tag{5.20}$$

where $\alpha_{sFit} = \sum_i (w_i W_i) / \sum_i (w_i W_i)^2$ also has the sWeights taken into account.

Table 5.8: Measured MC scale factors for all the long tracks of the five decay channels [64].

	$B_s^0 \to J/\psi\,\phi$	$B^0 \to J/\psi\,K^{*0}$	$B^+ \to J/\psi\,K^+$	$B^0 \to J/\psi\,K_S^0$	$\Lambda_b^0 \to J/\psi\,\Lambda$
μ^+	1.28 ± 0.05	1.20 ± 0.05	1.25 ± 0.05	1.07 ± 0.04	1.06 ± 0.06
μ^-	1.20 ± 0.05	1.14 ± 0.04	1.15 ± 0.04	1.06 ± 0.04	1.04 ± 0.06
$K^\pm$	–	1.47 ± 0.12	1.04 ± 0.09	–	–
K^+	1.49 ± 0.15	–	–	–	–
K^-	1.65 ± 0.18	–	–	–	–
$\pi^\pm$	–	1.23 ± 0.12	–	–	–

5.4 Decay time acceptances

All the techniques used to correct for decay time acceptance effects are described in Chap. 4. In this section, the results related to decay time acceptances for this analysis are presented.

5.4.1 VELO reconstruction efficiency

The procedure to obtain a parametrisation for the VELO track reconstruction and its calibration is explained in Sec. 4.4.3. The MC scale factors, described in Sec. 4.4.3, obtained from MC are summarised in Table 5.8.

5.4.2 Trigger and stripping

Since the inclusive J/ψ detached line must be used to remove the decay time acceptance effects, the trigger and stripping acceptances are obtained using the overlap technique described in Sec. 4.3.2 on events that pass the exclusive lines. The measured product of the trigger and stripping acceptances are shown in Figs. 5.2, 5.3 and 5.4 for both real and MC data, and MC with and without the requirement on the exclusive stripping line to be passed. It can be noticed that demanding that the candidates pass the exclusive line improves the efficiency for small decay times. The acceptance effects for $B^0 \to J/\psi\,K_S^0$ and $\Lambda_b^0 \to J/\psi\,\Lambda$ are found to be similar due to their similar topology. Since the precision of the histograms for $B^0 \to J/\psi\,K_S^0$ are significantly better than the ones from $\Lambda_b^0 \to J/\psi\,\Lambda$, it was decided to use the $B^0 \to J/\psi\,K_S^0$ acceptances for $\Lambda_b^0 \to J/\psi\,\Lambda$. Any difference in Λ_b^0 lifetime observed in MC between the fit result of the $\Lambda_b^0 \to J/\psi\,\Lambda$ decay time distribution with $B^0 \to J/\psi\,K_S^0$ efficiency histogram and that with the $\Lambda_b^0 \to J/\psi\,\Lambda$ acceptance histogram is included in the final correction. The effect due to the requirement that the exclusive line needs to be passed is included in the final correction.

5.4.3 Summary

Figures 5.5, 5.6 and 5.7 show the lifetime obtained by fits performed on simulation data after each reconstruction and selection step for $B^+ \to J/\psi\, K^+$ ($\tau_{\text{gen}} = 1.638$ ps), $B^0 \to J/\psi\, K^{*0}$ ($\tau_{\text{gen}} = 1.525$ ps) and $B_s^0 \to J/\psi\, \phi$ ($\tau_{\text{gen}}^{\text{eff}} = 1.430$ ps) without applying any correction to reduce the bias and with all the corrections presented in Sec 4.4. Figures 5.8 and 5.9 show the deviation of the fit value from the lifetime used for the MC generation after each reconstruction and selection step for $B^0 \to J/\psi\, K_S^0$ and $\Lambda_b^0 \to J/\psi\, \Lambda$. This difference is subtracted from the lifetime measured in data to obtain the final result.
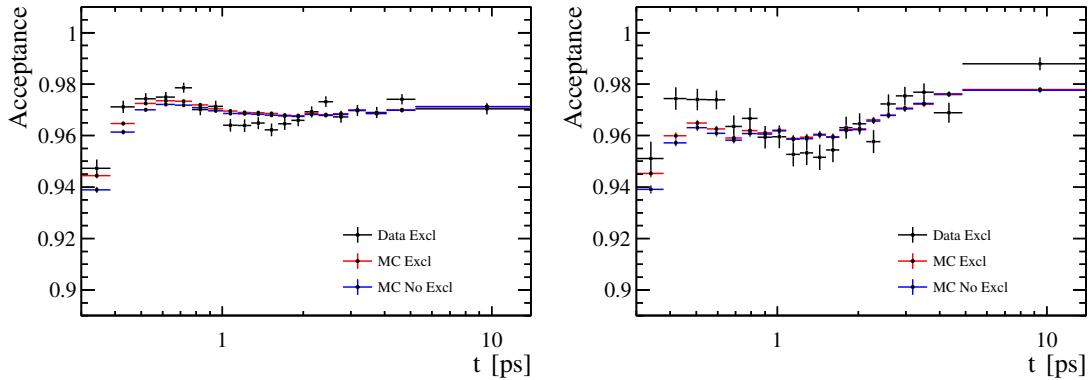
Figure 5.2: $B^+ \to J/\psi\, K^+$ (*left*) and $B^0 \to J/\psi\, K^{*0}$ (*right*) trigger and stripping acceptances measured in data, MC and MC without the requirement on the exclusive line to be passed.
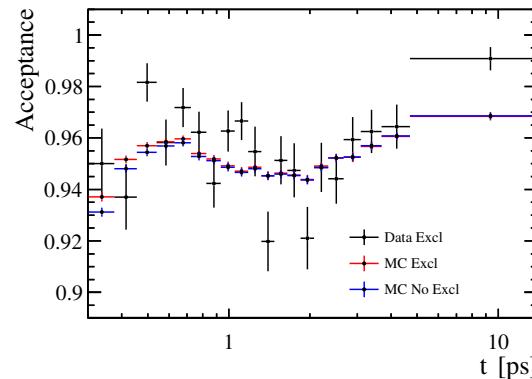
Figure 5.3: $B_s^0 \to J/\psi\, \phi$ trigger and stripping acceptances measured in data, MC and MC without the requirement on the exclusive line to be passed.
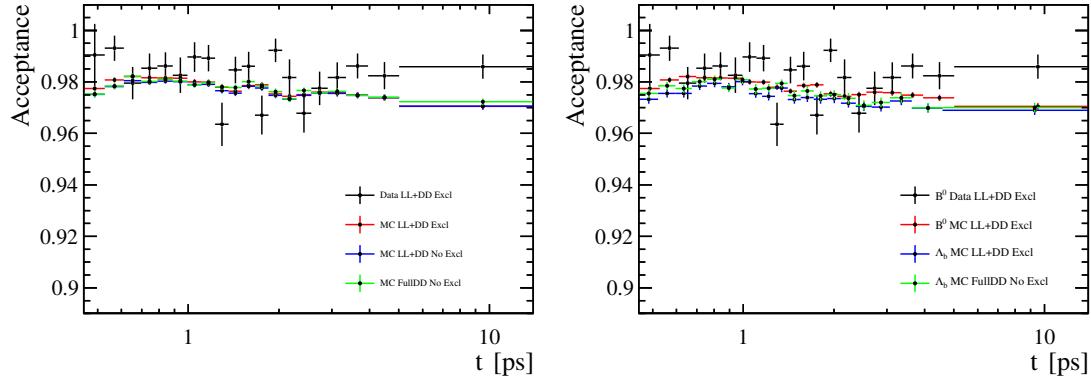
Figure 5.4: $B^0 \to J/\psi K_S^0$ (*left*) trigger and stripping acceptances measured in data and MC with K_S^0 reconstructed as LL+DD. The acceptances found in MC without the requirement on the exclusive line to be passed with K_S^0 reconstructed as LL+DD and FullDD. The right-hand plot shows the acceptances for $B^0 \to J/\psi K_S^0$ events found in data and MC compared to that of $\Lambda_b^0 \to J/\psi \Lambda$ reconstructed as LL+DD for which the exclusive stripping was passed and FullDD without the exclusive line requirement.
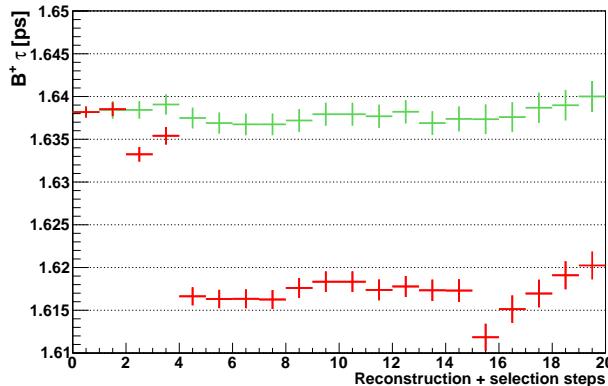
Figure 5.5: Measured lifetime after each reconstruction and selection step for the $B^+ \to J/\psi K^+$ channel with (green points) and without (red points) corrections applied. 0: All generated candidates, 1: Fiducial cuts, 2: hasVelo, 3: hasVeloAndT, 4: isVeloRec and hasVeloAndT, 5: isLongReconstructed, 6: isReconstructed, 7: isTrackChi2, 8: isJpsiSelected, 9: isPhiPIDmass, 10: isPhiVtx, 11: isBIPChi2, 12: isBDTF, 13: is2ndBestIP, 14: isL0Triggered, 15: isHLT1Triggered, 16: isHLT2Triggered, 17: isStrip, 18: isBiasedTriggered, 19: Reconstructed lifetime. The selection of each step is given in Appendix C [64].
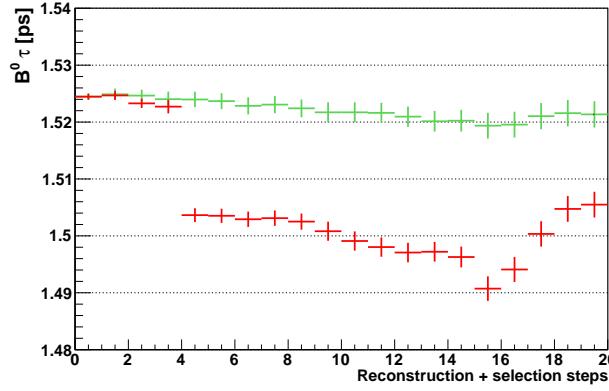
Figure 5.6: Measured lifetime after each reconstruction and selection step for the $B^0 \to J/\psi K^{*0}$ channel with (green points) and without (red points) corrections applied. 0: All generated candidates, 1: Fiducial cuts, 2: hasVelo, 3: hasVeloAndT, 4: isVeloRec and hasVeloAndT, 5: isLongReconstructed, 6: isReconstructed, 7: isTrackChi2, 8: isJpsiSelected, 9: isPhiPIDmass, 10: isPhiVtx, 11: isBIPChi2, 12: isBDTF, 13: is2ndBestIP, 14: isL0Triggered, 15: isHLT1Triggered, 16: isHLT2Triggered, 17: isStrip, 18: isBiasedTriggered, 19: Reconstructed lifetime. The selection of each step is given in Appendix C [64].
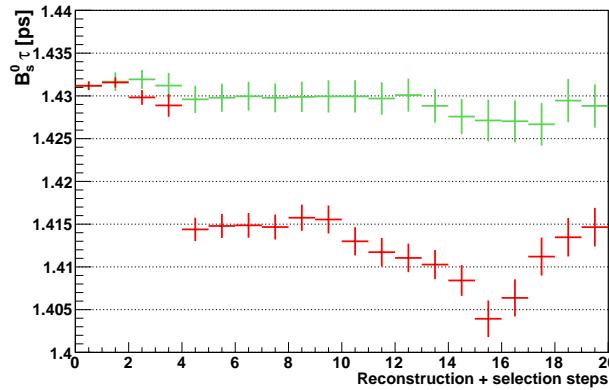
Figure 5.7: Measured lifetime after each reconstruction and selection step for the $B_s^0 \to J/\psi \phi$ channel with (green points) and without (red points) corrections applied. 0: All generated candidates, 1: Fiducial cuts, 2: hasVelo, 3: hasVeloAndT, 4: isVeloRec and hasVeloAndT, 5: isLongReconstructed, 6: isReconstructed, 7: isTrackChi2, 8: isJpsiSelected, 9: isPhiPIDmass, 10: isPhiVtx, 11: isBIPChi2, 12: isBDTF, 13: is2ndBestIP, 14: isL0Triggered, 15: isHLT1Triggered, 16: isHLT2Triggered, 17: isStrip, 18: isBiasedTriggered, 19: Reconstructed lifetime. The selection of each step is given in Appendix C [64].
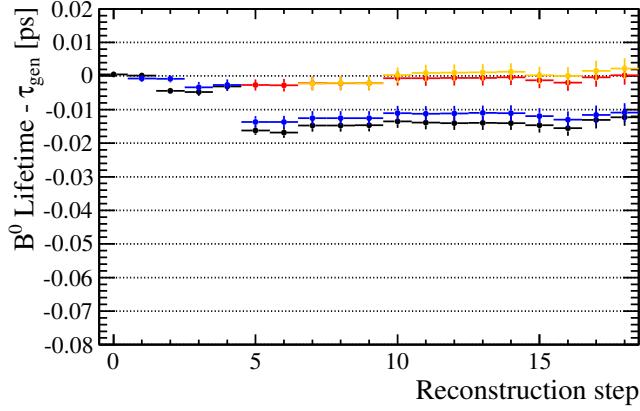
Figure 5.8: Difference between measured lifetime and lifetime used in the event generation after each reconstruction and selection step for the $B^0 \to J/\psi K_s^0$ channel with K_s^0 reconstructed as FullDD. No correction (black points), fiducial cuts (blue points), full corrections (red points) and full corrections with tighter cuts involving an uncertainty applied such as $\chi^2_{\text{DTF(B+PV)}}/\text{nDoF}$, χ^2_{IP} for example (orange points). 0: All generated candidates, 1: Momenta, 2: hasMuVelo, 3: hasMuVeloAndPiPiTT, 4: hasMuVeloAndPiPiTTAndT, 5: isMuVeloOfflineRec and hasMuVeloAndPiPiTTAndT, 6: isLLFullDDReconstructed, 7: isKSVtxSelected, 8: isJpsiVtxSelected, 9: isTrackSelected, 10: isKSDLSSelected, 11: isKSSelected, 12: isJpsiSelected, 13: isBVtxSelected, 14: isBSelected, 15: isSelected, 16: isL0Triggered, 17: isHlt1Triggered, 18: isHlt2Triggered. The selection of each step is given in Appendix C.

Figure 5.9: Difference between measured lifetime and lifetime used in the event generation after each reconstruction and selection step for the $\Lambda_b^0 \to J/\psi \Lambda$ channel with Λ reconstructed as FullDD. No correction (black points), fiducial cuts (blue points), full corrections (red points) and full corrections with tighter cuts involving an uncertainty applied such as $\chi^2_{\text{DTF(B+PV)}}/\text{nDoF}$, χ^2_{IP} for example (orange points). 0: All generated candidates, 1: Momenta, 2: hasMuVelo, 3: hasMuVeloAndPPiTT, 4: hasMuVeloAndPPiTTAndT, 5: isMuVeloOfflineRec and hasMuVeloAndPPiTTAndT, 6: isLLFullDDReconstructed, 7: isLambdaVtxSelected, 8: isJpsiVtxSelected, 9: isTrackSelected, 10: isLambdaDLSSelected, 11: isLambdaSelected, 12: isJpsiSelected, 13: isBVtxSelected, 14: isBSelected, 15: isSelected, 16: isL0Triggered, 17: isHlt1Triggered, 18: isHlt2Triggered. The selection of each step is given in Appendix C.

94

Table 5.9: Mean and RMS of the decay time resolution distribution $t_{\mathrm{reco}} - t_{\mathrm{gen}}$ found in MC [64].

Channel	Mean [fs]	RMS [fs]
$B^+ \to J/\psi\, K^+$	-0.3	43.7
$B^0 \to J/\psi\, K^{*0}$	-0.1	39.7
$B_s^0 \to J/\psi\, \phi$	$+0.1$	47.8
$B^0 \to J/\psi\, K_S^0$	$+1.1$	64.8
$\Lambda_b^0 \to J/\psi\, \Lambda$	$+1.0$	65.3

5.5 Decay time resolution

The decay time resolution of decay products composed of only long tracks was already studied in detail, for example in the ϕ_s analysis using $B_s^0 \to J/\psi\, \phi$ decays. The decay time resolution was measured to be about 45 fs in data [21]. For the decay modes with long-lived daughters in the final state, only the case where the K_S^0's are reconstructed as LL and DD was studied for the $B_s^0 \to J/\psi\, K_S^0$ lifetime analysis [84], but not the FullDD case. Therefore, a study is required to determine the resolution and bias of the decay time measurement. From simulation, the mean and RMS of the distributions of the lifetime residuals for the five decay channels are summarised in Table 5.9. A decay time resolution of about 45 fs is found for $B^+ \to J/\psi\, K^+$, $B^0 \to J/\psi\, K^{*0}$, $B_s^0 \to J/\psi\, \phi$ decays and about 65 fs for the $B^0 \to J/\psi\, K_S^0$ and $\Lambda_b^0 \to J/\psi\, \Lambda$ decays.

The inclusive high p_{T} line and the prescaled exclusive line described in Sec. 4.2 are used to measure the decay time resolution from data.

The decay time resolution can be measured from data by fitting the measured decay time distribution for events where a prompt J/ψ is combined to a prompt K_S^0. To separate real J/ψ's and K_S^0's from background, the sPlot technique is applied simultaneously on both the J/ψ and K_S^0 mass distributions to extract the sWeights. A fit is then performed to the sWeighted decay time distribution using the following PDF:

$$
\begin{aligned}
f(t) &= (N_{\mathrm{Prompt}}\, \delta(t) + N_{\mathrm{LL}}\, f_{\mathrm{LL}}(t)) \otimes f_{\mathrm{res,core}}(t) + N_{\mathrm{WrongPV}}\, G(t; \Delta, \sigma_3)), \\
f_{\mathrm{LL}}(t) &= f_{LL}\, e^{-t/\tau_{LL1}} + (1 - f_{LL})\, e^{-t/\tau_{LL2}}, \\
f_{\mathrm{res,core}}(t) &= f\, G(t; \Delta, \sigma_1) + (1 - f)\, G(t; \Delta, \sigma_2),
\end{aligned}
\tag{5.21}
$$

where $\delta(t)$ is the delta function, N_{Prompt} the yield of prompt J/ψ with a prompt K_S^0 yield, $f_{\mathrm{LL}}(t)$ two exponential functions to describe the component due to the decay of partially reconstructed long-lived hadrons with N_{LL} the yield for this component, $f_{\mathrm{res,core}}(t)$ two Gaussian functions which model the decay time resolution with a common mean Δ and two widths σ_1 and σ_2. The component for events where a wrong PV is associated is modelled by a single Gaussian with mean Δ and width σ_3 with N_{WrongPV} the wrong-PV component yield [21].

Table 5.10: Mean, effective resolution of the core (2G) and effective resolution including the wrong-PV component (2G+G) extracted from data are summarised for $B^0 \to J/\psi\, K_S^0$.

$B^0 \to J/\psi\, K_S^0$	FullDD HighPT	LL+DD HighPT	LL+DD Excl	LL HighPT	LL Excl	DD HighPT	DD Excl
Mean [fs]	-3.7±0.3	-3.6±0.3	-4.2±0.3	-4.3±0.4	-3.9±0.4	-3.4±0.3	-4.7±0.3
Eff RMS Core [fs]	60.8	55.1	57.9	45.8	49.6	60.1	62.0
Eff RMS 2G+G [fs]	69.6	62.6	91.1	51.2	65.0	68.1	105.6

Results obtained from real data on the mean, the effective resolution $\left(\sigma^{\text{eff}} = \sqrt{\sum_i f_i \sigma_i^2}\right)$ of the core (2G) and the effective resolution including the wrong-PV component (2G+G) are summarised in Table 5.10.

The non-zero shift of the mean is not a problem when measuring lifetimes because shifting the time in the exponential just results in a change of normalisation. A possible issue my arise from the acceptance effect at small decay times. The decay time efficiency is obtained for reconstructed decay times which means that the acceptance is outside of the convolution. If there is any significant change in the decay time mean and resolution between the data and the control sample used for the acceptance study, a shift in the measured lifetime can occur. This could happen for $B^0 \to J/\psi\, K_S^0$ since the acceptance histograms are obtained from a sample of LL+DD exclusive detached stripping line whereas the sample for lifetime measurements is the FullDD one. No significant change in efficiency between LL+DD and FullDD is observed in both MC and data.

The core decay time resolution for $B^0 \to J/\psi\, K_S^0$ and $\Lambda_b^0 \to J/\psi\, \Lambda$ decays is about 50% worse than $B^+ \to J/\psi\, K^+$, $B^0 \to J/\psi\, K^{*0}$ and $B_s^0 \to J/\psi\, \phi$. Since the lower decay time bound is set to 0.3 ps for $B^+ \to J/\psi\, K^+$, $B^0 \to J/\psi\, K^{*0}$ and $B_s^0 \to J/\psi\, \phi$ to suppress the prompt background component, if the resolution is 50% worse then it suggests to push further the lower decay time bound to 0.45 ps for $B^0 \to J/\psi\, K_S^0$ and $\Lambda_b^0 \to J/\psi\, \Lambda$ decay modes.

Table 5.11: Signal and background yields found in data.

Channel	Signal Yield	Background Yield
$B^+ \to J/\psi\, K^+$	$229\,434 \pm 503$	$44\,083 \pm 261$
$B^0 \to J/\psi\, K^{*0}$	$70\,534 \pm 312$	$48\,366 \pm 276$
$B^0 \to J/\psi\, K_S^0$	$17\,045 \pm 174$	$14\,350 \pm 167$
$B_s^0 \to J/\psi\, \phi$	$18\,663 \pm 153$	$22\,514 \pm 165$
$\Lambda_b^0 \to J/\psi\, \Lambda$	$3\,960 \pm 89$	$8\,022 \pm 110$

5.6 Results

The measured signal and background yields obtained from a fit to the mass distribution using the total mass PDF (Eq. 5.18) in the full mass range are summarised in Table 5.11. The mass and decay time projections of the cFit for the five decay modes are shown in Figs. 5.10 to 5.14. The projections of the sFit can be found in Appendix E. The uncorrected measured lifetimes in data and MC using the cFit and sFit techniques are summarised in Table 5.12. The final corrections to the lifetimes are summarised in Table 5.13. The corrected measured lifetimes using the cFit technique and the computed lifetime ratios from the lifetime measurements are summarised in Table 5.14 with their statistical uncertainties. Using Eqs. 5.8 and 5.9, with the lifetimes measured in $B^0 \to J/\psi\, K^{*0}$ and $B^0 \to J/\psi\, K_S^0$, the world-average on the angle $\beta = (21.5^{+0.8}_{-0.7})°$ [76], $\Delta\Gamma_d = -0.029 \pm 0.016\ \mathrm{ps}^{-1}$ and $\Gamma_d = 0.656 \pm 0.003\ \mathrm{ps}^{-1}$ are obtained. Combined, this gives:

$$\frac{\Delta\Gamma_d}{\Gamma_d} = -0.044 \pm 0.025. \tag{5.22}$$

The systematic uncertainties of all these quantities are described in Sec. 5.7.
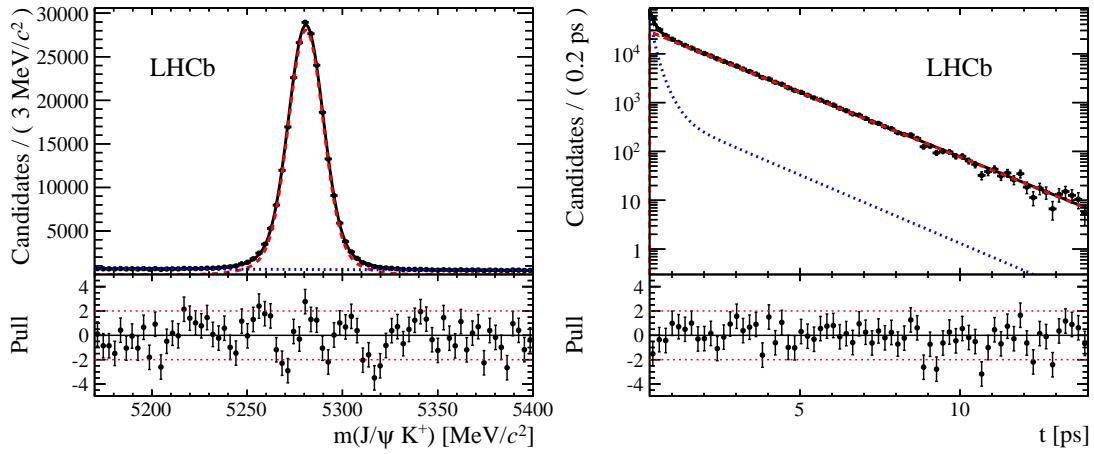

Figure 5.10: Distributions of mass (*left*) and decay time (*right*) for $B^+ \to J/\psi\, K^+$ where the black points are the data, the dashed red line is the signal shape, the dotted blue line is the background shape and the black line is the sum of the two obtained by the cFit technique.

Table 5.12: Uncorrected lifetime results for the five decay modes obtained using the cFit and sFit techniques on data and MC.

Channel	cFit τ data	sFit τ data	cFit τ MC	sFit τ MC
$B^+ \to J/\psi\,K^+$	1.6398 ± 0.0035	1.6399 ± 0.0036	1.6412 ± 0.0017	1.6412 ± 0.0017
$B^0 \to J/\psi\,K^{*0}$	1.5219 ± 0.0061	1.5217 ± 0.0063	1.5226 ± 0.0023	1.5226 ± 0.0023
$B^0_s \to J/\psi\,\phi$	1.4808 ± 0.0114	1.4807 ± 0.0117	1.4307 ± 0.0023	1.4307 ± 0.0023
$B^0 \to J/\psi\,K^0_S$	1.5011 ± 0.0128	1.4993 ± 0.0131	1.5279 ± 0.0028	1.5279 ± 0.0028
$\Lambda^0_b \to J/\psi\,\Lambda$	1.4187 ± 0.0265	1.4208 ± 0.0275	1.3839 ± 0.0036	1.3839 ± 0.0036
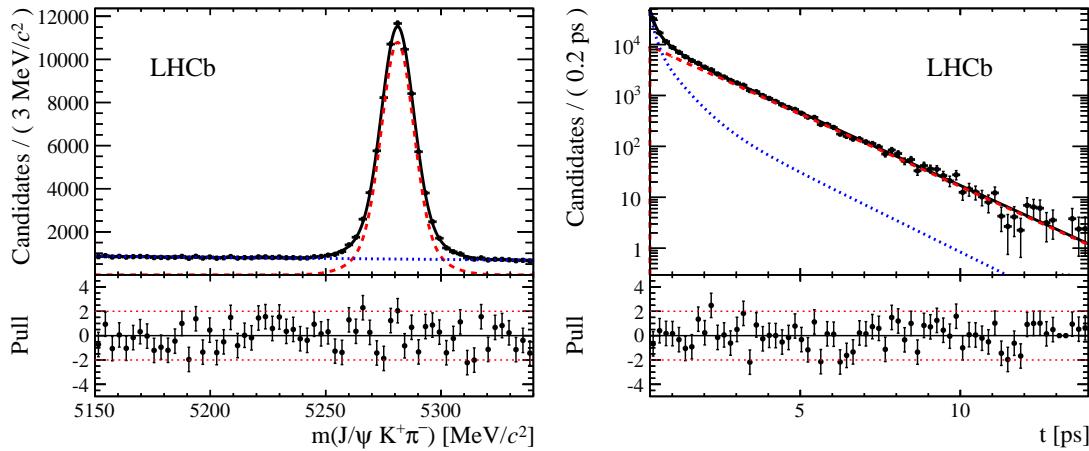
Figure 5.11: Distributions of mass (*left*) and decay time (*right*) for $B^0 \to J/\psi\,K^{*0}$ where the black points are the data, the dashed red line is the signal shape, the dotted blue line is the background shape and the black line is the sum of the two obtained by the cFit technique.
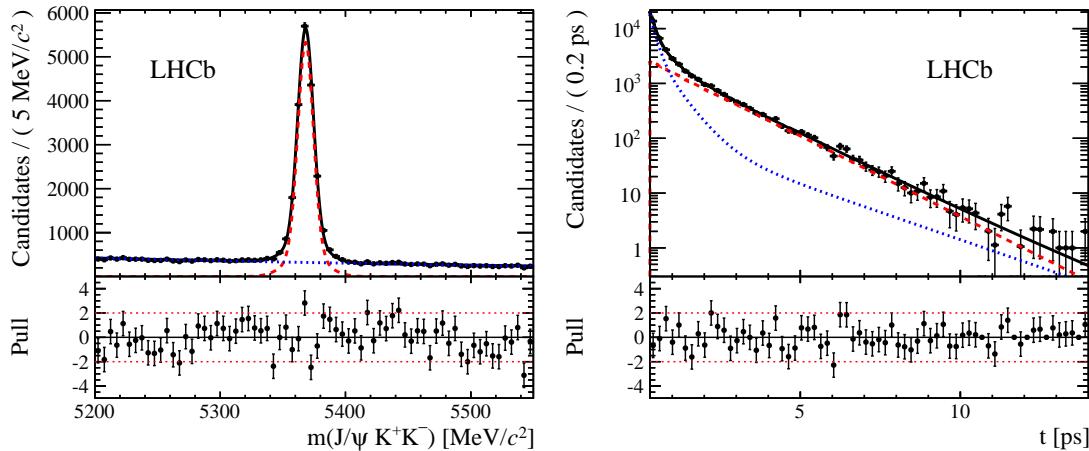
Figure 5.12: Distributions of mass (*left*) and decay time (*right*) for $B^0_s \to J/\psi\,\phi$ where the black points are the data, the dashed red line is the signal shape, the dotted blue line is the background shape and the black line is the sum of the two obtained by the cFit technique.

Table 5.13: Lifetime corrections to be subtracted to measured lifetimes in data.

Channel	Lifetime correction [fs]
$B^+ \to J/\psi\, K^+$	$+3.0 \pm 1.7$
$B^0 \to J/\psi\, K^{*0}$	-1.9 ± 2.3
$B^0_s \to J/\psi\, \phi$	-0.5 ± 2.4
$B^0 \to J/\psi\, K^0_S$	$+2.5 \pm 2.9$
$\Lambda^0_b \to J/\psi\, \Lambda$	$+3.5 \pm 3.7$
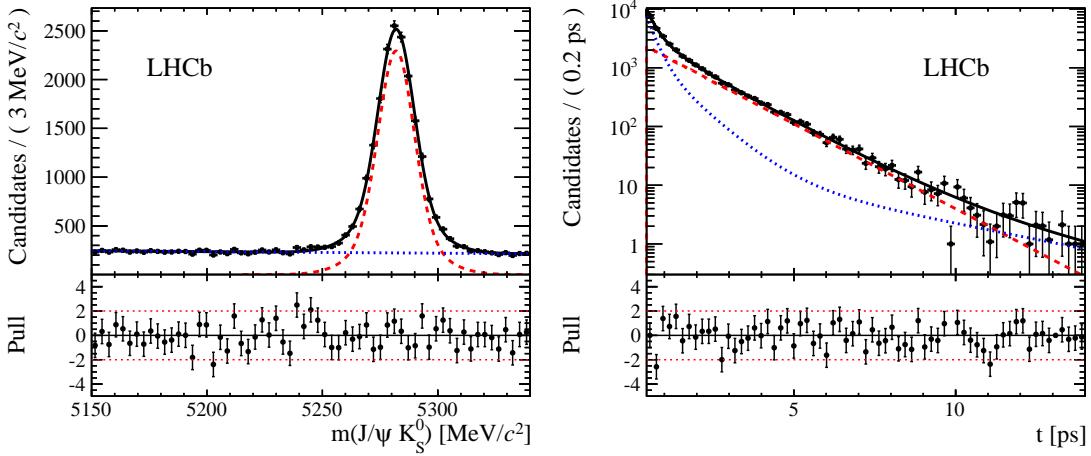
Figure 5.13: Distributions of mass (*left*) and decay time (*right*) for $B^0 \to J/\psi\, K^0_S$ where the black points are the data, the dashed red line is the signal shape, the dotted blue line is the background shape and the black line is the sum of the two obtained by the cFit technique.
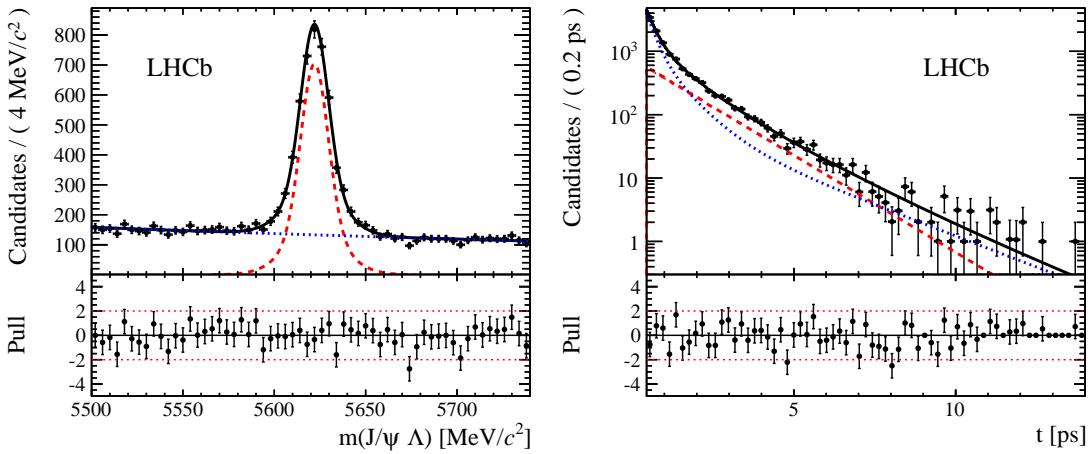
Figure 5.14: Distributions of mass (*left*) and decay time (*right*) for $\Lambda^0_b \to J/\psi\, \Lambda$ where the black points are the data, the dashed red line is the signal shape, the dotted blue line is the background shape and the black line is the sum of the two obtained by the cFit technique.

Table 5.14: Measured lifetimes after corrections for the five decay modes obtained using the cFit technique on data, and lifetime ratios calculated from those measurements.

Quantity	Result
$\tau_{B^+ \to J/\psi K^+}$ [ps]	1.637 ± 0.004
$\tau_{B^0 \to J/\psi K^{*0}}$ [ps]	1.524 ± 0.006
$\tau_{B^0 \to J/\psi K^0_S}$ [ps]	1.499 ± 0.013
$\tau_{\Lambda^0_b \to J/\psi \Lambda}$ [ps]	1.415 ± 0.027
$\tau_{B^0_s \to J/\psi \phi}$ [ps]	1.480 ± 0.011
$\tau_{B^+} / \tau_{B^0 \to J/\psi K^{*0}}$	1.074 ± 0.005
$\tau_{B^0_s} / \tau_{B^0 \to J/\psi K^{*0}}$	0.971 ± 0.009
$\tau_{\Lambda^0_b} / \tau_{B^0 \to J/\psi K^{*0}}$	0.929 ± 0.018
τ_{B^+} / τ_{B^-}	1.002 ± 0.004
$\tau_{\Lambda^0_b} / \tau_{\overline{\Lambda}^0_b}$	0.940 ± 0.035
$\tau_{B^0 \to J/\psi K^{*0}} / \tau_{\overline{B}^0 \to J/\psi \overline{K}^{*0}}$	1.000 ± 0.008

5.7 Systematic uncertainties

5.7.1 VELO reconstruction

The statistical uncertainty on the c parameter of the IP_z efficiency parametrisation is propagated to the measured lifetime as a systematic uncertainty. A second uncertainty on the measurements comes from the MC scale factors. It is assumed that these scale factors can be different between data and MC, but the fact that they different from unity is real, therefore only half of the scale factor difference to unity is propagated to the lifetime as a systematic uncertainty. These two contributions are combined in quadrature and assigned as the systematic uncertainty coming from the VELO track reconstruction.

5.7.2 Simulation statistics

Simulation studies (shown in Figs. 5.5 to 5.9) demonstrate that within statistical uncertainties due to the limited number of MC events, the measured lifetimes are unbiased after all the corrections applied at the different reconstruction and selection steps. Therefore, the statistical uncertainty on the fitted lifetime in MC after full selection is assigned as a systematic uncertainty.

5.7.3 Mass-time correlation

Both the *cFit* and the *sFit* techniques assume that the mass and decay time are uncorrelated. In order to estimate the degree of correlation between mass and decay time and its impact on the lifetime measurements, the parameters of the mass PDF are obtained from fits to the mass distribution in different decay time intervals. The sPlot technique is then applied to the data on the mass distribution of the whole set with the mass parameters determined from a given decay time and the sWeighted decay time distribution is fitted for the lifetime. The systematic uncertainty is obtained from a signal-yield weighted average of the lifetime difference to the nominal result as

$$\sigma_\tau^{\text{mass-time corr.}} = \sqrt{\frac{\sum_i (\tau_i - \tau)^2 N_i^{\text{sig}}}{\sum_i N_i^{\text{sig}}}}. \tag{5.23}$$

5.7.4 Trigger and stripping

The statistical uncertainty of each acceptance histogram is propagated to the measured lifetimes following the procedure described in Sec. 4.3.3, the result is assigned as a systematic uncertainty.

5.7.5 Fit differences

Lifetime differences measured using the *sFit* and the *cFit* techniques are assigned as systematic uncertainties.

5.7.6 Mass modelling

It is observed that two Gaussian functions are not enough to describe the mass distribution properly for high MC statistic samples. An alternative function was found, within LHCb, to be more suitable which uses an exponential of a hyperbola $\left(\exp(-\sqrt{1+x^2})\right)$ for the core and two Crystal Ball-like tails [85] for the sides. This function is called a *double-sided Apollonios* (DSA) function [86]. Using this function to fit the mass distribution of MC events, all parameters are found to be the same for the left and right sides of the DSA function except for the tail parameter n. Therefore, a simplified version of the DSA function is used:

$$A(m;\mu,b,\delta,a,n_l,n_r) \propto \begin{cases} e^{-b\sqrt{1+a^2}}\left(\frac{(n_r\sqrt{1+a^2}-a)/(ba)-a}{(n_r\sqrt{1+a^2}-a)/(ba)-(m-\mu)/\delta}\right)^{n_r} & , \text{ if } \frac{m-\mu}{\delta} > a \\ e^{-b\sqrt{1+(m-\mu)^2/\delta^2}} & , \text{ if } |\frac{m-\mu}{\delta}| \le a \\ e^{-b\sqrt{1+a^2}}\left(\frac{(n_l\sqrt{1+a^2}-a)/(ba)+a}{(n_l\sqrt{1+a^2}-a)/(ba)-(m-\mu)/\delta}\right)^{n_l} & , \text{ if } \frac{m-\mu}{\delta} < -a \end{cases} \quad (5.24)$$

where m is the measured mass, μ the mean, b the parameter that controls the shape of the hyperbola, δ the parameter that can be linked to the RMS of the distribution as $\sigma = \delta\sqrt{\frac{K_1(b)}{bK_0(b)}}$ (where $K_\lambda(b)$ are the Bessel functions of third kind), a the transition point between the core function and the tails and $n_l(n_r)$ the left(right) power-law components of the tails.

Figure 5.15 shows the fit to the mass distribution of MC $B^0 \to J/\psi K_s^0$ events with two Gaussians and the DSA function. The Kolmogorov test χ^2 is significantly better using the DSA function, *i.e.* the χ^2/nDoF changed from about 89 to 1.5. Figure 5.16 shows the fit to the mass distribution for real data for both functions. However, the χ^2/nDoF is only slightly better using the DSA function for real data, *i.e.* changed from 1.1 to 0.9. The difference in obtained lifetimes using these two functions is small for all the decay channels and these differences are assigned as systematic uncertainties.

5.7.7 Decay time resolution modelling

Fits are performed with a single Gaussian resolution of 30 and 100 fs and only changes in lifetime below 0.1 fs are found. Therefore, no systematic uncertainty is assigned.

5.7.8 Peaking backgrounds in the mass distribution

The presence of peaking backgrounds in the mass distribution is investigated using MC datasets of several b hadron decays reconstructed with a given decay mode selection. Also, for some backgrounds, the mass hypothesis of the charged particles is changed and the b-hadron

invariant mass is re-computed to check for peaking structures in the modified invariant mass distribution.

For $B^0 \to J/\psi K_S^0$ and $\Lambda_b^0 \to J/\psi \Lambda$, the only peaking backgrounds that survive the full selection are the *cross-feed backgrounds*, meaning $\Lambda_b^0 \to J/\psi \Lambda$ for $B^0 \to J/\psi K_S^0$ and $B^0 \to J/\psi K_S^0$ for $\Lambda_b^0 \to J/\psi \Lambda$ due to misidentification of particles. The effect on the $B^0 \to J/\psi K_S^0$ and $\Lambda_b^0 \to J/\psi \Lambda$ lifetimes of the cross-feed backgrounds is obtained by performing a simultaneous fit of $B^0 \to J/\psi K_S^0$ and $\Lambda_b^0 \to J/\psi \Lambda$ datasets where the cross-feed components are added. The mass shape for the cross-feeding channels are parametrised from MC using parabola functions and the results can be seen in Fig. 5.17. For the decay time fit, single exponential functions with β factors taken from MC are used to correct decay time effects affecting cross-finding channels.
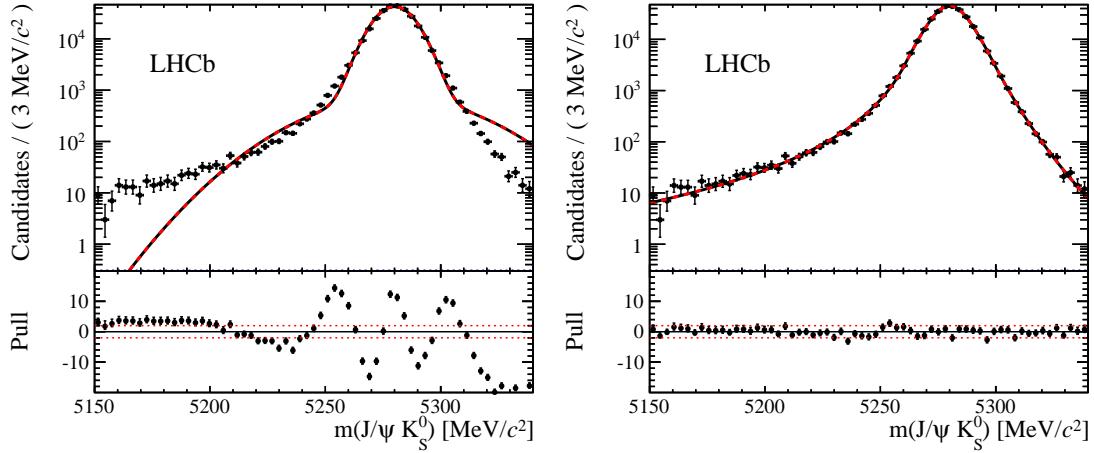
Figure 5.15: Fit to the true-MC mass distribution of $J/\psi K_S^0$ using two Gaussian functions (*left*) and the DSA function (*right*). Note the larger scale for the pull distributions.
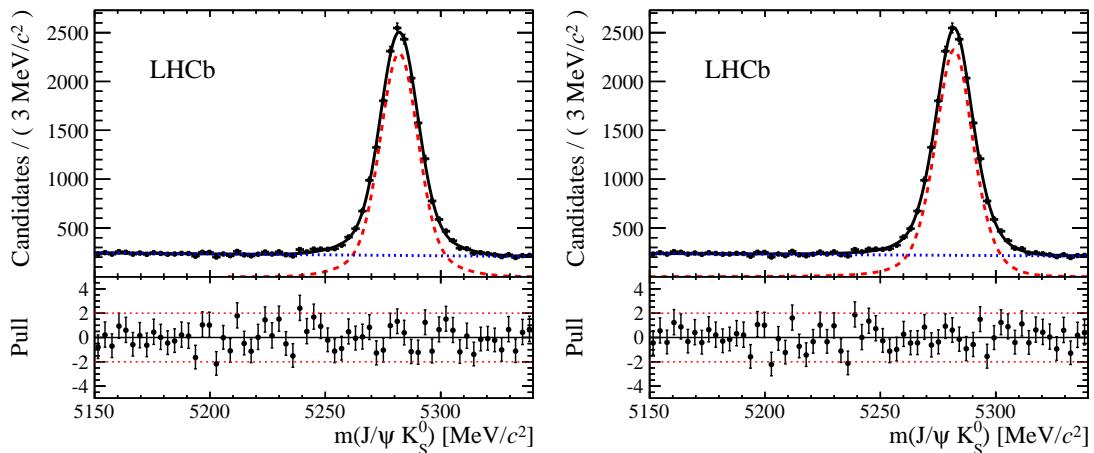
Figure 5.16: Fit to the mass distribution of $J/\psi K_S^0$ found in data using two Gaussian functions (*left*) and the DSA function (*right*).

103

Finally, the ratio of the yield for the cross-feeding channels of $B^0 \to J/\psi\, K_S^0$ over the yield of $B^0 \to J/\psi\, K_S^0$ and the same for $\Lambda_b^0 \to J/\psi\, \Lambda$ are taken from MC. The difference in the measured lifetime from the fit with and without this background component is found to be -0.3 fs for $B^0 \to J/\psi\, K_S^0$ and $+1.1$ fs for $\Lambda_b^0 \to J/\psi\, \Lambda$ which are taken as systematic uncertainties.

For $B_s^0 \to J/\psi\, \phi$, only the misidentified $\Lambda_b \to J/\psi\, pK^-$ decay is found as a peaking background. The mass distribution is parametrised using a Gaussian function and for the decay time, a single exponential. Including this extra component into the fit, the lifetime measured in $B_s^0 \to J/\psi\, \phi$ is changed by 0.4 fs which is taken as a systematic uncertainty.

For $B^+ \to J/\psi\, K^+$ and $B^0 \to J/\psi\, K^{*0}$, no sizeable peaking background is found.
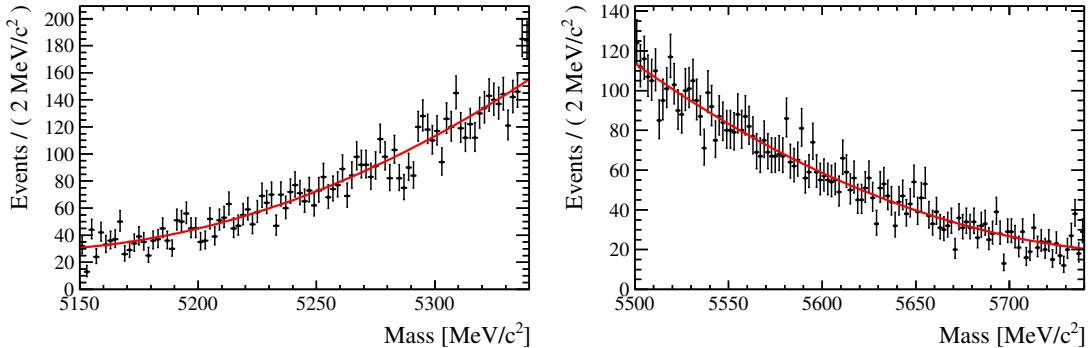
Figure 5.17: Parabola functions are fitted to the simulated mass distributions of $\Lambda_b^0 \to J/\psi\, \Lambda$ reconstructed as $B^0 \to J/\psi\, K_S^0$ (*left*) and $B^0 \to J/\psi\, K_S^0$ reconstructed as $\Lambda_b^0 \to J/\psi\, \Lambda$ (*right*).
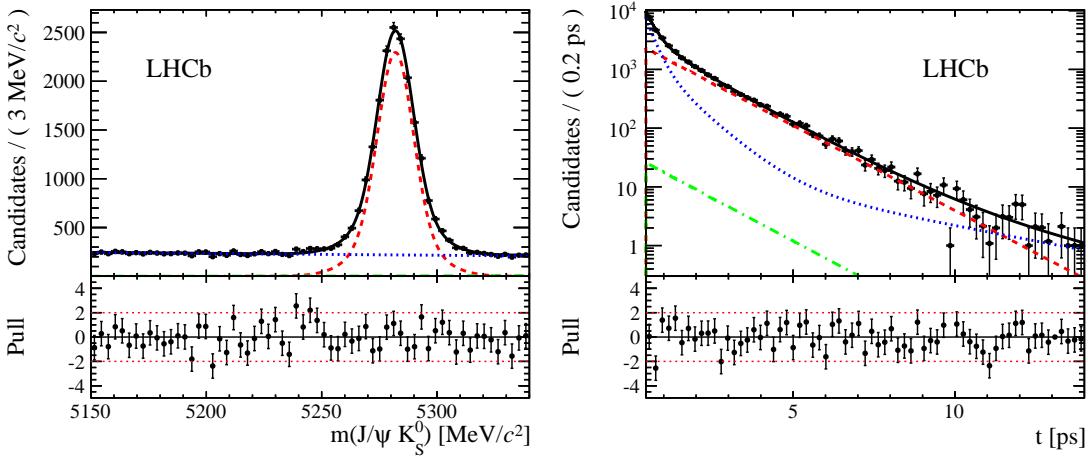

Figure 5.18: Distributions of mass (*left*) and decay time (*right*) for $B^0 \to J/\psi\, K_S^0$ where the black points are the data, the dashed red line is the signal shape, the dotted blue line is the combinatorial background shape, the dotted-dashed green line is the $\Lambda_b^0 \to J/\psi\, \Lambda$ background shape and the black line is the sum of all components by a fit to the distributions using the cFit technique.

5.7.9 Effective lifetime

The fact that in the $B_s^0 \to J/\psi\phi$ system $B_{s,L}^0$ and $B_{s,H}^0$ have different lifetimes and that the measured effective lifetime can be biased if the angular acceptance effect modifies the composition of the system. To get the systematic uncertainty due to the angular acceptance effect, each candidate is reweighted as $1/w_{\text{acc}}$ where w_{acc} is the angular acceptance weight obtained from the 3D angular efficiency map used in the ϕ_s analysis [21]. The lifetime obtained from the weighted fit is taken as a systematic uncertainty. In addition, what is measured is not only $B_s^0 \to J/\psi\phi$ but also $B_s^0 \to J/\psi K^+ K^-$ where $K^+ K^-$ has an invariant mass around the ϕ mass, but do not originate from a ϕ. This means that an extra S-wave component (CP-odd) from $B_s^0 \to J/\psi f_0(980)$ with $f_0(980) \to K^+ K^-$ can be present and might bias the lifetime. The variation in $B_s^0 \to J/\psi\phi$ lifetime observed in MC toy studies including an additional 1% S-wave component [87] is taken as a systematic uncertainty. The angular acceptance and S-wave uncertainties are added in quadrature and assigned as a systematic uncertainty.

5.7.10 Production asymmetry

A b production asymmetry can bias the lifetime measurement for $B^0 \to J/\psi K_S^0$ decays, due to CP violation and slow $B^0 - \overline{B}^0$ oscillations. The effective lifetime is modified as follows in the presence of production asymmetry A_p, assuming no direct and no indirect CP violation and a vanishing $\Delta\Gamma_d$:

$$\Delta\tau_{B^0 \to J/\psi K_S^0} \approx -A_p S_f \Delta m_d \frac{(\Gamma_d^2 - \Delta m_d^2)}{(\Gamma_d^2 + \Delta m_d^2)^2}. \tag{5.25}$$
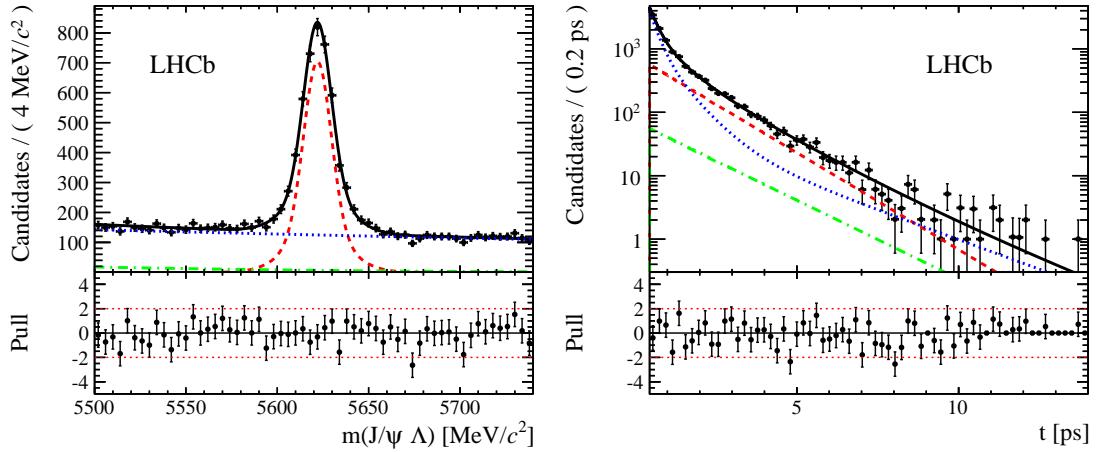
Figure 5.19: Distributions of mass (*left*) and decay time (*right*) for $\Lambda_b^0 \to J/\psi\Lambda$ where the black points are the data, the dashed red line is the signal shape, the dotted blue line is the combinatorial background shape, the dotted-dashed green line is the $B^0 \to J/\psi K_S^0$ background shape and the black line is the sum of all components by a fit to the distributions using the cFit technique.

The detailed calculation of $\Delta\tau_{B^0 \to J/\psi K_S^0}$ can be found in Appendix G. The b-hadron production asymmetry is measured to be $A_{\mathrm{p}} = 0.006 \pm 0.009$ [88]. Since it is compatible with zero, the one standard deviation of A_{p}, *i.e.* 0.009, is used for A_{p}. Using the central value of $S_f = \sin(2\beta) = 0.682 \pm 0.019$ [76], $\Delta m_d = 0.510 \pm 0.004$ ps^{-1} [89], $\Gamma_d = 0.656 \pm 0.003$ ps^{-1} measured in this analysis, a lifetime shift of 1.1 fs is found and assigned as a systematic uncertainty.

The production asymmetry is not a concern for $B_s^0 \to J/\psi\phi$ because the B_s^0 oscillation frequency is much faster [90]. This can be seen from Eq. 5.25, assuming $\Delta m_s >> \Gamma_s$ implies $\Delta\tau_{B^0 \to J/\psi K_S^0} \approx -A_{\mathrm{p}} S_f / \Delta m_s$ which is very small. Therefore, the effect of production asymmetry on this lifetime measurement vanishes. Finally, the $B^0 \to J/\psi K^{*0}$ channel is flavour specific and in this case the production asymmetry cancels in the total untagged rate.

5.7.11 Momentum scale

A simplified test of the effect of incorrect momentum measurement on the lifetime is performed. Comparing the K_S^0 average reconstructed mass with respect to the world average K_S^0 mass, a possible scale of about 0.1% to correct the momentum is found. The lifetime is measured from the ratio Lm/p. Scaling the momentum p by 0.1%(0.5%) and re-computing the mass m, a relative change of about $2 \times 10^{-5} (9 \times 10^{-5})$ on the ratio m/p is found. Therefore, the change on the lifetime is negligible.

5.7.12 Decay length scale

The VELO uncertainty on the z-scale (0.022%) [90] from metrology measurements is directly propagated to the decay length and therefore the lifetime. The shift in measured lifetime is assigned as a systematic uncertainty.

5.7.13 Cross-checks

The following cross-checks were performed, all of which show negligible effect on the lifetime [64]:

- A linear function for the VELO inefficiency parametrisation instead of a parabola function.

- An alternative algorithm to associate a MC reconstructed candidate to the generated particle.

- Random PV association instead of best $\chi^2_{\mathrm{DTF(B+PV)}}/\mathrm{nDoF}$.

- In bins of the b-hadron ϕ, tracks ϕ, spectrometer magnet polarity, assumed b-hadron momentum distribution, J/ψ mass, PV z position, number of tracks from the PV, b-hadron charge and number of PVs.

Table 5.15: Summary of the systematic uncertainties in fs for the five lifetime measurements.

Source	$\tau_{B^+ \to J/\psi K^+}$	$\tau_{B^0 \to J/\psi K^{*0}}$	$\tau_{B^0 \to J/\psi K_S^0}$	$\tau_{\Lambda_b^0 \to J/\psi \Lambda}$	$\tau_{B_s^0 \to J/\psi \phi}$
Statistical uncertainty	3.5	6.1	12.8	26.5	11.4
VELO reconstruction	2.0	2.3	0.9	0.5	2.3
Simulation statistics	1.7	2.3	2.9	3.7	2.4
Mass-time correlation	1.4	1.8	2.1	3.0	0.7
Trigger, stripping eff.	1.1	1.2	2.0	2.0	2.5
Fit differences	0.1	0.2	2.2	2.1	0.4
Mass modelling	0.1	0.2	0.4	0.2	0.5
Peaking background	–	–	0.3	1.1	0.4
Effective lifetime bias	–	–	–	–	1.6
B^0 production asym.	–	–	1.1	–	–
Resolution modelling	–	–	–	–	–
Decay length scale	0.4	0.3	0.3	0.3	0.3
Total systematic	3.2	3.9	4.9	5.8	4.6

5.7.14 Summary of systematic uncertainties on lifetimes

Table 5.15 summarises all the systematic uncertainties and their sources and total systematic uncertainties are calculated for each decay channel assuming the various sources of uncertainty are uncorrelated.

5.7.15 Systematic uncertainties on lifetime ratios and $\Delta\Gamma_d$

For the lifetime ratios $\frac{\tau_{B^+}}{\tau_{B^0}}$, $\frac{\tau_{B_s^0}}{\tau_{B^0}}$, $\frac{\tau_{\Lambda_b^0}}{\tau_{B^0}}$ and $\frac{\Delta\Gamma_d}{\Gamma_d}$, the uncertainties due to the resolution modelling and the decay length scale cancel in the ratio because they are identical for all channels. For the VELO reconstruction, only the systematic uncertainties related to the MC scale factors survive in the ratio. For the two different fits, the systematic uncertainty is obtained from the difference in lifetime ratio taken from lifetimes using sFit and cFit separately as $|(\tau_i/\tau_j)_{\text{sFit}} - (\tau_i/\tau_j)_{\text{cFit}}|$. All other uncertainties are directly propagated to the ratios from the lifetime systematic uncertainties under the assumption that they are uncorrelated.

For the CPT lifetime ratios $\frac{\tau_{B^+}}{\tau_{B^-}}$, $\frac{\tau_{B^0}}{\tau_{\overline{B}^0}}$, $\frac{\tau_{\Lambda_b^0}}{\tau_{\overline{\Lambda}_b^0}}$, in addition to the considerations described above, the MC scale factors, the mass-time correlation and the decay time acceptances cancel in the lifetime ratio. However, a new contribution from the b-production asymmetry arises in the $\frac{\tau_{B^0}}{\tau_{\overline{B}^0}}$ ratio. Assuming no direct and no indirect CP violation and a vanishing $\Delta\Gamma_d$, the shift is given by

$$\Delta\left(\frac{\tau_{B^0}}{\tau_{\overline{B}^0}}\right) \approx -4 A_{\text{p}} \frac{\Gamma_d^2 \Delta m_d^2}{(\Gamma_d^2 + \Delta m_d^2)^2}. \tag{5.26}$$

Using $A_{\text{p}} = 0.009$, $\Delta m_d = 0.510 \pm 0.004$ ps^{-1} [89] and $\Gamma_d = 0.656 \pm 0.003$ ps^{-1}, the lifetime ratio $\frac{\tau_{B^0}}{\tau_{\overline{B}^0}}$ is shifted by 8.5×10^{-3} and is assigned as a systematic uncertainty.

Table 5.16: Summary of the systematic uncertainties for the six lifetime ratios and $\Delta\Gamma_d/\Gamma_d$.

Source	τ_{B^+}/τ_{B^0}	$\tau^{\text{eff}}_{B^0_s}/\tau_{B^0}$	$\tau_{\Lambda^0_b}/\tau_{B^0}$	τ_{B^+}/τ_{B^-}	$\tau_{\Lambda^0_b}/\tau_{\overline{\Lambda}^0_b}$	$\tau_{B^0}/\tau_{\overline{B}^0}$	$\Delta\Gamma_d/\Gamma_d$
Statistical uncertainty	5.0	8.5	18.0	4.0	35.0	8.0	25.0
VELO reconstruction	1.6	1.7	1.1	–	–	–	3.1
Simulation statistics	2.0	2.2	2.8	2.1	5.3	3.0	6.3
Mass-time correlation	1.6	1.2	2.3	–	–	–	4.7
Trigger, stripping eff.	1.1	1.8	1.5	–	–	–	4.0
Fit differences	0.3	0.2	1.5	0.2	3.0	1.4	3.3
Mass modelling	0.2	0.4	0.2	0.1	0.2	0.2	0.8
Peaking background	–	0.3	0.7	–	–	–	0.5
Effective lifetime bias	–	1.0	–	–	–	–	–
B^0 production asym.	–	–	–	–	–	8.5	1.9
Total systematic	3.3	3.8	4.5	2.1	6.0	9.1	10.7

Finally, a wrong charge assignment can bias the *CPT* ratio if the true lifetime ratio is not unity. For a $\frac{\tau_{B^+}}{\tau_{B^-}}$ different from unity by 1%, a wrong charge assignment of 1% does not introduce any significant shift in the lifetime ratio. For the other two ratios, a double charge misassignment is required which renders this effect completely negligible.

Table 5.16 summarises all the systematic uncertainties with their sources. Total systematic uncertainties are calculated for each ratio assuming uncorrelated uncertainties.

Table 5.17: Lifetime measured in the decay modes $B^+ \to J/\psi\,K^+$, $B^0 \to J/\psi\,K^{*0}$, $B_s^0 \to J/\psi\,\phi$, $B^0 \to J/\psi\,K_S^0$ and $\Lambda_b^0 \to J/\psi\,\Lambda$ with their statistical and systematic uncertainties, respectively.

Channel	Lifetime result τ [ps]
$B^+ \to J/\psi\,K^+$	$1.637 \pm 0.004\,\text{(stat)} \pm 0.003\,\text{(syst)}$
$B^0 \to J/\psi\,K^{*0}$	$1.524 \pm 0.006\,\text{(stat)} \pm 0.004\,\text{(syst)}$
$B^0 \to J/\psi\,K_S^0$	$1.499 \pm 0.013\,\text{(stat)} \pm 0.005\,\text{(syst)}$
$\Lambda_b^0 \to J/\psi\,\Lambda$	$1.415 \pm 0.027\,\text{(stat)} \pm 0.006\,\text{(syst)}$
$B_s^0 \to J/\psi\,\phi$	$1.480 \pm 0.011\,\text{(stat)} \pm 0.005\,\text{(syst)}$

Table 5.18: Lifetime ratios $\frac{\tau_{B^+}}{\tau_{B^0}}, \frac{\tau_{B_s^0}}{\tau_{B^0}}, \frac{\tau_{\Lambda_b^0}}{\tau_{B^0}}$ and CPT lifetime ratios $\frac{\tau_{B^+}}{\tau_{B^-}}, \frac{\tau_{B^0}}{\tau_{\overline{B}^0}}, \frac{\tau_{\Lambda_b^0}}{\tau_{\overline{\Lambda}_b^0}}$ results with their statistical and systematic uncertainties, respectively.

Quantity	Result
$\tau_{B^+}/\tau_{B^0 \to J/\psi\,K^{*0}}$	$1.074 \pm 0.005\,\text{(stat)} \pm 0.003\,\text{(syst)}$
$\tau_{B_s^0}/\tau_{B^0 \to J/\psi\,K^{*0}}$	$0.971 \pm 0.009\,\text{(stat)} \pm 0.004\,\text{(syst)}$
$\tau_{\Lambda_b^0}/\tau_{B^0 \to J/\psi\,K^{*0}}$	$0.929 \pm 0.018\,\text{(stat)} \pm 0.004\,\text{(syst)}$
τ_{B^+}/τ_{B^-}	$1.002 \pm 0.004\,\text{(stat)} \pm 0.002\,\text{(syst)}$
$\tau_{\Lambda_b^0}/\tau_{\overline{\Lambda}_b^0}$	$0.940 \pm 0.035\,\text{(stat)} \pm 0.006\,\text{(syst)}$
$\tau_{B^0 \to J/\psi\,K^{*0}}/\tau_{\overline{B}^0 \to J/\psi\,\overline{K}^{*0}}$	$1.000 \pm 0.008\,\text{(stat)} \pm 0.009\,\text{(syst)}$

5.8 Summary

Lifetime measurements in the decays $B^+ \to J/\psi\,K^+$, $B^0 \to J/\psi\,K^{*0}$, $B_s^0 \to J/\psi\,\phi$, $B^0 \to J/\psi\,K_S^0$ and $\Lambda_b^0 \to J/\psi\,\Lambda$ using 1.0 fb^{-1} of data collected in 2011 are presented. These results are the most-precise to date in these decay modes. They are also the world best measurements of the b-hadron lifetimes with the exception of the Λ_b^0 lifetime where the best measurement was performed by LHCb using the $\Lambda_b^0 \to J/\psi\,pK^-$ decay mode. All the measurements are compatible with current world-averages. The effective lifetime computed from the CP violation parameters and angular amplitudes obtained in the analysis of CP violation in $B_s^0 \to J/\psi\,\phi$ is given by $1.466 \pm 0.010\,\text{(stat)} \pm 0.014\,\text{(syst)}$ ps [21]. The overlap between the ϕ_s analysis dataset and the one of this analysis is about 60% which leads to a statistical uncertainty of about 12 fs. The two results are therefore fully compatible. The lifetime ratios $\frac{\tau_{B^+}}{\tau_{B^0}}, \frac{\tau_{B_s^0}}{\tau_{B^0}}, \frac{\tau_{\Lambda_b^0}}{\tau_{B^0}}$ and CPT lifetime ratios $\frac{\tau_{B^+}}{\tau_{B^-}}, \frac{\tau_{B^0}}{\tau_{\overline{B}^0}}, \frac{\tau_{\Lambda_b^0}}{\tau_{\overline{\Lambda}_b^0}}$ are measured. The lifetime ratios $\frac{\tau_{B^+}}{\tau_{B^0}}, \frac{\tau_{B_s^0}}{\tau_{B^0}}$ are also the most precise measurements to date. The first three lifetime ratios are also compatible with current world-averages and theoretical predictions. The CPT lifetime ratios are the first measurements of these quantities and no sign of CPT violation is observed. Finally, the decay width difference $\Delta\Gamma_d$ over the average decay width Γ_d of the B^0 system is measured to be $\frac{\Delta\Gamma_d}{\Gamma_d} = -0.044 \pm 0.025\,\text{(stat)} \pm 0.011\,\text{(syst)}$ which is compatible with the world-average [76] and the theoretical predications of [80,81]. These results are published in [75].

6 Conclusion

Work on several aspects of the calibration and monitoring of the LHCb tracking system are presented in this thesis. Starting from the base algorithms already available to perform the TELL1 boards calibration, these algorithms have been improved and a consistent software has been written to perform the various steps of the calibration process. This allows the parameters used for the signal processing by the TELL1 boards to be monitored as a function of time and discovers possible new effects on the signals sent by the front-end chip of the IT and TT due to the content of the header part of the signal chain. Changes in the front-end chip configuration and the way the data samples are used to perform the calibration here been revisited and an improved header correction method has been developed. After implementing these changes, the parameters of the IT and TT TELL1 boards were calibrated and found to be stable as a function of time. They are monitored in a daily basis.

The monitoring of the IT and TT hit efficiencies have been significantly improved by changing several parts of the algorithm used is their calculation and using clean samples of J/ψ mesons decaying to a muon pair. Hit efficiencies of the IT and TT were found to be better than 99% which is required for excellent reconstruction of high multiplicity b-hadron decays. Hit resolutions and signal-to-noise ratios have been measured, the results are in good agreement with expectations except in the case of the TT where significantly larger misalignments than expected were recorded. No visible degradation of the IT and TT performances have been observed after more than two years of intensive data taking.

A novel approach has been proposed to align the LHCb tracking system in the vertical direction exploiting the presence of insensitive regions in the tracking system perpendicular to the vertical axis. The method relies on special runs taken at the beginning of each year where the magnetic field of the spectrometer dipole was turned off. Using simulation, the method has been validated and applied to real data. A precision better than 200 μm on the vertical positions was obtained for the IT boxes, the TT box and the OT stations. Results have been checked by measuring, for example, the vertical active lengths of silicon sensors and distances between gaps present in the vertical distribution of hits due to the inactive regions of the tracking system. Some unexpected results have been obtained, however, mainly in the case of the OT, and a further investigation of these issues is suggested.

After these various and successful contributions to the calibration and the monitoring of the LHCb tracking system, the second part of this thesis has been devoted to the measurements of the lifetime of various b hadrons. For this purpose, reconstruction efficiencies as a function of b-hadron decay times has to be understood. In this thesis, the focus was put on the understanding and the measurement of the efficiency drops appearing at small decay times due to the selection applied at the trigger and pre-selection levels to suppress uninteresting physics processes. New methods are proposed to measure these efficiency dependences as a function of decay time using real data and were applied successfully to the measurements of the b-hadron lifetimes using the 1.0 fb^{-1} of data collected in 2011 by LHCb for five decay modes: $B^+ \to J/\psi K^+$, $B^0 \to J/\psi K^{*0}$, $B^0 \to J/\psi K_S^0$, $B_s^0 \to J/\psi \phi$ and $\Lambda_b^0 \to J/\psi \Lambda$. The lifetimes in these decay modes are measured to be:

$$\tau_{B^+ \to J/\psi K^+} = 1.637 \pm 0.004 \,(\text{stat}) \pm 0.003 \,(\text{syst}) \,\text{ps},$$

$$\tau_{B^0 \to J/\psi K^{*0}} = 1.524 \pm 0.006 \,(\text{stat}) \pm 0.004 \,(\text{syst}) \,\text{ps},$$

$$\tau_{B^0 \to J/\psi K_S^0} = 1.415 \pm 0.027 \,(\text{stat}) \pm 0.006 \,(\text{syst}) \,\text{ps},$$

$$\tau_{B_s^0 \to J/\psi \phi} = 1.499 \pm 0.013 \,(\text{stat}) \pm 0.005 \,(\text{syst}) \,\text{ps},$$

$$\tau_{\Lambda_b^0 \to J/\psi \Lambda} = 1.480 \pm 0.011 \,(\text{stat}) \pm 0.005 \,(\text{syst}) \,\text{ps}.$$

These measurements are the world's best results of these quantities and they are all compatible with theoretical predictions and current world averages. From the measurements of lifetimes in the $B^0 \to J/\psi K^{*0}$ and $B^0 \to J/\psi K_S^0$ decay modes, the ratio of the decay-width difference, $\Delta\Gamma_d$, to the average decay width, Γ_d, for the $B^0 - \overline{B}^0$ system is measured to be

$$\frac{\Delta\Gamma_d}{\Gamma_d} = -0.044 \pm 0.025 \,(\text{stat}) \pm 0.011 \,(\text{syst}),$$

which is also compatible with world averages and theoretical predictions.

A Silicon Tracker performance plots
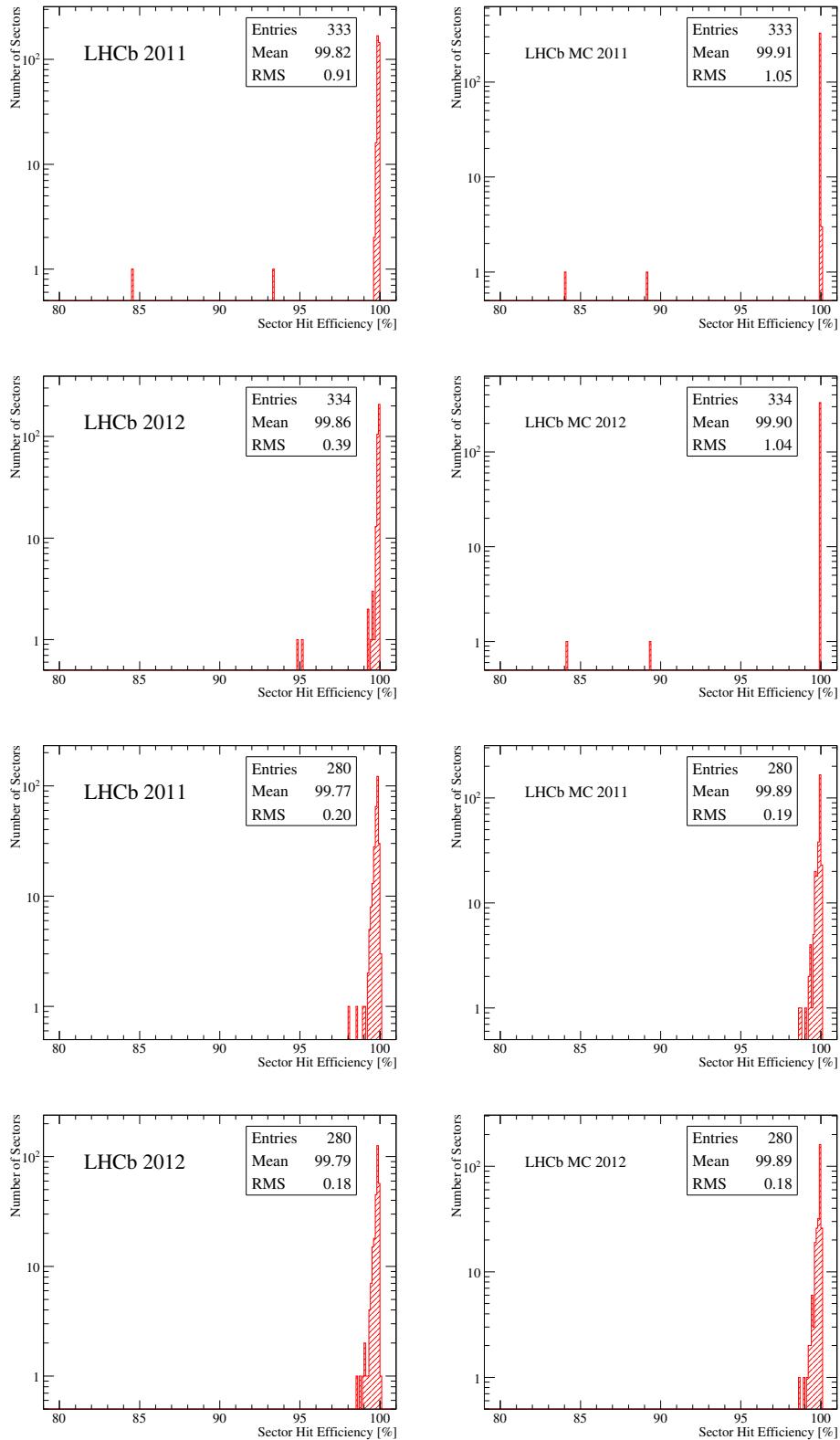
Figure A.1: Sectors hit efficiency measured using 2011 and 2012 real data and MC samples for IT (*four top plots*) and TT (*four bottom plots*).
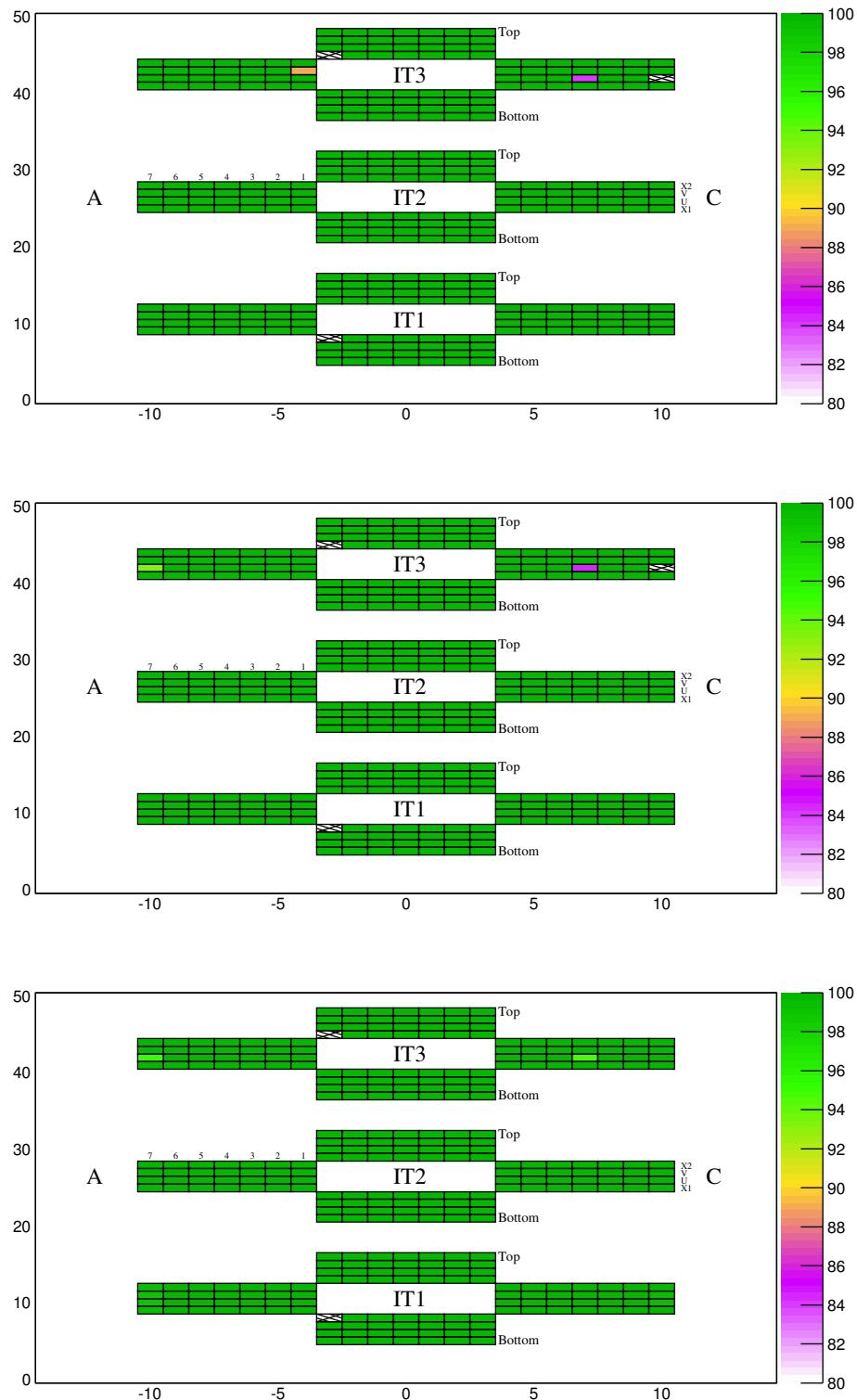
Figure A.2: 2D map of sectors hit efficiencies measured using 2011 MC (*top*), 2011 (*middle*) and 2012 (*bottom*) real data samples for IT.
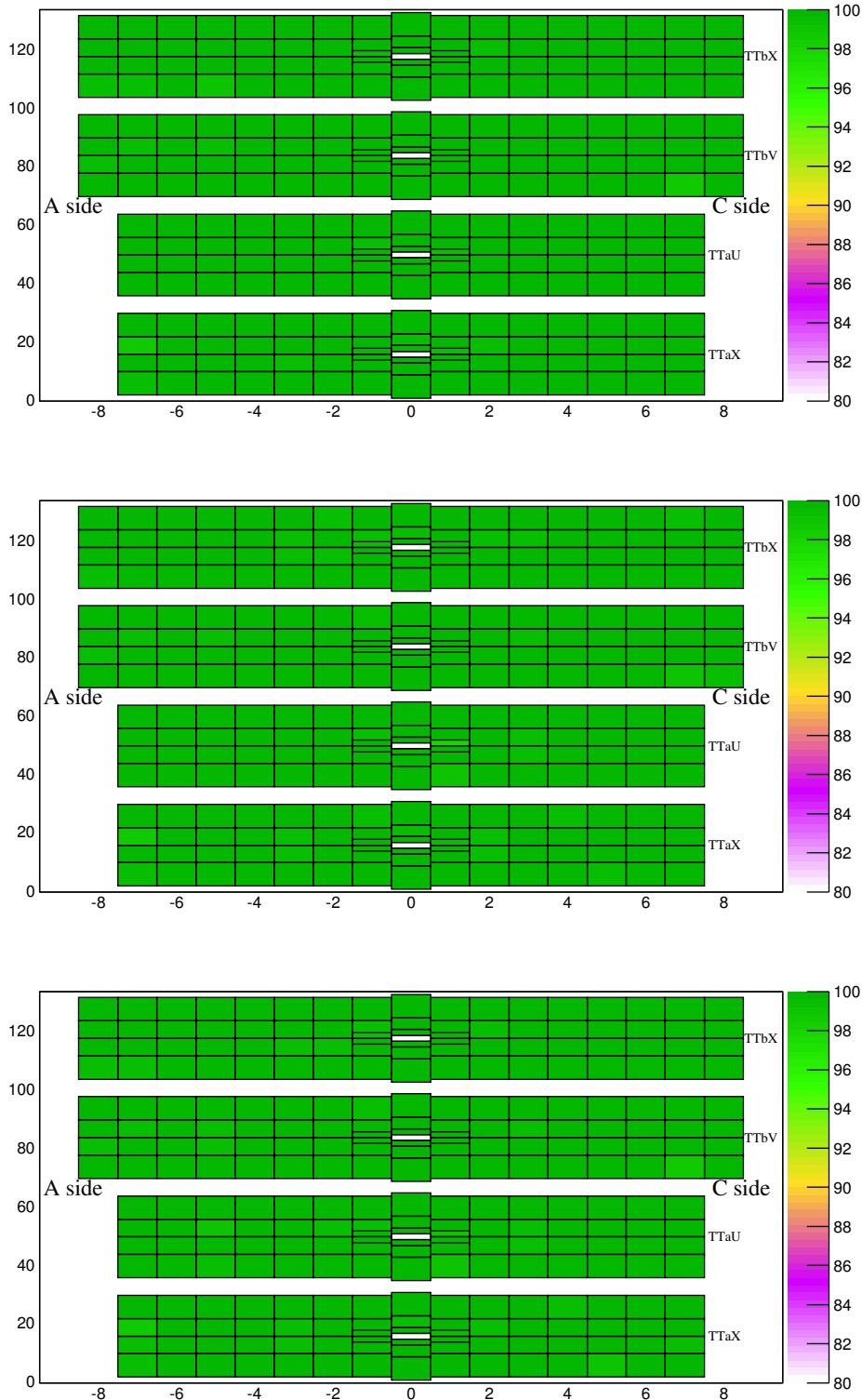
Figure A.3: 2D map of sectors hit efficiencies measured using 2011 MC (*top*), 2011 (*middle*) and 2012 (*bottom*) real data samples for TT.
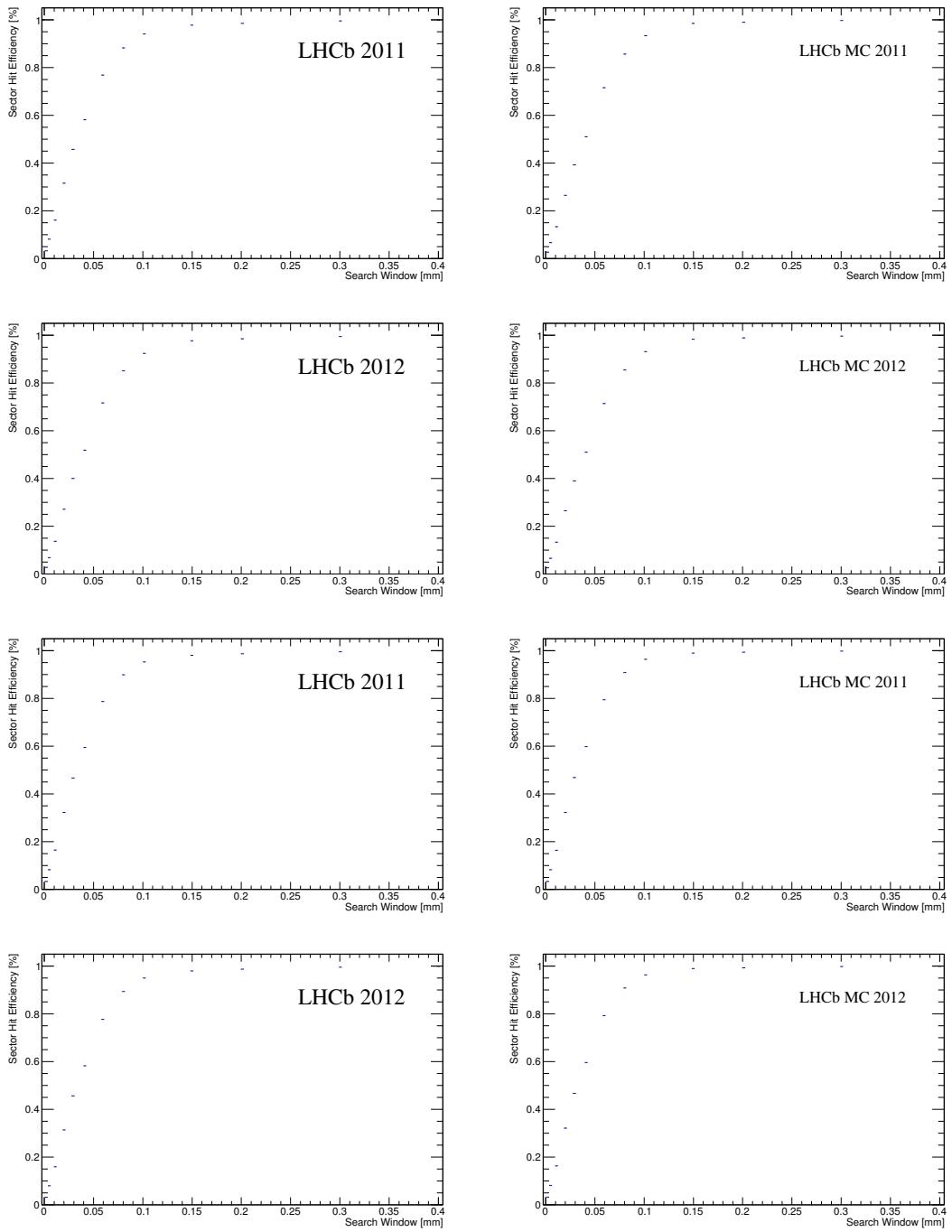
Figure A.4: Hit efficiency as a function of the search window for a random sector measured using 2011 and 2012 real data and MC samples for IT (*four top plots*) and TT (*four bottom plots*).

Figure A.5: Hit resolution measured using 2011 and 2012 real data and MC samples for IT (*four top plots*) and TT (*four bottom plots*).
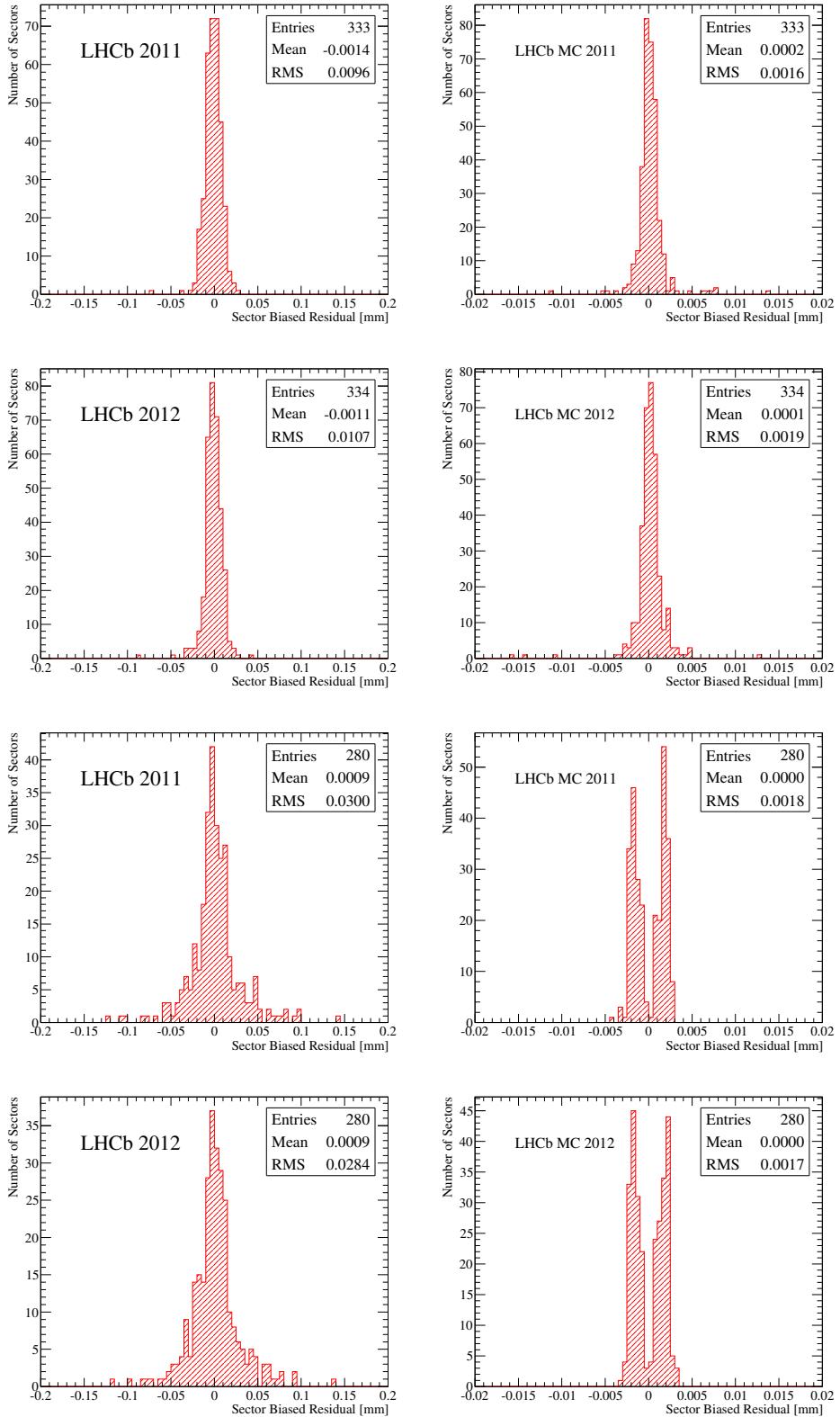
Figure A.6: Sectors biased resolution measured using 2011 and 2012 real data and MC samples for IT (*four top plots*) and TT (*four bottom plots*).

Figure A.7: 2D map of sectors biased resolutions measured using 2011 MC (*top*), 2011 (*middle*) and 2012 (*bottom*) real data samples for IT.
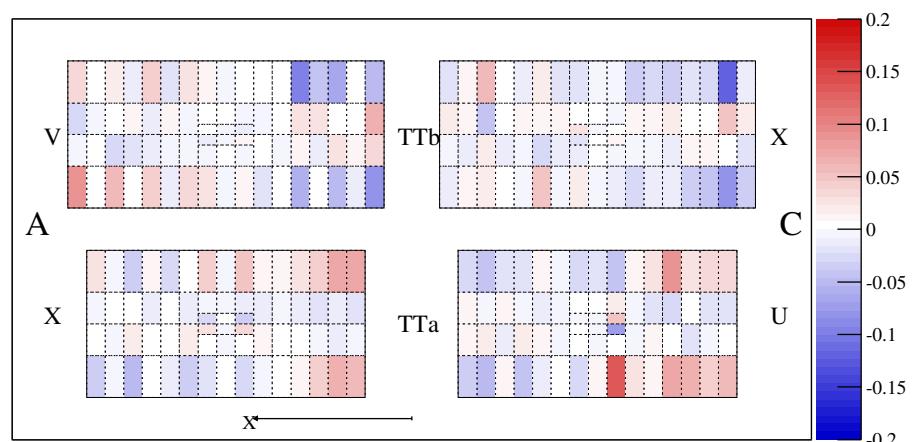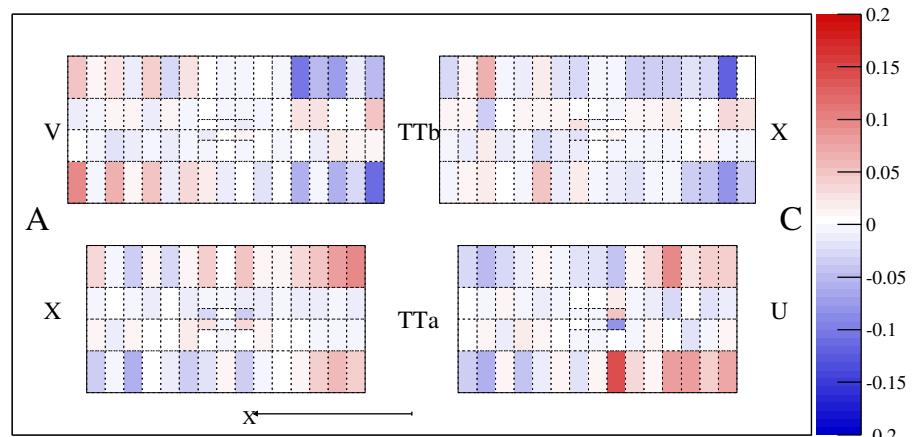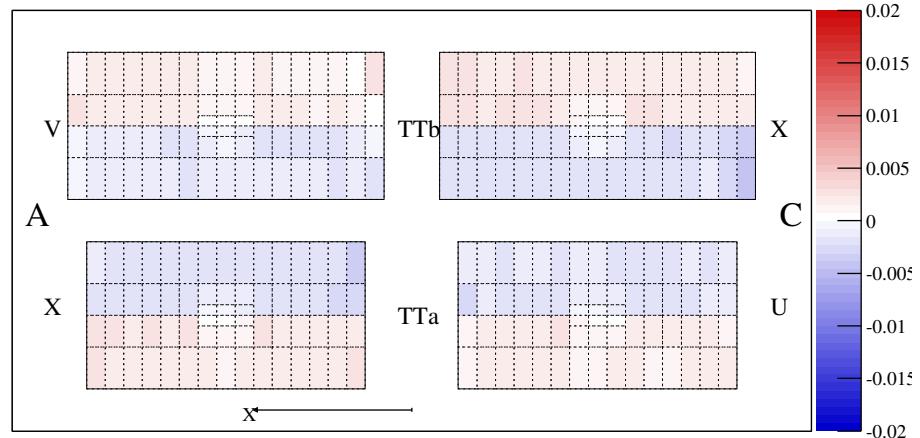
Figure A.8: 2D map of sectors biased resolutions measured using 2011 MC (*top*), 2011 (*middle*) and 2012 (*bottom*) real data samples for TT.

Figure A.9: Signal-over-noise ratio measured using 2011 and 2012 real data and MC samples for IT (*four top plots*) and TT (*four bottom plots*).
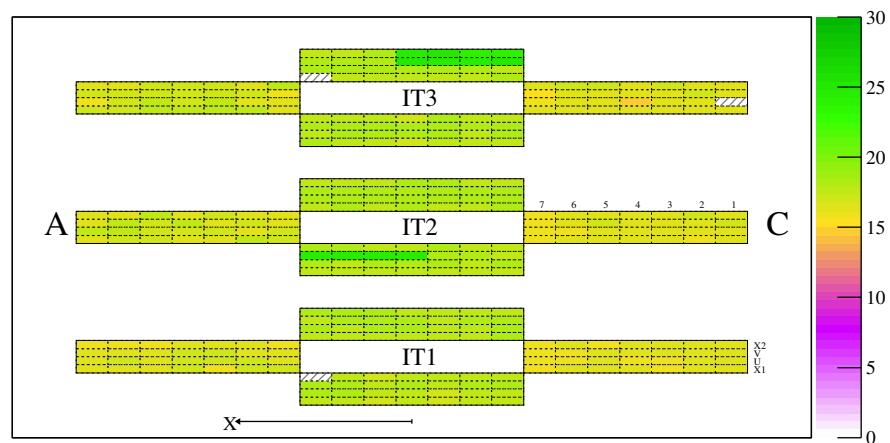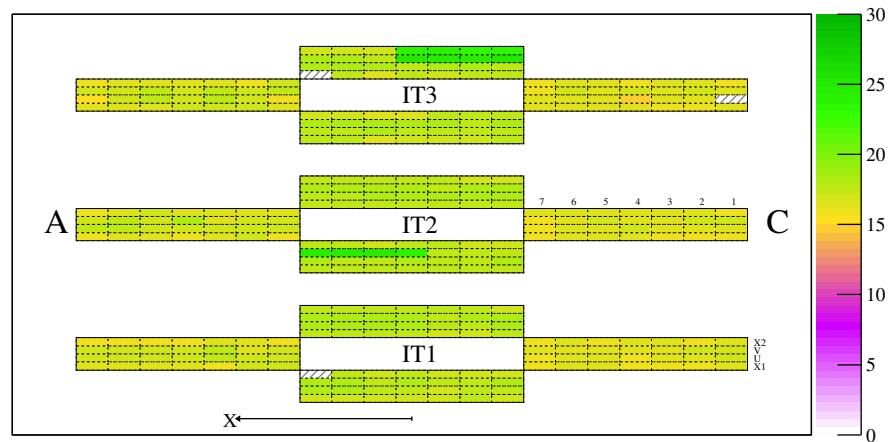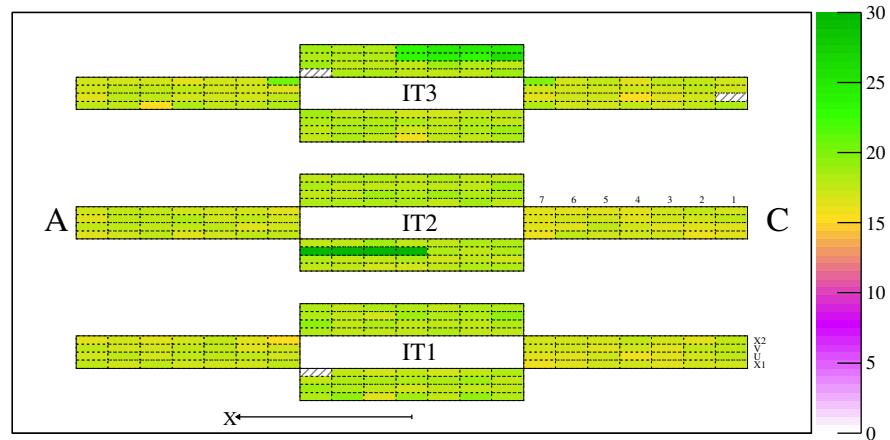
Figure A.10: 2D map of signal-to-noise ratios measured using 2011 MC (*top*), 2011 (*middle*) and 2012 (*bottom*) real data samples for IT.

Figure A.11: 2D map of signal-to-noise ratios measured using 2011 MC (*top*), 2011 (*middle*) and 2012 (*bottom*) real data samples for TT.

B Vertical alignment plots
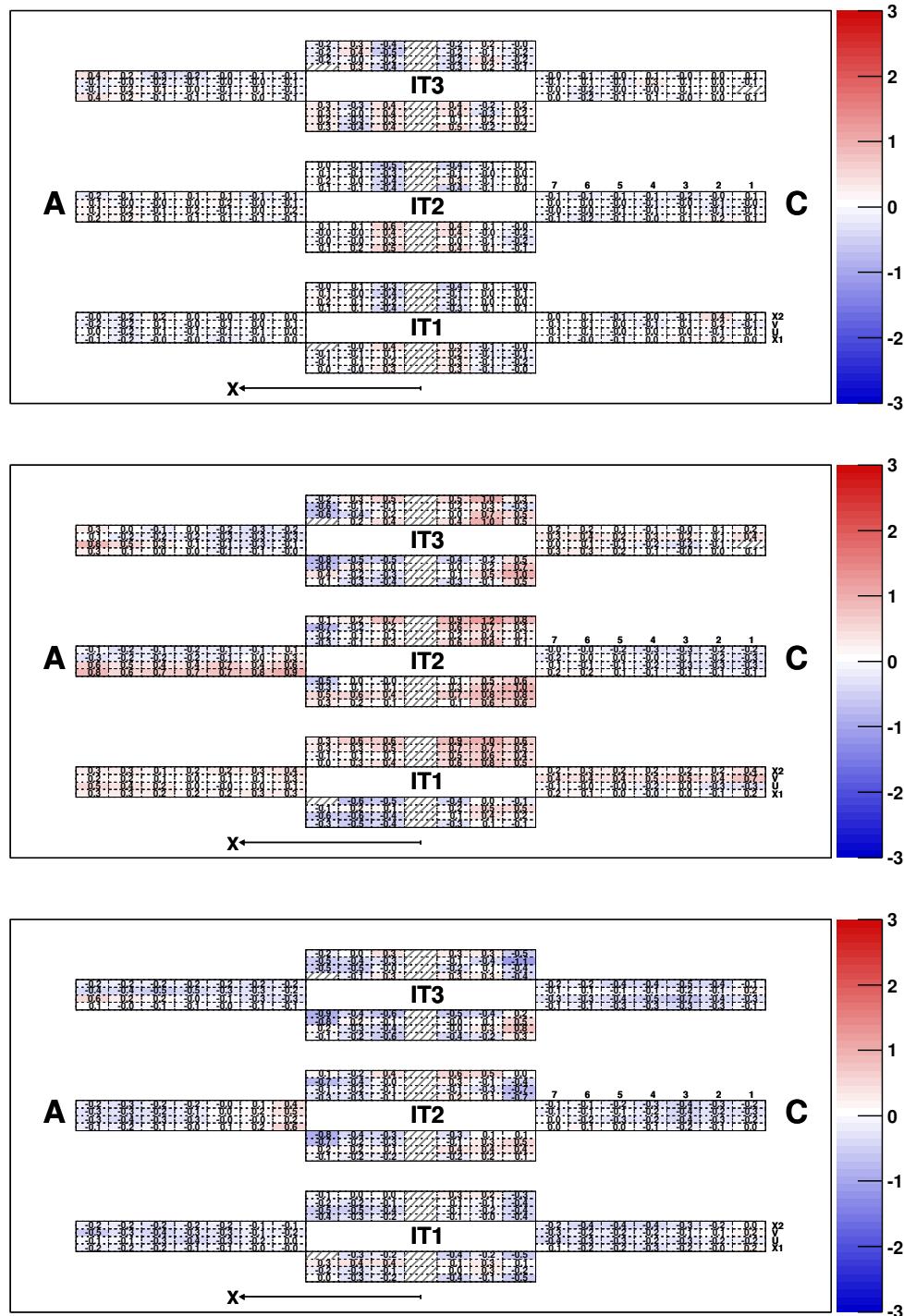
Figure B.1: 2D map of *y* positions measured using 2011 MC (*top*), 2011 (*middle*) and 2012 (*bottom*) real data samples for IT sectors.
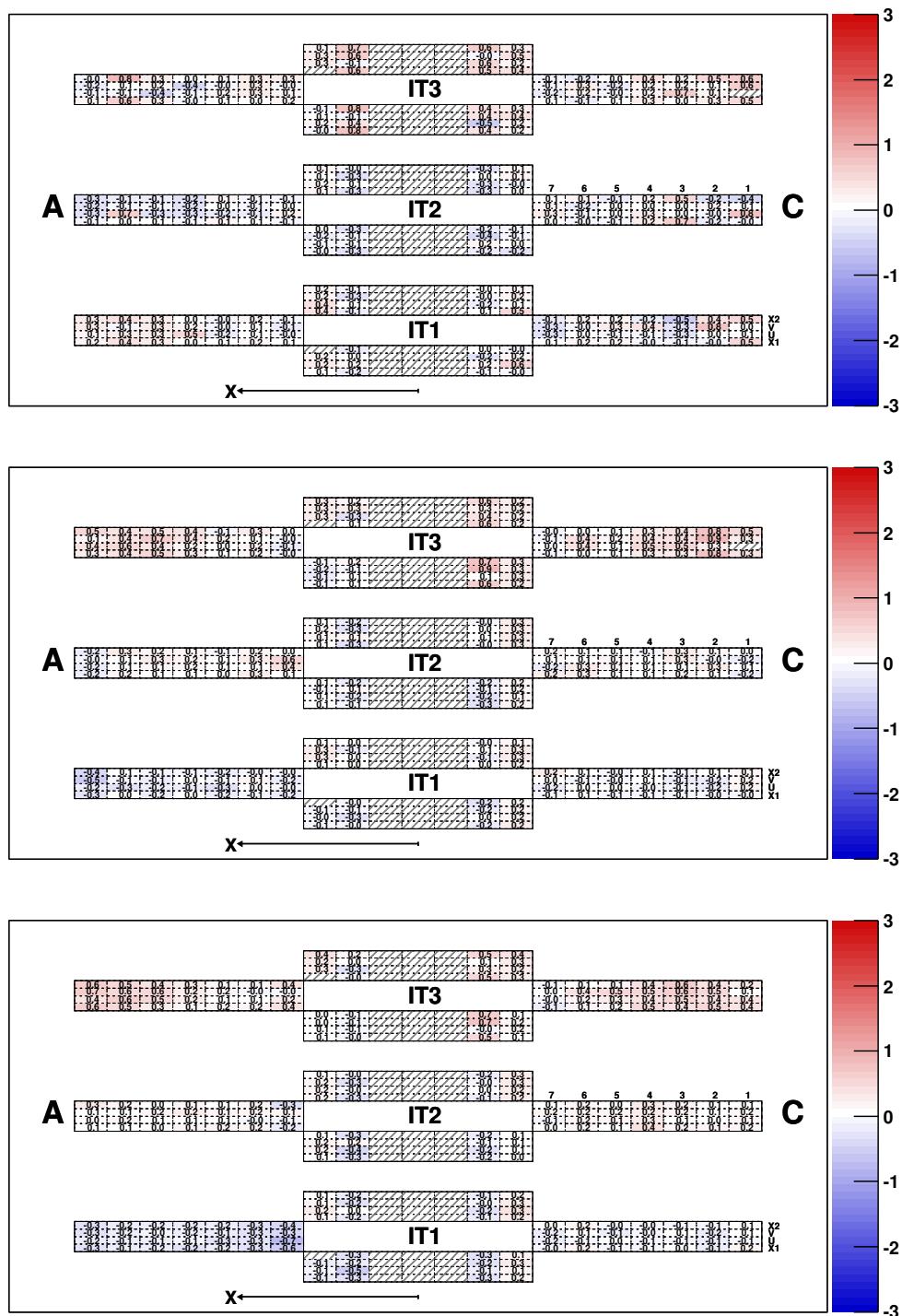
Figure B.2: 2D map of active lengths measured using 2011 MC (*top*), 2011 (*middle*) and 2012 (*bottom*) real data samples for IT sectors.
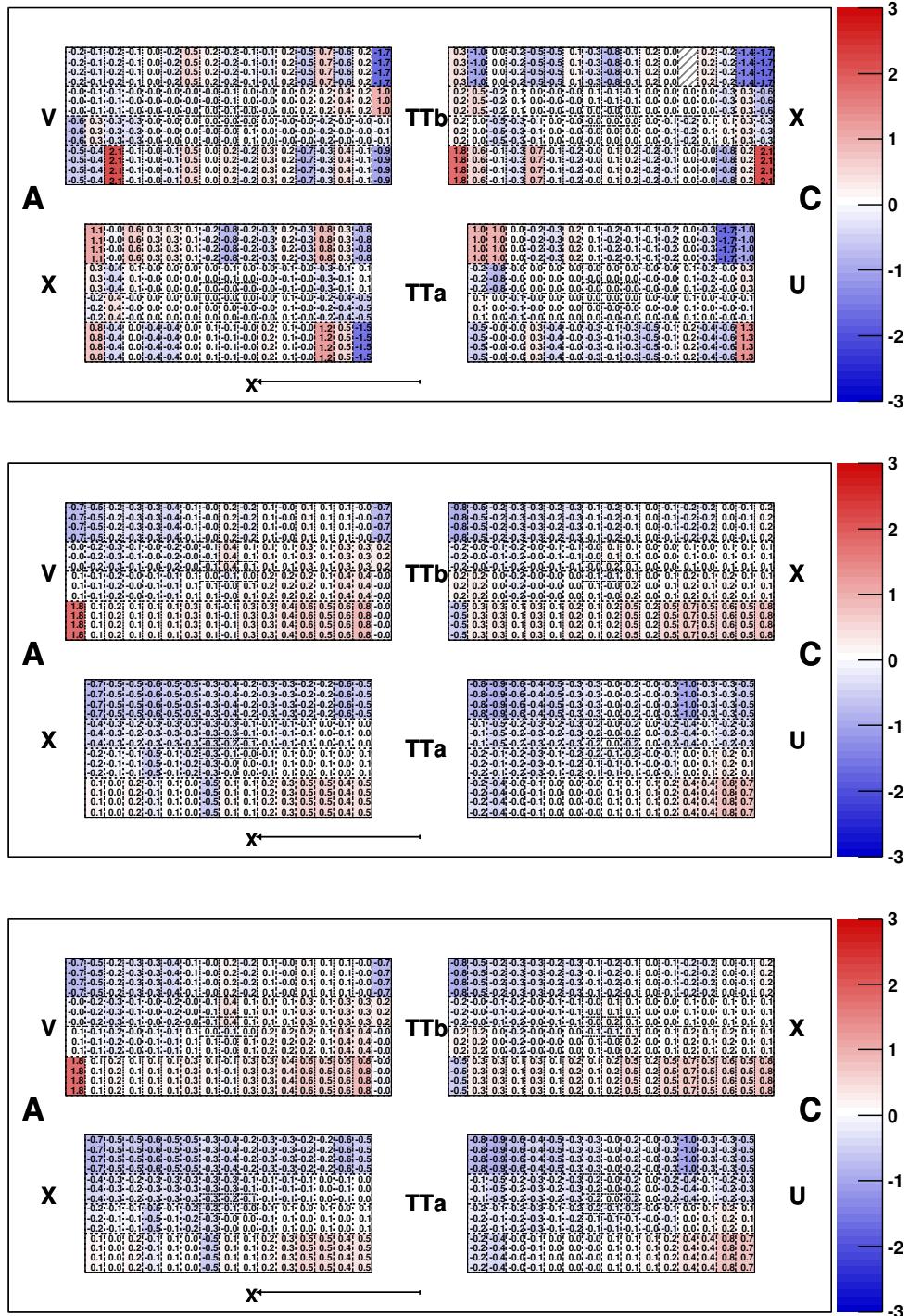
Figure B.3: 2D map of *y* positions measured using 2011 MC (*top*), 2011 (*middle*) and 2012 (*bottom*) real data samples for TT sectors.
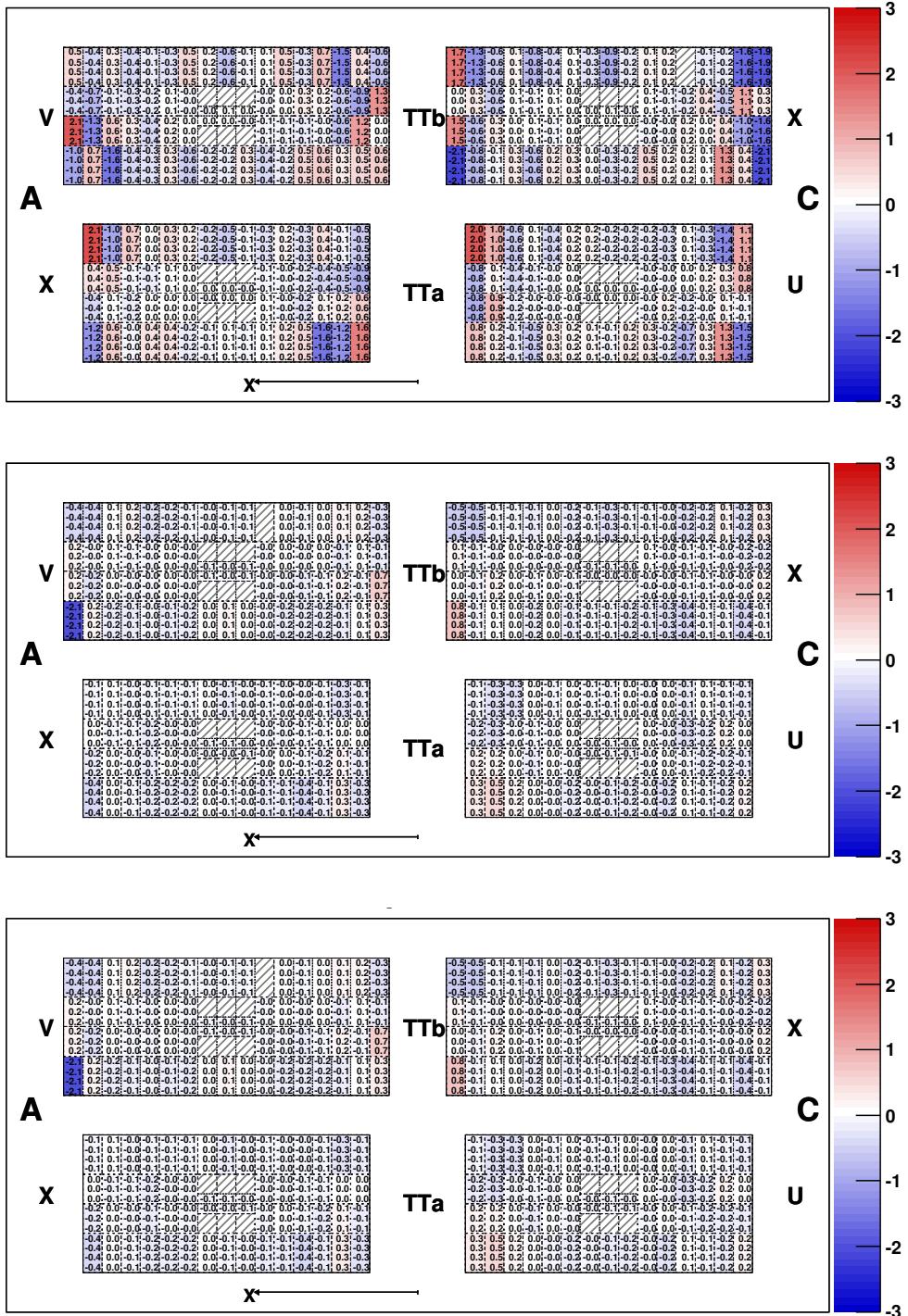
Figure B.4: 2D map of active lengths measured using 2011 MC (*top*), 2011 (*middle*) and 2012 (*bottom*) real data samples for TT sectors.
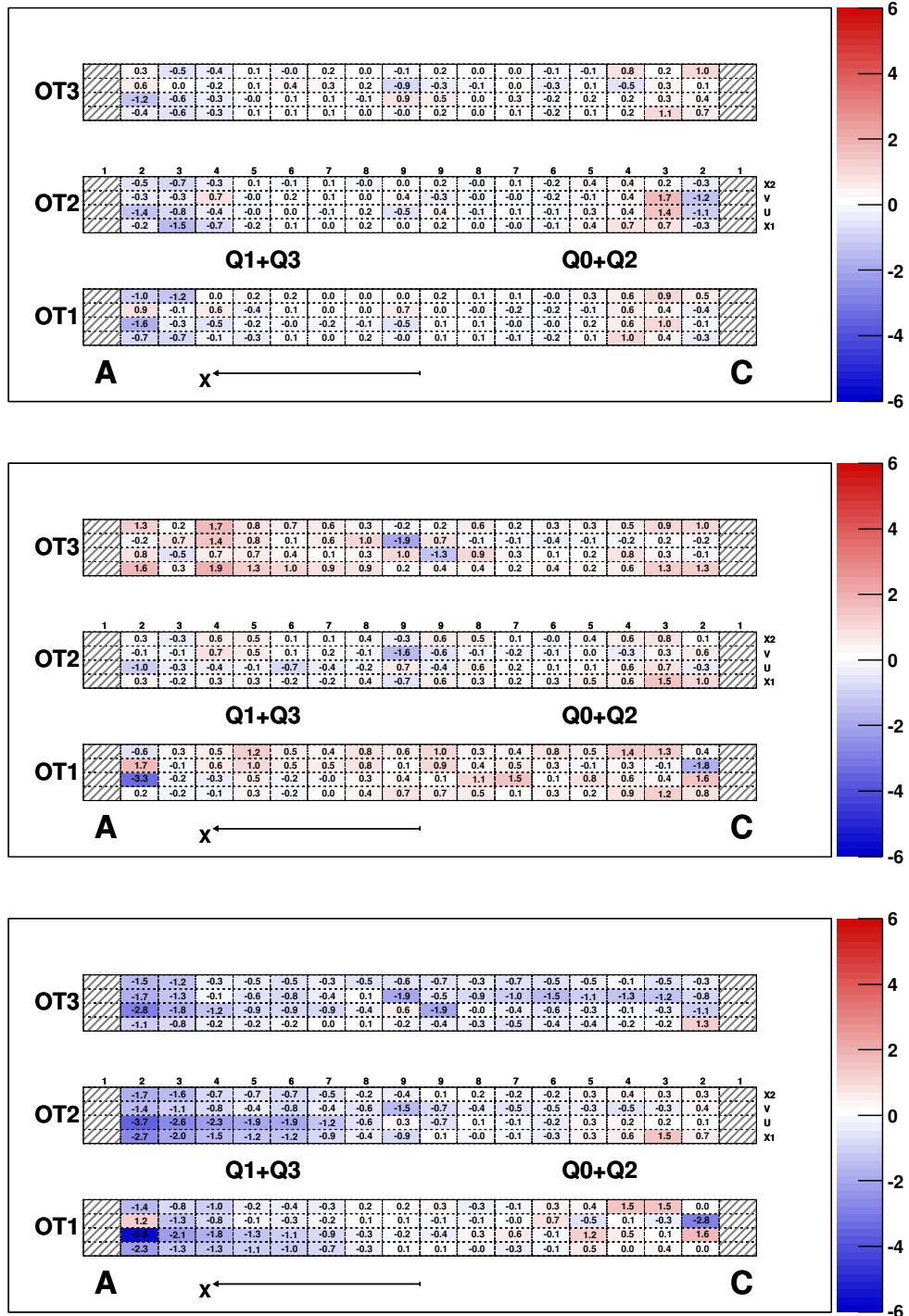
Figure B.5: 2D map of *y* positions measured using 2011 MC (*top*), 2011 (*middle*) and 2012 (*bottom*) real data samples for OT modules.
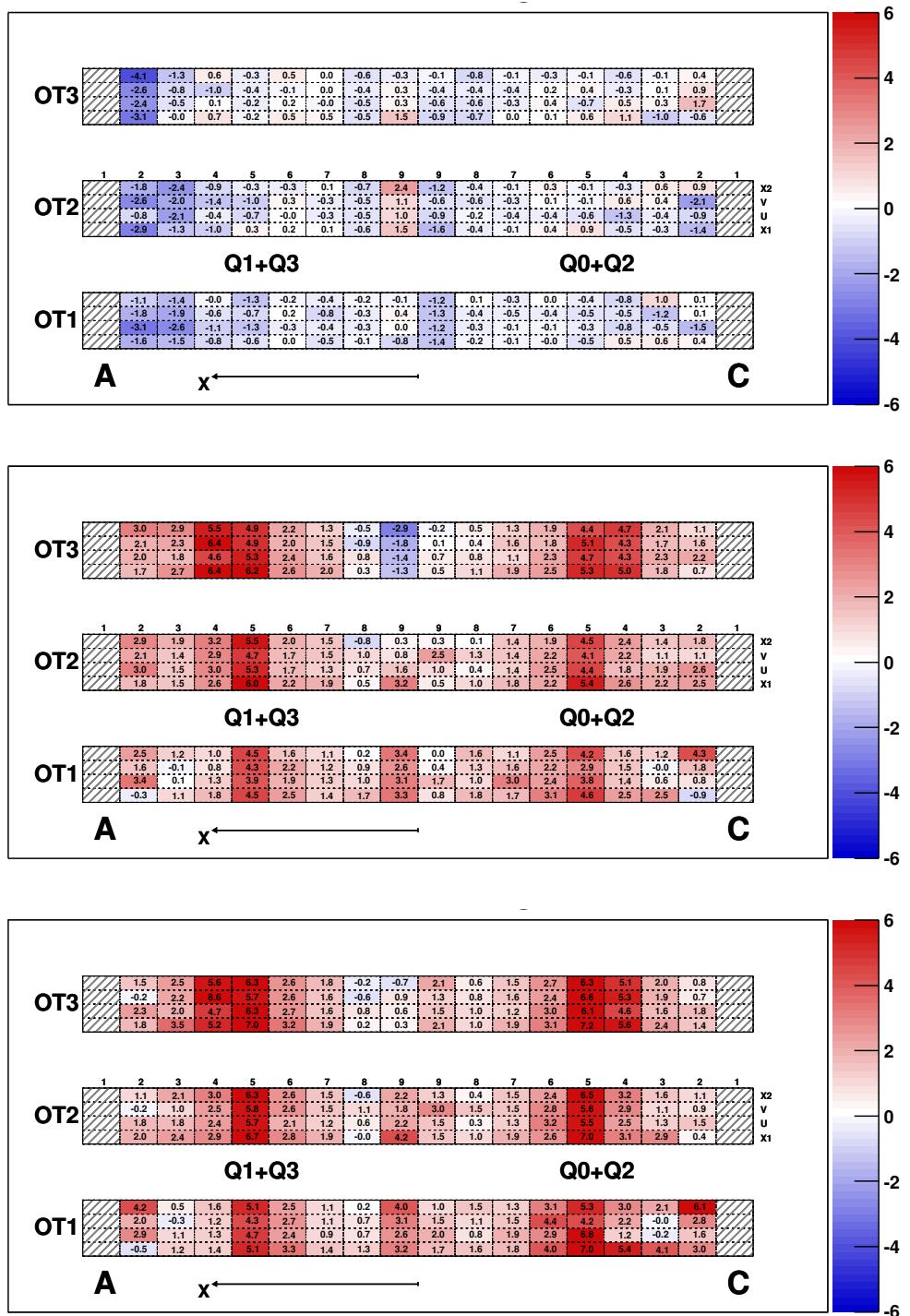
Figure B.6: 2D map of gaps widths measured using 2011 MC (*top*), 2011 (*middle*) and 2012 (*bottom*) real data samples for OT modules.
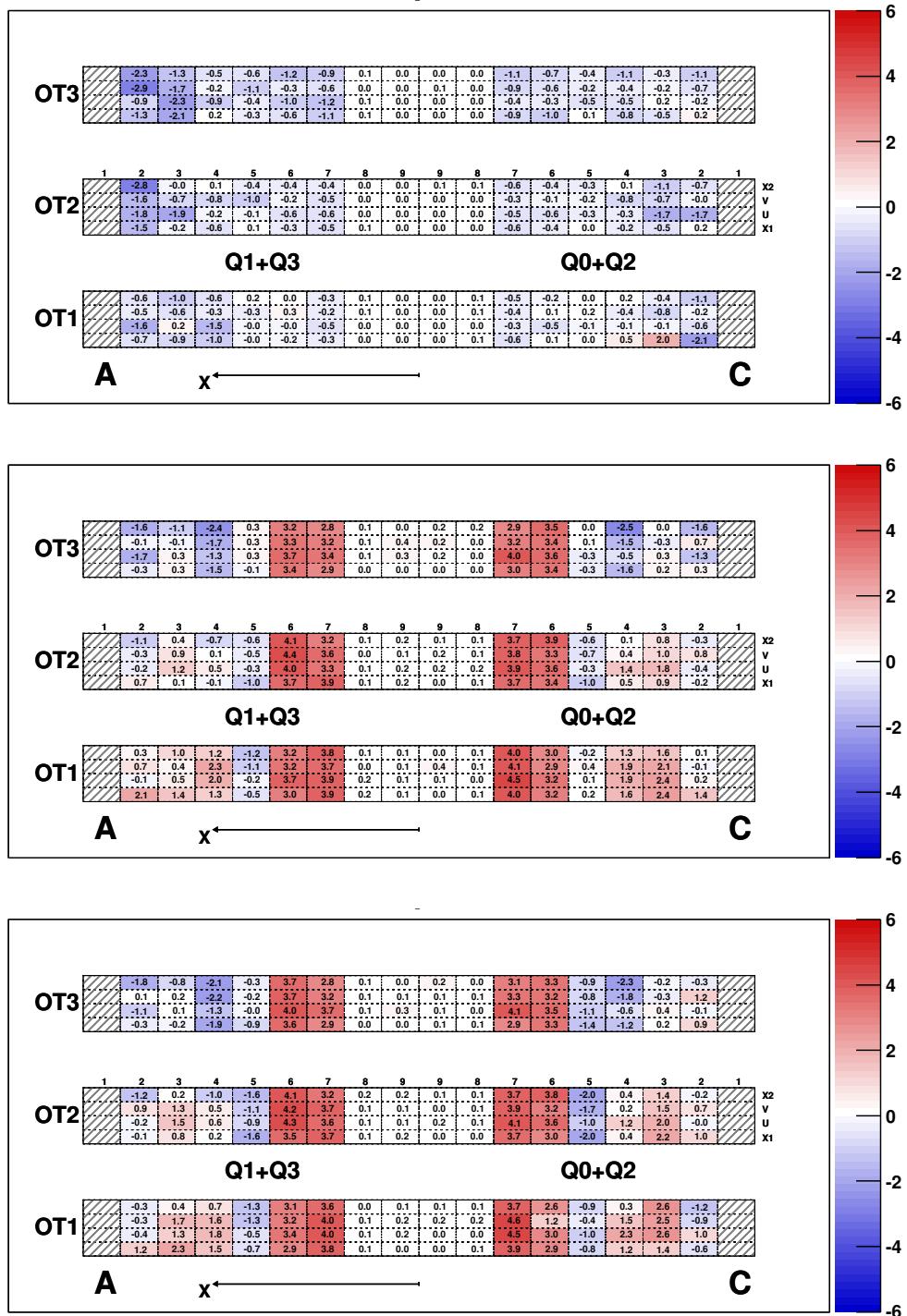
Figure B.7: 2D map of two gaps distances measured using 2011 MC (*top*), 2011 (*middle*) and 2012 (*bottom*) real data samples for OT modules.

C Legends of the reconstruction and selection step plots

$B^+ \to J/\psi K^+$ decay channel

The consecutive requirements and selections without and with corrections for Fig. 5.5:

0. No requirement
1. All tracks $2 < \eta < 4.5$, $|\text{PV}_z| < 100$ mm, muons $p_\text{T} > 550$ MeV/c, kaon $p_\text{T} > 1$ GeV/c and $p > 10$ GeV/c
2. –
3. All tracks are reconstructible as VELO segments
4. All tracks are reconstructible as long tracks
5. All tracks are reconstructed as VELO segments
6. All tracks are reconstructed as long tracks
7. All the decay chain is reconstructed
8. All tracks $\chi^2_\text{track}/\text{nDoF} < 4$
9. J/ψ $\chi^2_\text{vtx}/\text{nDoF} < 16$, mass $\in [3030; 3150]$ MeV/c^2 and muons $\Delta\ln\mathscr{L}_{\mu\pi} > 0$
10. Kaon $\Delta\ln\mathscr{L}_{K\pi} > 0$, $\Delta\ln\mathscr{L}_{Kp} > $ -2
11. –
12. B^+ $\chi^2_\text{IP} < 25$
13. B^+ $\chi^2_\text{vtx}/\text{nDoF} < 10$ and B^+ $\chi^2_\text{DTF(B+PV)}/\text{nDoF} < 5$
14. B^+ $\chi_\text{IP,next} > 50$
15. L0 triggered
16. `Hlt1DiMuonHighMass` Dec (TOS) triggered
17. `Hlt2DiMuonJPsi` TOS triggered
18. Inclusive J/ψ stripping passed
19. `Hlt2DiMuonDetachedJPsi` TOS triggered
20. Reconstructed decay time

$B^0 \to J/\psi K^{*0}$ decay channel

The consecutive requirements and selections without and with corrections for Fig. 5.6:

0. No requirement
1. All tracks $2 < \eta < 4.5$ and $|\text{PV}_z| < 100$ mm, muons $p_\text{T} > 550$ MeV/c, and kaon and pion $p_\text{T} > 300$ MeV/c
2. K^* $p_\text{T} > 1.5$ GeV/c
3. All tracks are reconstructible as VELO segments
4. All tracks are reconstructible as long tracks
5. All tracks are reconstructed as VELO segments
6. All tracks are reconstructed as long tracks
7. All the decay chain is reconstructed
8. All tracks $\chi^2_\text{track}/\text{nDoF} < 4$
9. J/ψ $\chi^2_\text{vtx}/\text{nDoF} < 16$, mass $\in [3030; 3150]$ MeV/c^2 and muons $\Delta \ln \mathcal{L}_{\mu\pi} > 0$
10. Kaon $\Delta \ln \mathcal{L}_{K\pi} > 0$, pion $\Delta \ln \mathcal{L}_{K\pi} < 0$, K^* $p_\text{T} > 1.5$ GeV/c and mass $\in [826, 966]$ MeV/c^2
11. K^* $\chi^2_\text{vtx}/\text{nDoF} < 16$ ($-$)
12. B^0 $\chi^2_\text{IP} < 25$
13. B^0 $\chi^2_\text{vtx}/\text{nDoF} < 10$ ($-$) and B^0 $\chi^2_\text{DTF(B+PV)}/\text{nDoF} < 5$
14. B^0 $\chi_\text{IP,next} > 50$
15. L0 triggered
16. `Hlt1DiMuonHighMass` Dec (TOS) triggered
17. `Hlt2DiMuonJPsi` TOS triggered
18. Inclusive J/ψ stripping passed
19. `Hlt2DiMuonDetachedJPsi` TOS triggered
20. Reconstructed decay time

$B_s^0 \rightarrow J/\psi\,\phi$ decay channel

The consecutive requirements and selections without and with corrections for Figs. 4.17, 4.20 and 5.7:

0. No requirement
1. All tracks $2 < \eta < 4.5$ and $|\mathrm{PV}_z| < 100$ mm, muons $p_\mathrm{T} > 550$ MeV/c, and kaons $p_\mathrm{T} > 250$ MeV/c
2. $\phi\ p_\mathrm{T} > 1$ GeV/c
3. All tracks are reconstructible as VELO segments
4. All tracks are reconstructible as long tracks
5. All tracks are reconstructed as VELO segments
6. All tracks are reconstructed as long tracks
7. All the decay chain is reconstructed
8. All tracks $\chi^2_\mathrm{track}/\mathrm{nDoF} < 4$
9. $J/\psi\ \chi^2_\mathrm{vtx}/\mathrm{nDoF} < 16$, mass $\in [3030; 3150]$ MeV/c^2 and muons $\Delta\ln\mathscr{L}_{\mu\pi} > 0$
10. Kaons $\Delta\ln\mathscr{L}_{K\pi} > 0$, $\phi\ p_\mathrm{T} > 1$ GeV/c and mass $\in [1008, 1032]$ MeV/c^2
11. $\phi\ \chi^2_\mathrm{vtx}/\mathrm{nDoF} < 16$ (−)
12. $B_s^0\ \chi^2_\mathrm{IP} < 25$
13. $B_s^0\ \chi^2_\mathrm{vtx}/\mathrm{nDoF} < 10$ (−) and $B_s^0\ \chi^2_\mathrm{DTF(B+PV)}/\mathrm{nDoF} < 5$
14. $B_s^0\ \chi_\mathrm{IP,next} > 50$
15. L0 triggered
16. `Hlt1DiMuonHighMass` Dec (TOS) triggered
17. `Hlt2DiMuonJPsi` TOS triggered
18. Inclusive J/ψ stripping passed
19. `Hlt2DiMuonDetachedJPsi` TOS triggered
20. Reconstructed decay time

$B^0 \to J/\psi\,K_s^0$ decay channel

The consecutive requirements and selections without and with corrections for Figs. 4.22 and 5.8:

0. No requirement
1. Muons $p_T > 550$ MeV/c, pions $p_T > 250$ MeV/c and pions $p > 2$ GeV/c
2. Muons are reconstructible as VELO segments
3. Pions are reconstructible as TT segments
4. Muons are reconstructible as long tracks and pions as downstream tracks
5. Muons are reconstructed as VELO segments
6. Muons are reconstructed as long tracks and pions as downstream tracks
7. All tracks clone distances > 5000 and $K_s^0\ \chi^2_{vtx}/$nDoF < 16 (25)
8. $J/\psi\ \chi^2_{vtx}/$nDoF < 16
9. All tracks $\chi^2_{track}/$nDoF < 4
10. K_s^0 DLS > 3 wrt B^0 vertex
11. $K_s^0\ p_T > 1$ GeV/c and mass window ± 25 MeV/c^2
12. J/ψ mass $\in [3030; 3150]$ MeV/c^2
13. $B^0\ \chi^2_{vtx}/$nDoF < 10 (25)
14. $B^0\ \chi^2_{IP} < 25$, $\chi^2_{DTF(B+PV)}/$nDoF < 4 and mass $\in [5150, 5340]$ MeV/c^2
15. $B^0\ \chi_{IP,next} > 50$
16. L0 triggered
17. `Hlt1DiMuonHighMass` TOS triggered
18. `Hlt2DiMuonJPsi` TOS triggered

$\Lambda_b^0 \to J/\psi\,\Lambda$ decay channel

The consecutive requirements and selections without and with corrections for Fig. 5.9:

0. No requirement
1. Muons $p_T > 550$ MeV/c, proton $p_T > 500$ MeV/c, pion $p_T > 100$ MeV/c, and protons and pions $p > 2$ GeV/c
2. Muons are reconstructible as VELO segments
3. Proton and pion are reconstructible as TT segments
4. Muons are reconstructible as long tracks, and proton and pion as downstream tracks
5. Muons are reconstructed as VELO segments
6. Muons are reconstructed as long tracks, and proton and pion as downstream tracks
7. All tracks clone distances > 5000 and Λ $\chi^2_{\mathrm{vtx}}/\mathrm{nDoF} < 16$ (25)
8. J/ψ $\chi^2_{\mathrm{vtx}}/\mathrm{nDoF} < 16$
9. All tracks $\chi^2_{\mathrm{track}}/\mathrm{nDoF} < 4$
10. Λ DLS > 3 wrt Λ_b^0 vertex
11. Λ $p_T > 1$ GeV/c and mass window ± 6 MeV/c^2
12. J/ψ mass $\in [3030; 3150]$ MeV/c^2
13. Λ_b^0 $\chi^2_{\mathrm{vtx}}/\mathrm{nDoF} < 10$ (25)
14. Λ_b^0 $\chi^2_{\mathrm{IP}} < 25$, $\chi^2_{\mathrm{DTF(B+PV)}}/\mathrm{nDoF} < 4$ and mass $\in [5500, 5740]$ MeV/c^2
15. Λ_b^0 $\chi_{\mathrm{IP,next}} > 50$
16. L0 triggered
17. `Hlt1DiMuonHighMass` TOS triggered
18. `Hlt2DiMuonJPsi` TOS triggered

# D Decay time resolution for b hadrons decaying a K^0_S meson
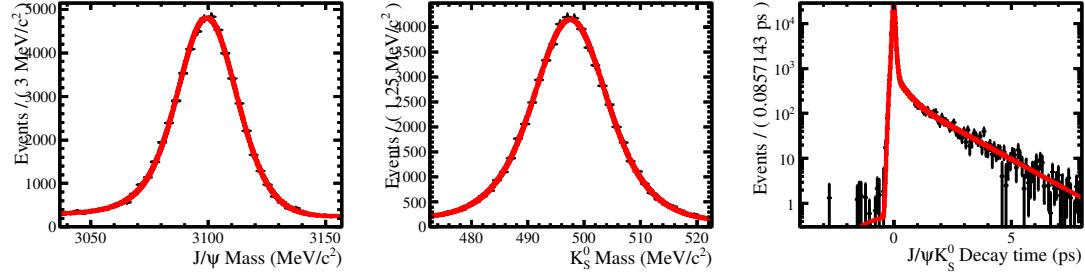
Figure D.1: J/ψ mass distribution (*left*), K^0_S mass distribution (*middle*) and $J/\psi+K^0_S$ sWeighted decay time distribution for $B^0 \to J/\psi\,K^0_S$ decays from the high p_T J/ψ stripping with LL K^0_S.

Figure D.2: J/ψ mass distribution (*left*), K^0_S mass distribution (*middle*) and $J/\psi+K^0_S$ sWeighted decay time distribution for $B^0 \to J/\psi\,K^0_S$ decays from the exclusive stripping with LL K^0_S.

Figure D.3: J/ψ mass distribution (*left*), K_S^0 mass distribution (*middle*) and $J/\psi+K_S^0$ sWeighted decay time distribution for $B^0 \rightarrow J/\psi K_S^0$ decays from the high p_T J/ψ stripping with DD K_S^0.
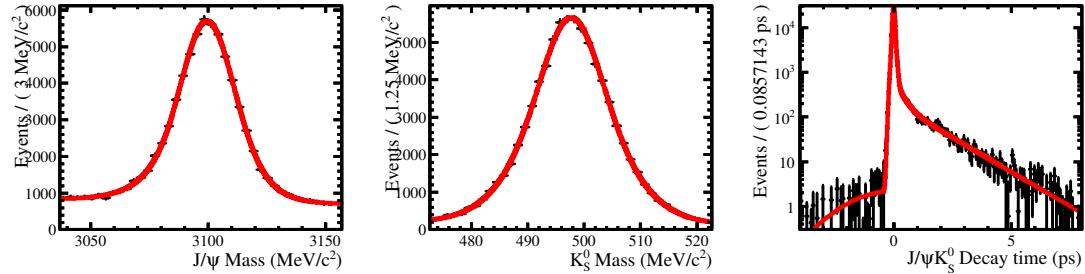
Figure D.4: J/ψ mass distribution (*left*), K_S^0 mass distribution (*middle*) and $J/\psi+K_S^0$ sWeighted decay time distribution for $B^0 \rightarrow J/\psi K_S^0$ decays from the exclusive stripping with DD K_S^0.


Figure D.5: J/ψ mass distribution (*left*), K_S^0 mass distribution (*middle*) and $J/\psi+K_S^0$ sWeighted decay time distribution for $B^0 \rightarrow J/\psi K_S^0$ decays from the high p_T J/ψ stripping with LL+DD K_S^0.
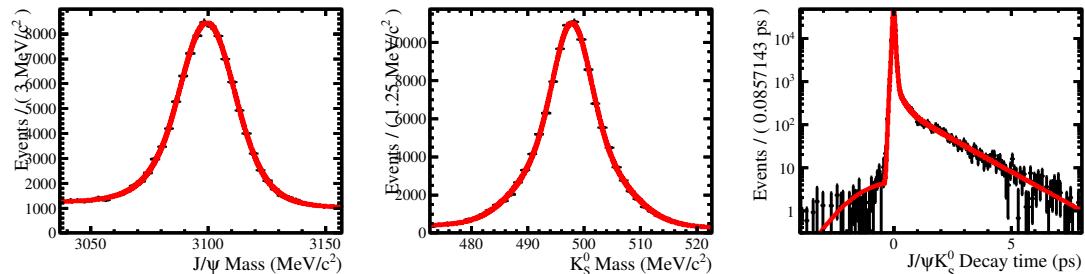
Figure D.6: J/ψ mass distribution (*left*), K_S^0 mass distribution (*middle*) and $J/\psi+K_S^0$ sWeighted decay time distribution for $B^0 \rightarrow J/\psi K_S^0$ decays from the exclusive stripping with LL+DD K_S^0.
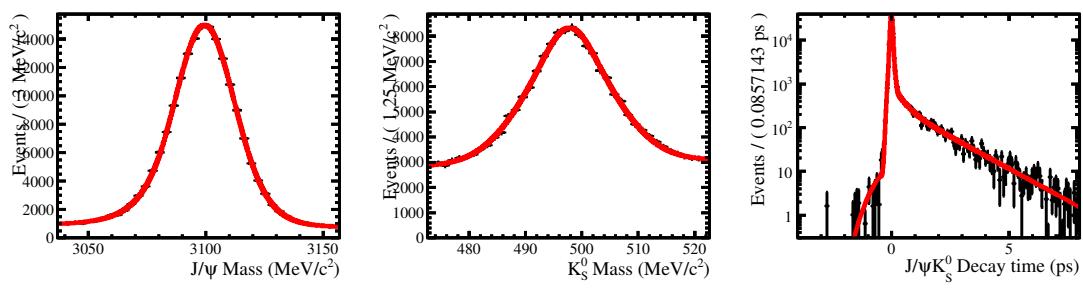
Figure D.7: J/ψ mass distribution (*left*), K_S^0 mass distribution (*middle*) and $J/\psi+K_S^0$ sWeighted decay time distribution for $B^0 \to J/\psi K_S^0$ decays from the high p_T J/ψ stripping with FullDD K_S^0.

# E Mass and decay time projections using the sFit technique
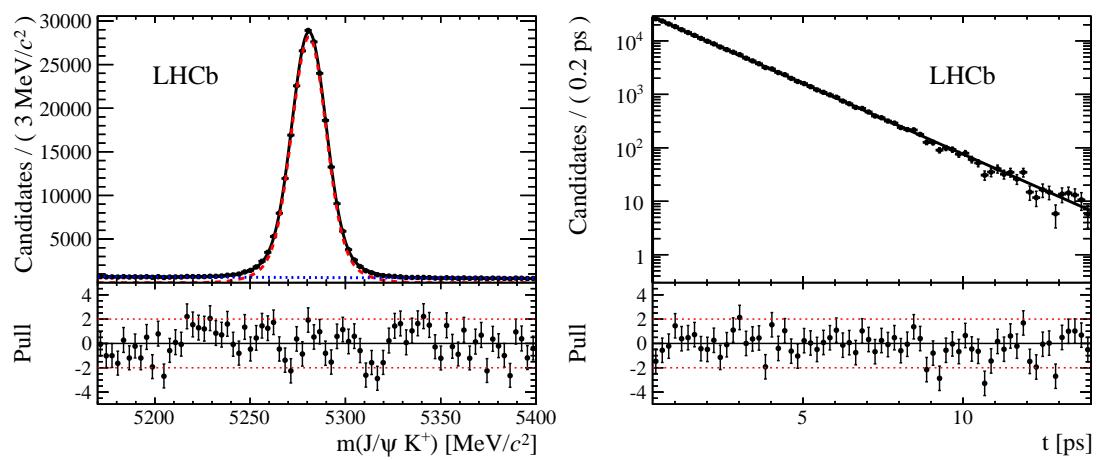
Figure E.1: Distributions of mass (*left*) and decay time (*right*) for $B^+ \rightarrow J/\psi\,K^+$ where the black points are the data, the dashed red line is the signal shape, the dotted blue line is the background shape and the black line is the sum of the two obtained by the sFit technique.
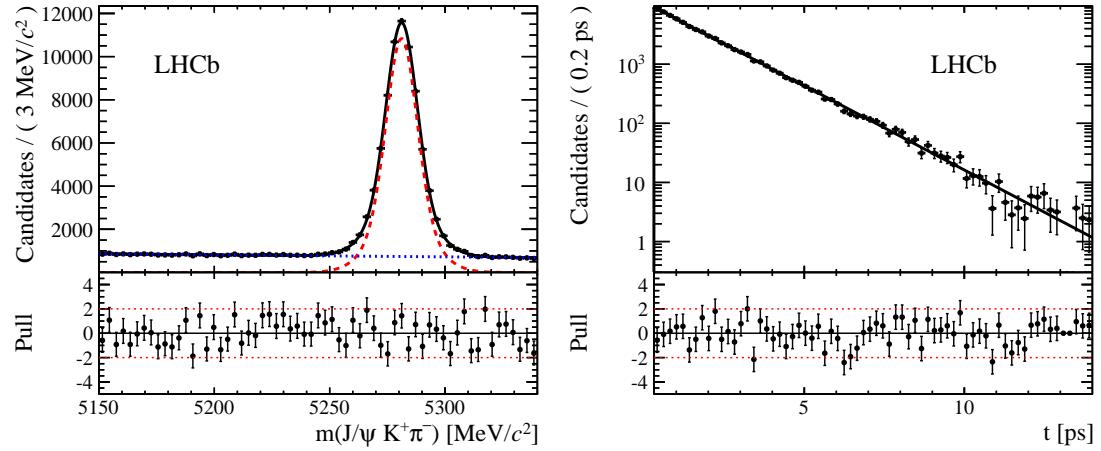
Figure E.2: Distributions of mass (*left*) and decay time (*right*) for $B^0 \to J/\psi\, K^{*0}$ where the black points are the data, the dashed red line is the signal shape, the dotted blue line is the background shape and the black line is the sum of the two obtained by the sFit technique.
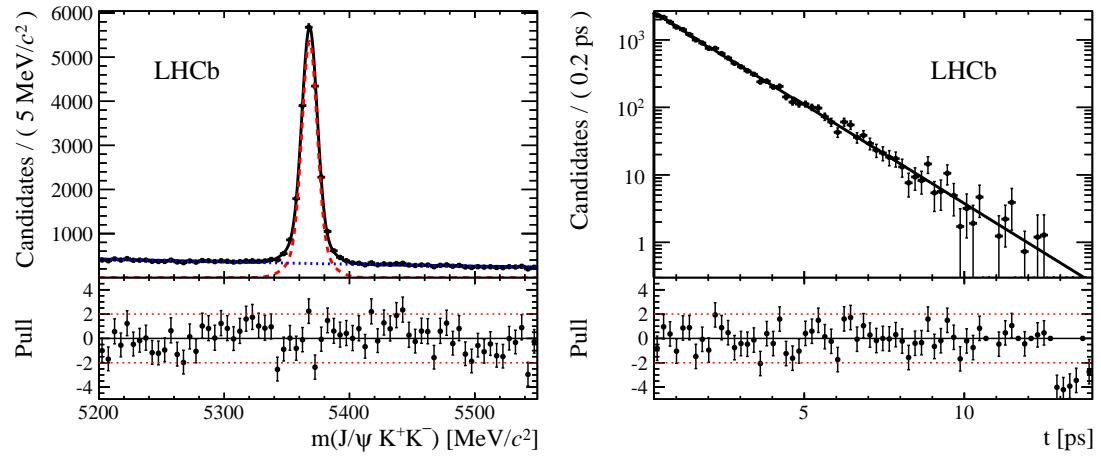
Figure E.3: Distributions of mass (*left*) and decay time (*right*) for $B^0_s \to J/\psi\, \phi$ where the black points are the data, the dashed red line is the signal shape, the dotted blue line is the background shape and the black line is the sum of the two obtained by the sFit technique.

144
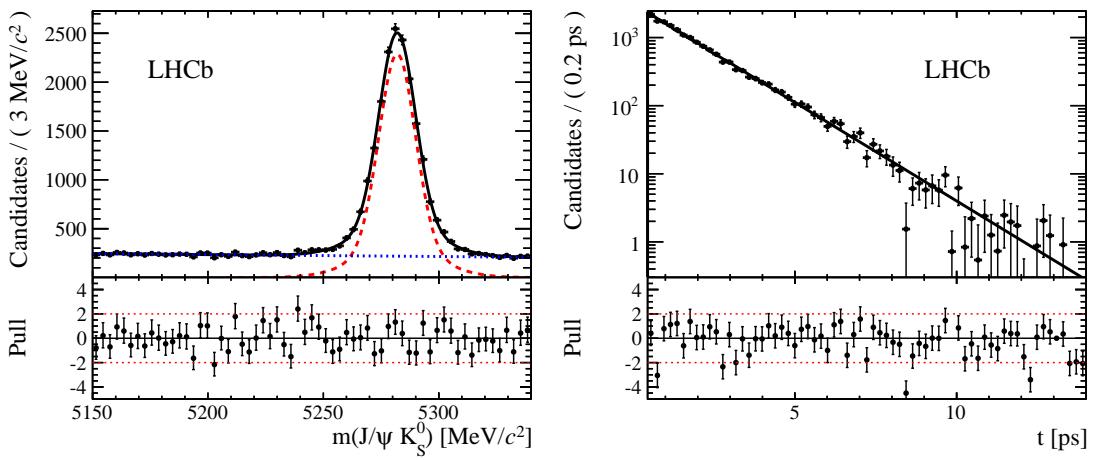
Figure E.4: Distributions of mass (*left*) and decay time (*right*) for $B^0 \rightarrow J/\psi K_S^0$ where the black points are the data, the dashed red line is the signal shape, the dotted blue line is the background shape and the black line is the sum of the two obtained by the sFit technique.
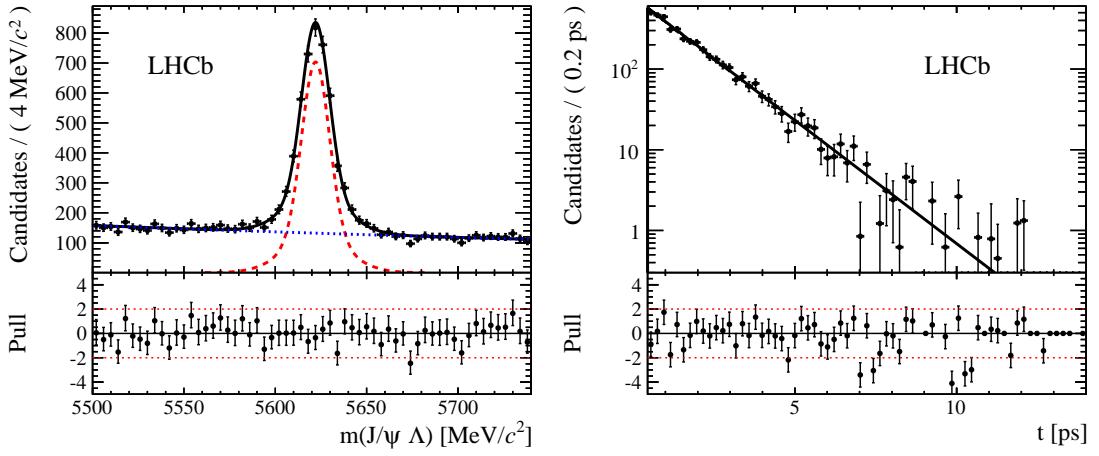

Figure E.5: Distributions of mass (*left*) and decay time (*right*) for $\Lambda_b^0 \rightarrow J/\psi \Lambda$ where the black points are the data, the dashed red line is the signal shape, the dotted blue line is the background shape and the black line is the sum of the two obtained by the sFit technique.

145

# F Decay time distributions in the mass sidebands
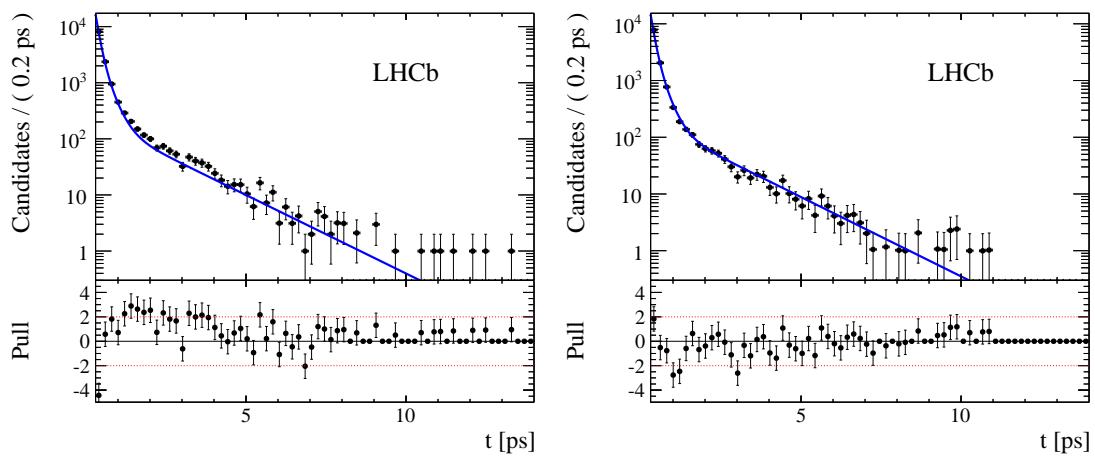
Figure F.1: Decay time distribution in the lower (*left*) and upper (*right*) mass sidebands with the background shape is overlay for $B^+ \to J/\psi\, K^+$ decays.
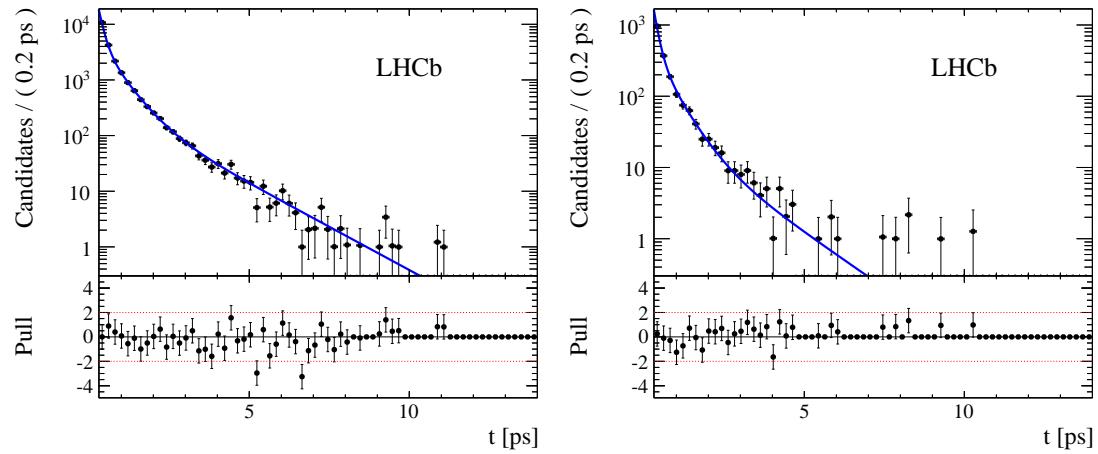
Figure F.2: Decay time distribution in the lower (*left*) and upper (*right*) mass sidebands with the background shape is overlay for $B^0 \to J/\psi K^{*0}$ decays.
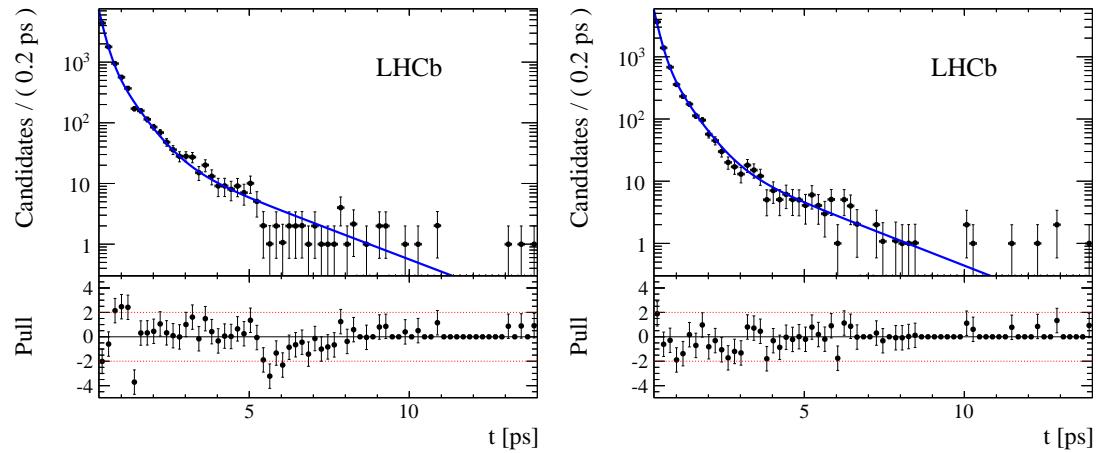
Figure F.3: Decay time distribution in the lower (*left*) and upper (*right*) mass sidebands with the background shape is overlay for $B_s^0 \to J/\psi \phi$ decays.
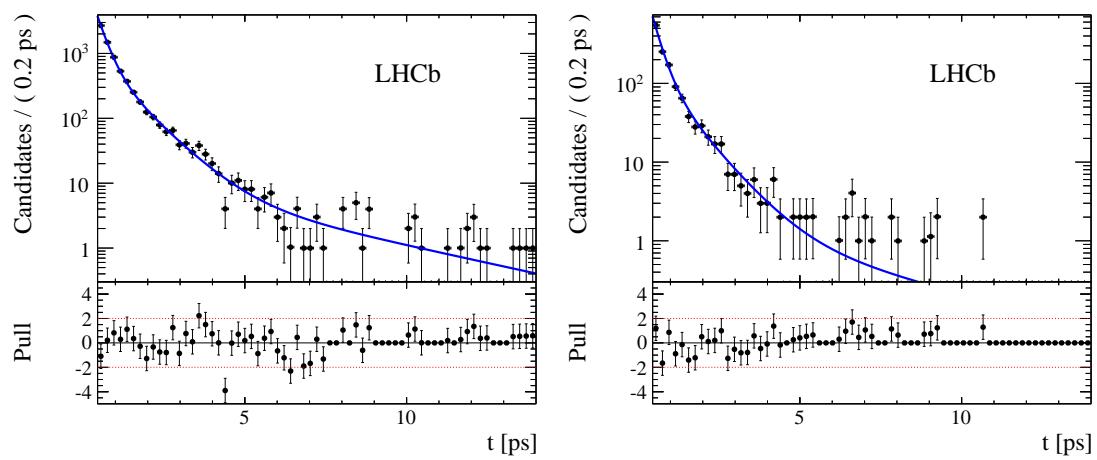
Figure F.4: Decay time distribution in the lower (*left*) and upper (*right*) mass sidebands with the background shape is overlay for $B^0 \to J/\psi K^0_S$ decays.
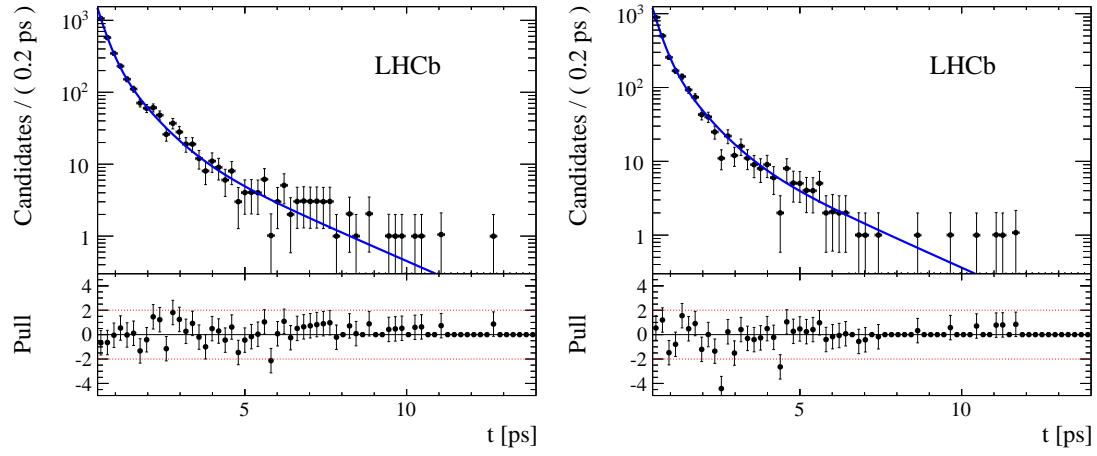

Figure F.5: Decay time distribution in the lower (*left*) and upper (*right*) mass sidebands with the background shape is overlay for $\Lambda^0_b \to J/\psi \Lambda$ decays.

G Lifetime and lifetime ratio with b production asymmetry

$B^0 \to J/\psi\, K^0_S$ lifetime

Assuming no direct and indirect CP violation for a decay to a CP-odd final state $B^0 \to J/\psi\, K^0_S$ ($A_f = \cos(2\beta)$, $C_f = 0$, $S_f = \sin(2\beta)$), the untagged time-dependant decay rates 5.1 and 5.2 are reducing, in presence of a production asymmetry A_p, to

$$\frac{\mathrm{d}\Gamma(f)}{\mathrm{d}t} = N_f |A_f|^2 e^{-\Gamma_d t}(1 - A_p S_f \sin\Delta m_d t). \tag{G.1}$$

The effective lifetime $\tau^{\mathrm{eff}}_{f_{CP}}$ for $B^0 \to J/\psi\, K^0_S$ are given by

$$\tau^{\mathrm{eff}}_{f_{CP}} = \frac{\int_0^\infty t\, \frac{\mathrm{d}\Gamma(f_{CP})}{\mathrm{d}t}\, \mathrm{d}t}{\int_0^\infty \frac{\mathrm{d}\Gamma(f_{CP})}{\mathrm{d}t}\, \mathrm{d}t} = \frac{\int_0^\infty t\, e^{-\Gamma_d t}(1 - A_p S_f \sin\Delta m_d t)\, \mathrm{d}t}{\int_0^\infty e^{-\Gamma_d t}(1 - A_p S_f \sin\Delta m_d t)\, \mathrm{d}t}, \tag{G.2}$$

where the integrals are

$$\int_0^\infty e^{-\Gamma_d t}\, \mathrm{d}t = \frac{1}{\Gamma_d}, \tag{G.3}$$

$$\int_0^\infty t\, e^{-\Gamma_d t}\, \mathrm{d}t = \frac{1}{\Gamma_d^2}, \tag{G.4}$$

$$\int_0^\infty e^{-\Gamma_d t} \sin\Delta m_d t\, \mathrm{d}t = \frac{\Delta m_d}{\Gamma_d^2 + \Delta m_d^2}, \tag{G.5}$$

$$\int_0^\infty t\, e^{-\Gamma_d t} \sin\Delta m t\, \mathrm{d}t = \frac{2\Gamma_d \Delta m_d}{(\Gamma_d^2 + \Delta m_d^2)^2}. \tag{G.6}$$

Appendix G. Lifetime and lifetime ratio with b production asymmetry

The effective lifetime $\tau^{\text{eff}}_{f_{CP}}$ is further developed for a small production asymmetry ($A_p << 1$):

$$\tau^{\text{eff}}_f = \frac{1}{\Gamma_d} \frac{1 - A_p S_f \frac{2\Gamma_d^3 \Delta m_d}{(\Gamma_d^2 + \Delta m_d^2)^2}}{1 - A_p S_f \frac{\Gamma_d \Delta m_d}{\Gamma_d^2 + \Delta m_d^2}} \approx \frac{1}{\Gamma_d} \left[1 - A_p S_f \left(\frac{2\Gamma_d^3 \Delta m_d}{(\Gamma_d^2 + \Delta m_d^2)^2} - \frac{\Gamma_d \Delta m_d}{\Gamma_d^2 + \Delta m_d^2} \right) \right]$$

$$= \frac{1}{\Gamma_d} \left(1 - A_p S_f \frac{\Gamma_d \Delta m_d (\Gamma_d^2 - \Delta m_d^2)}{(\Gamma_d^2 + \Delta m_d^2)^2} \right) \tag{G.7}$$

where the approximation $\frac{1}{1 \pm x} = 1 \mp x + \mathcal{O}(x^2)$ is used.

$\tau_{B^0} / \tau_{\overline{B}^0}$ lifetime ratio

Assuming no direct and indirect CP violation for a flavour specific $B^0 \to J/\psi K^{*0}$ decay ($A_f = 0$, $C_f = 1$, $S_f = 0$), the untagged time-dependant decay rates 5.1 and 5.2 are reducing, in presence of a production asymmetry A_p, to

$$\frac{\mathrm{d}\Gamma(f)}{\mathrm{d}t} = N_f |A_f|^2 e^{-\Gamma_d t} (1 + A_p \cos \Delta m_d t), \tag{G.8}$$

$$\frac{\mathrm{d}\Gamma(\overline{f})}{\mathrm{d}t} = N_f |A_f|^2 e^{-\Gamma_d t} (1 - A_p \cos \Delta m_d t). \tag{G.9}$$

The effective lifetimes $\tau^{\text{eff}}_{f,\overline{f}}$ for final states f or $\overline{f}$ are given by

$$\tau^{\text{eff}}_{f,\overline{f}} = \frac{\int_0^\infty t \, \frac{\mathrm{d}\Gamma(f,\overline{f})}{\mathrm{d}t} \, \mathrm{d}t}{\int_0^\infty \frac{\mathrm{d}\Gamma(f,\overline{f})}{\mathrm{d}t} \, \mathrm{d}t} = \frac{\int_0^\infty t \, e^{-\Gamma_d t} (1 \pm A_p \cos \Delta m_d t) \, \mathrm{d}t}{\int_0^\infty e^{-\Gamma_d t} (1 \pm A_p \cos \Delta m_d t) \, \mathrm{d}t}, \tag{G.10}$$

where the integrals are

$$\int_0^\infty e^{-\Gamma_d t} \, \mathrm{d}t = \frac{1}{\Gamma_d}, \tag{G.11}$$

$$\int_0^\infty t \, e^{-\Gamma_d t} \, \mathrm{d}t = \frac{1}{\Gamma_d^2}, \tag{G.12}$$

$$\int_0^\infty e^{-\Gamma_d t} \cos \Delta m t \, \mathrm{d}t = \frac{\Gamma_d}{\Gamma_d^2 + \Delta m_d^2}, \tag{G.13}$$

$$\int_0^\infty t \, e^{-\Gamma_d t} \cos \Delta m t \, \mathrm{d}t = \frac{\Gamma_d^2 - \Delta m_d^2}{(\Gamma_d^2 + \Delta m_d^2)^2}. \tag{G.14}$$

The effective lifetimes $\tau_{f,\bar{f}}^{\text{eff}}$ are further developed for a small production asymmetry ($A_p << 1$):

$$\tau_f^{\text{eff}} = \frac{1}{\Gamma_d} \frac{1 \pm A_p \frac{\Gamma_d^2(\Gamma_d^2 - \Delta m_d^2)}{(\Gamma_d^2 + \Delta m_d^2)^2}}{1 \pm A_p \frac{\Gamma_d^2}{\Gamma_d^2 + \Delta m_d^2}} \approx \frac{1}{\Gamma_d} \left[1 \pm A_p \left(\frac{\Gamma_d^2(\Gamma_d^2 - \Delta m_d^2)}{(\Gamma_d^2 + \Delta m_d^2)^2} - \frac{\Gamma_d^2}{\Gamma_d^2 + \Delta m_d^2} \right) \right]$$

$$= \frac{1}{\Gamma_d} \left(1 \mp 2 A_p \frac{\Gamma_d^2 \Delta m_d^2}{(\Gamma_d^2 + \Delta m_d^2)^2} \right) \tag{G.15}$$

where the approximation $\frac{1}{1 \pm x} = 1 \mp x + \mathcal{O}(x^2)$ is used. Finally, the lifetime ratio $\tau_{B^0} / \tau_{\overline{B}^0}$ is given by

$$\frac{\tau_{B^0}}{\tau_{\overline{B}^0}} = \frac{1 - 2 A_p \frac{\Gamma_d^2 \Delta m_d^2}{(\Gamma_d^2 + \Delta m_d^2)^2}}{1 + 2 A_p \frac{\Gamma_d^2 \Delta m_d^2}{(\Gamma_d^2 + \Delta m_d^2)^2}} \approx 1 - 4 A_p \frac{\Gamma_d^2 \Delta m_d^2}{(\Gamma_d^2 + \Delta m_d^2)^2} \tag{G.16}$$

where the approximation $\frac{1}{1 \pm x} = 1 \mp x + \mathcal{O}(x^2)$ is again used.

Bibliography

[1] S. Glashow, *Partial-symmetries of weak interactions*, Nucl. Phys. **22 (4)** (1961) 579.

[2] S. Weinberg, *A model of leptons*, Phys. Rev. Lett. **19 (21)** (1967) 1264.

[3] A. Salam, *Elementary particle physics: relativistic groups and analyticity*, proceedings of the 8$^{\text{th}}$ Nobel symposium (1968) 367.

[4] F. Englert and R. Brout, *Broken symmetry and the mass of gauge vector mesons*, Phys. Rev. Lett. **13 (9)** (1964) 321.

[5] P. Higgs, *Broken symmetries and the masses of gauge bosons*, Phys. Rev. Lett. **13 (16)** (1964) 508.

[6] G. Guralnik, C. Hagen, and T. Kibble, *Global conservation laws and massless p articles*, Phys. Rev. Lett. **13 (20)** (1964) 585.

[7] ATLAS collaboration, G. Aad *et al.*, *Observation of a new particle in the search for the Standard Model Higgs boson with the ATLAS detector at the LHC*, Phys. Lett. **B716** (2012) 1, `arXiv:1207.7214`.

[8] CMS collaboration, S. Chatrchyan *et al.*, *Observation of a new boson at a mass of 125 GeV with the CMS experiment at the LHC*, Phys. Lett. **B716** (2012) 30, `arXiv:1207.7235`.

[9] N. Cabibbo, *Unitary Symmetry and Leptonic Decays*, Phys. Rev. Lett. **10** (1963) 531.

[10] M. Kobayashi and T. Toshihide Maskawa, *CP Violation in the Renormalizable Theory of Weak Interaction*, Prog. Theor. Phys. **49** (1973) 652.

[11] L. L. Chau and W. Y. Keung, *Comments on the Parametrization of the Kobayashi-Maskawa Matrix*, Phys. Rev. Lett. **53** (1984) 1802–1805.

[12] L. Wolfenstein, *Parametrization of the Kobayashi-Maskawa Matrix*, Phys. Rev. Lett. **51** (1983) 1945–1947.

[13] A. J. Buras *et al.*, *Waiting for the Top Quark Mass, $K^+ \to \pi^+ \nu\overline{\nu}$, $B_s^0 - \overline{B}_s^0$ Mixing and CP Asymmetries in B-Decays*, Phys. Rev. **D50** (1994) 3433, `arXiv:hep-ph/9403384`.

Bibliography

[14] J. Charles *et al.*, *Predictions of selected flavour observables within the Standard Model*, Phys. Rev. **D84** (2011) 033005, `arXiv:1106.4041`, with updated results and plots available at http://ckmfitter.in2p3.fr.

[15] A. Ceccucci, Z. Ligeti, and Y. Sakai, *The CKM quark-mixing matrix*, published in Ref. [68].

[16] D. Kirkby and Y. Nir, *CP violation in meson decays*, published in Ref. [68].

[17] O. Schneider, $B^0 - \overline{B}^0$ *mixing*, published in Ref. [68].

[18] T. Nakada, *Physics of atoms, nuclei and elementary particles*, EPFL lecture notes.

[19] T. Nakada, *CP violation, current status and future prospect*, Lecture given at the Vth Moscow School of Physics, XXXth ITEP Winter School of Physics, Feb. 2012.

[20] S. Ali, E. Rodrigues, and M. Schiller, *Time-dependent cp measurements: Master equations and conventions*, LHCb-PUB-2011-002.

[21] LHCb collaboration, R. Aaij *et al.*, *Measurement of CP-violation and the B_s^0-meson decay width difference with $B_s^0 \to J/\psi K^+ K^-$ and $B_s^0 \to J/\psi \pi^+ \pi^-$ decays*, Phys. Rev. **D87** (2013) 112010, `arXiv:1304.2600`.

[22] ALICE collaboration, L. Evans and P. Bryant, *LHC Machine*, JINST **3** (2008) S08001.

[23] ATLAS collaboration, G. Aad *et al.*, *The ATLAS Experiment at the CERN Large Hadron Collider*, JINST **3** (2008) S08003.

[24] CMS collaboration, S. Chatrchyan *et al.*, *The CMS experiment at the CERN LHC*, JINST **3** (2008) S08004.

[25] ALICE collaboration, S. Chatrchyan *et al.*, *The ALICE experiment at the CERN LHC*, JINST **3** (2008) S08002.

[26] A. Kozlinskiy, *Outer Tracker calibration and open charm production cross section measurement at LHCb*, PhD thesis, Vrije University of Amsterdam, 2012, CERN-THESIS-2012-338.

[27] LHCb collaboration, A. A. Alves Jr. *et al.*, *The LHCb detector at the LHC*, JINST **3** (2008) S08005.

[28] LHCb collaboration, P. R. Barbosa Marinho *et al.*, *LHCb VELO (VErtex LOcator) : Technical Design Report*, CERN-LHCC-2001-011.

[29] LHCb collaboration, R. Antunes Nobrega *et al.*, *LHCb reoptimized detector design and performance : Technical Design Report*, CERN-LHCC-2003-030.

[30] LHCb collaboration, A. Franca Barbosa *et al.*, *LHCb inner tracker : Technical Design Report*, CERN-LHCC-2002-029.

[31] LHCb collaboration, P. R. Barbosa Marinho *et al.*, *LHCb outer tracker : Technical Design Report*, CERN-LHCC-2001-024.

[32] A. Powell *et al.*, *Particle identification at LHCb*, PoS **ICHEP2010** (2010) 020, LHCb-PROC-2011-008.

[33] LHCb collaboration, S. Amato *et al.*, *LHCb calorimeters : Technical Design Report*, CERN-LHCC-2000-036.

[34] A. A. Alves Jr *et al.*, *Performance of the LHCb muon system*, JINST **8** (2013) P02022, `arXiv:1211.1346`.

[35] LHCb collaboration, R. Antunes Nobrega *et al.*, *LHCb trigger system : Technical Design Report*, CERN-LHCC-2003-031.

[36] The LHCb collaboration, *MOORE - The LHCb Trigger Program*, http://lhcb-release-area.web.cern.ch/LHCb-release-area/DOC/moore/.

[37] The LHCb collaboration, *BRUNEL - The LHCb Reconstruction Program*, http://lhcb-release-area.web.cern.ch/LHCb-release-area/DOC/brunel/.

[38] The LHCb collaboration, *DAVINCI - The LHCb Analysis Program*, http://lhcb-release-area.web.cern.ch/LHCb-release-area/DOC/davinci/.

[39] ROOT web site. http://root.cern.ch/.

[40] RooFit web site. http://root.cern.ch/drupal/content/roofit.

[41] T. Sjöstrand, S. Mrenna, and P. Skands, *PYTHIA 6.4 physics and manual*, JHEP **05** (2006) 026, `arXiv:hep-ph/0603175`.

[42] I. Belyaev *et al.*, *Handling of the generation of primary events in* GAUSS*, the LHCb simulation framework*, Nuclear Science Symposium Conference Record (NSS/MIC) **IEEE** (2010) 1155.

[43] D. J. Lange, *The EvtGen particle decay simulation package*, Nucl. Instrum. Meth. **A462** (2001) 152.

[44] P. Golonka and Z. Was, *PHOTOS Monte Carlo: a precision tool for QED corrections in Z and W decays*, Eur. Phys. J. **C45** (2006) 97, `arXiv:hep-ph/0506026`.

[45] Geant4 collaboration, J. Allison *et al.*, *Geant4 developments and applications*, IEEE Trans. Nucl. Sci. **53** (2006) 270.

[46] Geant4 collaboration, S. Agostinelli *et al.*, *Geant4: a simulation toolkit*, Nucl. Instrum. Meth. **A506** (2003) 250.

[47] M. Clemencic *et al.*, *The LHCb simulation application,* GAUSS*: design, evolution and experience*, J. Phys. Conf. Ser. **331** (2011) 032023.

[48] The LHCb collaboration, *BOOLE - The LHCb Digitalisation Program*, http://lhcb-release-area.web.cern.ch/LHCb-release-area/DOC/boole/.

Bibliography

[49] LHCb collaboration, R. Aaij *et al.*, *Prompt K_S^0 production in pp collisions at $\sqrt{s} = 0.9$ TeV*, Phys. Lett. **B693** (2010) 69, `arXiv:1008.3105`.

[50] S. Löchner and M. Schmelling, *The Beetle Reference Manual - chip version 1.3, 1.4 and 1.5*, LHCb-2005-105.

[51] D. Esperante Pereira, *Design and Development of Electronics and the Control Software for the Silicon Tracker of LHCb*, PhD thesis, Santiago de Compostela University, 2010, CERN-THESIS-2010-238.

[52] A. Vollhardt, *An Optical Readout System for the LHCb Silicon Tracker*, PhD thesis, Zurich University, 2005, CERN-THESIS-2005-025.

[53] G. Haefeli *et al.*, *The LHCb DAQ interface board TELL1*, Nucl. Instrum. Meth. **A560** (2006) 494.

[54] J. Luisier, *Configuration of TELL1 boards from XML database with PVSS*, LHCb-INT-2011-017.

[55] A. Keune *et al.*, *Emulation of the ST TELL1 Algorithms*, LHCb-INT-2011-040.

[56] J. Luisier and M. Needham, *Measurement of the Inner Tracker Efficiency*, LHCb-INT-2010-031.

[57] F. Dupertuis, *A novel alignment procedure and results for the LHCb Silicon Trcker*, Nuclear Science Symposium and Medical Imaging Conference (NSS/MIC) **2011 IEEE** (2011) 1314.

[58] V. Blobel, *Software alignment for tracking detectors*, Nucl. Instrum. Meth. **A566** (2006) 5.

[59] P. Bruckman, A. Hicheur, and S. J. Haywood, *Global χ^2 approach to the alignment of the ATLAS silicon tracking detectors*, ATL-INDET-PUB-2005-002.

[60] A. Bocci and W. Hulsbergen, *TRT alignment for SR1 cosmics and beyond*, ATL-INDET-PUB-2007-009.

[61] S. Borghi *et al.*, *First spatial alignment of the LHCb VELO and analysis of beam absorber collision data*, Nucl. Instrum. Meth. **A618** (2010) 108.

[62] J. Amoraal *et al.*, *Application of vertex and mass constraints in track-based alignment*, Nucl. Instrum. Meth. **A712** (2013) 48, `arXiv:1207.4756`.

[63] LHCb collaboration, *b-hadron lifetime measurements with exclusive $b \to J/\psi X$ decays reconstructed in the 2010 data*, LHCb-CONF-2011-001.

[64] Y. Amhis *et al.*, *b-hadrons absolute lifetime measurements*, LHCb-ANA-2011-055.

[65] V. Gligorov, C. Thomas, and M. Williams, *The HLT inclusive B triggers*, LHCb-PUB-2011-016.

[66] V. Gligorov, *A single track HLT1 trigger*, LHCb-PUB-2011-003.

[67] R. Aaij and J. Albrecht, *Muon triggers in the High Level Trigger of LHCb*, LHCb-PUB-2011-017.

[68] Particle Data Group, J. Beringer *et al.*, *Review of particle physics*, Phys. Rev. **D86** (2012) 010001 and 2013 partial update for the 2014 edition.

[69] V. V. Gligorov and M. Williams, *Efficient, reliable and fast high-level triggering using a bonsai boosted decision tree*, JINST **8** (2013) P02013, `arXiv:1210.6861`.

[70] W. Hulsbergen, *Decay chain fitting with a Kalman filter*, Nucl. Instrum. Meth. **A552** (2005) 566, `arXiv:physics/0503191`.

[71] V. Gligorov *et al.*, *Swimming: A data driven acceptance correction algorithm*, J. Phys. Conf. Ser. **396** (2012) 022016.

[72] R. Aaij *et al.*, *Tagged time-dependent angular analysis of $B_s^0 \to J/\psi \phi$ decays with 1.03 fb^{-1}*, LHCb-ANA-2012-004.

[73] O. Callot, *FastVelo, a fast and efficient pattern recognition package for the Velo*, LHCb-PUB-2011-001.

[74] M. Pivk and F. R. Le Diberder, *sPlot: a statistical tool to unfold data distributions*, Nucl. Instrum. Meth. **A555** (2005) 356, `arXiv:physics/0402083`.

[75] LHCb collaboration, R. Aaij *et al.*, *Measurements of the B^+, B^0, B_s^0 meson and Λ_b^0 baryon lifetimes*, JHEP **04** (2014) 114, `arXiv:1402.2554`.

[76] Heavy Flavor Averaging Group, Y. Amhis *et al.*, *Averages of b-hadron, c-hadron, and τ-lepton properties as of early 2012*, `arXiv:1207.1158`, updated results and plots available at: `http://www.slac.stanford.edu/xorg/hfag/`.

[77] B. Pal, S. Stone, and L. Zhang, *Measurement of the Λ_b^0 lifetime in the $J/\psi p K^-$ final state*, LHCb-ANA-2013-086.

[78] R. Fleischer and R. Knegjens, *Effective lifetimes of B_s decays and their constraints on the B_s^0-$\bar{B}_s^0$ mixing parameters*, Eur. Phys. J. **C71** (2011) 1789, `arXiv:1109.5115`.

[79] T. Gershon, *$\Delta\Gamma_d$: a forgotten null test of the standard model*, J. Phys. **G38** (2011) 015007, `arXiv:1007.5135`.

[80] A. Lenz and U. Nierste, *Theoretical update of $B_s - \bar{B}_s$ mixing*, JHEP **06** (2007) 072, `arXiv:hep-ph/0612167`.

[81] A. Lenz, *Theoretical status of B_s-mixing and lifetimes of heavy hadrons*, Nucl. Phys. Proc. Suppl. **177-178** (2008) 81, `arXiv:0705.3802`.

Bibliography

[82] A. S. Dighe, I. Dunietz, H. J. Lipkin, and J. L. Rosner, *Angular distributions and lifetime differences in $B_s \to J/\psi\phi$ decays*, Phys. Lett. **B369** (1996) 144, `arXiv:hep-ph/9511363`.

[83] Y. Xie, *sFit: a method for background subtraction in maximum likelihood fit*, `arXiv:0905.0724`.

[84] LHCb collaboration, R. Aaij *et al.*, *Measurement of the $B_s^0 \to J/\psi K_S^0$ effective lifetime*, Nucl. Phys. **B873** (2013) 275, `arXiv:1304.4500`.

[85] T. Skwarnicki, *A study of the radiative cascade transitions between the Upsilon-prime and Upsilon resonances*, PhD thesis, Institute of Nuclear Physics, Krakow, 1986, DESY-F31-86-02.

[86] D. M. Santos and F. Dupertuis, *Mass distributions marginalized over per-event errors*, submitted to Nucl. Instrum. Meth. A (2013) `arXiv:1312.5000`.

[87] LHCb collaboration, R. Aaij *et al.*, *Amplitude analysis and branching fraction measurement of $\bar{B}_s^0 \to J/\psi K^+ K^-$*, Phys. Rev. **D87** (2013) 072004, `arXiv:1302.1213`.

[88] LHCb collaboration, R. Aaij *et al.*, *First measurement of time-dependent CP violation in $B_s^0 \to K^+ K^-$ decays*, JHEP **10** (2013) 183, `arXiv:1308.1428`.

[89] LHCb collaboration, R. Aaij *et al.*, *Measurement of the B^0–$\bar{B}^0$ oscillation frequency Δm_d with the decays $B^0 \to D^- \pi^+$ and $B^0 \to J/\psi K^{*0}$*, Phys. Lett. **B719** (2013) 318, `arXiv:1210.6750`.

[90] LHCb collaboration, R. Aaij *et al.*, *Precision measurement of the $B_s^0 - \bar{B}_s^0$ oscillation frequency Δm_s in the decay $B_s^0 \to D_s^+ \pi^-$*, New J. Phys. **15** (2013) 053021, `arXiv:1304.4741`.

Frédéric Dupertuis

Physicist

Ch. de la Grosse-Pierre 6
1110 Morges
☏ +41 79 789 65 75
✉ frederic.dupertuis@gmail.com
28 year old, Swiss citizen, Single
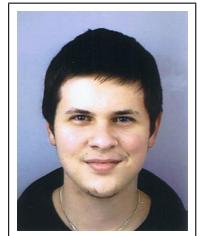
Education

Feb. 2010 - May 2014
PhD in Particle Physics, *Ecole Polytechnique Fédérale de Lausanne (EPFL)*, Switzerland.
Measurements of b-hadron lifetimes and the calibration and performance of the LHCb tracking system.

Sep. 2009 - Feb. 2010
Master Thesis in Particle Physics, *Ecole Polytechnique Fédérale de Lausanne (EPFL)*, Switzerland.
Inclusive Branching Fraction Measurement of $B \to D_s^{\pm} X$ and Search for Direct CP Violation in $B \to D_s^{(*)} D^{(*)}$ at Belle. Grade: 6.00/6.00.

Sep. 2008 - Sep. 2009
Master of Science (MSc), Physics / Engineering Physics, *Ecole Polytechnique Fédérale de Lausanne (EPFL)*, Switzerland.
Specialisation in Particle Physics. Grade: 5.40/6.00.

Oct. 2005 - Sep. 2008
Bachelor of Science (BSc), Physics, *Ecole Polytechnique Fédérale de Lausanne (EPFL)*, Switzerland.
General physics. Grade: 5.30/6.00.

Academic Experiences

Sep. 2009 - May 2014
Assistant and Tutor for Physics Lectures, Projects and Labs, *Ecole Polytechnique Fédérale de Lausanne (EPFL)*, Switzerland.
General physics, particle physics, general physics labs, nuclear physics labs and data analysis projects on LHCb.

2 Jul. 2009 - 6 Aug. 2009
CERN Summer Student, *CERN*, Geneva, Switzerland.
Working for the GEANT4 collaboration on the validation of electromagnetic models for thin layers of silicon.

Schools

6-17 Aug. 2012
2012 Fermilab-CERN Hadron Collider Physics Summer School, *Fermi National Accelerator Laboratory*, Batavia, Illinois, USA.
Various experimental and theoretical lectures on particle physics.

22-27 Jan. 2012
CHIPP PhD Winter School 2012, Engelberg, Switzerland.
Various experimental and theoretical lectures on particle physics.

2 Jul. 2009 - 6 Aug. 2009
CERN Summer Student Lectures, *CERN*, Geneva, Switzerland.
Various experimental and theoretical lectures on particle physics.

Scientific Activities

Publications (main author)

Measurements of the B^+, B^0, B_s^0 meson and Λ_b baryon lifetimes, JHEP04 (2014) 114, arXiv:1402.2554.

Mass distributions marginalized over per-event errors, Submitted to NIM, arXiv:1312.5000.

Measurement of CP-violation and the B_s^0-meson decay width difference with $B_s^0 \to J/\psi K^+ K^-$ and $B_s^0 \to J/\psi \pi^+ \pi^-$ decays, Phys. Rev. D87 (2013) 112010, arXiv:1304.2600.

Tagged time-dependent angular analysis of $B_s^0 \to J/\psi \phi$ decays with 1.03 fb^{-1} at LHCb, *conference note*, LHCb-CONF-2012-002.

Prospects for time-dependent asymmetries at LHCb, *proceedings*, CKM 2012, Seventh Workshop on the CKM Unitary Triangle, arXiv:1301.0406.

A novel alignment procedure and results for the LHCb Silicon Tracker, *proceedings*, 2011 Nuclear Science Symposium Conference Record (NSS/MIC).

Talks

Apr. 2013   **Beauty 2013, 14th International Conference on B-Physics at Hadron Machines**, Bologna, Italy.
Measurements of CP violation and mixing in B_s^0 decays at LHCb

Sep. 2012   **CKM 2012, Seventh Workshop on the CKM Unitary Triangle**, Cincinnati, Ohio, USA.
Prospects for time-dependent asymmetries at LHCb.

Jun. 2012   **2012 SPS National Conference**, Zürich, Switzerland.
Tagged time-dependent angular analysis of $B_s^0 \to J/\psi \phi$ decays at LHCb.

Apr. 2011   **2011 IEEE NSS Conference**, Valencia, Spain.
A novel alignment procedure and results for the LHCb Silicon Tracker.

Poster

Mar. 2012   **2012 LHCC students poster session**, *CERN*, Geneva, Switzerland.
Tagged time-dependent angular analysis of $B_s^0 \to J/\psi \phi$ decays at LHCb.

Skills

Software

Programming	**C++, python**	MS	**Windows, Office**
Data Analysis	**ROOT, Matlab**	Other	**LaTeX, Linux, bash, tcsh**

Languages

French	**Native**	English	**Fluent**